On Cooling Low-Dimensional Electrons

Stefanos Dimitriadis

Submitted for the degree of
Doctor of Philosophy

June 2020

I, Stefanos Dimitriadis, declare that this thesis and the work presented in it is entirely my own. Where I have consulted the work of others it is clearly stated.

_____

Stefanos Dimitriadis

Dedicated to my family and friends for their support and patience. Thank you for putting up with me, I hope we meet again soon. Finally, to my grandfather - I wish I had more time with you.

Aknowledgements

I thank my supervisor Dr James Nicholls whose support, multitude of discussions and inquisitive approach to experimentation made this work possible. I also wish to thank Dr Rais Shaikhaidarov for all the help with anything clean-room related and my adviser Prof Vladimir Antonov for always willing to help and teaching me how to bond. I am very grateful for sharing a group with Dr Jan Nyeki for his unlimited knowledge of low-temperature techniques, Dr Andrew Casey and Prof John Saunders for their expertise and discussions moving research forward. A special thanks also to John and Lev for being great mentors and friends.

None of the work would have been possible without the wafers grown in the Cavendish Laboratory by Dr Ian Farrer and Dr Harvey Beere or the collaboration, advice and help of Dr Joanna Waldie and Dr Patrick See which was essential to this project. Patrick's fabrication quality is perhaps only rivalled by Joanna's organisation and enthusiasm to research.

I would also like to thank Prof Chris Ford for making CryoMeas, a data acquisition program for LabView which saved me from a lot of block diagram 'wire connecting' - most of the data in this thesis was taken using CryoMeas.

Grateful for the vast amounts of liquid helium provided by Harpal Sandhu, but mostly for the numerous discussions at the cryogenics facility. Many thanks also the the workshop team: Richard Elsom, Paul Bamford, Ian Higgs and John Taylor, for being uplifting as people and for their outstanding work in producing all components asked of them swiftly and to a high standard and Tom Crane for his vast knowledge and support on all things electronic.

Description of collaborations

There are many collaborations integral to my research and the success of this result. Firstly, in Royal Holloway, University of London (RHUL), the Low-Temperature and Semiconductor group, lead by Prof Saunders, held regular meetings ("ND3 meetings") to determine progress and guide experiments in the collaboration between experiments on cryostats ND3 and Kelvinox. Various meetings were held from the start of my PhD to early 2019 to track progress (typically bi-weekly) and involved Prof Saunders, Dr Andrew Casey, Dr Jan Nyeki, Dr Lev Levitin, my supervisor Dr Nicholls and, in the first year

of my studies, then post-doctoral researcher Dr John Quilter and final year PhD student, Dr Harriet van der Vliet. Dr Quilter left the semiconductor group in summer 2017 and PhD students Christopher Beauchamp and Terje Theisen joined in late 2017 and 2019, respectively.

The ND3 and ND4 cryostats are nuclear demagnatisation fridges of the RHUL Low-Temperature group. The ND3 cryostat is run by Dr Levitin and the ND4 cryostat by Dr Andrew Casey. The Kelvinox cryostat is run by the Semiconductor group of Dr Nicholls. The general idea behind this collaboration is that since the ND3 cryostat can achieve very low temperatures, but has a long turnaround time, devices can be characterised in the Kelvinox at low-temperature quickly and then swapped over to ND3 cryostat for ultra-low-temperature measurements. Later, coinciding with a fault in the liquifier facilities resulting in significant downtime of cryogen based dilution fridges, the ND4 cryostat was made available as a cryogen-free fast low-temperature platform significantly reducing turnover time.

The Cavendish Laboratory provided all the wafers used for fabrication in this thesis, fabrication on W-wafers (grown by Dr Ian Farrer) was done by then UCL collaborator Dr Creeth at the Cavendish laboratory, from 2015 up until early 2017. A low-resistance device was fabricated in early 2016, with results integral to the experiments that followed. Additionally, samples fabricated in the Assessment Laboratory, some of which were also measured at RHUL to cross-calibrate our measurements at different temperatures, were fabricated by Dr Tribble.

Subsequently, over summer 2017, samples on V-wafers (grown by Dr Harvey Beere) were fabricated by Dr See (NPL) in collaboration with Dr Waldie (Cambridge) in several batches which were characterised at RHUL. The purpose was to process the previously unused V-wafers to produce samples compatible with low-temperature research requirements. The collaboration continued after results proved successful with the production of gated devices in December 2017 compatible with our requirements for low-temperature work. Samples produced by Dr See were some of the cleanest and most consistent samples I have had the pleasure of measuring. This, combined with the enthusiasm of Dr Waldie and drive to problem-solve, advanced the understanding of the devices for both groups. The imaging work of Dr Waldie was essential to determine that our devices are no different than any other group

conducting experiments to such devices in the past 30 years. This imaging study is presented in chapter 3 (section 3.3.3).

Through the above collaboration a consistent recipe for low-resistance ohmic contacts was determined through electrical characterisation (Chapter 4) and combined with the imaging study of the contacts and an extensive literature review on the contacting mechanism and compounds in the alloy (Chapter 3) increased the understanding of ohmic contacts, a necessary but surprisingly complicated component of any device. Furthermore, this resulted in a satisfactory explanation of the resistance jump seen on the sample that achieved the μK boundary and gave an explanation to why it has been historically so hard to cool such devices (Chapter 5) - the contacts to these widely-used devices superconduct, something previously missed in the field.

Abstract

This thesis highlights the challenges faced when cooling low dimensional electrons through the progress made towards achieving the coldest possible electron temperature and optimisation of cooling methods.

AlGaAs/GaAs heterostructures are two dimensional systems and provide an interesting playground for understanding quantum mechanics. Many fundamental physical phenomena can be explored, including using common effects for thermometry, metrology studies as well as many body effects.

At low temperatures, the electrons isolate from the lattice due to phonon freezing and the main source of cooling is through leads. The two–dimensional electron gas is connected to the cryostat by AuGeNi ohmic contacts in order to conduct as well as thermalise through leads to the coldest point of a dilution refrigerator.

In order to achieve low electron temperature the contact resistance of the electrical contacts to the sample needs to be minimised. The sample itself must have high enough mobility and sufficient carrier density, while having low resistance to allow thermalisation throughout the system of study. The fabrication, use and characterisation of such devices upon investigating their compatibility with ultra-low-temperature measurements in the micro-Kelvin regime is described.

Optimisation of ohmic contacts to these devices was achieved through a systematic study of the contact resistance and investigation of the contacting mechanism. The optimal annealing condition for layered AuGeNi contacts was found to be a rapid thermal anneal at 430°C for 80 seconds, giving a reproducibly low contact resistance of 1 Ωmm. Measurement techniques at 4.2 K are compared, with direct electrical measurements made possible by a new test device giving insight into contact resistance. A study of our ohmic contact structure through systematic imaging studies (SEM/EDS) shows they are similar to those in literature.

Measurements of standard two-dimensional electron gases showed a superconducting transition below 1 K. This is due to superconductivity in the ohmic contacts to the devices, in series with the measurement, and can be observed. AuGeNi ohmic superconductivity was investigated at low-temperature on samples of different wafers, annealing conditions and geometries.

Through investigation of the contacting mechanism, drawing from literature and the study on our ohmic contacts, this superconductivity is attributed to gold-gallium compounds forming in the contact. The experimental results and their implications are discussed as well as advances to achieving the coldest possible electron temperature. The implications on cooling low-dimensional electrons to less than 1 mK are considered.

Contents

List of Figures

List of Tables

Chapter 1

Introduction

Motivations for the work described in this thesis have been to achieve low electron temperatures with an aim to investigate effects that arise in that regime and to optimise the necessary processes to achieve this goal.

The aim of the project was to investigate novel physics of low-dimensional electrons at low temperatures and measure an accurate low electron temperature for such effects. In practice, to achieve cooling of electrons to low temperatures, the samples needed to be of low total resistance. To achieve this aim, a study of the AuGeNi ohmic contacts to our devices was conducted with an aim to determine a recipe of optimal contact resistance as well as consistency of sample quality. The contact resistance is an important parameter, which is necessary to characterise and understand well as low-resistance contacts are essential for cooling, but also because the contact itself is in series with any measurement on the device. Following the optimisation of our devices, contact resistance was investigated at low temperatures.

Before presenting the details of the study and its results the necessary background theory and challenge of cooling low-dimensional devices is addressed. The chapters that follow are intended to be as stand-alone as possible. Chapter 2, drawing upon literature, introduces the samples, explains the way they were fabricated by the Cavendish Laboratory – how a low-dimensional system is achieved in practice and provides an overview of the experimental setup. Chapter 3 discusses AuGeNi ohmic contacts in detail, combining an extensive literature review on the contacting mechanism with an imaging study done in our laboratories. Chapter 4 presents methods of characterisation of devices intended for low temperatures and the results of

the study on optimising contact resistance on V-wafers, including testing and using standard (e.g. TLM, an industry method of characterisation) and non-standard methods (direct resistance measurements using a new mask designed specifically for this purpose). It presents measurements of contact resistance parameters, attempts to simplify the system (e.g. through using resistor models), and the progress made in the development of samples for ultra-low-temperature work. Chapter 5 explains the low-temperature results. It presents the results of cooling samples chosen through the characterisation of Chapter 4, and combines knowledge gained from the extensive characterisation of previous chapters to explain the significance of this study to the advances on cooling low-dimensional electrons. Chapter 6 presents further analysis done on data taken in concert with the investigation of ohmic contact superconductivity along with motivations for future work from the infrastructure already set by the work described in this thesis. Chapter 7 has conclusions of this study, with recommendations for future work at low-temperature using devices with gold-based ohmic contacts.

1.1 Semiconductors at Low-Temperature

Moore's law is a famous empirical observation that the number of transistors in an integrated circuit doubles every two years for minimum production cost. To achieve this, devices are typically made smaller, with more components stacked onto the same sample size. In this process of miniaturisation, quantum effects become relevant and the wish to implement quantum logic becomes more realistic.

In 2D systems, electrons are confined to a plane by growth and there is less chance of overall scattering by the lattice due to developments in fabrication techniques; this is called ballistic motion and improves mobility dramatically compared to 3D transistors. This is the reason why heterojunctions, as well as other 2D systems, are good candidates for extending Moore's law.

Quantum computing relies upon the use of coherent and distinct states. Such an example in a 2D semiconductor are those states arising from electron-electron interactions such as spin-chains, with potential transmission of quantum information through spin with high fidelity [1]. Interesting novel phenomena in low-dimensional systems can be discovered such as quantisation of

conductance in a magnetic field producing the fractional quantum Hall effect (FQHE), a phenomenon of 2D electron planes in which resistance plateaus at precise fractional values of states, relating to fundamental concepts of metrology and theories of fractional charge. Electrons confined in narrow one-dimensional (1D) channels occupy discrete energy levels or subbands, causing the measured conductance to be quantized in units of $G_0 = \frac{2e^2}{h} \sim 77.48\ \mu S$. In contrast to the classical Hall effect, the quantum Hall effect and FQHE can only be observed in thin semiconductor materials, typically achieved by devices called heterostructures in a low-noise and isolated system at low-temperature. Heterostructures are grown in such a way as to increase mobility with sufficient carrier density for the semiconductor to be metal-like upon cooling ($R \propto T$).

Low-temperature transport measurements are used in a variety of fields ranging from novel research into physical effects such as superconductivity, condensates, localised or quantised states to industrial applications in established systems, to improve performance. Fundamentally, cooling allows for a more precise measurement which is achieved from low-noise measurements in the isolated system. This regime is promising to study electron-electron interactions that can result in the realisation of quantum phenomena such as fractional quantum Hall plateaus, spin-chains [2] and new nanostructures [3, 4]. Other interesting phenomena include electron-electron interactions and many-body effects [5], spin-charge separation in Tomonaga-Luttinger Liquids [6], quantum Hall effect fractions [7], using Aharonov-Bohm [8] and Shubnikov de Haas [9] effects for thermometry as well as other fundamental physics [10].

The main cooling techniques are dilution and adiabatic demagnetisation and there are typically two types of cryostats: wet and dry, based on whether a cryogenic liquid is used as a thermal reservoir. For the fridges used for experiments in this thesis, the Kelvinox 400 cryostat is a wet dilution refrigerator, ND3 is a wet nuclear-demagnetisation dilution refrigerator and ND4, a dry nuclear-demagnetisation refrigerator. Although the micro-Kelvin regime is readily available, following advances in refrigeration and low-temperature techniques, electrons in low-dimensional devices are notoriously difficult to cool, as discussed in detail in section 1.2.

1.1.1 Physics at Low Temperatures

The mean free path is defined as the average distance before a carrier is scattered at a large angle by an impurity or from the lattice. The mean free path, l_e can be defined from the momentum relaxation time, τ_m (average scattering time), as $l_e = v_F \tau_m$, where v_F is the Fermi speed defined as $v_F = \frac{\hbar k_F}{m}$.

This expression can be used to define the diffusion constant $D = \frac{1}{2} v_F l_e$. For inelastic scattering events, τ_m represents the timescale in which the carrier loses its phase coherence, and is replaced by the phase relaxation time, τ_ϕ. For a device to have a coherent path, it's size must be below that of the phase relaxation length, L_ϕ. This is the length as defined from the diffusion constant, D, and the phase relaxation time

$$L_\phi = \sqrt{D\tau_\phi}. \tag{1.1}$$

At low temperatures the phase relaxation length can be much longer than the mean free path. This means that limiting the device size to this upper bound would give an ensemble average of coherent current flow. At low temperatures where phonons freeze out, this can span hundreds of microns and therefore if one wishes to study fundamental electron effects in an isolated system, low temperatures are desired. The mean free path is proportional to mobility and advances in fabrication techniques have improved mobility dramatically.

Among low-disorder systems of condensed matter, the high-mobility two-dimensional electron gas (2DEG) confined in an AlGaAs/GaAs heterostructure is an ideal platform for the discovery of new electronic states driven by strong Coulomb interactions [11]. Molecular beam epitaxy (MBE), an ultra-high vacuum (UHV) thin-film deposition technique, produces the highest quality 2DEGs and has played a central role in a number of discoveries such as the quantum Hall effect [12] and the fractional quantum Hall effect [13] that have at their root the interplay of reduced dimensionality, strong electron-electron interactions and disorder. At low-enough temperatures Heisenberg spin-chains are predicted and it is therefore interesting to see how such new states may interact.

Fermi Wavelength, Confinement and Quantisation

A sample is considered low-dimensional if one or more of its relevant length scales is comparable to the Fermi wavelength, this is the de Broglie wavelength of electrons at the Fermi Energy, E_F:

$$\lambda_F = \frac{h}{\sqrt{2m^* E_F}} \ , \tag{1.2}$$

with m^* being the effective mass of electrons in the system.

The Fermi wavelength is larger in semiconductors than in metals, due to their lower carrier density. For a sample of carrier density $n_e = 2 \times 10^{11}$ cm^{-2}, as is typical for our devices, the Fermi wavelength is $\lambda_F = \sqrt{2\pi/n_e} \sim 50$ nm. The Fermi wavelength of electrons in a semiconductor can be as big as 100 nm so that this is the effective feature size of low dimensional semiconductor devices. This length scale is inversely proportional to the carrier density, the number of electrons in the system.

Determining the carrier density, n_{2D}, gives a direct information about the system through the Fermi wavelength and therefore the maximal working feature size of a quantum device. The electron density can be found by magnetoresistance measurements such as the Hall, Quantum Hall and Shubnikov de Haas effects.

The average distance an electron travels, with its initial momentum unaffected by scattering from the lattice or impurities, is defined as the mean free path, l_e, and is expressed by the momentum relaxation time τ_m and the Fermi velocity, v_F as $l_e = \tau_m v_F$. For devices like ours, the mean free path ~ 40 μm.

The phase relaxation length, L_ϕ determines whether quantum interference effects are important. For systems studied in this thesis, typically $L_\phi \gg l_e$ at low temperatures. Comparing the phase relaxation length with the other length scales of the system (e.g. sample size), there are different regimes of electron transport: ballistic, quasi-ballistic and diffusive. In low temperature experiments with a low number of scattering events and device size comparable to the Fermi wavelength, we are investigating systems in the ballistic regime. Scattering reduces mean free path and by cooling to low temperatures electron-phonon interactions are minimised.

Additional confinement can occur from an applied magnetic field, confin-

ing motion further in circular orbits. The magnetic length, $l_B = \sqrt{\frac{\hbar}{eB}}$ is a length scale corresponding to the extent of the wavefunction in the lowest Landau level in applied magnetic field.

1.1.2 Low-Dimensional Electron Gases: Schrödinger Equation and Density of States

Wave-particle duality is described by de Broglie's relation:

$$p = \frac{h}{\lambda} = \hbar k \tag{1.3}$$

and the time-independent Schrödinger equation is written:

$$\mathcal{H}\Psi(\mathbf{r}) = E\Psi(\mathbf{r}). \tag{1.4}$$

Without any applied potential, the Hamiltonian $\mathcal{H}$ is simply the kinetic energy $\mathcal{H} \rightarrow \frac{p^2}{2m}$ of the free electron. This expression may be rewritten using the momentum operator $\mathbf{p} = \frac{\hbar}{i}\nabla$

$$\frac{p^2}{2m} = -\frac{\hbar^2}{2m}\nabla^2. \tag{1.5}$$

With the addition of a time independent potential $V(\mathbf{r})$, this becomes:

$$\mathcal{H} = KE + PE = -\frac{\hbar^2}{2m}\nabla^2 + V(\mathbf{r}). \tag{1.6}$$

The potential formed at the interface of a heterostructure is triangular and can be calculated numerically.

1. 3D $\rightarrow$ 2D confinement is achieved from growth conditions. In semiconductors such as GaAs it is possible to control the bandgap, E_g through a process called bandgap engineering (more on how this is practically achieved on chapter 2). An example of such a confinement is that of a two-dimensional electron gas at the interface of a heterostructure.

2. 2D $\rightarrow$ 1D confinement of a 2DEG can be induced by an additional potential applied to the system, in practice from a metal electrode

called a gate. When sufficient voltage is applied, there is an extra degree of control of carrier density in the sample. A 1D wire, or quantum point contact (QPC) can be created in this way. Where motion of the conducting electrons is restricted to 1 degree of freedom.

3. There is also 1D $\rightarrow$ 0D confinement by additional gating of a sample, such that there is a finite constriction defined by a gate pair, and an additional gate to tune the carriers through the constriction, this is a split-gate/top gate pair. The most typical 0D device is what is referred to as a dot, which defines an "island" a pair of electrons can tunnel into.

1.1.3 2DEGs in Magnetic Fields

Applying a perpendicular magnetic field to a 2DEG, the translational motion becomes restricted further in cyclotron orbits by the Lorentz force. Electrons travelling with a velocity v move in circles. Assuming ballistic motion without scattering, the centrifugal force must equal the Lorentz force $evB = m\omega^2 r$, so that using the angular frequency, $\omega \equiv v/r$:

$$\omega_c = \frac{eB}{m^*},\ r_c = \frac{v}{\omega_c}. \tag{1.7}$$

The motion of these orbits is harmonic in time, quantising the energy spectrum

$$E_l = \left(l + \frac{1}{2}\right)\hbar\omega_c\ , \tag{1.8}$$

with $\omega_c \equiv eB/m^*$ being the cyclotron frequency.

When the magnetic field is changed, the oscillation period changes proportionally. The resulting energy spectrum is made up of Landau levels, E_l, separated by the cyclotron energy. Landau levels are further split by the Zeeman energy. In each Landau level the cyclotron and Zeeman energies and the number of electron states (eB/h) all increase linearly with magnetic field.

Depending on the geometry of the device, electrons in these orbits can continue this motion several times before scattering. Defining τ as the scattering time we have the condition $\omega_c\tau > 1$ for a strong field regime where

the Lorentz force becomes significant [14]. A further condition must exist for confinement to this orbit: that the thermal broadening should be small compared to this spacing of the orbit, such that $k_B T \ll \hbar\omega_c$. At high enough fields, Zeeman splitting occurs and lifts the degeneracy of these levels, adding a term $\pm\, sg\mu_B B$ to the energy. Each subband n, in 2D has a density of states of the form:

$$D(E) = \frac{2eB}{h} \sum_l \delta(E - E_l) \ , \tag{1.9}$$

with each level having a degeneracy of $2eB/h$. The density of states is discontinuous (δ-function) and the Fermi level jumps from one Landau level to the other when the applied magnetic field is changed, resulting in an oscillatory response in the 2DEG. A typical measurement of this oscillatory response is the Shubnikov-de Haas effect of longitudinal magnetoresistance. In this approach, each 2D subband has a dispersion of a 1D system and the Landau levels are no longer degenerate. At high enough magnetic fields, electrons are pushed towards the edges of the device by the Lorentz force, resulting in *edge states* that have dissipativeless motion and carry current in opposite directions, resulting in dramatic resistance effects, quantised resistance plateaus, as observed in the famous Quantum Hall Effect [12].

1.2 Low Electron Temperature

In metals, electrons are free moving, there is no gap between the conduction and valence bands and it is easy for electrons to be thermally excited, with each state being occupied by at most two electrons of antiparallel spin orientations, according to the Pauli exclusion principle. Populating the energy states in this way, the states fill up to the Fermi energy (E_F). One can define the Fermi temperature from this energy as $T_F = E_F/k_B$, k_B being the Boltzmann constant. Because of the high value of the Fermi temperature for metals order of 10^5 K, room temperature is already low temperature [15]. As such, an electron gas in a metal is mostly in the ground state, as determined by the Fermi-Dirac distribution:

$$f(\epsilon_i) = \frac{1}{e^{(\epsilon_i - E_F)/k_B T} + 1} \ , \tag{1.10}$$

with ϵ_i being the energy ϵ at a state i, E_F the Fermi energy of the system and $k_B \sim 8.617$ eV/K with $k_B T \sim 0.025$ eV at room temperature. The properties of metals at low temperatures are determined by electrons in energy states close to the Fermi energy. In semiconductors, there is a bandgap and the Fermi energy lies in the middle of the gap between the conduction and valence bands, therefore it is harder for electrons in semiconductors to conduct and they remain non-degenerate. Furthermore, semiconductors can be tuned by doping, ensuring the carrier density is still enough for them to conduct at low temperatures.

Low-dimensional heterostructures are historically difficult to cool. Thermal transport between electrons and phonons at low-temperature is described by a weak $\propto T^5$ coupling [16, 17], while below ∼10 mK phonons are 'frozen out' [15]. Appleyard *et al.* [18] measured the temperature dependence of a 2DEG upon heating through the conductance of a 1D channel. The electrons were heated and a $\propto T^5$ dependence was measured as the power loss due to phononsand a T^2 dependence on cooling through leads, while thermometry using the amplitude of the Shubnikov de Haas gave a T^3 dependence and with electrons being hotter than the lattice ($T_e > T_L$), as shown in Figure 1.1. A number of other experiments using Shubnikov de Haas amplitude thermometry [9, 19, 20] have also determined this $\dot{Q} \propto T^3$ dependence at low-temperature. This dependence dominates in comparison to the $\propto T^5$ phonon-coupling. Hence, in that regime, the dominant mode of cooling will be primarily through the leads to the sample [18] as defined by the Wiedemann-Franz law (WF) of heat transfer of the conducting electrons through the contact.

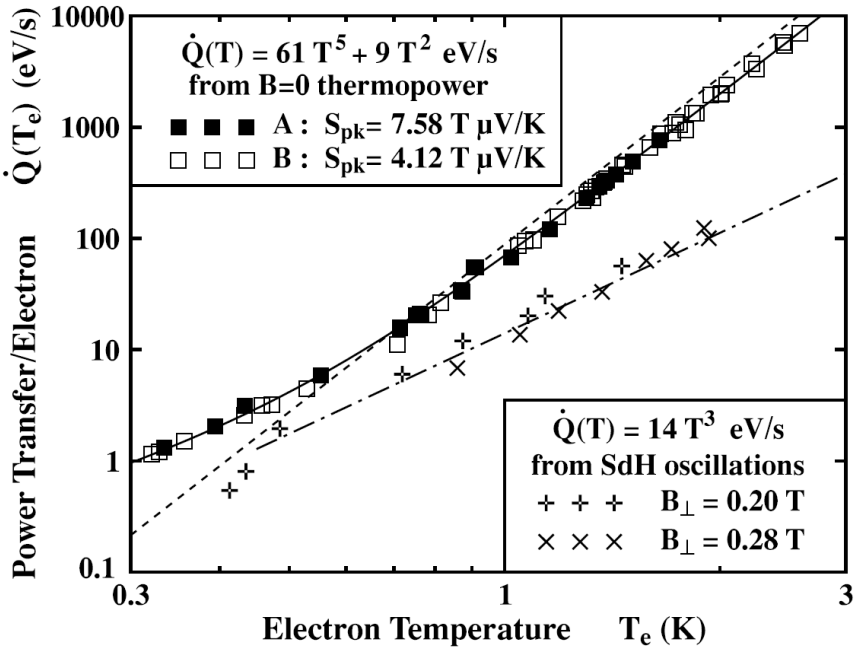

Figure 1.1: Heat flow, $\dot{Q}$, from thermopower data for two 1D constrictions. Joule heating is induced in the 2DEG, with electrons thermalising at a temperature T_e, the rate of heat loss to the lattice temperature is $P = \dot{Q}(T_e) - \dot{Q}(T_L)$. It is determined that the temperature of electrons decouples from the lattice, with cooling dominated by a T^2 dependence from the contacts compared to a T^5 dependence on electron-phonon cooling, as shown in the expression in the top inset. Shubnikov de Haas amplitude thermometry gave a $\propto T^3$ dependence. From Appleyard *et al.* [18].

Many groups cooling low-dimensional devices do not have thermometers thermally coupled to the device in such a way as to extract and verify an accurate low electron temperature. This is in part due to the modifications needed to optimise such a setup with an in-situ thermometer. Often the temperature given is an estimate or inferred, without accurate verification from a primary thermometer. The work of Samkharadze *et al.* [21] is an example of this statement, the thermometer used in this work is not directly thermalised to the sample, but to the heat sink and therefore the heat bath.

Iftikhar *et al.* [22] developed a technique allowing for in situ thermometry, verifying an electron temperature of 6 mK for micron scale circuits using three different mesoscopic phenomena: quantum shot noise, back action of a resistive circuit and conductance oscillations. Primary thermometry de-

pendent on universal effects is perhaps the most reliable way of measuring low electron temperatures without significant changes to the experimental setup. Such an effect is Coulomb Blockade thermometry. Noteworthy electron thermometry of this type that has been attempted are by Casparis *et al.* [23] using Coulomb Blockade thermometry to determine a 7.5 mK sample temperature and Spietz *et al.* [24] using Shot Noise measurements for thermometry down to 10 mK.

The National High Magnetic Field Laboratory [25] first used a ^{3}He immersion cell for transport measurements using tuning fork thermometry in magnetic fields. This design inspired the immersion cell in our group (see work in [26]) and specifically the design of the immersion cell of the Kelvinox cryostat, discussed in chapter 2, as well as the general technique of immersion cooling. Xia *et al.* quote a 2DEG temperature of 4 mK. This electron temperature was determined from observations of the temperature dependent $\nu = \frac{5}{2}$ quantum Hall fraction [27]. To date, the lowest published electron temperature in low-dimensional electron systems has been by Bradley *et al.* [28] of 3.7 mK, using a large array of metallic islands placed inside the mixing chamber and determining the temperature from Coulomb Blockade thermometry. As touched on at the start of this section, it is easier to cool a metal and previous attempts in 2DEGs using Coulomb Blockade thermometry reached a temperature of 7.5 mK [23], while work by Nicolí *et al.* [29] cooled a gated quantum dot to 6.7 mK using an immersion cell on a standard dilution fridge.

Low temperature groups are developing novel techniques such as on-chip demagnetisation by Bradley *et al.* [30] and other techniques described best in a detailed review by Lancaster and Basel [31] on the progress of cooling electrons so far. It is worth noting that, even with techniques such as demagnetisation of the electrical contacts, the contact resistance of the sample will limit cooling through leads and this key parameter is not quoted.

In the RHUL low temperature group, provisions were taken on the ND3 cryostat specifically for measurement of accurate electron temperatures using a current-sensing noise thermometer coupled to the sample through a Au bond-wire. In summary, these provisions were: making a ^{3}He immersion cell, cooling the sample in an ultra-low-temperature environment, reduction of the heat leak to the 2DEG using filters, minimisation of contact resistance to thermalise through leads and the use of in-situ thermometry to measure

the 2DEG temperature directly. These points had already been addressed in previous work in the RHUL group, on the ND3 cryostat and using a ^{3}He immersion cell cooled by a copper nuclear demagnetisation stage a 2DEG device reached the coldest reported electron temperature in such a system of $T_e = 1.0 \pm 0.1$ mK, as measured using in-situ current-noise-sensing thermometry (see details in [26]). The temperature dependence of this sample is presented at the beginning of chapter 5. Due to fabrication issues, a contact resistance comparably low to the sample that achieved the μK temperature boundary was not reproduced on a similar device after many attempts. In the following section, the importance of contact resistance for sample thermalisation is highlighted. Due to the fabrication issues at the start of this study, the primary focus was to understand and solve the high resistance problem. This was achieved through the characterisation presented in Chapter 4, the investigation of the contacting mechanism to the 2DEG (Chapter 3) and concluding with experiments on contact resistance at low-temperature (Chapter 5).

1.3 Thermal Model

Contact resistance is often defined as any resistance at the interface of two different materials. This can be a resistance forming between wires of different parts of the fridge, wires to the sample's electrical contacts and the interface of the alloy of the contact to the semiconductor. In this thesis, contact resistance refers to the latter: the resistance between the contacting alloy and the semiconductor. This is because all other resistances have been minimised with well-known low-temperature techniques, and this is the primary resistance impeding cooling of the sample through wires. Contact resistance is a series resistance to the sample and therefore is an important parameter to optimise for achieving thermalisation, especially at low-temperature. Contact resistance is explained in more detail in chapters 3 and 4.

In order to infer an electron temperature for this system, the thermalisation of the sample needs to be modelled. The WF law relates the ratio of thermal (κ) and electrical (σ) conductivity of a metal due to the flow of conducting electrons, which is the dominant form of cooling in this regime (as argued in the previous section). The ratio is proportional to the temperature,

$$\frac{\kappa}{\sigma} = LT, \tag{1.11}$$

with the constant of proportionality being the Lorentz number, L.

Known violations of the WF law occur in some materials like silver, where a modified Lorenz constant $L = 0.1L_0$ [32] is needed due to different scattering process ($\tau_\kappa < \tau_\sigma$) and in superconductors where current flows in Cooper pairs which do not carry heat and the ratio of thermal and electrical conductivity vanishes. In measurements on 2DEGs the WF law is obeyed [33] down to the mK regime, as well as for tunneling transport [34].

The 2DEG can be modelled as a simple resistor, connected at two ends to a thermal reservoir (source-drain ohmic contacts) that are in perfect equilibrium with the bath. Heat flows across this resistor with each end at temperature $T_{\text{bath}} = T_L$, the temperature of the lattice at thermal equilibrium with the bath. Considering heat flow from two reservoirs at temperatures T_e, the electron temperature, and the lattice temperature, T_L. The total transfer of heat is then:

$$\dot{Q} = \dot{Q}_{\text{L}\to\text{e}}(T_{\text{L}}) - \dot{Q}_{\text{e}\to\text{L}}(T_{\text{e}}). \tag{1.12}$$

When thermal equilibrium is reached, $\dot{Q} = 0$, when $T_{\text{e}} = T_{\text{L}} = T_{\text{bath}}$ (from 2^{nd} law of Thermodynamics). Thermal conductance is then defined as the linear response of heat flow to a temperature gradient ΔT:

$$G(T) = \frac{\dot{Q}}{\Delta T}. \tag{1.13}$$

With the same scattering processes determining electrical and thermal transport in a 2DEG, one can define a scattering time such that $\tau_\sigma = \tau_\kappa = \tau$, in order to define the electrical, σ, and thermal, κ, conductivities:

$$\sigma = \frac{ne^2\tau_\sigma}{m}, \ \kappa = \frac{\pi^2 n k_B^2 T \tau_\kappa}{3m}. \tag{1.14}$$

Then, using (1.11), we can write:

$$\frac{\kappa}{\sigma} = LT \to L = \frac{\pi^2 k_B^2}{3e^2}, \tag{1.15}$$

where n is the carrier density, e the charge of electrons, m their mass and k_B the Boltzmann constant. Treating the sample (2DEG and ohmic contacts) as

a resistor of temperature independent resistance R, length l and cross-section α, the electrical conductivity gives an expression for the thermal conductivity of:

$$\sigma = \frac{l}{\alpha R} \rightarrow \kappa = L\sigma T = \frac{LTl}{\alpha R}. \tag{1.16}$$

Applying Fourier's law of heat conduction and using the equation for thermal conductivity above [35], Fourier's law at position x may be written:

$$\dot{Q}(x) = -\alpha\kappa(T)\frac{dT}{dx} \rightarrow \dot{Q}(x) = -\frac{Ll}{2R}\frac{d(T^2)}{dx}. \tag{1.17}$$

To determine the temperature at the middle of the sample, we must consider the effect of uniformly applied heat to the whole sample. Initially, the individual power transmitted by each end (source/drain) can be considered as separate contributions and we can infer that if one edge is thermally anchored to the bath (at $x = 0$), and heat is applied to the other end ($x = l$), uniform heat flow will occur from towards the cold end so that $\dot{Q}(x) = -\dot{Q}$, such that:

$$-\frac{Ll}{2R}\frac{d(T^2)}{dx} = -\dot{Q}\ . \tag{1.18}$$

So the temperature at position x is given by:

$$T^2(x) = T_e^2 + \frac{2Rx}{Ll}\dot{Q} \tag{1.19}$$

and we can write:

$$T_L^2 = T(l)^2 = T_{\mathrm{e}}^2 + \frac{2R}{L}\dot{Q}\ . \tag{1.20}$$

This may be rewritten as:

$$\dot{Q} = \frac{L}{2R}(T_{\mathrm{L}}^2 - T_{\mathrm{e}}^2)\ . \tag{1.21}$$

Note that this is completely independent of the resistor geometry. This relationship holds between thermal and electrical conductivity in any arbitrary resistor as long as $\kappa = L\sigma T$. The total heat flow in the middle of the bar is then:

$$\dot{Q} = \frac{L}{2R}(T_L^2 - T_e^2) \ \text{ and Conductance : } \ G(T) \equiv \frac{LT}{R}. \tag{1.22}$$

Next, uniform applied power to the whole of the resistor is considered, with one end thermally anchored at T_{L}. All heat flows to the cold end and

heat flow at position x is the fraction of power generated in a length greater than x, x/l. Therefore

$$\dot{Q}(x) = -\dot{Q}\left(1 - \frac{x}{l}\right) \tag{1.23}$$

and using (1.17):

$$-\dot{Q}\left(1 - \frac{x}{l}\right) = -\frac{Ll}{2R}\frac{d(T^2)}{dx}. \tag{1.24}$$

Rearranging for temperature gives

$$T^2(x) = T_{\mathrm{L}}^2 + \frac{2R}{L}\left(\frac{x}{l} - \frac{x^2}{2l^2}\right)\dot{Q} \tag{1.25}$$

and

$$T_{\mathrm{e}}^2 = T_{\mathrm{L}}^2 + \dot{Q}\frac{R}{L}. \tag{1.26}$$

Comparing to the expression of heat applied to one end, it is seen that uniformly applied heat is less efficient in cooling than power applied as a point source.

Finally, let us consider applied uniform heat flow to the whole resistor, with both ends thermally anchored to the bath, at T_{L} (as shown in Figure 1.2). By symmetry, there is no heat flow at $x = \frac{l}{2}$ and by writing the resistor as two identical (left/right) split contributions of resistance $R/2$ and length $l/2$, using the equation derived earlier for uniform applied power, we may write:

$$T^2(x) = T_{\mathrm{L}} + \frac{R}{L}\left(\frac{x}{l} - \frac{x^2}{l^2}\right)\dot{Q}. \tag{1.27}$$

Such that the highest temperature is reached at the middle of the bar:

$$T_{\mathrm{max}}^2 = T^2(l/2) = T_{\mathrm{L}}^2 + \frac{R}{4L}\dot{Q} \tag{1.28}$$

the temperature at the middle of the resistor is then:

$$T_e^2 - T_L^2 = \frac{R^{I^+I^-}}{4L}\dot{Q}_e \ , \tag{1.29}$$

with T_e being the electron temperature as measured from the middle of the

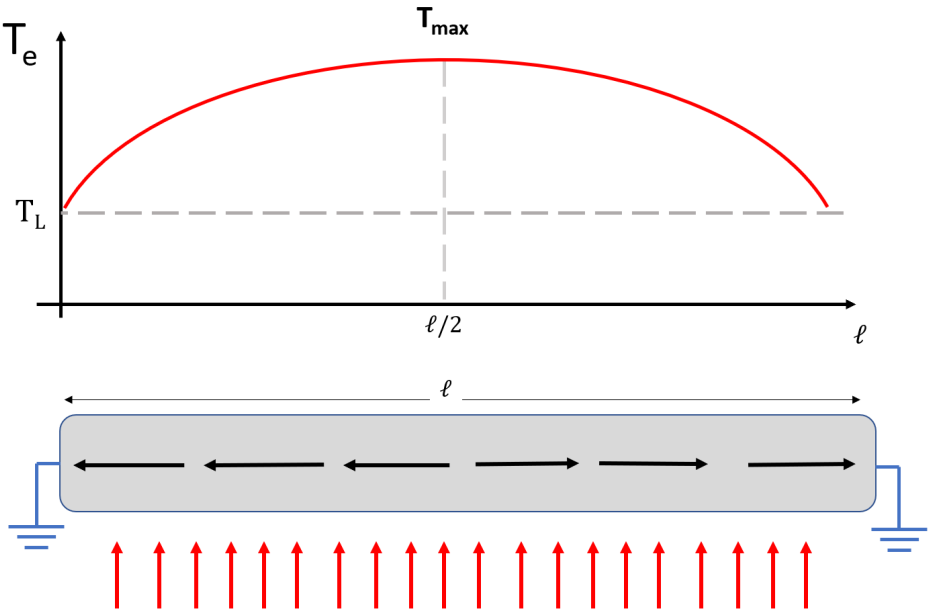

Figure 1.2: Uniform applied power to an arbitrary bar, with both ends thermally anchored at an equilibrium temperature $T_e = T_L$. Simulating lattice cooling of a 2DEG, with source-drain contacts (the two ends) anchored to fridge temperature. In such a setup, the maximum electron temperature can be measured at the middle of the sample.

bar and $R^{I^+I^-}$ being the total resistance of the sample.

From this expression, it is evident that to achieve a low electron temperature of a 2DEG, the total (end to end resistance) of the sample including the 2DEG and the ohmic contacts to it need to be minimised. Minimisation of the 2DEG resistance can readily be achieved by the sample geometry, while the resistance of the contacts can be characterised and optimised (details in chapter 4), an ideal value for this resistance is $\sim$1 Ω.

1.4 Summary

With the aim of achieving low electron temperature of a low-dimensional semiconductor, experimental cooling techniques have been established by various groups. In this chapter an overview of the background theory necessary for understanding 2DEGs at low temperatures and typical methods

and techniques used in cooling these devices were introduced. A literature review of electron temperatures achieved to date was included in the context of comparing cooling metals to cooling low-dimensional electron systems. The methods used to optimise thermal contact of the sample to the fridge were introduced and a thermal model treating the 2DEG as a simple resistor was discussed in terms of cooling the sample through leads.

In the following chapter, the fabrication techniques of low-dimensional systems are presented, along with an overview of the low-temperature setup and techniques used on the Kelvinox fridge.

Chapter 2

2DEGs at GaAs/AlGaAs Heterostructure

This chapter describes devices fabricated on GaAs/AlGaAs heterostructure. It will start with an introduction to two-dimensional electron gases, their fabrication by Molecular Beam Epitaxy (MBE) and describe the most common ways confinement (low dimensions) are achieved in practice. Finally, it will describe the way a typical sample is fabricated and how it is characterised. An overview of the low-temperature experimental setup of our Kelvinox 400 cryostat is given.

2.1 Semiconductor Structures

Quantum phenomena are fragile effects, heavily dependent on the system under study. In experiments like ours, we wish to study electrons in an isolated environment, without impurities. The best way to address this requirement is by precise and careful growth, via Molecular Beam Epitaxy (MBE) and ensuring all fabrication machines and equipment are kept clean from any impurities at every step of fabrication.

Heterostructures used in this study are grown using MBE. The Cavendish Laboratory provided all the samples used in this thesis *. The heterostructure consists of GaAs/$Al_xGa_{1-x}As$, x referring to molar composition of aluminium which is present in the AlGaAs, typically around 0.33 for wafers such as ours.

*See Acknowledgements for details.

This chapter will begin with a description of the system, the fabrication processes of our samples, from MBE growth to gating for more complicated devices.

Two-Dimensional Electron Gas

A two-dimensional electron gas (2DEG) is formed in a High Electron Mobility Transistor (HEMT) at the interface of the two materials of the heterostructure, mainly at the undoped GaAs region. The difference in energy bandgaps allows for thermal activation of electrons out of donors in the AlGaAs layer into the conduction band of GaAs and due to this mismatch a triangular potential is formed. The charge density discontinuity only extends $\sim$10 nm away from the interface of the heterostructure so the electrons are free to move in the $x-y$ plane only, z being the direction of growth, thus restricting current flow to 2D. A heterostructure is the most effective way to produce a two-dimensional electron gas, as discussed further on in this section. The MBE technique allows for creating pure, defect-free and well-defined heterojunctions in a stacked semiconductor structure called a wafer.

Further confinement is achieved in these systems by deposition of a gate onto the semiconductor, forming a Schottky barrier, allowing a potential to be applied to the gate and depleting the 2DEG, such that a 2D heterostructure can have a region that is 1D or even 0D ("dot" or "antidot"), depending on the experimental aim and device type.

The device's geometry is subsequently etched out with a photolithographic mask, resulting in a raised structure onto the wafer called a mesa. Electrical contacts are then made onto the mesa by annealing a metal alloy onto the sample to be able to measure the two-dimensional electron structure.

Further processing can follow, depending on the system one wishes to study. Photolithographic techniques are very useful and low cost, but for devices of scale smaller than 1 μm electron beam lithography must be used, which is covered in section 2.3. The following section 2.2 will provide further detail into fabrication techniques for semiconductor structures.

2.2 Semiconductor Growth

2.2.1 Epitaxy

There are two methods of forming conductive GaAs surface layers on bulk GaAs substrates: epitaxy and ion implantation. The latter is an economic, well established method with high impurity and low yield, but widespread availability. It usually involves implanting dopants of high energy into the substrate and subsequently annealing to allow dopants to reach lattice sites [36]. Implanting dopants comes at a cost - the ionised donor regions forming scattering interfaces - for this reason this technique is not favoured for research-grade materials used to study a ballistic system.

Epitaxy etymologically means 'an arrangement onto', implying the existence of an ordered structure, as such it is used to express the process of growing additional layers of surface onto a substrate, resulting in what is called a wafer. In our case, this consists of growing GaAs material on top of the surface of a bulk GaAs substrate in a manner that preserves the crystal structure. Ga and As atoms are brought together under appropriate conditions (calibrated pressures, high temperatures and in a vacuum), resulting in crystalline growth.

Dopants can be included during this growth process to be incorporated into lattice sites of the crystal. Epitaxial layers generally result in a crystal structure with fewer impurities than the substrate, the ability to control dopant concentration is favourable to produce devices to the exact specifications of an experiment. If a doped layer of GaAs is grown on a substrate some of the impurities and defects of the substrate can extend to the active region, so that buffer layers of undoped GaAs are usually grown before depositing doped epitaxial layers depending on the complexity of the device needed. Figure 2.1 shows advances to sample mobility from different fabrication methods.

MBE is the most reliable and versatile approach for epitaxial growth, which demands a high manufacturing cost and a lot of maintenance. Advances in this technique involve modulation doping, which is a technique of band-gap engineering based on adding dopants to layers to increase the active carrier density. Samples in this thesis are grown by MBE, as we wish to study high mobility low dimension samples.

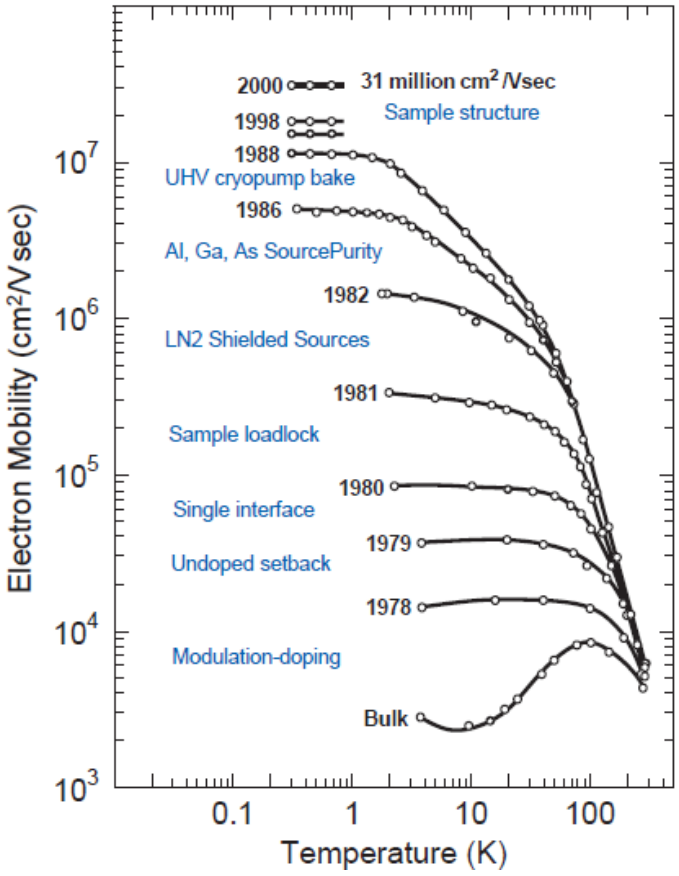

Figure 2.1: Advancements in sample mobility on GaAs, from Pfeiffer [37]

.

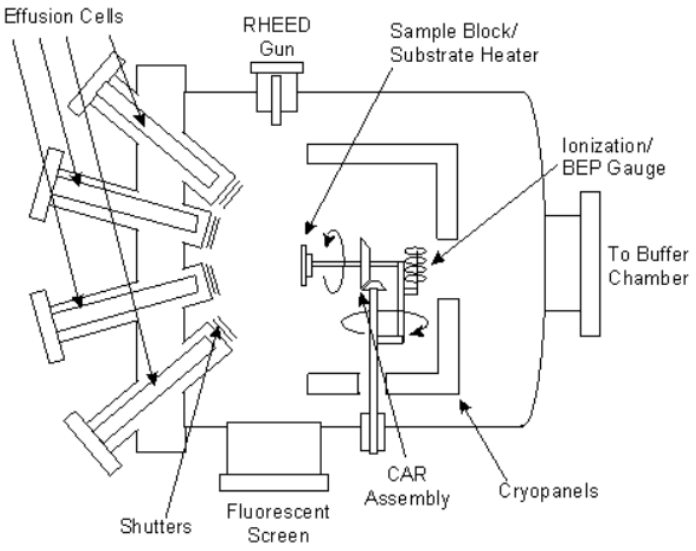

(a) Schematic of an MBE chamber. The RHEED gun monitors growth, shutters adjust the source beams originating from the effusion cells which contain high purity elements. The substrate is heated to allow material to be deposited onto it, while the rotator allows for favourable growth, depending on the crystal's characteristics [38].

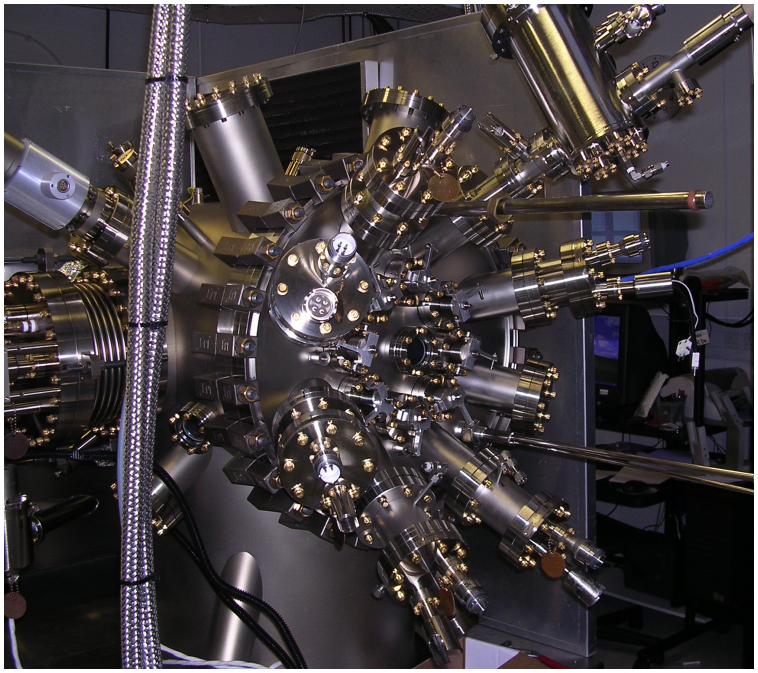

(b) Veeco ModGENII MBE machine at Cavendish Laboratory.

Figure 2.2: Schematic of MBE chamber and picture of an MBE machine at Cavendish Laboratory.

2.2.2 Molecular Beam Epitaxy and 2DEGs

For the purposes of research carried out in this study, GaAs is used and more specifically, GaAs/AlGaAs heterostructures produced by the MBE technique, though the technique is not limited to these materials and a lot of these processes are generic [39, 40].

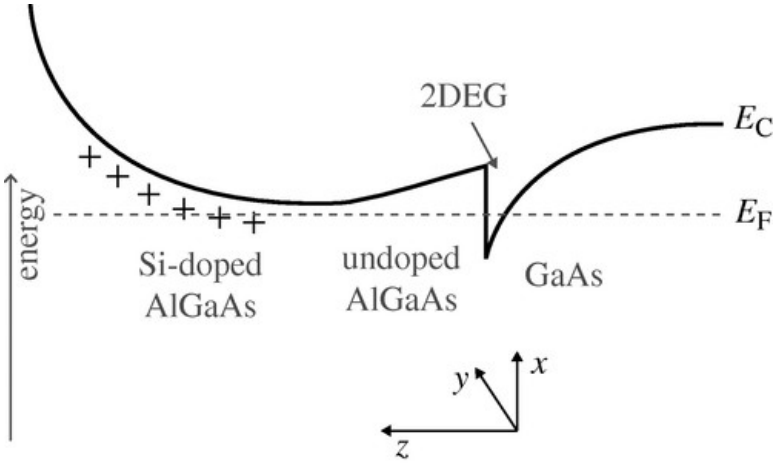

Figure 2.3: Conduction Band profile of an AlGaAs/GaAs heterostructure. Doped n-$Al_xGa_{1-x}As$ creates a region of ionized charge and the donated electrons fall into the GaAs conduction band and are attracted back towards the donor. The spacer layer, which is undoped, blocks these carriers from moving past the interface, creating a strong electric field (order of 10^5 V/cm^2, resulting in a sharp potential that bends the conduction band below the Fermi level. A triangular potential well is formed at the interface, confining electrons in the direction of growth to only the ground state, at the interface of the undoped (spacer) AlGaAs layer and the GaAs layers. Image from [41].

A two-dimensional electron gas is one that is confined at a 2-D plane due to its kinetic/thermal energy not being sufficient to excite it from the ground state. Historically, this was achieved in practice by gating Metal-Oxide Semiconductor Field Effect Transistors (MOSFETs), where a metal deposited on top of the bulk 3D semiconductor controlled the quantum well dimensions. A more advanced and recent method is confinement from growth, which for our purposes is achieved by MBE, with the 2DEG forming at the interface of two very similar crystalline materials in a sandwich called a heterostructure. To understand the process of forming a two-dimensional electron gas, one must first consider the conduction band of the layered crystal structure.

Figure 2.3 shows the conduction band profile of an AlGaAs/GaAs interface, the bending of the conduction band forms a triangular potential well. MBE's advantageousness comes from the ability to engineer the bandgap, by varying the thickness of the layered materials, the heterostructure.

Dingle *et al.* [42] first demonstrated the capability of fabricating a series of quantum wells to high precision, while work by Chang [43] and Tsu [44] determined limits for this growth. In the same work, Dingle *et al.* demonstrated that variation of molar density of the $Al_xGa_{1-x}As$ layer adjusts the size of the well and some upper and lower limits for useful numbers of molar composition were determined. If the well is narrow enough (order of 10 nm), the energy levels are widely separated and electrons are trapped in the ground state in the direction of growth, while free to move in the parallel 2D plane, this is a 2DEG forming by confinement from growth.

A technique developed by Störmer, Dingle, Gossman and Wiegmann [45, 46], referred to as modulation doping, allows for even cleaner fabrication, reducing impurity scattering. In principle, adding doped (p-doped, usually with Silicon) AlGaAs layers before an undoped spacer layer and undoped GaAs produces a strong electric field, drawing electrons from the GaAs down to the undoped AlGaAs/GaAs interface. Any growth incorporating doping of alternating layered structures may be referred to as Modulation Doping as long as the dopants are far enough removed from the outer interfacial AlGaAs/GaAs layers. Heterostructures fabricated with this technique are also referred to as MODFETs (Modulation Doped Field Effect Transistors).

The most important feature of modulation doping is the resultant high mobility. High mobility is achieved from the transfer of carriers into the material of the narrower gap (in our case GaAs) which is physically separated from the ions used to create them in the wide bandgap material, so that the electrons at interface with the spacer layer are only weakly scattered by the ions from the spacer layer. Modulation doping enables injection of more carriers in the interface due to the strong electric field attracting electrons from the donor layer to the interface with the undoped AlGaAs, increasing mobility further. For this purpose, a lot of modern devices use a superlattice (also referred to as setback layers/modulation layers) of thickness in the order of nanometres. The modulation doping growth technique made High Electron Mobility Transistors (HEMTs) such as the devices which made this

work possible. The 1998 Nobel Prize was awarded to Laughlin, Störmer and Tsui for the discovery of fractional excitations, the Fractional Quantum Hall Effect, resulting from this technique [7, 45].

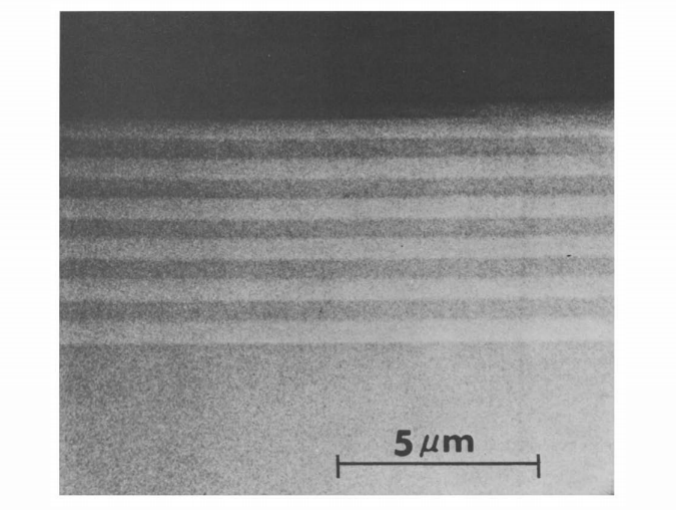

Figure 2.4: Scanning Electron Micrograph of a cleaved section of alternating 5000 Å layers of GaAs and Al_x $Ga_{1-x}As$, produced by MBE. From original work done at Bell Laboratories by Cho and Arthur [47]. The ability to grow thin epitaxial layers revolutionised research in the semiconductor industry.

In a MBE machine, a wafer of GaAs is placed in an ultra-high-vacuum chamber, in which high purity Al, Ga, As and Si contained in effusion (Knudsen) cells can be evaporated onto the substrate with molecular precision. Knudsen cells have a small orifice with shutters and collimators and produce a well defined molecular beam of ballistic atoms of material aimed at the substrate. Material placed in the effusion cells (in our case, mainly Ga and As) is then aimed at the substrate. Atoms from the molecular beam arrange themselves in energetically favourable positions, in a lattice [11].

A high degree of precision can be achieved using constant monitoring techniques such as reflection high-energy electron diffraction (RHEED) [48] and the use of shutters to adjust the deposition beams. The crystal is therefore able to grow by atomic layer precision and high quality; complicated structures with sharp transitions or doping profiles can be formed. The rate of growth is about 1 μm per hour [49].

During deposition, due to the close lattice matching of GaAs with AlAs (and also AlGaAs) the material deposited onto the substrate will not have

significant lattice strain defects. Arsenic itself is highly volatile when heated, so that any arsenic that does not react with the substrate gallium or aluminium will not be deposited [50]. RHEED monitoring of the deposition, while adjusting the As amount can control the growth process, achieving a much higher degree of quality, up to monolayer growth.

In order to grow a high quality (mobility) crystal, the layer sequence consisting of different materials, needs to have close matching of lattice constants to reduce strain and dislocations. Figure 2.5 shows lattice constants of various common materials used in the semiconductor industry. Vegard's law [51] is an empirical way of determining the lattice constant, α, between a mixture of two materials:

$$\alpha_{A_{1-x}B_x} = (1-x)\alpha_A + x\alpha_B \tag{2.1}$$

Due to the close lattice matching of GaAs and AlAs, a mixture of GaAs with a small amount x of Aluminium, $Al_xGa_{1-x}As$, under the same empirical rule is also closely lattice matched for quantities of Aluminium typically $x < 0.5$. In our work, x= 0.33.

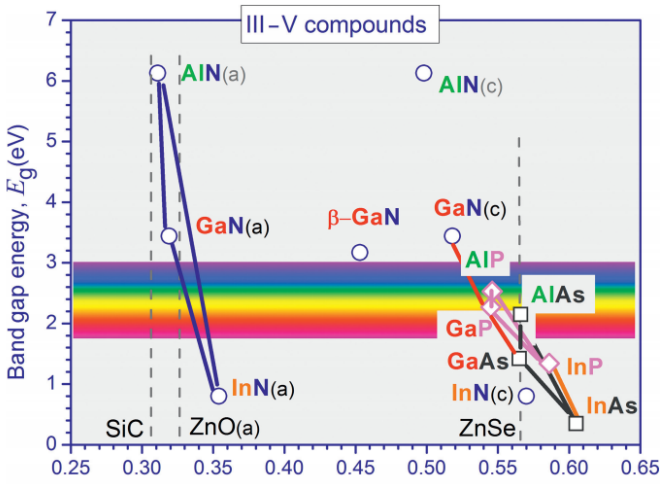

Figure 2.5: Lattice Constants and Bandgap Energies for various III-V semiconductor materials. The close lattice matching between GaAs and AlAs is unlike any other two materials. The difference in their Bandgaps results in confinement in a potential well. Note that both GaAs and AlAs band-gaps lie in the red part of the light spectrum, illumination by such wavelength can excite carriers over the bandgap. Figure taken from [52].

Table 2.1: Growth characteristics of wafers used in this thesis. Growth of W wafers was done by Dr. Ian Farrer and V wafers by Dr Harvey Beere, at the Cavendish Laboratory. Molar composition of Al to Ga is $x = 0.33$ in the $Al_xGa_{1-x}As$. All these wafers are modulation doped, however W wafers have a superlattice buffer below the interface to achieve higher mobilities. Thickness of layers in nm.

Wafer	GaAs (cap)	AlGaAs (Si doped)	AlGaAs spacer	GaAs	2DEG depth	Superlattice
W475	10	40	40	1000	90	Yes 250 (2.5/2.5)
W476	10	40	40	1000	90	Yes 250 (2.5/2.5)
V827	10	40	40	1000	90	No
V834	10	40	40	1000	90	No

As such $\alpha_{Al_{0.33}Ga_{0.67}As} = 5.65$ Å, which is also a Zincblende structure, with lattice constant identical to that of GaAs, so that by nature and a bit of tuning during fabrication, the AlGaAs/GaAs heterostructure is the ideal crystal to produce high mobility 2D samples (easily above 10^6 cm^2/Vs). The matching of lattice structures between GaAs and AlGaAs therefore allows a region of band gap change to be formed at the heterointerface without change in crystal structure and therefore no lattice defects due to dislocation.

In binary semiconducting systems, the bandgap is a linear function of the lattice parameter. So that by extension of Vegard's law, a relationship between composition and bandgap can be made:

$$E_{g,AlGaAs} = xE_{g,GaAs} + (1-x)E_{g,AlAs} \tag{2.2}$$

In our case this energy is $E_{g,Al_{0.33}Ga_{0.67}As} \sim 1.834$ eV, corresponding to a wavelength of ~ 676 nm, that of red light. This means that illuminating with a red LED, carriers can be excited from deep donor states.

Devices grown with MBE therefore have typically fewer impurities, leading to higher mobilities and cleaner systems. Table 2.1 shows growth characteristics of wafers used for samples in this thesis.

2.2.3 Scattering Mechanisms

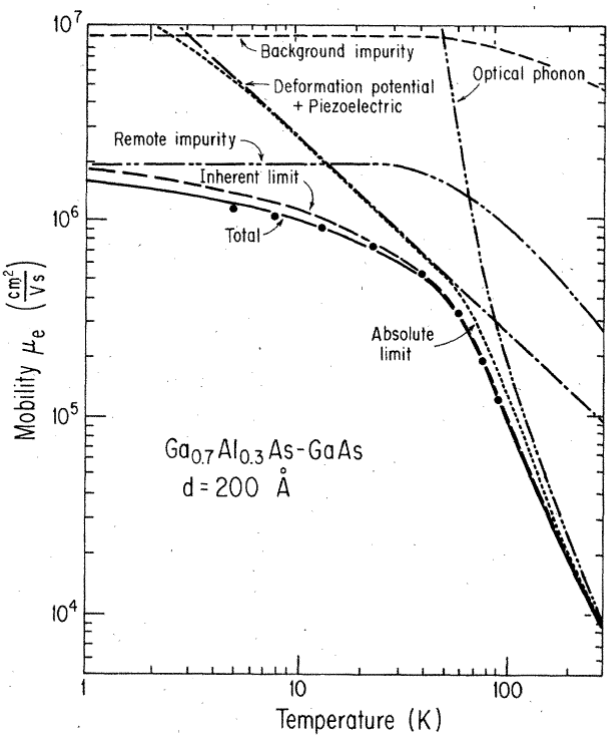

Figure 2.6: Temperature dependence of mobility due to different scattering mechanisms. The points are experimental data, while the curves are calculated mobilities for a set carrier density of 3×10^{11} cm^{-2}. From Walukiewicz *et al.* [53].

For a two-dimensional electron gas in a GaAs/AlGaAs heterostructure there are several possible scattering mechanisms that one needs to consider. The main mechanisms affecting 2DEG mobility are Coulomb scattering, from remote and ionized impurities and interaction with bulk phonons (optical or acoustic). Figure 2.6 shows the influence of various scattering mechanisms on the mobility of a heterostructure.

Coulomb scattering

Coulomb scattering occurs from ionized impurities in the undoped GaAs (background impurities) and ionised dopants in the doped AlGaAs layer (remote impurities). The density of remote impurities is typically higher, from doping, but due to their distance from the heterojunction (due to the 20 -

120 nm undoped spacer layer), the main scatterers are background GaAs impurities. These types of impurities interact with the 2DEG via the Coulomb force, dominating momentum relaxation at low temperatures, making mobility temperature independent at temperatures low enough for the phonon modes of the lattice to freeze out. This type of scattering is elastic and on average scattering processes scale inversely with sample area.

In most cases in our low dimensional devices used in this study, we are in the diffusive regime, in which transport is dominated by elastic scattering processes and the mean free path, l_e, is smaller than the length scales of the conductor ($L,\ W$). Conductivity and conductance in this case are directly related by $G = \sigma\frac{W}{L}$.

Phonon Scattering

At low enough temperatures, $k_B T \sim \hbar\omega_{max}$, there exist only a small number of acoustic phonons with a characteristic temperature dependence $\propto T^5$. In this regime, the 2DEG is strongly degenerate which results in significant electron-phonon scattering reduction.

Samples are cooled to low temperatures because phonon scattering is a major inhibitor to electron mobility, reducing the mean free path at higher temperatures.

2.3 Gating Devices

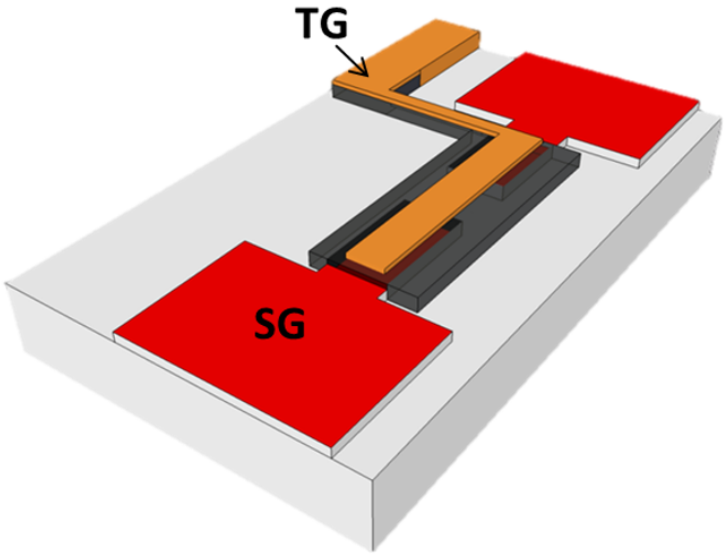

Figure 2.7: Schematic of a 1D device: a 1D channel defined by the gap of a Split-Gate (SG, red). A Top-Gate (TG, gold) is added above the split gate, insulated by a cross-linked PMMA layer (dark grey) for adjusting the carrier density in the 1D wire. 2DEG shown in light grey.

There are two main ways to achieve confinement:

1. As described in the previous section, through growth of inhomogeneous layered structures, where confinement occurs in the growth (perpendicular to sample) direction.

2. Lithographic techniques, patterning/depositing a metal electrode onto the sample, that can be biased to produce additional potential barriers.

Gating is the most common way to tune a sample's carrier density. The Split-Gate technique [54] is probably the most versatile used in such devices, which allows for selective depletion and current flow to be further restricted to 1D due to the formation of an electrostatic potential barrier.

Split gates form quantum point contacts (quantum wires), regions in which electrons are restricted to flowing in one dimension only. This extra confinement results in quantisation of current under appropriate (low)

temperature conditions. Split-Gate devices are electrodes (in our case, typically Au with a small percentage of Ti for adhesion) deposited onto the mesa, with an additional layer of insulator in-between. Adding a negative voltage onto these electrodes depletes carriers from the region in a controlled way due to the produced electrostatic field. The gap between the two electrodes allows the current to flow through a limited path, of a well defined (through electron-beam lithography) narrow path of order 700 nm, this is a one-dimensional channel.

At sufficiently low temperatures, the conductance of the sample through the narrow 1D channel becomes quantised, showing plateaus at values of $G_0 = 2\frac{e^2}{h}$, the conductance quantum ~ 77.48 μS. This conductance value corresponds to a resistance value of approximately 13 kΩ and is a large resistance. This is why these devices are typically measured with 2-terminal conductance measurements.

Gating is achieved through optical photolithography (for feature sizes above 5 μm) and electron-beam lithography (EBL) for smaller structures.

Gates and Lower Dimensions

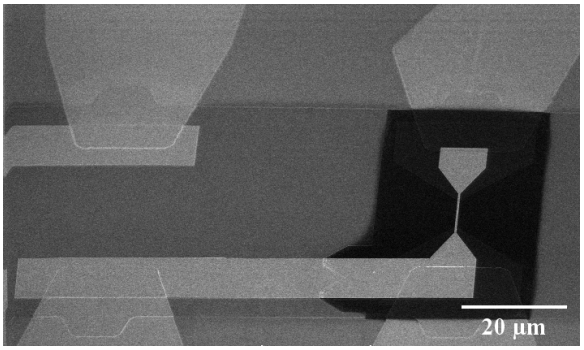

Figure 2.8: Tilted SEM image of Split-Gate/Top-Gate device insulated by a cross-linked PMMA (dark grey) layer fabricated onto a Hall bar, as in the schematic of Figure 2.7. Fabricated and imaged at Cavendish Laboratory.

Additional gating can control the carrier density of the 1D quantum channel and depending on geometry, even reduce dimensionality to 0D. Depending on the geometry of the device and the characteristics we wish to measure there exist a various range of designs.

The schematic of Figure 2.7 shows a Split-Gate/Top-Gate structure. There is an added layer of insulator to protect the sensitive Top-Gate electrode and ensure that it only acts over the region of interest, over the narrow channel defined by the Split-Gate. Figure 2.8 is an SEM image of the 1D device.

2.4 Wafer Characterisation

The main characteristic parameters describing a GaAs/AlGaAs heterostructure are carrier density and mobility. A wafer is typically patterned into a Hall bar, in order to assess its properties.

Hall Bar

The Hall bar is by far the most common geometry used for characterisation. It is designed so that uniform current flow can occur from source to drain, significantly longer than it's width, with sufficient contacts on either side of the main current path to measure voltage drops and voltage changes in an applied magnetic field.

The CAD drawing of Figure 2.9 shows the design pattern for a photolithographic mask of a Hall bar. The processing steps to fabricate a Hall bar sample from a wafer are the following:

1. Align in favoured (1 0 0) orientation of high mobility.
2. First expose the mesa mask (blue, in Figure 2.9) to define the geometry of the device, covering with resist. Wet chemical etch (typically with HCl) of mesa pattern.
3. Remove the resist using Acetone and IPA rinse.
4. Use the ohmic contact photolithographic mask (green, in Figure 2.9) to cover with resist.
5. Evaporate the ohmic metallisation using a clean thermal evaporator.
6. Remove the resists used to define the contacts (using Acetone and IPA) and lift-off the mask.

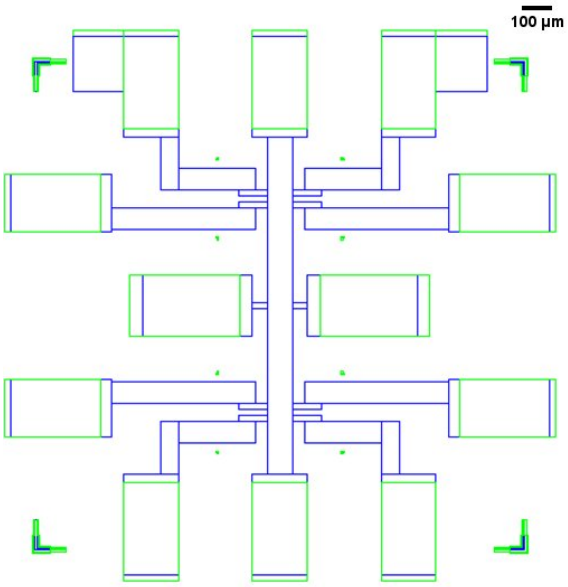

Figure 2.9: Standard J9 Hall bar, designed with the voltage probes to be 9 squares apart (as defined by the width of the sample divided by it's length). Devices such as this allow for a measurement of the transverse (Hall) and longitudinal (Shubnikov de Haas) resistances which are key parameters for device characterisation of carrier density and mobility. Hall bars such as these are used as a standard in semiconductor physics and the industry as a whole in sample characterisation. This design is from the Cavendish Laboratory.

7. Anneal contacts in a Rapid Thermal Annealer in a nitrogen/forming gas environment.

A Hall bar is designed with voltage probes so that the longitudinal and perpendicular voltage drops can be measured. Schematic of Figure 2.10 shows the basic measurements done on a Hall Bar type sample in an applied magnetic field. The longitudinal voltage is used to measure the Shubnikov-de Haas effect, a damped harmonic oscillation driven by the electrons, due to the Lorentz force (strongly temperature dependent but typically high field) while the voltage probes opposite to each other are used to measure the Hall effect, which is linear at low fields (classical) and typically becomes quantised in fields over 0.5 T, depending on the carrier density of the sample. Such that

$$R_{xx} = \frac{V_{xx}}{I_{sample}}, \; R_{xy} = \frac{V_{xy}}{I_{sample}} \tag{2.3}$$

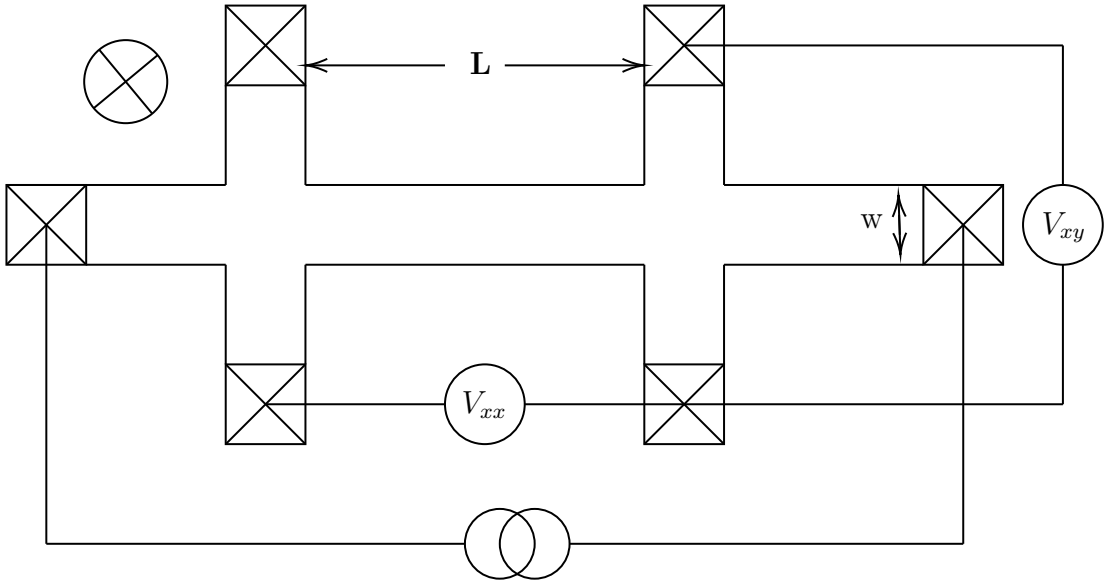

Figure 2.10: Basic characterisation setup of a Hall Bar sample. V_{xx} provides the longitudinal resistance, measured by the voltage probes on the same side of the bar, while V_{xy} provides the Hall voltage, measured across the bar.

For two-dimensional samples, resistivity reduces to resistance per square of 2DEG, with the ratio of length to width defining the 'number of squares' of the device: $R_{\square} = \frac{\rho W}{L}$. When a perpendicular magnetic field is applied, electrons flowing through the 2DEG will experience the Lorentz force $\mathbf{F} = q(\mathbf{E}+\mathbf{v}\times\mathbf{B}) \propto \mathbf{I}\times\mathbf{B}$, $\mathbf{I}$ being the current flowing through the sample. The change in current flow due to the Lorentz force is detected as a voltage drop on opposite sides of the width of the conductor and is the manifestation of the Hall effect. In a 2D sample, the measured voltage relates to the current flowing in the sample and the magnetic field as

$$V_H = IR_HB \tag{2.4}$$

with R_H being the Hall coefficient, which can be defined at $B = 1\mathrm{T}$ as:

$$R_H \equiv -\frac{B}{ne} \rightarrow R_H(1T) = -\frac{1}{ne} \tag{2.5}$$

Thus, the slope of V_H vs B can be used to calculate the carrier density and type of carrier of the sample. Using a 4-terminal measurement of the

resistance along the current path, a R_{xx} measurement, the resistance per square of 2DEG, $R_{\square}$ can be determined, using:

$$\mu = \frac{1}{neR_{\square}} = \frac{R_H}{R_{\square}} \tag{2.6}$$

From equations (2.5), (2.6), the carrier density and mobility of a sample can easily be characterised, by two simple voltage measurements across and along the bar, as in the setup of Figure 2.10. Note that the sample dimensions do not enter into the expressions for Hall voltage or carrier density.

At high perpendicular magnetic fields and sufficiently low temperatures, the transverse (Hall) resistance shows quantised plateaus, while the longitudinal resistance starts oscillating to resistive and dissipation-free states, due to the applied Lorentz force from the magnetic field to the motion of the electrons, known as the Shubnikov-de Haas effect.

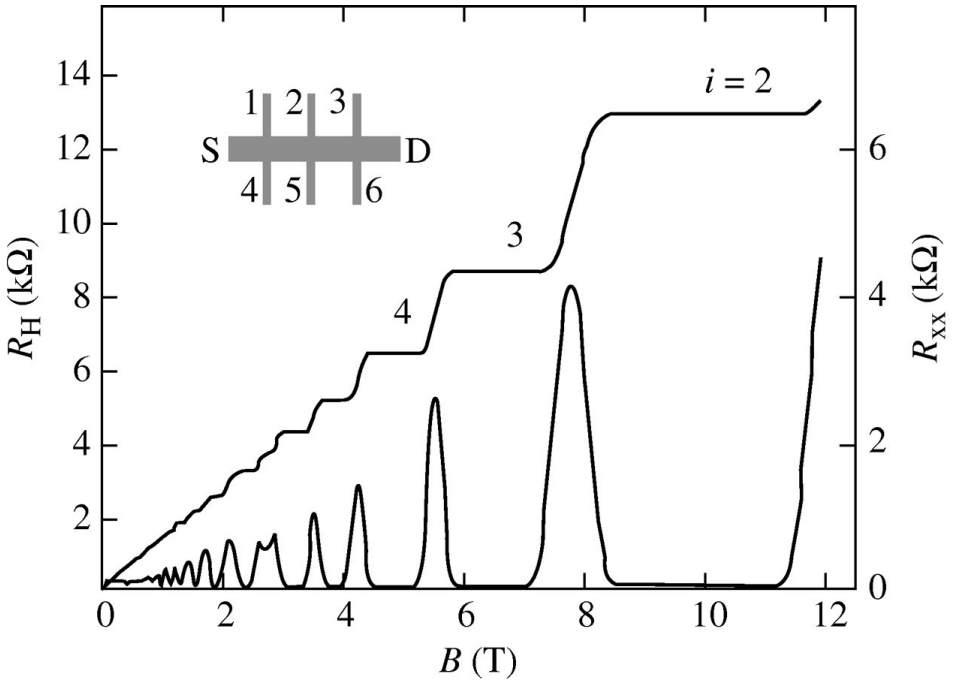

Figure 2.11: Hall and Shubnikov-de Haas effect. The Hall resistance becomes quantised at points the longitudinal resistance is at vanishing values. Image from [55].

Magnet Dipping Probe

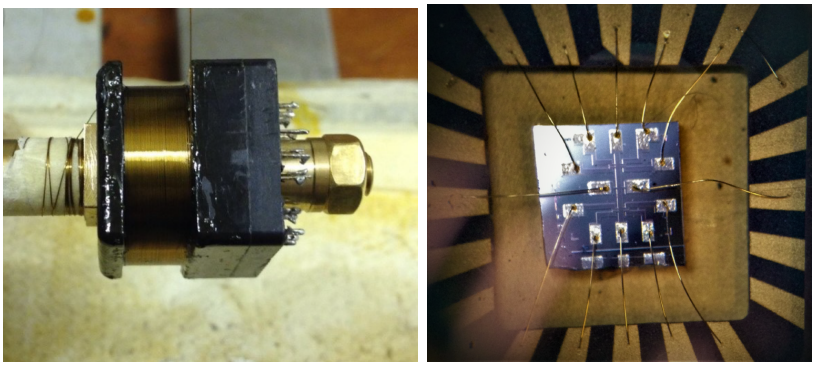

(a) (b)

Figure 2.12: (a) Probe magnet being wound with Nb/Ti 0.71 μm wire around a standard 20-pin PLCC socket (OD: 20.6 $\pm$ 0.05mm) using a manual coil winder at RHUL prep room. The first iteration of this magnet had 1000 turns of wire, with a density of 115 $\pm$ 0.6 turns per length producing a field with B/I ratio of 61.0 $\pm$ 0.2 mT/A. (b) W476 Assessment sample 1 under an optical microscope, mounted on a 20-pin LCC, sample is tilted so the mesa and Hall bar geometry is visible.

For magnetoresistance measurements at 4.2 K, a probe equipped with a magnet wound around the sample holder was made to allow for characterisation of device density and mobility. This is in part due to fabrication problems at the time resulting in samples of low mobility but also to account for general variation in wafer. When a wafer is produced, the Assessment laboratory usually fabricates two Hall bars from the middle of a wafer in order to characterise quality and performance. This means devices fabricated further from the centre of the wafer may vary in quality. This probe was designed with an aim to characterise this potential variation and also indicate whether devices are of sufficient quality.

A standard PLCC chip holder was modified and wound with 0.71 μm superconducting Nb/Ti wire and insulated with GE varnish. This version of the probe had a B/I ratio of 61.0 $\pm$ 0.2 mT/A with a 7A current limit, as shown in Figure 2.12. Assessment Sample 'J9' Hall bar 1 for wafer W476, gave identical carrier density as that measured in the Assessment laboratory, but lower mobility, due to the difference in the two temperatures of the measurement.

Check with Assessment Lab data

To establish the accuracy of measurements in our lab and quality of samples after fabrication, the magnetoresistance of samples was measured in our laboratory at 4.2 K, to compare with Assessment laboratory data of when the wafer is initially made and characterise other devices from these wafers. Upon fabrication of a wafer, a Hall bar is fabricated from the middle of the wafer, to characterise carrier density and mobility in a pumped ^{4}He cryostat at a temperature of approximately 1.5 K. These samples are called assessment samples and give the quoted value of a wafer. Samples from wafers W475, W476, V827 and V834 were calibrated additionally using the magnet probe at 4.2 K.

Key parameters indicating the performance of a sample are carrier density and mobility. The carrier density is the property that has the highest accuracy in the measurement as it is a property of the sample that is independent of temperature differences and easily determined from the Hall effect. Mobility is what eventually determines a samples performance in low temperature transport measurements, however, it is temperature dependent and varies even in the range $4 \rightarrow 1.5$ K, with an increase of $\sim 30\%$.

Historically, there were mobility issues with most samples and especially gated devices. Table 2.2 shows magnetoresistance dipping data at 4.2 K of wafer W475. The gated devices produced by this wafer were significantly deteriorated post-fabrication, with a resulting mobility - after illuminating to saturation - that was in instances worse than that of the Assessment sample in the dark, an effect most likely a result of impurities in the fabrication process, as the samples were deteriorated even in regions not under gates, in which regions depletion is expected. The assessment chip was cross-calibrated to ensure that the discrepancy between quoted values and the resulting characteristics was not a systematic error. The assessment sample properties were identical to the quoted values, taking into account the mobility difference of measuring it at a higher temperature of 4 K instead of $\sim$1.5 K.

Table 2.2: Characterisation of magnetoresistance of Assessment Chip (J9) and gated (J11) devices on W475 wafer measured at 4K using the magnet probe. Sample W475 J11 2A was also measured at low-temperature on the Kelvinox cryostat and showed various unexpected inhomogeneities arising in that cooldown, including random telegraph signals on conductance traces (from impurities).

Samples	Dark		Flashed	
W475	n ($\times 10^{11}$cm^{-2})	μ ($\times 10^6$ cm^2/Vs)	n ($\times 10^{11}$cm^{-2})	μ ($\times 10^6$ cm^2/Vs)
1A	1.7	0.6	3.6	1.8
1B	1.7	0.7	3.2	1.6
1C	1.8	0.7	3.4	1.4
2A*	1.8	0.9	3.5	1.9
J9 Assessment Chip	1.9	2.2	3.4	5.5

Table 2.3 shows results from magnetoresistance characterisation at 4.2 K, which determined agreement with Assessment laboratory data. Comparison of the two assessment chips (J9) with gated devices (J11) of a subsequent batch on wafers V827 and V834.

This test established that the wafers are homogenous and samples can be made from them without significantly reducing mobility as in the past. The samples showed satisfactory gate traces on macroscopic, split-gates as well as split-gate/top-gate quantum point contacts without a significant reduction in mobility when compared to the assessment chip. Such samples labeled "SG" have 6 pairs of gates along a Hall bar that is 11 squares of 2DEG (J11) long. The large array of gates can significantly detriment mobility, from causes such as strain, electrostatic charge buildup in the insulator or deterioration due to fabrication [56], therefore such a result is significant in comparison to fabrication history in our collaboration, as well as other groups.

Following this satisfactory result, focus shifted into optimising the contact resistance for samples on these wafers, in order to produce samples compatible for low and ultra-low temperature experiments, described in detail in chapter 4.

Table 2.3: Hall Probe Measurements at 4.2 K, assessment and gated sample comparison. Minor drop in mobility is seen on the gated devices, as expected from depletion under the gates. The overall sample quality improved by using a dedicated evaporator to anneal the contacts to the devices.

	Dark			Flashed		
Sample	n ($\times 10^{11}$ cm^{-2})	μ ($\times 10^6$cm^2/Vs)	$R_\square$ (Ω)	n ($\times 10^{11}$ cm^{-2})	μ ($\times 10^6$cm^2/Vs)	$R_\square$ (Ω)
W475 J9	1.9	2.2	15.0	3.4	5.5	3.4
V834 J9	1.6	1.1	35.2	3.6	2.8	6.1
V827 J9	1.6	1.2	34.0	3.4	2.5	7.2
V827 J11 SG2	1.6	0.9	44.1	3.5	2.4	7.4
V834 J11 SG1	1.6	0.6	70.7	3.7	2.0	8.5

2.5 Carrier Density, Mobility and Persistent Photoconductivity

When a red LED is shone onto the device it can excite carriers from the lattice into the conduction band. At low temperatures (4.2 K and below) this effect persists and is referred to as persistent photoconductivity. The wavelength of the type of red LED used on our dipping probes and fridges has been calibrated at low temperatures.

Illumination is used to change the carrier density of a system, typically increasing it three-fold, in situ. Any such sample at low temperatures has therefore two different states, dark and illuminated ("flashed") state, with also intermediate states being available by shining the LED with short pulses and tuning the carrier density. This effect persists until the sample is cycled thermally.

Incremental Flashing

Incremental flashing refers to illuminating a sample with short pulses, to investigate the persistent photoconductivity mechanism occurring in the sample. This was achieved using an accurate voltage source, an IOtech 488/4 DAC as a trigger for an Agilent 33210A waveform generator to pulse the LED with an accurate waveform, while taking magnetoresistance traces at states of intermediate illumination, before saturation.

Illuminating a sample, provides the opportunity to measure the sample anew, and with the persistent photoconductivity effect providing irreversible

memory to this sample until the next thermal cycle, it is of importance to understand this behaviour, or determine ways to empirically use it.

Due to fabrication issues with gates, samples in the past showing evidence of parallel conductivity, a significant reduction in mobility due to post-fabrication impurities and charge buildup, the purpose of this series of experiments was to determine whether such tuning of carrier density can instead be done using illumination.

Hall and longitudinal magnetoresistance traces were initially taken in the dark, and subsequently the sample was pulsed with a red LED at 2V (I=10 μA), using an Agilent waveform generator to provide accurate pulsing, 250 μs pulses were the favoured duration, although slower and longer pulses were also attempted.

The limiting factor to choosing a very small duration is that one needs to also wait for the sample to relax after the flashing process, due to the effect of recombination and/or scattering from remote impurities (referred to as DX centres) [57, 58] and in order to account for resistance drift over time. Very short pulses might make this experiment carry on much longer than necessary to reach the saturated values of the fully illuminated state. Alternatively, long pulses might saturate the sample faster, losing detail. Typically, a 3 min illumination is required to fully saturate the sample at a 10 mA current through the LED and the sample is considered stable when resistance stops drifting, a process that takes about a minute. 250 μs pulses resulted in fine detail, indicating the ability to tune the carrier density in such a way (however, such pulsing would take more than a year to aggregate to the 3 min saturated value).

This was also attempted at low temperatures, taking magnetoresistance traces of the longitudinal resistance and measuring the Shubnikov de Haas effect at low-field, with incremental pulsing presented in chapter 5. The problem with those attempts was that the W475 wafer was inhomogenous and parallel conducting, resulting in inconsistencies with what was expected from Assessment lab data for those samples. The W-wafers are made using a superlattice, which might be the cause of parallel conduction, as V-wafers do not show characteristics of parallel conduction.

2.6 Experimental Techniques For Low Temperatures

Devices are characterised at 4.2 K for performance, as described in chapter 4. This characterisation is done using dipping probes in a liquid ^{4}He dewar. To achieve lower temperatures, special considerations, methods and setups are needed, addressed in this section.

2.6.1 Low-noise, Low-Temperature Environment

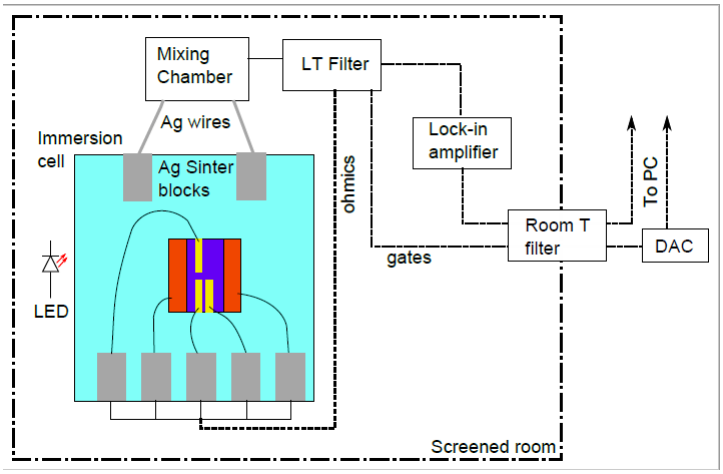

Figure 2.13: Schematic of low-temperature measurement setup for our Kelvinox 400 cryostat. The sample sits in a ^{3}He immersion cell, with silver-sintered bond-pads, thermally anchored to the Mixing Chamber. An (optional) AIVON low-pass filter can be included in the setup (on the mixing chamber) to reduce noise in the measurement lines. The cryostat sits in a pit inside a screened room, instruments are connected to the cryostat through room temperature telephone filters and controlled by a computer.

Noise reduction and elimination through filtering is vital for sensitive low-temperature measurements. Use of lock-in amplifiers allows the ability to measure a very small signal by detecting the signal at a specific frequency and eliminating the rest of the signal (noise) from the spectrum. The signal frequency of input current is chosen to be far from the mains (50 Hz) frequency and its harmonics.

The measured signal is checked using a spectrum analyser or an oscilloscope to check for noise in the circuit. 50 Hz and RF noise are considered to be the main source of noise in the electrical measurement system.

To further reduce external noise and radiation heating, our cryostat is contained in a screened room, along with the measuring equipment, coupled to the computers outside it using a GPIB/optical fiber interface and a telephone filter box of 8 lines fitted with BNC connectors. The whole dewar is in a pit, placed underground and on anti-vibration airmounts. The full experimental setup is depicted in Figure 2.13. To achieve low temperatures we use cooling through leads inside a ^{3}He bath as described in section 2.6.3.

2.6.2 The Modified Kelvinox Cryostat

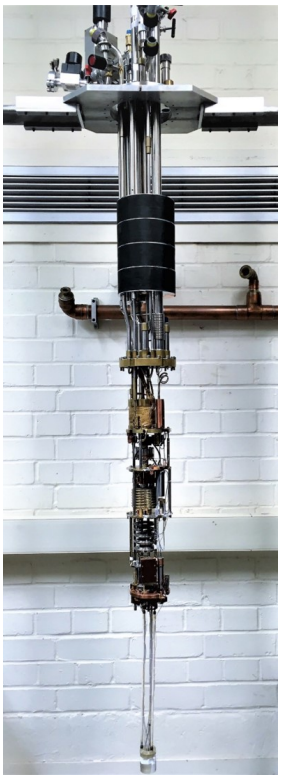

Figure 2.14: The Kelvinox 400 cryostat insert.

The Kelvinox 400 cryostat has been modified with an immersion cell for optimal thermal contact between the sample and the mixing chamber, the

coldest point of our fridge reaching 6 mK. For optimising magnetotransport measurements, the sample must sit at the center of our (up to 16 T) magnetic field, this is achieved by mounting an immersion cell on alumina rods and thermally connecting it to the mixing chamber via silver sintered leads clamped to the copper plate of the mixing chamber plate. There are three further stable temperatures apart from the mixing chamber available on dilution fridges; that of the helium bath at 4.2 K, the 1 K pot ($\sim$1.6 K) and that of the still, where distillation takes place of $\sim$0.6 K, all of which are stages a sample can be mounted on depending on the required temperature of the experiment and number of available lines.

To improve thermal contact over this distance we use silver sintered wires, thermally clamped to the mixing chamber copper plate on one end, and embedded onto silver sintered heat exchangers inside a stycast ^{3}He immersion cell on the other. More details for the immersion cell are provided in the next section, 2.6.3.

For the Kelvinox, on previous runs our noise thermometer read just under 6 mK for base temperature and was cross-calibrated with the resistive thermometers of the fridge as well as a tuning fork thermometer. Thermometry methods viable for this fridge can be found in Appendix E.

2.6.3 The Immersion Cell

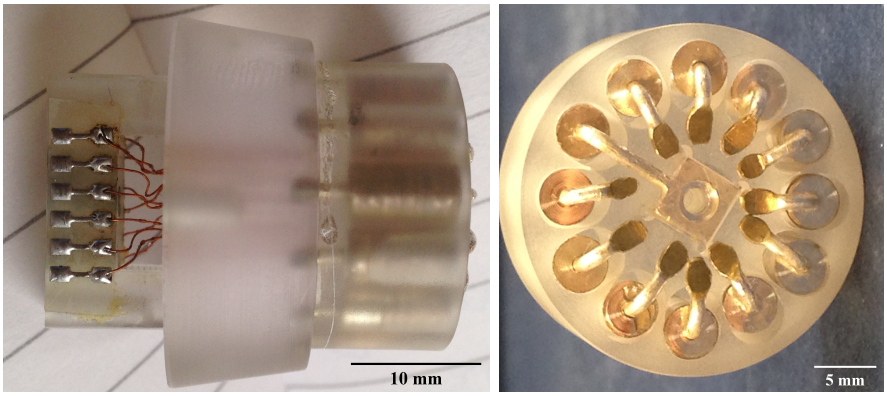

(a) (b)

Figure 2.15: Lid for 1266 stycast immersion cell designed by the RHUL ultra-low-temperature group for measuring samples in a perpendicular magnetic field (a) side view: showing the measurement wires embedded in the silver sintered heat exchangers, (b) front view: one line is a dedicated thermal ground for efficient cooling of the lattice of the sample, 11 more gold-plated silver sintered measurement lines are positioned around. It can comfortably host a sample of 5 mm $\times$ 5 mm size.

The 1266 stycast immersion cell composes of a body fixed on the fridge and a lid that the sample mounts onto. The lid is screwed into the body in a leak tight tapered seal which serves to hold the ^{3}He bath for our sample. The sample is bonded to the heat exchangers of the immersion cell with gold bond-wires, thus optimising thermal contact.

In our setup, the leads are heat-sunk by clamping silver sintered wires onto the mixing chamber copper plate, the coldest point of the dilution fridge. The limiting factor in cooling the sample is therefore the thermal resistance due to the contact resistance between the very low-resistance wires themselves and the resistance of the contacts of the actual sample.

For optimal thermalisation, silver sinter is pressed into wires which are thermally clamped to the copper mixing chamber stage. The wires extend to the immersion cell body which is affixed on the fridge and terminate on silver sinter heat exchangers, providing extra area, low thermal resistance and therefore cooling power. The heat exchangers form the main component of the body of the cell along with a tuning fork thermometer. The extra area

provided by the sintered heat exchangers allows for more thermal contact such that when the cell is immersed in ^{3}He there is excellent thermal contact and electrical insulation as a result of this immersion. A detailed description of the original immersion cell design on ND3, along with cooling techniques can be found in [26].

^{3}He is chosen due to it being normal in this temperature regime (down to 6 mK) so that there is no chance of a superfluid leak out of the cell. Additionally, the viscosity of ^{3}He is temperature dependent and therefore a quartz tuning fork thermometer can be used to determine temperature from viscometry. The immersion cell design was inspired by the work of Samkharadze *et al.* [59] and Xia *et al.* [25].

Two primary components make up the immersion cell: the body, which is fixed on the cryostat with the sintered-silver wires and heat exchangers, containing the tuning fork permanently affixed in a cavity such that it can give accurate temperature readings of the ^{3}He bath and the lid; where the sample is mounted. There are two variations of the lid that exist for the Kelvinox cryostat, one for measurements in perpendicular field and the other in parallel field. Both versions of the lid are affixed by screwing into a tapered seal that is wetted by a thin layer of APIEZON N vacuum grease.

The Kelvinox and ND3 cryostats are equipped with a stycast 1266 immersion cell, which has desirable thermal properties and also contracting at low temperatures making a better vacuum seal, designed by Dr Levitin. The sample sits on the immersion cell tapered seal lid (Figure 2.15), to allow for easy moving from one cryostat to another without the need to rebond or make any otherwise dangerous modifications to the sample.

The immersion cell lid hosts the sample and is removable, with two orientations, depending on the requirements of the experiment as in Figure 2.16. Available are 11 sintered-silver pads to bond to, the 12$^{\text{th}}$ line is a dedicated thermal ground to make sure the lattice cools as well. A copper plate sits on the thermal ground and the sample is mounted onto it with Ag paint or GE varnish. Methodology for mounting samples into the immersion cell can be found in Appendix B.

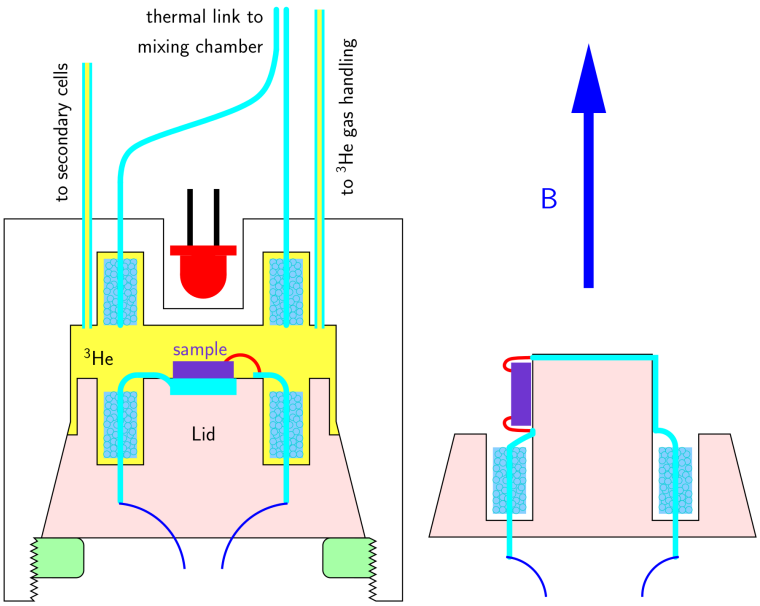

Figure 2.16: Schematic of the immersion cell lids for the Kelvinox immersion cell for mounting a sample in perpendicular or parallel field. The schematic on the left hand side also depicts the tapered seal to the cell body, the ^{3}He gas lines, thermal link to mixing chamber and the LED used for illumination.

2.7 Summary

Advancements in MBE allowed for the creation of samples with monolayer accuracy. An overview of 2DEGs in practice was given through the fabrication processes used to create them at the interface of a heterostructure, as well as the most common ways confining this system further. The standard characterisation of a wafer was explained, highlighting the steps necessary after production to determine sample quality in order to fabricate samples intended for low-temperature work. The low-temperature experimental setup was presented with focus on the immersion cell addition to the Kelvinox fridge.

In the following chapter, the contacting mechanism of AuGeNi ohmic contacts is discussed.

Chapter 3

AuNiGe Ohmic Contacts

In order to connect to a 2DEG electrically, it needs ohmic contacts. This chapter describes ohmic contacts drawing from past studies in the literature and our own results through a series of systematic imaging. An overview of the most prevalent gold-nickel-germanium alloy is given and the contacting mechanism to heterostructures is investigated. It is concluded that our low-resistance ohmic contacts have a typical microstructure which is similar to previous studies of other groups.

3.1 Introduction to AuGeNi Ohmic Contacts

The contact to the device needs to be ohmic, such that electrical current can flow in and out of the semiconductor in a well defined way. Furthermore, it needs to be of low-resistance in order to contribute as little as possible parasitic resistance in the measurement and upon cooling. Achieving a reproducible low-resistance ohmic contact to a semiconductor device is a mix of trial and error as well as an art. The main underlying problem in fabrication is that annealing a metal onto a semiconductor such as GaAs typically results in a Schottky (diode) contact [36] so that ohmicity is not achieved without doping the contact to lower the bandgap enough such that electrons can tunnel.

By far the most common metallisation used to contact GaAs devices (and by extension also modulation-doped AlGaAs/GaAs HEMTs) is the gold-nickel-germanium metallisation, a well-established technique since first pro-

posed by Braslau in 1967 [60] which has achieved the most optimal contacts as far as reproducibility and ohmicity are concerned.

Practically, an ohmic contact (also referred to as "ohmic") that is highly resistive can overheat a large integrated circuit [61], while in our work a highly resistive contact will inhibit cooling the device to the ultra-low temperature limit by a large series thermal resistance as well as Joule heating. Characterisation of ohmic contacts to determine the ideal annealing conditions for the fabrication of our contacts is described in detail in Chapter 4.

Conduction Mechanism of Ohmic Contacts

A good ohmic contact is such that it is a source of carriers with non-zero internal resistance, the contact resistance, which obeys Ohm's Law for all current densities that are of interest to the use of the device.

When a metal is applied on the surface, the conduction and valence bands bend so that the Fermi levels of the metal and semiconductor are equal (thermal equilibrium). A metal on the surface of a III-V semiconductor results in a Schottky barrier and behaves as a diode [36]. Schottky diodes conduct through the process of thermionic emission [36], however, this process would be inaccessible at low temperatures. We want the contact to work at the lowest temperatures possible and, in this regime, the main mode of transport has to be tunneling since there is not enough thermal energy for thermionic emission.

Figure 3.1 shows the band model of GaAs when a metal is alloyed on the surface, before and after applying a voltage through the barrier. In general, the barrier height is independent of the metallisation and only on the semiconductor [36]. The barrier for GaAs is experimentally found to be ~ 0.8 eV [62]. The potential difference needed for electrons to tunnel through this barrier is the origin of contact resistance.

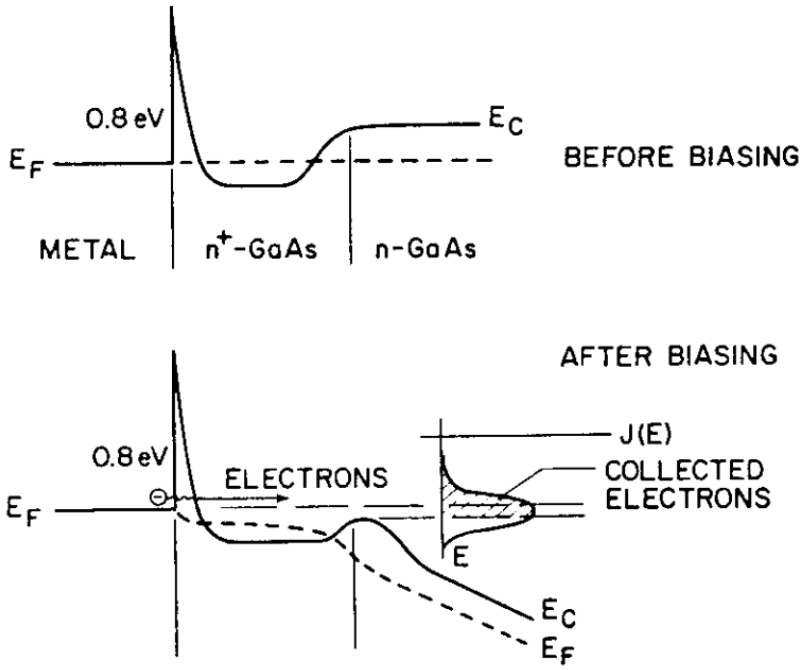

Figure 3.1: Band model of metal-GaAs ohmic contact before and after bias is applied. Schematic from [63].

The probability that an electron may tunnel from the metal into the semiconductor depends on the height and width of the barriers, which can be estimated by the WKB approximation or calculated by analytically solving the Schrödinger equation for the depletion region [64]. In either case, the barrier width decreases as the square root of doping concentration and therefore the tunneling current increases as the square root of the doping concentration.

The fundamental strategy used when developing ohmic contacts is to dope the semiconductor sufficiently to ensure that the dominant conduction mechanism is tunneling, for GaAs a great such doping element is Ge. Figure 3.2 shows the proposed conduction mechanism by Braslau [63], whereby conduction is through the (Ni)Ge inclusions of the alloy.

Although the general underlying physics is well established, exactly what occurs during the process of annealing to result in an ohmic contact is more ambiguous [36], as such investigation of the microstructure of the contact is important. In this chapter we will see that ohmic contacts have a distinct

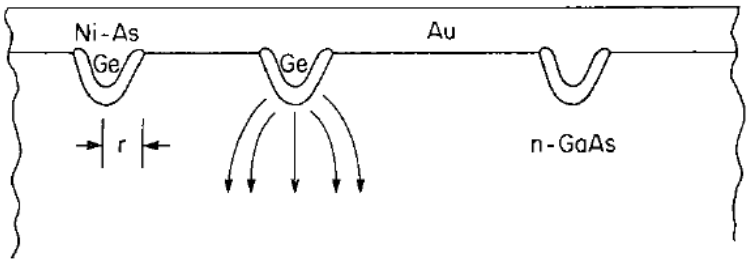

Figure 3.2: Schematic of contacting model of AuGeNi metallisation to GaAs, from [63]. Conduction is through an array of Ge-rich inclusions of negligible contact resistance compared to the spreading resistance between them. The measured contact resistance is then $R_c \sim \langle A \rangle^2 [\rho_n \pi \langle r \rangle + R_c / 2\pi f \langle r \rangle^2]$, $\langle r \rangle$ is the mean radius of the inclusions, ρ_n is their resistivity and $\langle A \rangle$ is their mean separation. A gold overlayer shorts these Ni-Ge-As islands together.

surface morphology and microstructure characteristic of the processes that occur during the formation of the contact.

3.1.1 A brief history of ohmic contacts

AuGe ohmic contacts on GaAs were first used in making Gunn diodes, by Gunn [65]. Initially only Au was used, but Gunn noticed that the addition of Ge (up to 12% wt.) dropped the melting temperature of the eutectic to 361°C, significantly lower than the melting point of Au, over 1000°C. The significantly lower temperature required for annealing was very beneficial for fabricating onto temperature sensitive semiconductors such as GaAs. This eutectic composition is still used to this day and has proved to be a successful way of contacting GaAs devices.

AuGe contacts suffered from irreproducibility, as they are very temperature sensitive and tend to form islands of ohmic material (Au-rich island) and areas of semiconductor material, making them non-uniform and often resistive [36, 66, 67]. A significant improvement resulted by adding Ni to AuGe, originally this occurred due to a contamination of the tungsten evaporator boat, using a common annealer with another experiment, a story best described in the original review by Gunn on his discovery [68]. Gunn noticed the effect of decrease of surface roughness and Braslau [69] later suggested that wetting with Ni reduces this non-uniformity and improves surface morphology, and proposed a mechanism for the contacting model. The addition

of a small amount of Ni improved surface roughness, making the contacts more uniform by improving surface adhesion, as is a common use of Ni in industrial applications (e.g. plating).

Further work showed that the effect of the addition of Ni (up to 2.67% wt.) increases solubility of GaAs in the eutectic AuGe [70]. This solubility is otherwise relatively low below 500°C and the addition of Ni enhances the diffusivity of the dopant, Ge, into GaAs [60, 71], working as a catalyst in the contact formation. Ni acts as a wetting agent, increasing the reaction of the surface area of the semiconductor, as it getters the native GaAs oxide film, which can inhibit alloying [72]. While Ni enhances Ge diffusion, it is Au that dissociates Ga from the lattice, making the interplay of both important for the formation of the contact [73]. The concentration of Ni_2GeAs phases at the GaAs interface has been correlated with low-resistance contacts [74] and the contact resistance, R_C, is dependent on the ratio of this Ni-rich phase to the Au-rich (typically β-AuGa) phase [75–77]. Furthermore, the presence of Ge in the GaAs lattice is not enough to ensure a good ohmic contact, it must also be located exclusively on the lattice site, with an appropriate doping (carrier density) of the order of $2{\times}10^{19}$ cm^{-3} [78].

Due to the significant improvement by the addition of Ni, its effect in the formation of the contacts has been investigated systematically. Notably [79] fabricated devices of different Ni content, concluding that Ni is a dominant factor in the resulting microstructure and composition of the contact, the morphology of the metal and the total amount of GaAs consumed are limited or enhanced by the amount of Ni. An increase of Ni content, results in more GaAs deformation during alloying and at high concentrations can even reach and damage the heterostructure. In low amounts, the alloy material has monolayer structure, with sparse grains of variable thickness. The optimal AuGe/Ni ratio has been determined to be below 0.2 for low-resistance, with an increase in this ratio having adverse effects to both resultant morphology as well as electrical resistance [77].

Finally, equivalence between the rate of ohmic contact formation on GaAs and AlGaAs has been demonstrated [80] by annealing Au and AuGe metallisations on the two substrates and monitoring the arsenic evolution with a mass spectrometer. This is an important result in linking work on bulk GaAs and 2DEGs made on GaAs/AlGaAs heterostructures, as it conclu-

sively shows that the amount of aluminium does not impede the process of formation of the contact, as long as it has not oxidised.

Annealing of AuGeNi metallisation

The annealing process is complicated and the exact mechanism of how the contact forms is not yet fully understood. Research groups develop recipes that are usually self-consistent within a fabrication facility, sometimes only specific to a dedicated evaporator.

Annealing a metal onto a semiconductor is an efficient way to dope it in order to lower the Schottky barrier sufficiently so that tunneling is possible. In the past this was done in a furnace over long timescales, significant improvements in the process are achieved using a rapid thermal annealer (RTA). Typically annealing occurs in the range of 400-450°C from 20 seconds to several minutes, with larger temperatures usually requiring less anneal time (less total integrated heat to the metallisation).

RTA machines have a quartz chamber, a heater and a supply of forming gas to minimise oxidation. The chamber of the machine needs to be purged with high purity forming gas in order to remove oxygen, as oxides would introduce impurities, resulting in a resistive sample. A chamber with impurities may lead to a very poor yield and irreproducible contacts.

The general parabolic trend of Figure 3.3 of AuGeNi contact resistance is widely reported in the literature from the initial days to now - on 2DEGs (see excellent reviews by Murakami [81] and Baca [82]) and has been linked to surface roughness, with the leftmost side of the curve (underannealed) showing a smoother appearance, a rough appearance (minimum, low-resistance) and at the rightmost side a dendritic appearance (overannealed). As explained previously, the temperature calibration is subject to the apparatus used and is not necessarily the temperature the actual process occurs in. Under conditions like RTA this is even harder to deduce, so the x axis of this curve is a bit arbitrary but nevertheless it shows a consistent trend. Following fabrication, test devices need to be made to standardise quality of fabrication. This is typically done internally within a group, with minor modifications to the recipe, to optimise the underlying processes of contacting the substrate.

Measurements on ohmic contacts at different annealing conditions are presented in chapter 4, samples produced at 430°C for 80 s have reproducibly

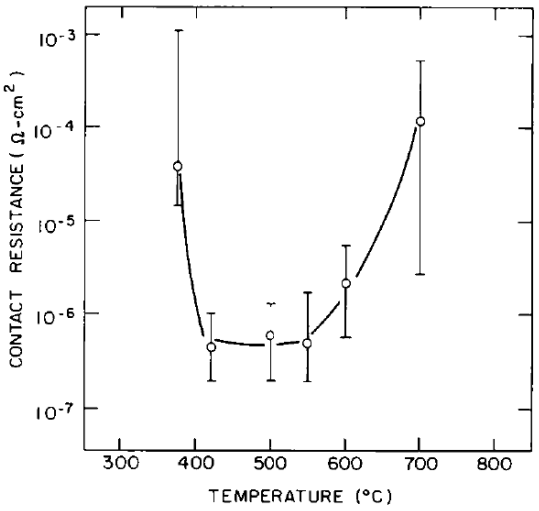

Figure 3.3: Contact resistance of AuGeNi contacts annealed at different temperatures [81].

low contact resistance, using a consistent recipe in a dedicated annealer. The contacting mechanism is described in more detail in section 3.2.1.

Processing steps

The typical processing steps for the production of a simple resistor with a defined geometry (mesa) and contacted with ohmic contacts are:

1. Optical lithography of mesa (using a mask).
2. Etching mesa pattern.
3. Optical Lithography of contact.
4. Evaporation of ohmic material.
5. Annealing (AuGeNi alloy: eutectic or in steps, layered) ohmic material onto the etched mesa of the sample for electrical measurements.
6. Cleave and clean samples.
7. Mount onto chip carrier (LCC).
8. Wire-bond onto a chip carrier for characterisation.

3.2 AuNiGe Ohmic Microstructure

3.2.1 AuGeNi Contacting Mechanism in the Literature

Most studies of AuGeNi ohmic contacts are on n-GaAs, they have been widely used for decades and are considered the standard of contacting GaAs [82] due to their ohmic and low contact resistance. More recent studies have been done on heterostructures [76, 83–85], expanding upon and agreeing with results on n-GaAs [60], further suggesting the contacting mechanism remains the same for heterostructures [76, 84], with only slight variations in morphology due to using different compositions (e.g. Ni wetting improving roughness [86]).

Equivalence to typical n-GaAs substrates is mostly due to close lattice matching between GaAs and AlGaAs and in this case there exists a small amount of aluminium in the heterostructure (~80 nm in our wafers), which can interact with the ohmic alloy. This amount of aluminium is not expected to play a very important role due to its comparatively small concentration other than perhaps slowing down reaction time [85, 87]. Work from [87] suggested that aluminium bubbles out onto the surface and finally produces a very thin insulating oxide that is thin enough not to persist after bonding to the sample electrically, while a study by [85] suggests that this may simply form a barrier impeding penetration of ohmic material further into the 2DEG until really high temperatures are reached.

Further investigation determined that there is no difference in anneal time or temperature upon the formation of the contact on GaAs or AlGaAs, if the AlGaAs surface has been cleaned prior to deposition, and that the amount of arsenic dissociated from the lattice is proportional to the amount of Ga that is dissolved in Au [80]. Evidence further concluded that the often reported interfacial damage to the substrate is proportional to the amount of Au of the alloying material, with results being identical when using the eutectic AuGe in the standard composition with the same amount of Au [88].

The literature [60, 82] describes the contacting mechanism as follows; AuGe begins to melt and Ga diffuses in this alloy, while the Ge replaces vacancies in the lattice acting as a dopant (forming NiGeAs compounds [60, 74]). AuGe is essential for low-resistance, however ohmicity cannot be

achieved without Ni in the mixture, likely due to its propensity to bind to As [61, 89, 90], forming stoichiometric compounds at the metal-semiconductor interface. AuGe eutectic has a tendency to bubble, or 'ball up', without the addition of nickel resulting in poor contact with the semiconductor. A small amount of Ni is typically used (few nm) as a wetting layer to prevent balling up (creation of Au-rich islands) [82], a common use of Ni in industrial applications (e.g. plating, glass blowing), resulting in an overall improvement in morphology [61]. In addition, Ge diffusion into the substrate results in ohmicity through doping, but is "less important" than forming NiAs compounds [77, 79, 91], which also have close lattice matching with GaAs [89].

From our own work, presented later in this chapter, we see no difference with or without a Ni wetting layer for alloys with similar quantities of Ni, which was always kept at a low ratio, and evidence from our cross-sectional SEM study (section 3.3.3) suggests that Ni travels to the metal-semiconductor interface, regardless of the order of deposition, this is reported in the literature as a necessary condition for low-resistance ohmic contacts [77]. A series of detailed morphological studies [60, 79, 84, 85] have determined the primary contacting mechanism to be Ni_xGeAs compounds, forming the doping region of the contact at the metal-semiconductor interface. During RTA, there is a dramatic redistribution of Ni [74], so Ni wetting prior to deposition might only aid the growth of NiGeAs compounds at the interface slightly, improving thermal stability [61, 76, 86]. In both ohmic contacts to GaAs and AlGaAs/GaAs heterostructures, NiGeAs is mainly situated in the interface, making complicated ternary stoichiometric compounds with the Ge dopant and the lattice, while AuGa is relatively segregated [85].

Furthermore, in the electrical characterisation of our contacts (presented in chapter 4) there was no evidence of a difference with or without an initial Ni wetting layer at 4.2 K. The lack of sensitivity of the contact formation to anything apart from keeping a roughly fixed Au/Ni ratio, suggests the underlying contacting mechanism is fundamentally the same, as proposed originally by Braslau [60] in his contact model. Studies on the effect of Ni in the contacts have determined that Ni is no longer magnetic after standard RTA processing conditions [92]. Most importantly, the addition of Ni needs to be controlled - an increase in Ni content can have adverse effects on the resultant morphology - with the ratio of Ni to the eutectic AuGe being the

primary component affecting the microstructure, metal composition of the contact, resultant morphology and amount of GaAs consumed from the semiconductor. The optimal ratio is fixed to 0.2 for low-resistance AuGe/Ni/Au ohmic contacts [77, 79, 92].

Figure 3.4 depicts a cross-sectional SEM image showing the widely reported two distinct regions: one Au-rich and the other Ni-rich, which include complex binary and ternary compounds with a mixture of phases [74, 85]. This microstructure was also observed by the cross-sectional SEM study conducted at the Cavendish laboratory, presented in section 3.3.3.

Lower annealing temperatures and more Ni are reported to improve morphology (reducing surface roughness) [61], but we have seen higher contact resistance and overall poor performance in contacts annealed below 430°C, even when annealed for a longer time, in those cases for our samples.

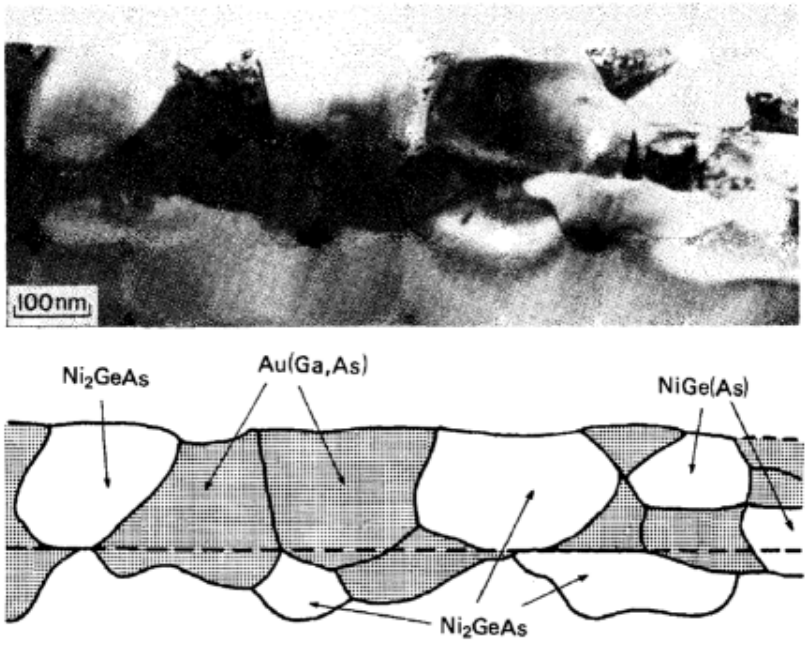

Figure 3.4: Image and schematic of cross-sectional SEM study by Kuan *et al.* [74] to determine ohmic structure. Ni-rich inclusions of various sizes are seen inside a Au-rich overlayer.

Figure 3.5 shows a cleaved SEM image of an ohmic contact of a high-Ni content sample [79]. The size of the Ni-rich grains of a high-Ni content sample can vary and, in some cases, even penetrate through the Au-rich overlayer,

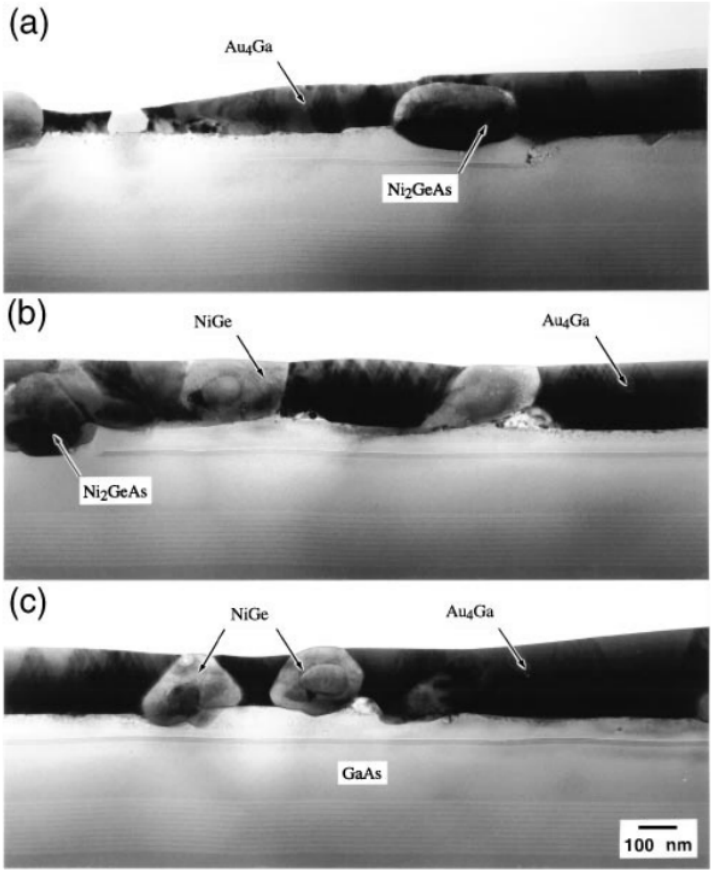

Figure 3.5: Cross-sectional SEM study by Lumpkin *et al.* [79] (a, b , c) are different sites of a high Ni content sample. This suggests it is hard to produce an even layer of Ni, as attempted by Murakami *et al.* [93].

suggesting a possible distinct Ni-rich layer between the Au-rich overlayer and the substrate is unlikely.

Both Figures 3.4 and 3.5 demonstrate an adverse effect of an abundance of Ni throughout the contact, the varying placement of Ni inclusions at longer anneal times or higher Ni content samples can result in adverse effects in the contact morphology as well as contact resistance. In addition to a controlled amount of Ni, low contact resistance requires the NiAsGe to be located in the metal/GaAs interface [77, 85].

3.3 Imaging of Ohmic Contacts

Looking at samples under an optical microscope, it is evident that the ohmic structure is complicated. Figure 3.6 shows a gated device, the gated material is mostly pure gold, with just a bit of titanium for adhesion, the contacts even with a Au capping layer do not have the same appearance, they are rougher on the surface and the colour is duller. This is because the contact is annealed, resulting in complex compounds in combination with the substrate, while the gate is deposited onto the substrate, with an insulating layer of PMMA in between.

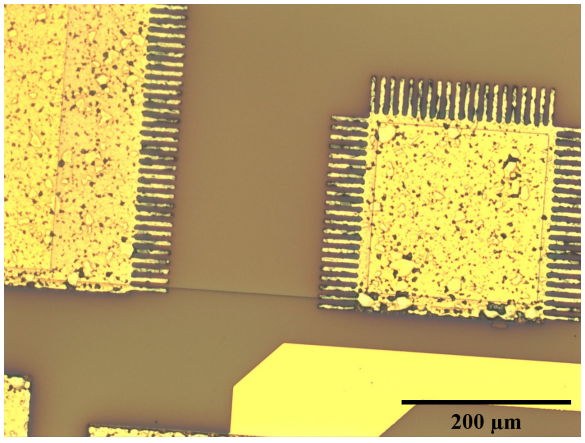

Figure 3.6: Zoomed-in image of a gated device with crenellated ohmic contacts. The ohmic contacts have an added gold capping layer, the 200 μm $\times$ 200 μm contact has very different morphology than that of the optical gate-arm (mostly un-annealed Au). The difference of the top layer of the metallisation of the contact is evidently not only pure gold, as often mistakenly reported in literature. Compared to Au deposited through EBL, the surface is rough and the colour of the contact is duller. Imaged at RHUL clean-room.

This difference in morphology is an indicator of the complex contacting mechanism of the alloy to the semiconductor. The ohmic contacts of our samples have been catalogued by taking images under optical microscope with the aim to connect their appearance with performance. Through optical imaging it was concluded that samples from the same annealing conditions have the same morphology, although that is also dependent on the sample geometry of the contact, as shown in the next section 3.3.1.

3.3.1 Optical Microscopy

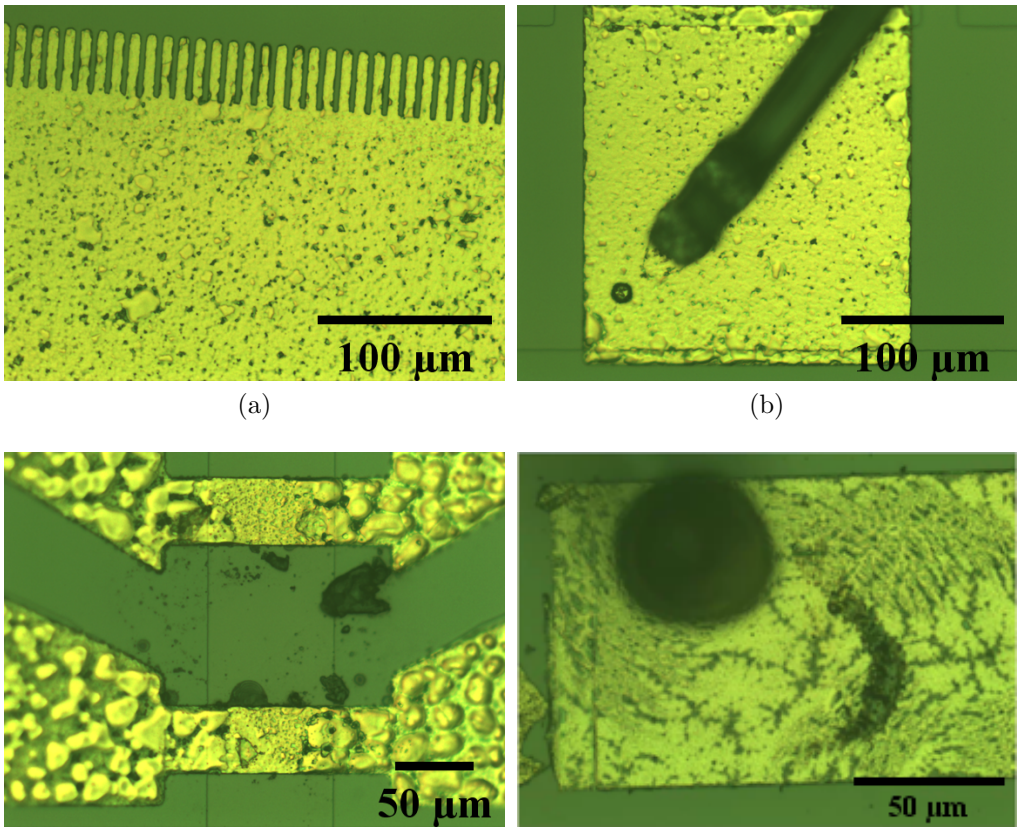

(a) (b)

(c) (d)

Figure 3.7: Ohmic contacts of different geometries and size on wafer V834: (a)-(c) annealed in the same batch at 430°C for 80 s in Ni/AuGe/Ni/Au layers, (d) annealed using a eutectic 'slug', standard Cavendish Assessment Lab recipe. Contact morphology is consistent for a given sample size throughout batch. Pictured: (a) 4 mm× 1 mm main ohmic, (b) 200 μm × 200 μm ohmic, (c) 80μm × 60 μm ohmic at optimal annealing conditions and (d) Assessment Chip Hall bar annealed at longer time. The alloy generally shows dendritic structure at long anneal times. Imaged at RHUL clean-room.

All our ohmic contacts were photographed under an optical microscope to catalogue their appearance. Although just the appearance of an ohmic could never replace measurement to determine its effectiveness, contacts annealed under the same conditions have the same rugged surface morphology. This is important for a quick consistency check between batches of samples, espe-

cially with fixed ohmic material composition and annealing conditions.

The literature has long concluded that appearance of ohmic contacts is linked to their performance [36, 93], the alloy (without an overlayer of Au) will appear "splotchy" under optical microscope which, through past literature studies as well as experience, is distinctive of low-resistance contacts.

Figure 3.7 (a-c) shows contacts annealed at optimal annealing conditions measured having reproducibly low resistance, throughout various batches of samples, while Figure 3.7 (d) shows the dendritic formation occurring from overannealing.

It is important to highlight the change in appearance of the contact when the device geometry changes, the contact of the TLM structure shown in Figure 3.7 (c), annealed on a mesa of width 80 μm is very different than that of the 4 mm or the 200 $\mu m \times$ 200 μm contacts depicted in Figure 3.7 (a) and (b). Imaging depends on ambient light conditions as well as focusing, for the purposes of this study the magnification and ambient conditions were kept as similar as possible, in the same cleanroom.

Figure 3.8 shows TLM bar devices with 80 μm mesa-ohmic overlap the samples labelled as "underalloyed" 3.8 (a)(b) were annealed at 400°C for 60 s and have a more uniform appearance than those of Figure 3.8 (c)(d), which are of low resistance and annealed at the optimal annealing condition of 430°C. The results of characterisation are presented in chapter 4.

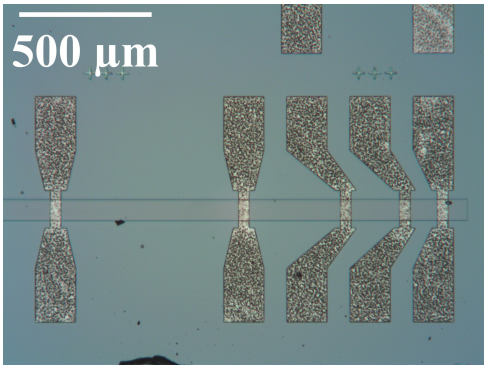

(a) Underalloyed TLM sample

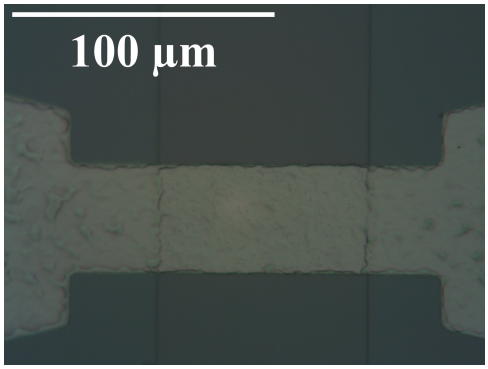

(b) Underalloyed TLM, ×50 mag

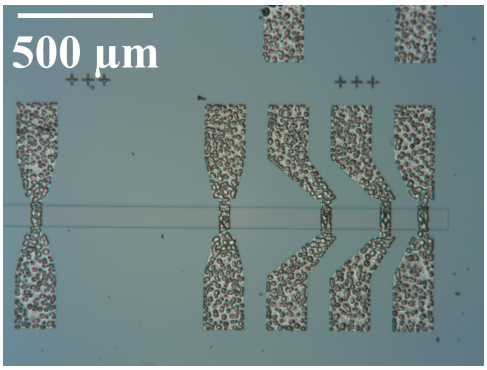

(c) Optimally annealed, 430°C, 80 s

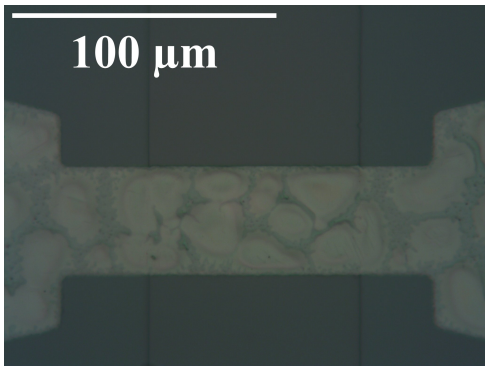

(d) Optimally annealed, 430°C, 80 s × 50 mag

Figure 3.8: Comparison of optical images of underalloyed (a)(b) and optimally alloyed (c)(d) devices at different magnifications. Imaging at the Cavendish Laboratory.

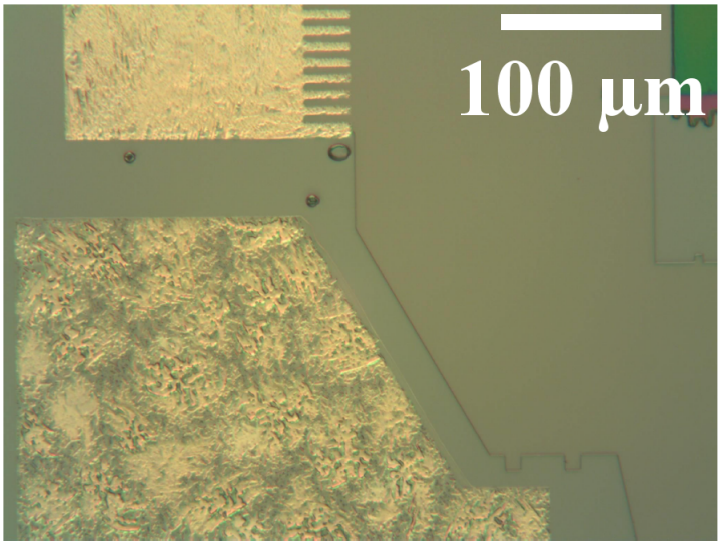

Figure 3.9: AuGeNi ohmic contacts annealed on and off-mesa. The crenellated ohmic is on the 200 nm high mesa, while the bottom left ohmic is off-mesa. Imaging at the Cavendish Laboratory.

The optical image of Figure 3.9 shows the difference of contacts annealed on and off mesa, in the same processing step (same annealing temperature and time). The key difference here is that the surface of GaAs is etched before the mesa is defined, and therefore this might be the cause of the difference in morphology. The resultant appearance is similar to that of the TLM bar ohmic morphology in Figure 3.7 (c), where the part of the ohmic on-mesa appears different than the part of the metal extending off-mesa.

Typically, underalloyed contacts appear to have a much more uniform and gold-like colour, while the overalloyed samples become bumpier, and often, if annealed for a long time, dendritic.

The consistent appearance of the ohmic with respect to device geometry and irrespective of wafer must therefore relate to the underlying microstructure of the contact through the formation of compounds necessary for electrical transport through the ohmic to the 2DEG, from compounds responsible for doping with minimal damage to the region underneath the contact and low sheet resistance of the alloy itself. The non-uniformity of the contacts extends to the semiconductor with irregular depressions, often referred to as "spikes" or "rounded blobs".

Kinsbron *et al.* [80] has shown equivalence of annealing ohmic material

on n-GaAs and AlGaAs, a reproducible result only when the AlGaAs layer is cleaned beforehand, due to the susceptibility of aluminium to oxidise which forms a barrier to arsenic evolution. The samples are cleaned with a HCl dip prior to deposition in a forming gas environment, that should remove and prevent any oxides forming. It is unclear at this time if potential oxidation might be the reason on and off-mesa contacts differ in their resultant morphology, as well as the morphology of contacts that extend past the mesa (such as those of the TLM bars) which show a variation in the span of the whole contact.

3.3.2 Scanning Electron Microscopy

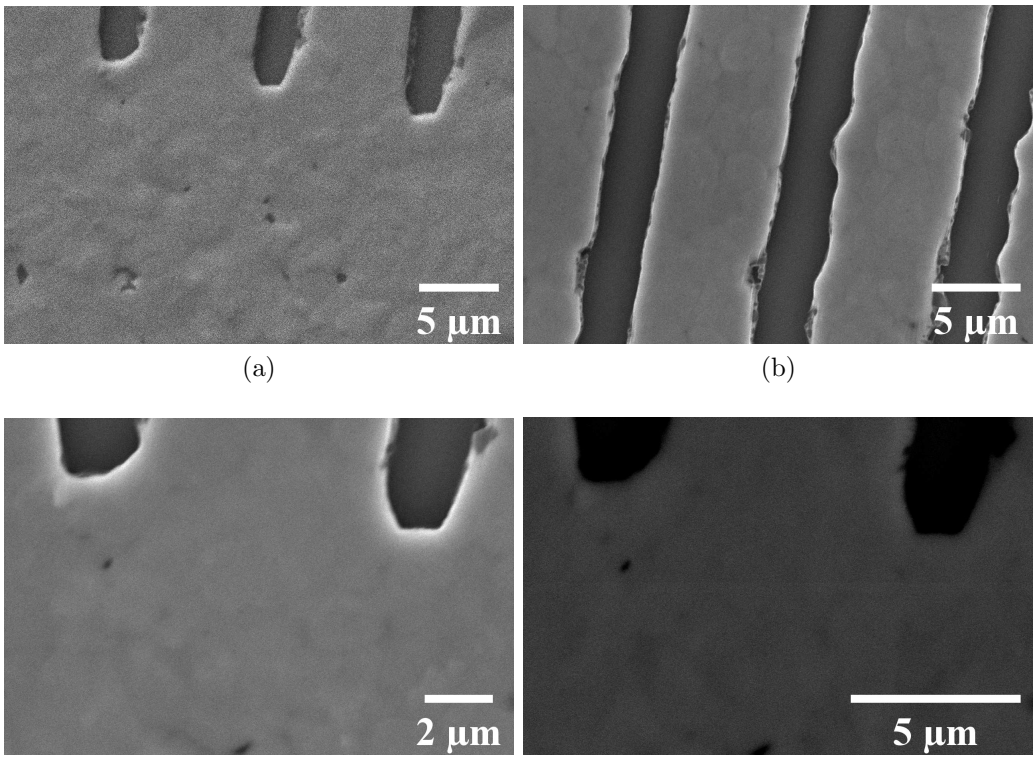

(a) (b)

(c) (d)

Figure 3.10: SEM images of a crenellated 4 mm ohmic contact, imaged at SuperFab, RHUL. (a) 3 mm large ohmic ×4000 magnification, using 2 detectors. (b) Crenellations of (a), at higher magnification. (c) Main contact area at higher magnification ×8500. (d) Same site as (c), using backscattered electrons. This sample, V834 4×4 B, was cooled to low temperatures on the Kelvinox cryostat.

The Scanning Electron Microscope (SEM) image of Figure 3.10 is of a large (approximately 3 mm size) ohmic contact of sample V834 4 × 4. The metallisation appears to have dark and light spots when imaged by SEM.

Various magnifications show that the rugged structure exists even in the 5 μm crenellations. The image taken using two detectors, pictured in Figure 3.10 (a) gives the best result for the indication of surface roughness of the structure - the rugged terrain of the surface of the contact consisting of "blobs" up to 1 micron in size.

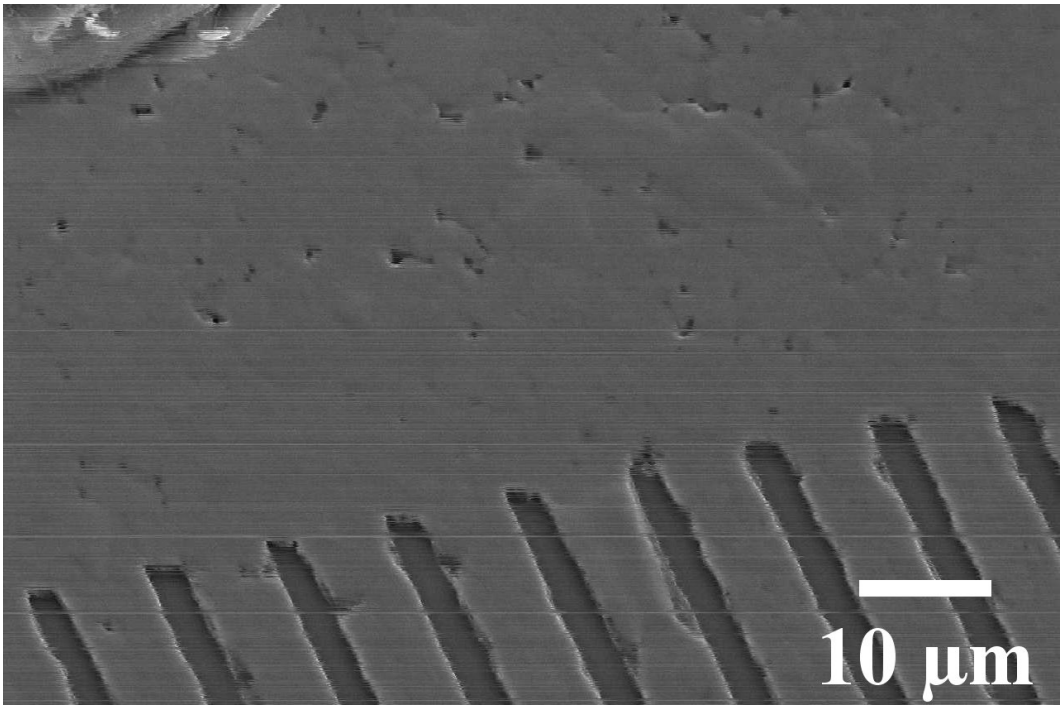

(a)

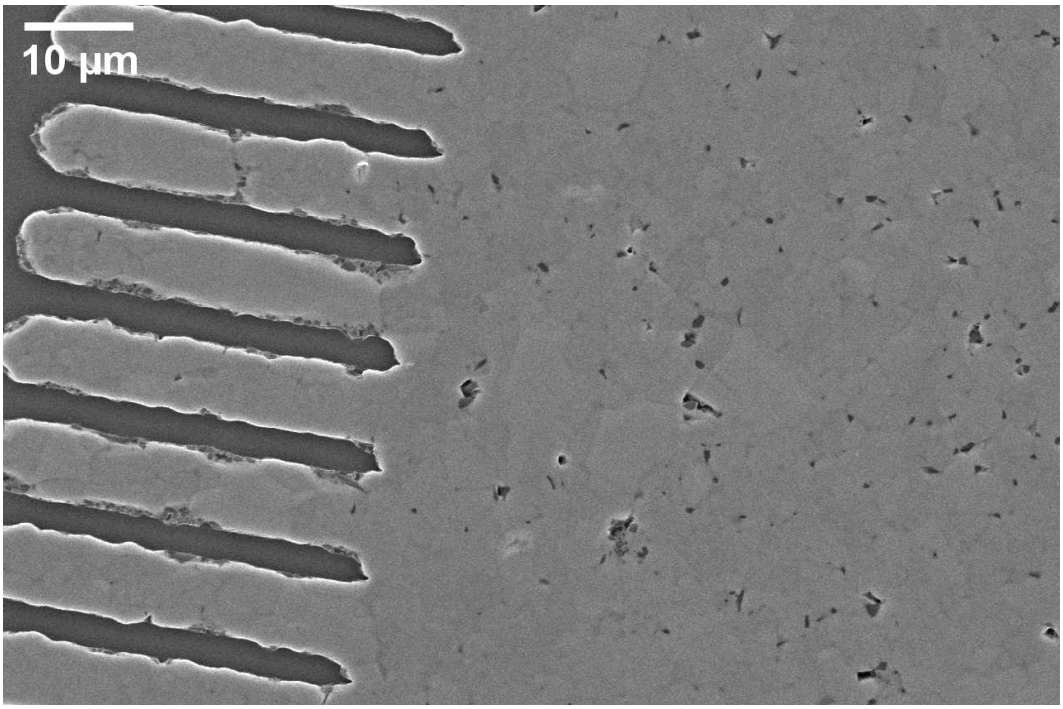

(b)

Figure 3.11: Tilted SEM image of a 200 μm $\times$ 200 μm contact of the same device as 3.10, magnification $\times$1300, 20° tilt angle. Imaged at SuperFab, RHUL.

The tilted SEM image of Figure 3.11 of a 200 μm $\times$ 200 μm contact gives an even better indication of the surface roughness, while at the same time showing equivalence between the large and small contacts of this device with the microstructure not showing any difference between the two geometries.

On wafer W475, a surface profilometer (AlphaStep) was used to determine surface roughness of such 200 $\times$ 200 contact to be on average less than 50 nm, while after etching Au from the contact with a KI solution depressions reached as far down as 0.3 μm, suggesting the Au-rich part penetrates in some cases up to the 90 nm deep 2DEG. However, those samples suffered from high resistance and inhomogeneities in the contacts and 2DEG. The contacts of those devices surprisingly looked much smoother and gold-like and were produced using a eutectic slug. For V-wafers, the cross-sectional SEM study - presented in the following section - provides insight into the contacting mechanism of low-resistance contacts.

3.3.3 Cross-Sectional Scanning Electron Microscopy

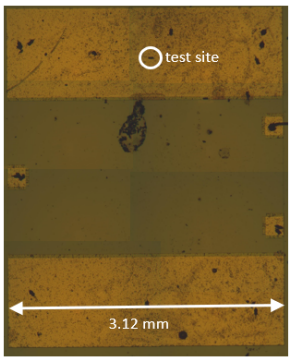

(a) V834 4 × 4 sample

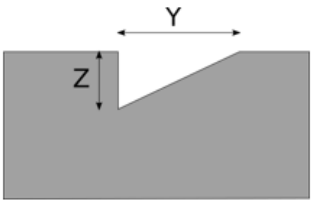

(b) Schematic of sample milling. $Z = 5\mu$m and $Y = 10\mu$m

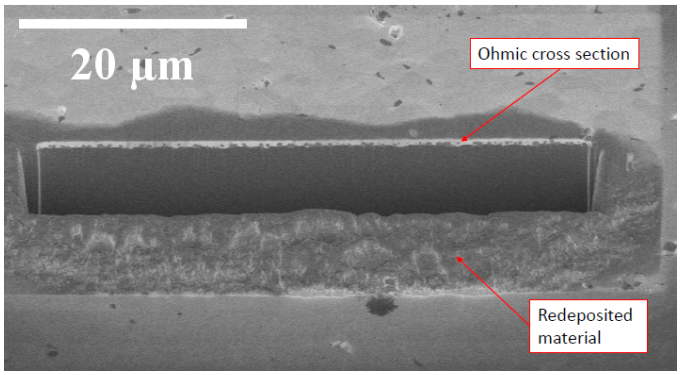

(c) Milled trench

Figure 3.12: (a) V834 4×4 optical image. The site at which the contact was milled is annotated. (b) Schematic of the trench dimensions. (c) Milled trench on the ohmic. Milling and imaging at Cavendish Laboratory.

In an attempt to understand the microstructure of the contacts, a cross-sectional SEM study was conducted at the Cavendish Laboratory*. Sample V834 4 × 4 B (cooled on the Kelvinox, Chapter 5) and depicted in the SEM pictures of section 3.3.2 was milled and imaged to determine the primary constituent compounds of the contact using Energy Dispersive X-ray (EDS) analysis. EDS is a standard technique used for identifying elements by measuring their X-ray emission peaks (and comparing their scattered K_α, L_α and M_α lines) to determine the type of elements being imaged.

*Study conducted by Dr Waldie, Cavendish Laboratory - see details in Acknowledgements.

A trench was milled, annotated in Figure 3.12, using a Ga ion-beam on a large ohmic of the 4×4 sample. The cross-section was subsequently imaged by SEM. Figures 3.13 include an SEM image and EDS analysis of the cross-section of the middle of an large ohmic.

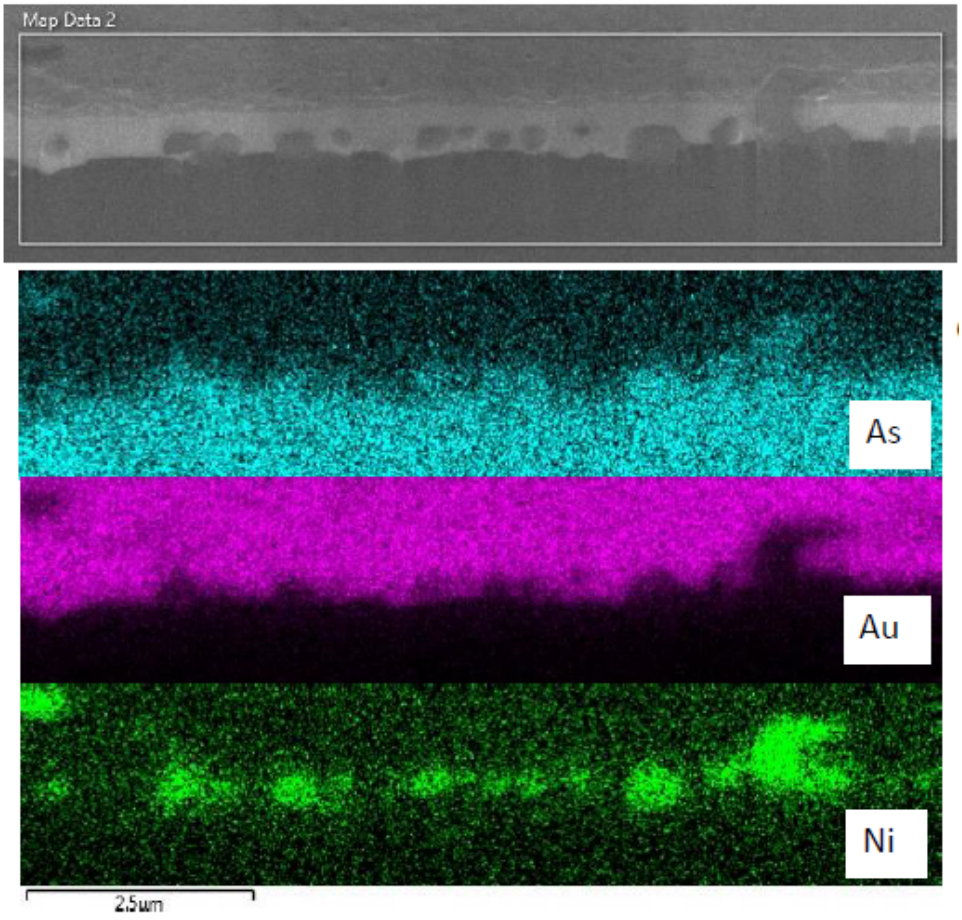

Figure 3.13: SEM image and EDS map of milled ohmic contact of V834 4×4 sample. Two predominant and distinct primary phases are clearly visible, that of gold and that of nickel. Imaging at the Cavendish Laboratory.

The results confirmed that the structure is typical to that of the literature, although very complex. The contact is seen to be composed of two distinct phases, an Au-rich overlayer with Ni inclusions.

Ga is seen everywhere in this analysis, due to it being one of the main constituents of the sample and also since the device was milled using a Ga ion beam, contaminating the sample. As is primarily seen in the substrate

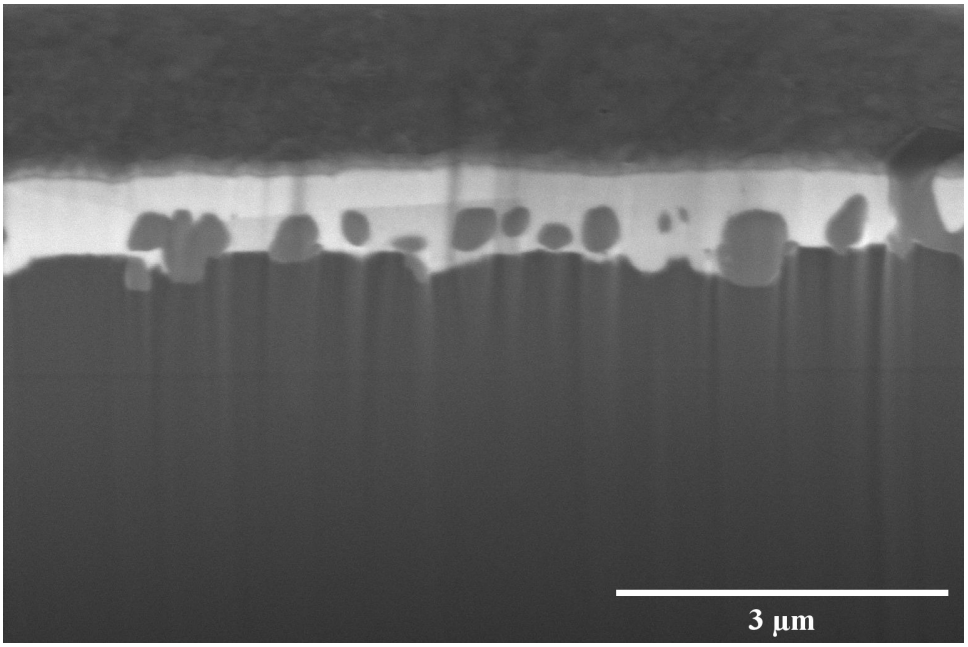

Figure 3.14: Ni-rich phases, dark 'blobs' are mostly located in the metal-semiconductor interface, in some cases they permeate all the way to the top, as the rightmost inclusion in this image. Imaging at Cavendish Laboratory, the vertical lines appearing due to different elements having different milling rates.

area, consistent with the literature suggestion that it bubbles out through the contact material upon annealing, while some remnants seem to gather in the region of the Ni "blobs", likely NiGe grains forming ternary stoichiometric compounds with As [74].

In some cases, such as the largest Ni-rich inclusion of Figure 3.13 and in more detail in Figure 3.14, the Ni-rich phases extend from the metal-GaAs interface all the way to the surface.

Historically, results were inconclusive whether contact resistance scales as the area or the perimeter of an ohmic contact to a heterostructure; this was the reason devices with crenellations were designed (to maximise perimeter for a fixed area). To investigate whether there is any difference in the perimeter of the sample and edge of the contact, a trench was dug along the crenellations, site shown in Figure 3.15 (a) and imaged along the rightmost "finger".

The EDS map of the second site, depicted in Figure 3.16, is along the crenellations of the ohmic. In this EDS analysis, the Ge map worked, con-

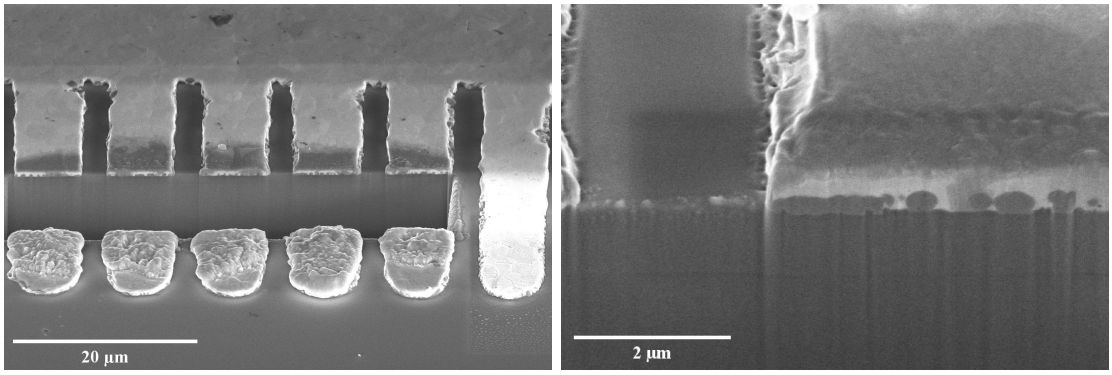

(a) Trench along crenellations (b) SEM image of cross-section

Figure 3.15: Second site of cross-sectional imaging, along the crenellations of the sample. Imaging at Cavendish Laboratory.

clusively showing the majority of Ge to be congregated in the Ni-rich phase. In agreement with the literature, with studies suggesting Ni is responsible for ohmicity, areas with Ni-rich phase do not have Au, while they have more of the dopant, Ge. Figure 3.16 (b) shows a stacked EDS map on top of the SEM image, to highlight these results.

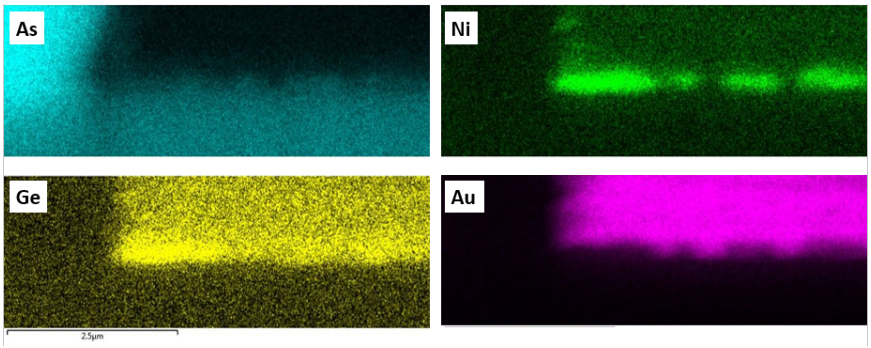

(a) EDS map

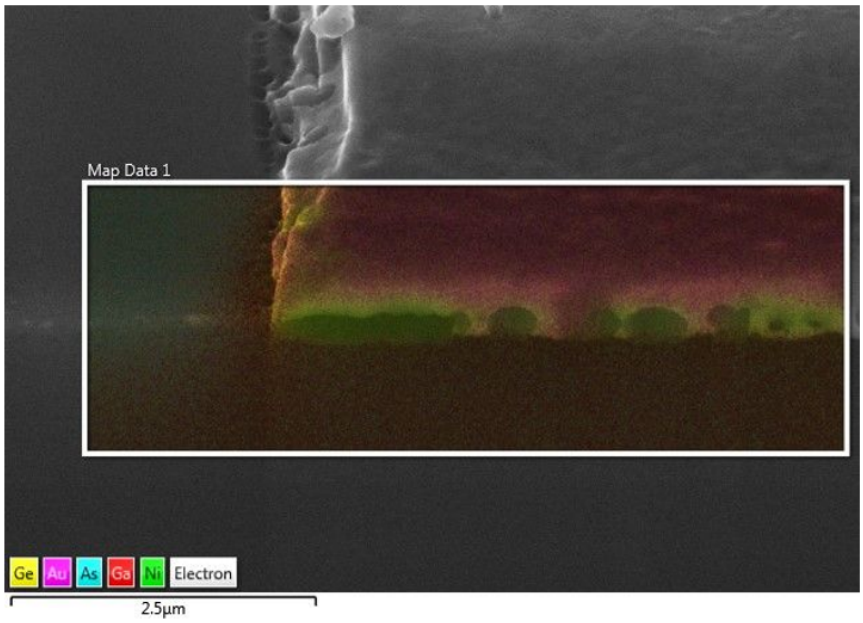

(b) SEM image with stacked EDS map

Figure 3.16: SEM image and EDS map of ohmic, along the crenellations. Ge map also shown here. As is everywhere apart from the Au-rich area of the ohmic, Ge is mostly in the contact region, with more abundance along the Ni-rich area. Au and Ni are segregated with a distinct Au-rich overlayer, with Ni "blob"-like inclusions. Imaging at Cavendish Laboratory.

The third imaging site is at the top of the contact, Figure 3.17. The top of the contact is subject to contamination from milling with a Ga ion beam, material redistributes to the surface as the milling is done and traces of material persist even after cleaning. This is the reason why Ni is seen more broadly in this map, Figure 3.17 (b). The same conclusions are reached, with Au-rich and Ni-rich phases being distinct, while it is also important to

highlight the higher concentration of As compounds in the regions that seem like pits, this is interpreted as a result of As dissociating and diffusing out as the literature suggests.

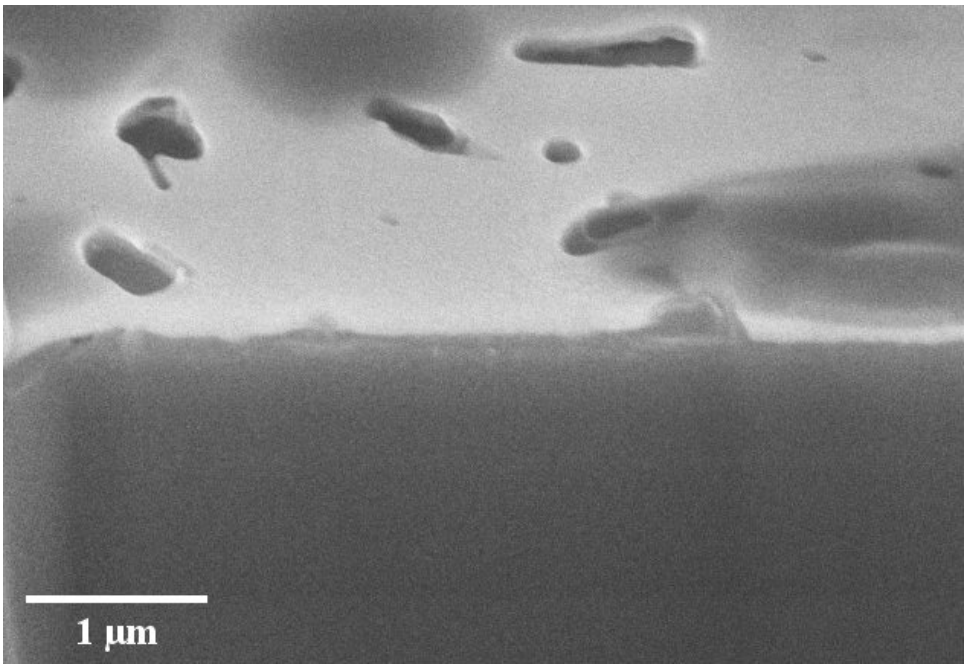

(a) SEM image of third site, middle of ohmic

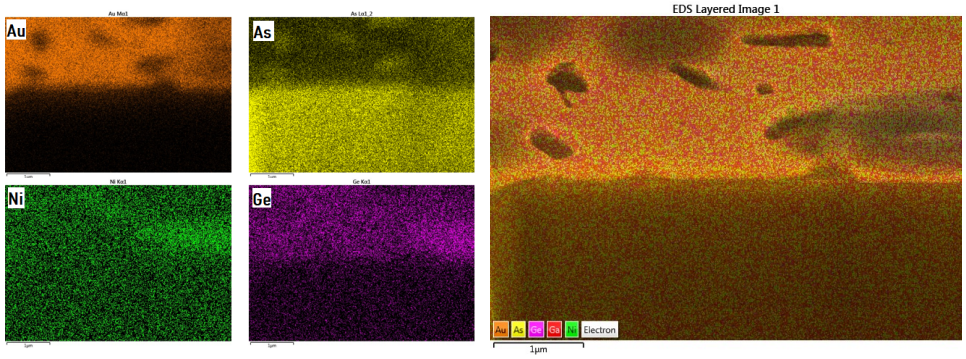

(b) EDS Map (c) Stacked EDS Map

Figure 3.17: Third cross-sectional SEM site, looking at the top of the contact, with more of the permeating Ni-rich inclusions visible. Imaged at Cavendish Laboratory.

3.3.4 Helium Focused Ion-Beam Milling and Imaging

To further investigate the microstructure of the contact, a helium focused ion-beam (FIB) was used to mill contact material at the top of the ohmic and image the Ni-rich inclusions. This technique is preferable to the Ga ion beam milling as an inert element such as He will not contaminate the sample.

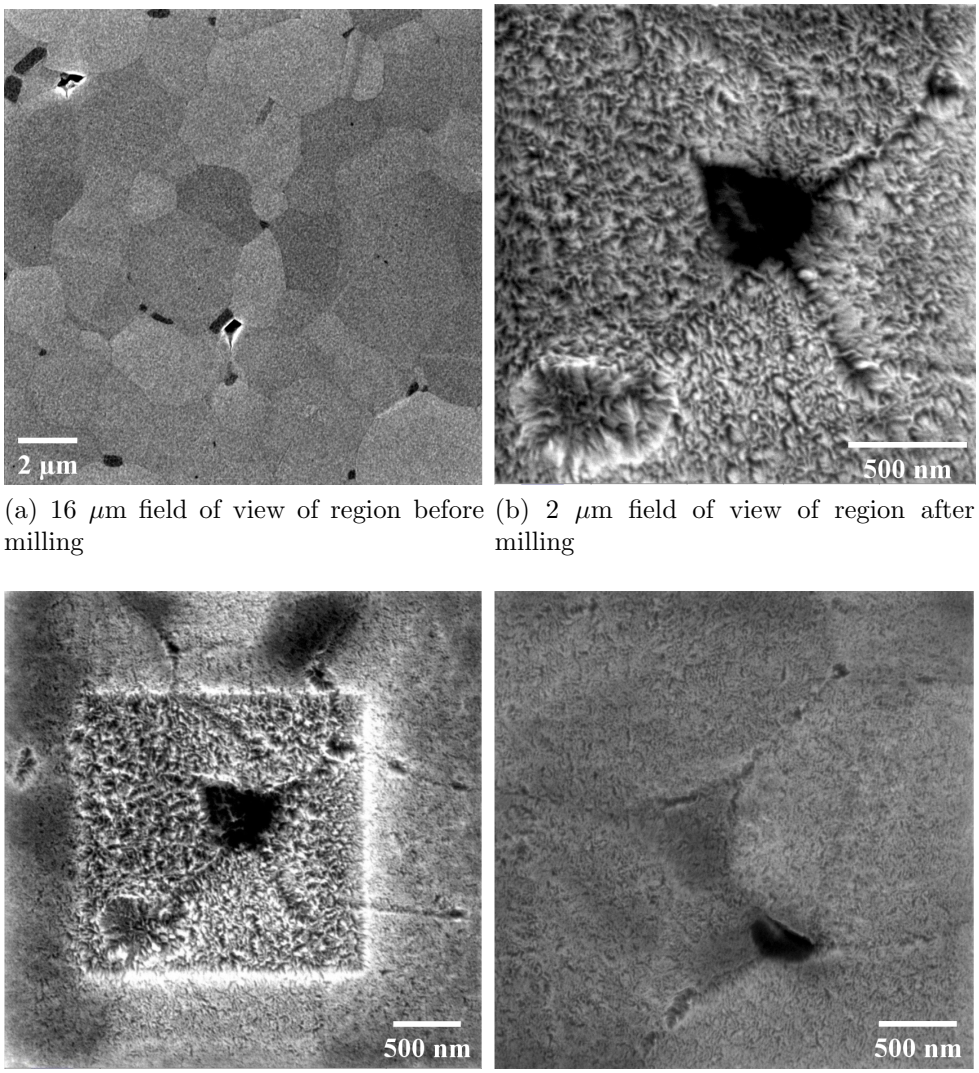

(a) 16 μm field of view of region before milling

(b) 2 μm field of view of region after milling

(c) 3.5 μm field of milled region

(d) 3.5 μm field of view of milled region, showing a Ni-rich inclusion

Figure 3.18: Imaging and milling of V834 4×4 B sample, using the Zeiss FIB and SEM machine at SuperFab.

The images of Figure 3.18 show (a) an image of the area before milling, with a 16 micron field of view, (b) the area after milling, (c) wider field of view image of the milled area and (d) an image of the structure of the underlying inclusion, including a dark spot nearby. The tiled microstructure of the contact suggests the existence of multiple phases. The Ni-rich inclusions are seen as dark grains only in the corners of the approximately hexagonal Au-rich phase.

3.4 Ohmic Cross-Section Imaging Results

1. The ohmic contact has a distinct rugged appearance, which is characteristic to the fabrication conditions and resultant contact resistance. A set alloy composition and annealing condition will produce a contact with the same morphology.

2. This consistent morphology holds between samples of the same geometry, while a limit is expected due to the size of the Ni-rich inclusions (up to a micron).

3. The metallisation contacts GaAs/AlGaAs forming two distinct regions, one Au-rich and the other Ni-rich.

4. The Ni-rich region forms ternary compounds, producing "blob" like structures, responsible for the surface roughness and also necessary for doping.

5. The Au-rich region extends from the top of the contact, engulfing the Ni-rich region and extending down to the furthest points that the metallisation penetrates into the semiconductor.

6. From the cross-sectional study, the 2DEG layer is further than the metallisation is seen to penetrate to, suggesting that the contact conducts by tunnelling from the Ni-rich inclusions to the 2DEG.

7. Our low-resistance contacts agree with the literature results, suggesting the existence of AuGa and NiGe(As) compounds are essential in the contacting mechanism.

3.5 The Gold-Gallium Binary System

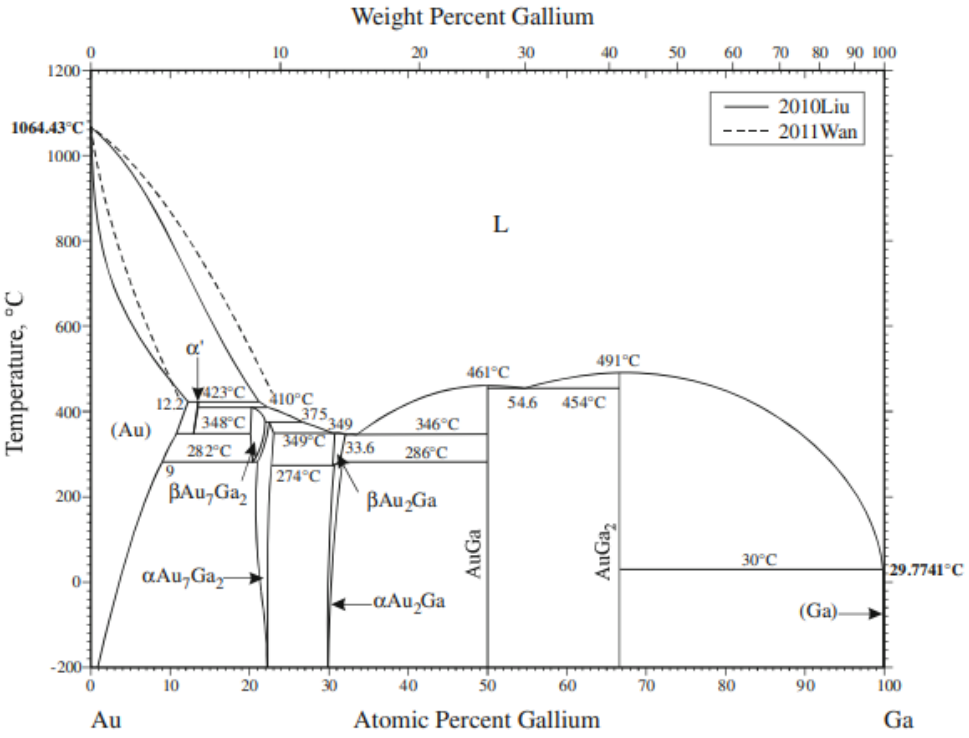

Figure 3.19: Binary phase diagram of the gold-gallium system, from [94].

To understand the effect of the gold-based eutectic metallisation in the ohmic formation, the Au+Ga binary phase diagram must be considered, shown in Figure 3.19. In a binary phase diagram, atomic weight compositions are plotted against temperature, with constant lines representing equilibrium. Since the diagram depicts all different possible phases of miscibility of one element to another, these constant lines are also called phase boundary lines and the diagram a phase boundary diagram.

The gold-gallium system has been under investigation for a wide range of applications from contacting III-V semiconductors to even jewelry and dentistry [95]. The most recent comprehensive studies done on the AuGa binary system were by Liu *et al.* [96] and Wang *et al.* [97].

Liu *et al.* conducted a thermodynamic analysis of the binary system, taking a solubility range of intermediate phases into account. While Wang *et al.*

did not consider these intermediate compounds, their results are nevertheless in good agreement. The diagram of Figure 3.19 compares their results, as in a supplementary study by Okamoto [94].

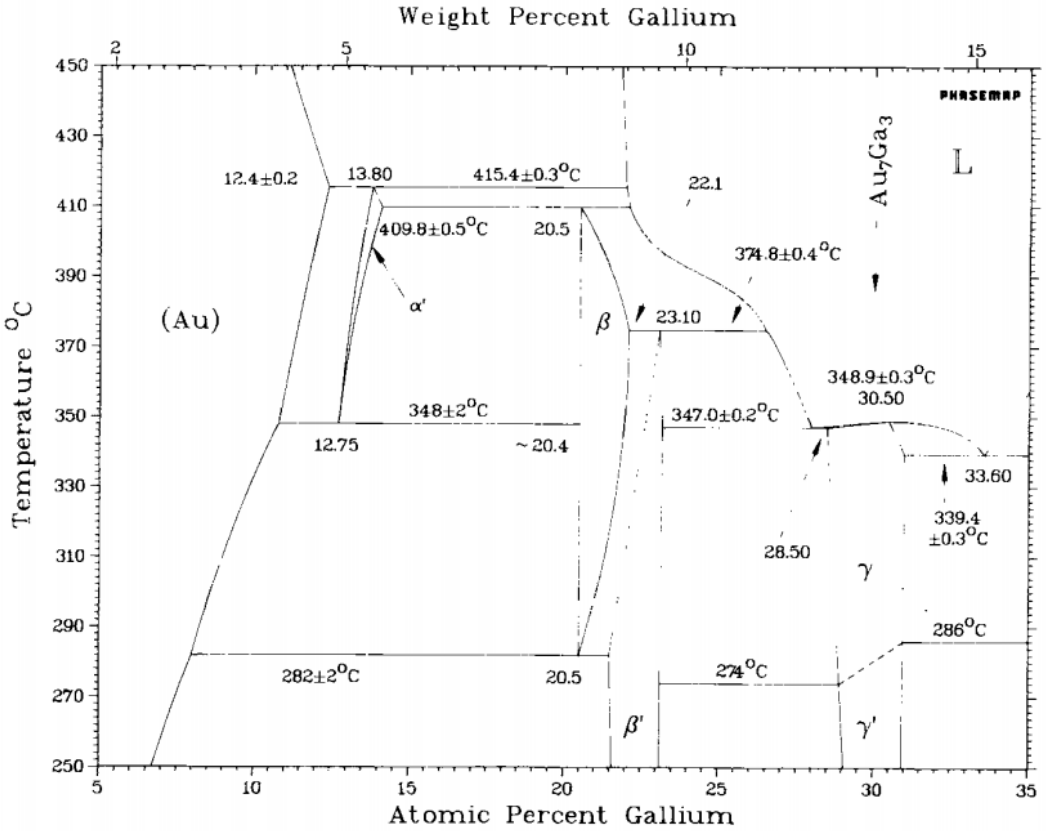

Figure 3.20: AuGa binary phase diagram by Elliott *et al.* [98], focusing on the gold-rich part of the binary system.

The full temperature range of the phase diagram need not be considered - discrepancies at high temperatures are academic and of no applicable interest to this work. At a temperature range of 350-500°C, there is good agreement between the two studies and at least 7 triple points exist on the AuGa phase diagram, marking conditions under which multiple phases can occur, depending on the relative concentration of the alloy.

The diagram of Figure 3.20 depicts the binary diagram in the gold-rich end, from a relatively dated study by Eliott *et al.* [98] which is in good agreement with more recent studies. This is the most relevant part for ohmic

contact processing as the amount of available gold is much less than the gallium in the substrate GaAs.

In the range of 10-30% Ga, there exist multiple phases of AuGa, highly temperature dependent and metastable. At higher gallium concentrations, from 30 to 100% Ga, only AuGa, $AuGa_2$ and Ga exist.

Previous studies found that Au "pitting" may reach depths of 300 nm and is unaltered by subsequent processing once the Au has been consumed [88], which would suggest that at that point the gold in the eutectic material has saturated in Ga. The compound formed in such "pyramidal pits" was detected as Au_2Ga [99]. Two main phases were determined after a typical anneal: that of hexagonal AuGa and Au_2Ga, while numerous stable and metastable phases in the Au+GaAs system are also reported, concluding that interfacial reactions between gold and GaAs proceed on "a submicrometer level" [99].

TEM analysis of Au alloying onto GaAs also reported a similar "pitting" effect for the alloying behaviour of Au on GaAs, detecting formations of AuGa compounds in the substrate [100], in-situ X-ray diffraction, showed the formation of AuGa and resolidification to β-AuGa upon cooling, or of $AuGa_2$ upon faster cooling [101], work which also highlighted the lack of attempt to associate various microstructural features in terms of phases other than the rectangular features of the β-AuGa phase in the literature. A study on the crystallographic orientation of AuGa phases demonstrates how difficult it is to separate some of these phases [102]. Disorder along the surface of layers of Au on GaAs is widely reported, which increases with increasing initial Au amount [88], while the top of the ohmic, mostly Au-rich, has less total available Ga such that any of the phases α, α', β and γ could form under RTA conditions.

Similarly, for ohmic contacts, $AuGa/Au_4Ga$ compounds are reported in the contact [79], while separate EDS analysis has detected various AuGa phases in the Au-rich part of the alloy, but without further specification. As previously mentioned, Bell Laboratories [80] showed equivalence of annealing Au and AuGe on GaAs and AlGaAs/GaAs by measuring the outdiffusion of arsenic during the annealing process of gold contact films using a mass spectrometer and discovered that arsenic dissociation occurs in the same rate, proportional to the thickness of the gold film, temperature and anneal

time.

TEM and EDS analysis on the microstructure of ohmic contacts to 2DEGs determined a wide array of gold alloys forming in the contact, the more abundant one being β-AuGa [77, 103]. Figure 3.21 shows the TEM micrograph of a low-resistance contact, annealed at 400°C for 60 s [77]. This annealing condition within our group is shown to produce samples that look "under-annealed", but it is important to stress again that these reported annealing conditions are specific to the annealer temperature calibration so that there may be variances, in the case of this contact more Ni is seen to spread in the contacting material, which is most likely due to the larger amount of Ni in their eutectic composition of AuGe(225nm)/Ni(45nm)/Au(300nm).

Finally, attempts at engineering a two-layer structure (distinct Ni-rich and Au-rich layers) in order to reduce non-uniformity and provide a viable solution for improving thermal stability for applications to a large number of integrated devices, where thermal stability and uniformity are necessary requirements, were systematically investigated [61, 93, 103]. Concluding, after many attempts, that Au should be excluded to improve the contact morphology and thermal stability [81].

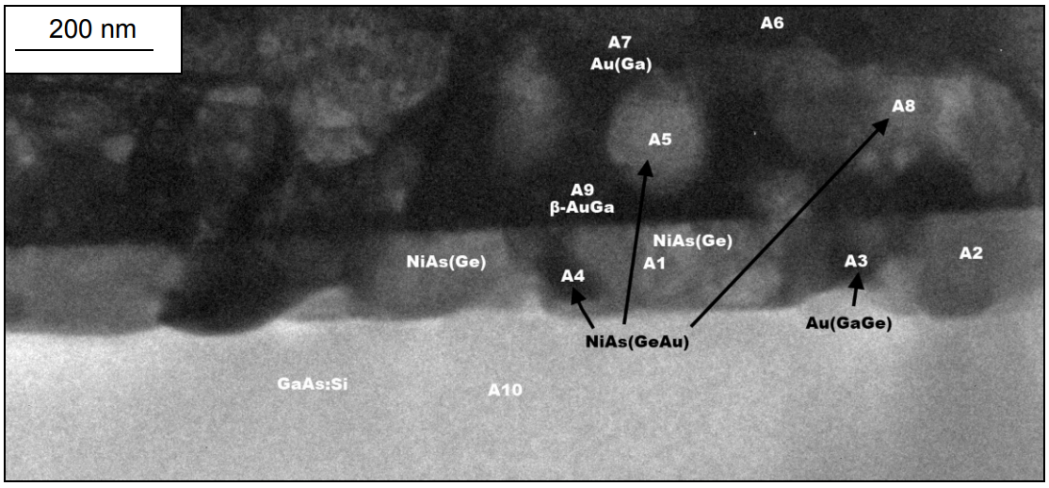

Figure 3.21: TEM image of a low-resistance ohmic contact annealed at 400°C for 60 s, by Baranska *et al.* [77]. Several gold phases are seen in the gold-rich (dark) layer, most prevalent being β-AuGa.

Results from our imaging study show our ohmic contacts are no different to that of the literature, even with variations in recipes and ratios, the con-

tacting mechanism is fundamentally the same. The effect of gold on GaAs is to degrade the substrate and is widely reported in the literature [77, 80, 88], the effect of Ni in the resultant improved morphology then is seemingly to wet the damaged and dislocated area, as such it is found on the metal/GaAs interface and improves the surface roughness.

The nickel-gold ratio is important, as enough nickel is needed to coat the damaged area as well as form stoichiometric compounds with germanium for doping, while at the same time not being too much to travel further up in the contacting alloy (as the results reported in [77, 79]) and getter all Ge. Suggestions that Ni acts merely as a catalyst in this process are simplified hypotheses based on the wide array of uses of Ni in industrial applications - it is crucial for doping, while also limiting the effect of Au on the substrate, working as a diffusion barrier once at the semiconductor-metal interface [104]. Au is essential in this system for dissociation of As and Ga - it is not a passive component.

3.6 Summary

The contacting mechanism of ohmic contacts is complicated, arising from the complex microstructure from the chaotic process of alloying onto the semiconductor. In this chapter, it is concluded that our AuGeNi contacts consist of multiple chemical compounds as a result of the process of annealing and which can be split into two distinct phases: one gold and one nickel rich. It is argued that the interplay of these two phases is important for the formation of a low-resistance ohmic contact.

A review of the literature determined our ohmic contacts have identical microstructure to those of other groups. While the literature generally agrees on the underlying process (e.g. importance of a controlled amount of nickel and gold, existence of nickel compounds in the alloy-semiconductor interface as well as the multiple phases of compounds formed in those regions) not enough attention is given to the gold-gallium phase, which is often thought of as a passive component. The AuGa binary system is described as an elementary way of understanding the various compounds that may form in the Au-rich region of the contact.

Chapter 4 presents results of characterisation of different batches of our

ohmic contacts, through the systematic study done to optimise contact resistance. In chapter 5 we will see that these ohmic contacts superconduct, attributed to the AuGa compounds forming in the contact.

Chapter 4

Characterisation of ohmic contacts at 4.2K

Electrical characterisation is described in this chapter, with an overview of what samples were fabricated and their purpose. Results at liquid helium temperature T = 4.2 K are presented and the importance of understanding contact resistance, R_C, the main parameter inhibiting cooling of such devices, is highlighted.

Thermal transport is proportional to area and therefore low electron temperatures ($T < 1\ K$) are usually realised in large area ($\sim$ 4mm $\times$ 4mm) samples with minimal processing other than annealing of ohmic contacts. These devices have the minimal necessary processing, with gating often resulting in a significant reduction of sample mobility due to impurities. Ohmic contacts are necessary to measure the sample and cool past the temperature at which electrons in a semiconductor decouple from the lattice, to ultra-low-temperature. The overall study to optimise 2DEG and contact resistance was motivated by an aim to cool such a device to as low electron temperatures as possible. The coldest published electron temperature is around 4 mK for such devices [59], despite the μK regime being readily available due to the advance in cooling techniques such as nuclear demagnetisation ([31] and references therein). The limiting factor to cooling electrons through leads is the contact resistance of the sample.

Following extensive characterisation at 4.2 K, a reliable recipe for reproducible low-resistance ohmic contacts was achieved, surpassing previous

benchmarks which had resulted in cooling a 2DEG to as low as 1.0 ± 0.1 mK on the ND3 cryostat, a factor 4 colder than previously reported for a 2DEG and a factor 10 hotter than what is predicted by our elementary thermal model, which follows the Wiedemann-Franz law of thermal and electrical transport.

4.1 Sample Characterisation at 4.2K

As discussed previously, our contacts are made from gold, nickel and germanium; an alloy that is ubiquitously used in the semiconductor industry and one of the most common ways of contacting to n-GaAs. Samples were fabricated on wafers V827 and V834 with a standard eutectic recipe and different annealing conditions, with an aim to establish a reproducible low-resistance ohmic contact recipe. Three batches of samples were fabricated for this purpose α, β and γ, investigating different annealing conditions for processing contacts onto the wafers. Two subsequent batches, δ and ϵ were of samples intended for ultra-low temperature experiments, using the newly optimised recipe. Table 4.1 shows the annealing conditions of devices used in this study.

Table 4.1: Batches of ohmics fabricated by Dr. Graham Creeth (W476) and Dr. Patrick See (α, β, γ, δ, ϵ) determined that the ideal annealing condition is a Rapid Thermal Anneal at 430°C for 80 seconds. Ohmic composition is presented in AuGe/Ni/Au layer thickness.

Wafers	Batch	Mask	Ni wetting	Ohmic Composition	RTA conditions
W476	Original 4x4	4x4 only	Yes, 30 nm	88:12 wt% AuGe eutectic slug	400°C, 90s
V827/V834/W475	α	TLM	No	130/50/164 nm, layered eutectic	
					430°C, 80s
					400°C, 60s
V827/V834	β	TLM/NTLM2	No	139/35/175 nm, layered eutectic	
					430°C, 80s
					370°C, 120s
V834	γ	NTLM2/ 4x4	Yes, 3 nm	136/30/180 nm, layered eutectic	
					430°C, 80s
					430°C, 140s
V834	δ	ULT MASK	Yes, 3 nm	136/30/180 nm, layered eutectic	430°C, 80s
V834	ϵ	NTLM3	No	123/30/200 nm, layered eutectic	430°C, 80s

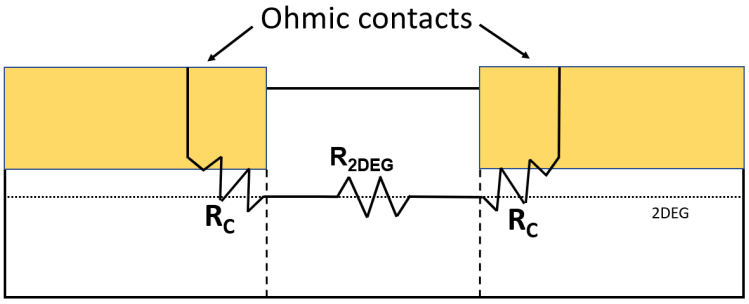

Figure 4.1: The contact resistance, R_C of a planar ohmic contact to the semiconductor is defined as the resistance between the metallisation and the plane at the edge and perpendicular to the semiconductor. Most current flows into the contact close to the edge, the magnitude of current in the semiconductor decreases exponentially from the contact edge in a phenomenon called current crowding. Schematic adapted from [36].

4.1.1 What is Contact Resistance?

Contact resistance is the intrinsic resistance of the metal-to-semiconductor junction. Figure 4.1 is a schematic of a planar ohmic contact to a 3D semiconductor of length L and contacting area A. A basic electrical measurement using the two contacts as a source-drain would give a total measured resistance of:

$$R = 2R_C + \rho L/A \tag{4.1}$$

For a 2D system such as in our devices, the resistivity ρ of the 2DEG becomes the resistance per square $R_\square$, such that for a 2-terminal measurement we have:

$$R^{2T} = 2R_C + R_\square \times \zeta \tag{4.2}$$

where ζ is the number of squares of two dimensional electron gas between the source and drain. An actual measurement in practice, would further include resistance of all external circuitry and wires to the sample; from bond-wires, probe-wires, to the wires connecting to the measuring apparatus itself.

The contact resistance is a function of device size, such that an appropriate way to quote it is to scale by the perimeter of interface of metal/semiconductor, typically denoted as r_C and quoted in Ωmm.

An important physical parameter defining the contact resistance, is the transfer length. Transfer length relates to the lateral distance of current

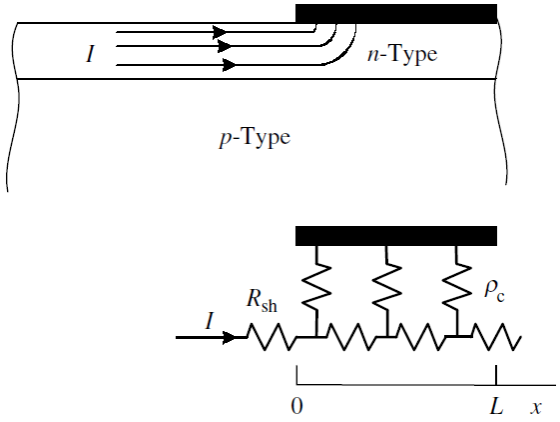

Figure 4.2: Schematic of current crowding under an ohmic contact, depicting an equivalent-circuit model of transfer length. Current falls exponentially along this length. R_{sh} is the sheet resistance of the semiconductor, L is the length of the contact, the total length that current passes under the contact defines the transfer length, in a more resistive region "under" the contact. Schematic from [105].

flowing into (and out of) the ohmic contact. All current must pass from the alloy to the semiconductor layer (and vice versa), but usually drops exponentially close to the contact edge, due to the typically low resistivity of the contacting metallisation. The diagram of Figure 4.2 shows this effect, the distance that the current from the edge of the semiconductor falls to the value of $1/e$ of its original value is defined to be the transfer length, L_t [105]. If the length of the contact is much smaller than the transfer length, $L \ll L_t$, the current does not penetrate sufficiently into the contact metal. For $L \gg L_t$, the current flows into the contact and the contact can be thought of as two contacts, each of length L_t and shorted by the contact resistance of the alloy at the top.

The industry standard of determining contact resistance and transfer length is the Transmission Line Model, discussed in section 4.1.4.

4.1.2 Current and Voltage Measurements Schemes

An ideal voltage measurement of a device needs to have an input current (I^+) from a source of high output impedance, a grounded lead (I^-), as well as two voltage probes of high input impedance, to measure the potential difference (V^+ and V^-). This is known as a 4-terminal or 4-wire measurement and is a

measurement of voltage, depicted in Figure 4.3. A simplified 4-terminal measurement is effectively one where the positive (I^+, V^+) and negative (I^-, V^-) leads are shorted together, a 4-wire 2-terminal measurement, similar to how resistance is measured with a handheld digital multimeter.

The advantage of a 4-terminal measurement lies in the voltage probes having effectively infinite input impedance, not allowing any current to pass through the measurement cables, such that the device under test is measured without extra resistances in series. It is therefore the preferable measurement when measuring on a fridge or a really low-resistance device in which the sample could have a resistance comparable to (or less than) that of the measurement wires.

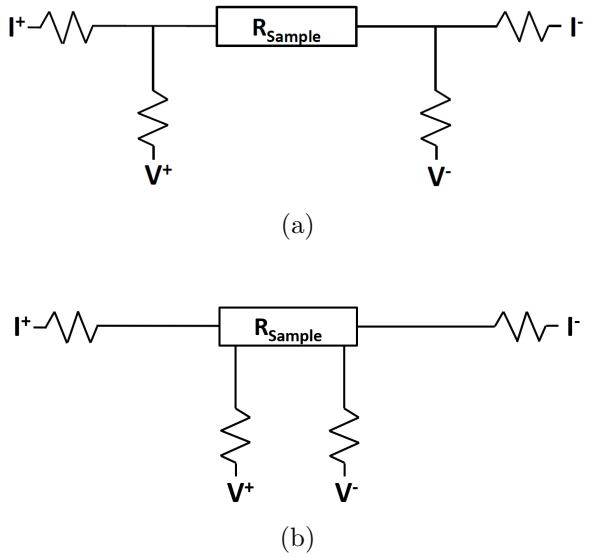

Figure 4.3: Standard 4-terminal Voltage measurement configuration. (a) The positive and negative leads are shorted before being attached to the device under test. The Voltage probes do not draw current due to their high input impedance > 1 MΩ. (b) Voltage probes on a separate contact, no wire resistance measured.

A 2-terminal (or 2-wire) measurement is a measurement of conductance, a measurement of current, and is similar to the well-known ammeter circuit, measuring the current passing through a device, at a known voltage. This measurement is typically used for resistive devices, or equivalently, measuring transistor devices that are gated. Low-dimensional transport measurements typically measure conductance, since the conductance quantum (G_0) is ap-

proximately 13 kΩ and the device is measured as the conductance of the channel approaches zero, which is an infinite resistance and otherwise immeasurable. A 2-terminal measurement is not an accurate way to measure low-resistance contacts, as lead resistance can vary and there can be more components contributing to the series resistance than the measurer may appreciate. A conductance measurement does not measure below 100 Ω accurately, without amplification or guarded/shielded circuit. A typical 2DEG sample can range from 10 Ω to 1 kΩ, and its contact resistance can vary from 2 Ω to 2 kΩ. For purposes of measuring a low-resistance sample accurately in a low-noise environment with input current below 1 mA, a four terminal voltage measurement needs to be used.

Before measuring a device for low-temperature transport measurements, the sample needs to be characterised at 4.2 K and checked for homogeneity and directional resistive symmetry. This is essential as large inhomogeneities can overcomplicate transport measurements. Resistive sections of the 2DEG can be attributed to various impurities occurring from variation during growth or during fabrication and low contact yield or inhomogeneities can completely ruin an experiment. Figure 4.3 depicts the most common measurement setup for characterising a sample, a 4-terminal measurement. On samples intended for measurement at low temperatures (pumped helium temperatures, on fridges) a series of resistance combinations of available electric contacts on the device is first systematically done. On samples that are not gated, this is as simple as measuring them with a digital multimeter, the standard 2-wire measurement. Even though a gateless 2DEG is not typically ESD sensitive, voltage spikes can occur with improper handling and extra care needs to be taken to ensure the sample is grounded to the measuring apparatus during these checks.

To accurately determine contact resistance on a fridge, the sample needs to be Y-bonded, so that a 4-terminal measurement can be made without having the resistances of the fridge wires in series, discussed in the following section 4.1.3.

4.1.3 Series Resistances, Accurate Measurement and Y-bonds

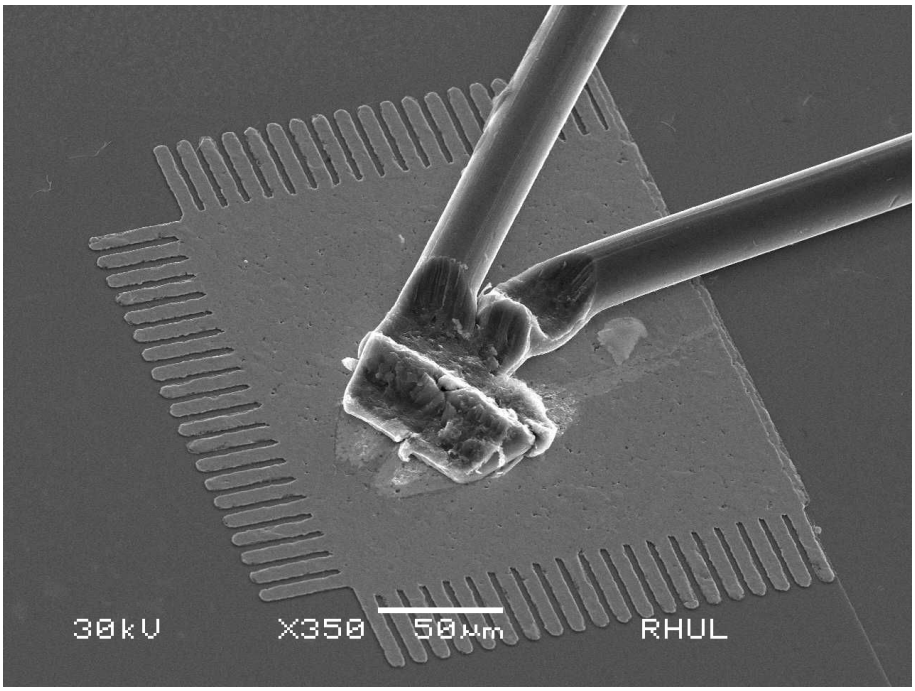

Figure 4.4: SEM image of a 200 μm $\times$ 200 μm ohmic contact, with 5 μm crenellations, bonded with a wedge bonder. A Y-bond of 20 μm Au wire is used to eliminate wire series resistance in measurement. The bond can be shorted on the contact or in a separate bond-pad as the resistance of the Au bond-wire is negligible. The contact pictured is a $4mm \times 4mm$ sample V834 4 $\times$ 4 B, cooled on the Kelvinox. The NTLM mask was designed with 200 μm $\times$ 200 μm contacts to establish a baseline for samples of the 4 $\times$ 4 type. Image taken at RHUL clean room, SuperFab.

Fridge wires are typically very resistive materials such as phosphor-bronze or constantan, which are chosen for their characteristic resistivity not changing significantly with temperature, even when cooled to ultra-low temperatures. Additionally, the measurement lines are often filtered, which provides extra series resistance, as such it is quite hard to measure low resistance (of order $<$ 1 Ω) accurately and even harder to separate the series resistance contributions from each other. To overcome this problem, one can bond a sample with a Y-bond so that the series resistance of the wires is omitted, as in Figure 4.4 and schematic (b) of Figure 4.3. Generally, this means shorting the bondwire

to an additional measurement line, through a gold pad (stitching the bond), or, as pictured, on the ohmic contact itself. The resistance of the gold wire is approximately 22 $\mu\Omega$/mm, so that it is negligible when in series with the resistance of an ohmic contact. This technique is not typically employed, however, as it requires dedicating 2 lines for a single ohmic contact, and LCC contacts as well as fridge lines are typically limited.

4.1.4 The Transmission-Line Model

Current flow analysis by Kennedy and Murley [106] in diffused semiconductors determined by 2D mathematical analysis that there is an effect of current crowding that occurs under the electrical contact metallisation to a 2D semiconductor, using a model of vanishing contact resistance. To determine the validity of this model and account for the current crowding phenomenon, the Transmision Line Model was postulated, Murrmann and Widmann [107] considered various geometries of contacts, while Berger [108, 109] simultaneously and independently extended the TLM model to determine contact resistance. In this treatment, however, the semiconductor sheet thickness is considered as being zero - this does apply for 2D devices such us ours but did not for 3D bulk devices. The Transmission Line Method quickly became the industry standard way of efficiently testing device yield and performance.

Confusingly, there is also a method for determining a key parameter related to current crowding, the transfer length; first proposed by Shockley and his group [110, 111], the Transfer Length Method (also TLM), which is related in concept and methodology but expands on the transmission line model to extract a key parameter from the measurements done on the device, indicating the length over which the current crowds under the contact from the data obtained by measuring the transmission-line. Due to the close relationship of the transmission line and transfer length methods, the abbreviation TLM is used almost interchangeably.

The transmission line measurement involves a series of resistance measurements that originate from the old problem of applying power over large distances, a problem just as important as it was for transmitting power through cities as it is for applying it to large integrated circuits without overheating, as well as to devices intended to achieve low temperatures. In all cases, contact resistance introduces undesirable loss of power from Joule

heating that needs to be characterised, minimised and compensated for, while also current crowding in a contact can cause catastrophic localised heating [105].

To overcome this problem a test device is typically built; The mesa is that of a typical Hall bar that might be studied (width typically 80 μm). Then, contacts are annealed on-mesa to get an average of the reproducibility of fabrication on such a device. This is a necessary first step before using up wafer to make more complicated gated devices as it readily determines the resistivity of the sample and its contacts.

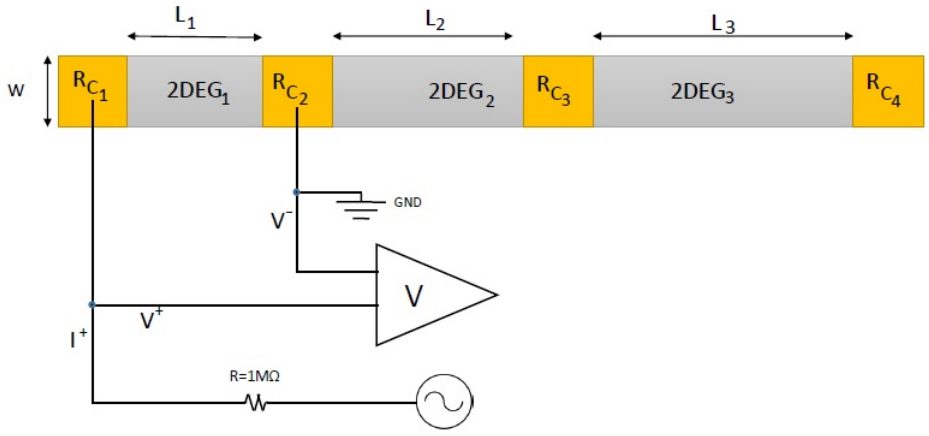

Figure 4.5: Schematic of a TLM bar with contacts annealed at different lengths $L_1 - L_3$, w is the width of the bar, a 4 terminal setup with leads shorted with a T-piece is arranged across successive contacts. The 1 MΩ resistor defines the current flowing through the sample, 1μA for a $V_{osc} = 1V$ oscillator input AC Voltage. The measured resistance is the sum of all resistances encountered: $R_{4-2T} = R_{wire} + R_{C_1} + R_{2DEG_1} + R_{C_2}$. Voltages measured down the bar are converted to resistance by dividing with the input current and are plotted against the corresponding length, L, of 2DEG. The probe's series resistance is measured and subtracted. This is the variation of the TLM used in the measurements in this work, traditionally the current is sent down the whole sample.

A Transmission Line Measurement involves measuring the resistance using successive 4-terminal measurements, as in Figure 4.5, along the length of a thin bar (named TLM bar) over successive pairs of ohmic contacts and plotting it over the various distances between them. The resistance per square of the 2DEG, average contact resistance and transfer length of the contacts

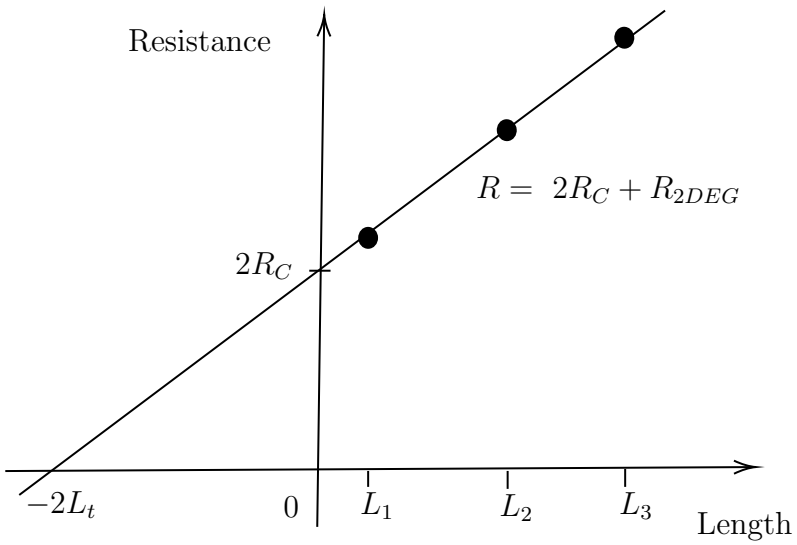

Figure 4.6: Transmission Line Model. Resistances are plotted against paths of increasing length of 2DEG. The slope of the fit is proportional to the resistance per square of 2DEG as $R_{2DEG} = \frac{L}{w} R_{\square}$ and the y-intercept is twice of the average contact resistance for the ohmics of the bar, as evident by choosing $L \to 0$. The absolute value of half the x-axis intercept is the transfer length of the device, L_t, with $|L_t| = \frac{2R_C w}{R_{\square}}$.

are then found in an efficient way, Figure 4.6 shows what can be extracted from a linear fit to data obtained in this way.

The resistance of the wires to the device is measured in series using this approach and therefore are independently measured in order to subtract from the measurement. To further eliminate the cause of additional resistances in the circuit to the device, it is preferable to have the contacts bonded with two wire bonds to separate pins of the chip carrier, what we refer to as a Y-bond, so that a 4-terminal measurement without the lead resistance in series can be conducted.

Figure 4.7 shows a CAD template for the photolithographic mask used by the Cavendish Laboratory for fabricating the typical TLM devices that were used to characterise sample quality over different annealing conditions. A series of 4-terminal voltage measurements are done in a liquid helium dipping station (4.2 K) and then the measured resistances are plotted as a function of the increasing length down the bar.

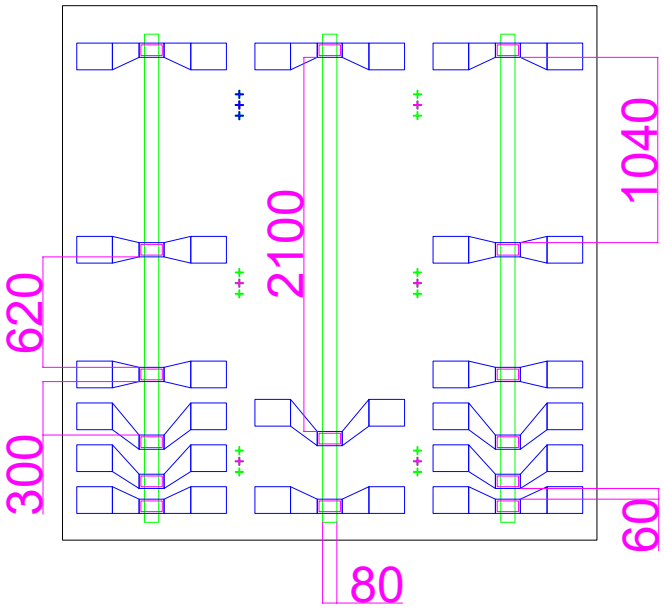

Figure 4.7: CAD template for photolithographic mask of a TLM test device, with annotated distances and all dimensions in micrometers. Green is the mesa, purple is the main region of the on-mesa contact and blue is an additional gold overlayer. Y-bonds to these devices were placed to short through the gold overlayer to the 60 μm $\times$ 80 μm ohmic contact.

Each resistance measurement contributing to a point on the TLM plot is the sum of a contribution of resistances:

$$R_{TLM} = R_{wire} + R_{C_1} + R_{2DEG} + R_{C_2}, \tag{4.3}$$

where the resistance of the measurement wires (R_{wire}) has to be measured independently, in our case typically in the order of 1 Ω. By this method of measurement it is assumed the two contact resistances (R_{C_1} and R_{C_2}) are equal and that this resistance consists of the resistivity of the contacting alloy and the metal-semiconductor interfacial resistance.

The process of extending this series of measurements across the whole bar provides an average of the contact resistance (obtained with a least-squares fit to the data with $L \to 0$) and an average of the resistance per square of the two dimensional gas, $R_{\square}$, obtained from the slope of the straight line fit divided by the width of the Hall bar, w. The equation of the line of best fit

is therefore [36]:

$$R = R_{\square}\frac{L}{w} + 2R_c \ , \tag{4.4}$$

where for this measurement the positive and negative leads shorted together onto the on-mesa contacts, $R_{\square}$ is the resistance per square of 2DEG, L is the length, w is the width of the TLM sample mesa and R_C is the contact resistance. This version of the TLM model was first proposed by Berger [108] in his extension of the Murrmann and Widmann model [107].

Due to the phenomenon of current crowding, depicted in the schematic of Figure 4.13, the actual resistance measured represents only the part of the contact that is seen by the current and the effective area of the contact can be written as $L_t w$. However, it is noted that the TLM model assumes this resistance per square to equal that of the unalloyed 2DEG and in practice this is not the case. Reeves and Harrisson [112] made the distinction that the resistance under the contact, R_{SK} is not the same as the sheet resistance of the unalloyed semiconductor. This is further addressed later (sections 4.2 and 4.3) in this chapter with new test devices enabling direct resistance measurements of contact resistance parameters.

Limitation of TLM model

The TLM model assumes that:

1. The 2DEG is homogeneous, the $R_{\square}$ value is obtained from slope of the fit and it does not account for variation throughout sample, since the contacts are on-mesa and therefore all measurements include the resistance of the contacts as a series resistance.

2. Assuming the 2DEG is homogeneous from growth and unaffected by the necessary annealing of contacts, the largest variation comes from difference in contact yield due to fabrication.

3. The Transfer Length, L_t, obtained by the TLM plot can vary significantly with small variation in the intercept of slope.

4. The resistance of the 2DEG is assumed to be the same under the contact.

This 2-terminal method of measurement is of questionable accuracy. However, it is used as a fast testing method for large batches of samples due to the efficiency of measurement and that it is indicative of sample quality in a self-consistent way. Furthermore, a large sample area is not required for a TLM measurement, such that wafer can be conserved for other devices. If a wafer exhibits non-uniformities in electrical parameters of the order 10-30%, error in contact resistance and calculated resistance under the contact can be as high as 100-1000%, as shown by statistical modelling of the TLM by Gutai [113, 114].

In our case, with a history of various fabrication difficulties, the TLM test device is not sufficient to unambiguously distinguish 2DEG inhomogeneity (due to wafer variation) or contact irreproducibility other than obtaining an average. The contribution of these resistances needs to be measured independently. For this purpose, a test device of similar type was designed. This new sample design, named New-TLM (NTLM), allowed for a standard TLM measurement to demonstrate equivalence with the TLM samples and with the addition of voltage probes for measurements of the 2DEG and each individual contacts. The NTLM samples and relevant measurements are described in section 4.2.

4.1.5 Transmission-Line Measurements

A series of Transmission-Line test devices were fabricated on wafers V827 and V834. The aim was to establish the annealing conditions appropriate for contacting these wafers*. The results of the TLM measurements done on the first batch, α, of these devices are shown in Table 4.2. The industry way of quoting contact resistivity, r_C, is in units of Ωmm, scaled by the width of the ohmic contact to the 2DEG.

*The samples were fabricated by Dr See at the Cavendish Laboratory, coated in PMMA for electrostatic protection and sent to RHUL for characterisation.

Table 4.2: Batch α TLM devices, characterised at 4.2K. Data for "A" samples annealed at 400°C for 60s were very resistive ($>$ 1 MΩ) before illumination, while that of "B" samples annealed at 430°C for 80s was reproducible throughout the batch, especially after illumination. From this characterisation, condition B, at 430°C, 80 s anneal was kept as the optimal condition. Eutectic composition AuGe/Ni/Au layers : 130/50/165.

Sample	Dark				Illuminated			
α	$R_\square$ (Ω/□)	R_c (Ω)	r_c (Ωmm)	L_t (μm)	$R_\square$ (Ω / □)	R_c (Ω)	r_c (Ωmm)	L_t (μm)
				A: 60s @ 400 ° C				
V827 A1					62.8	120.0	9.6	47.8
V834 A1					6.7	169.9	13.6	632.8
W475 A2								
V834 A2					43.1	58.4	4.7	33.9
V827 A2					7.3	229.3	18.3	790.8
W475 A1					19.8	158.2	12.7	199.5
				B: 80s @ 430 ° C				
V827 B1	514.0	40546.0	3243.7	1972.1	7.1	25.7	2.1	90.9
V827 B2	15.1	236.3	18.9	391.2	5.8	13.9	1.1	60.6
V834 B1	5318.0	625.0	50.0	2.9	18.8	14.4	1.2	19.2
V834 B2	36.2	55.7	4.5	122.9	8.1	11.0	0.9	108.4
W475 B1	2057.0	1028.0	82.2	12.5	7.9	25.8	2.1	81.8
W475 B2	4283.0	3116.0	249.3	18.2	12.2	35.9	2.9	74.0

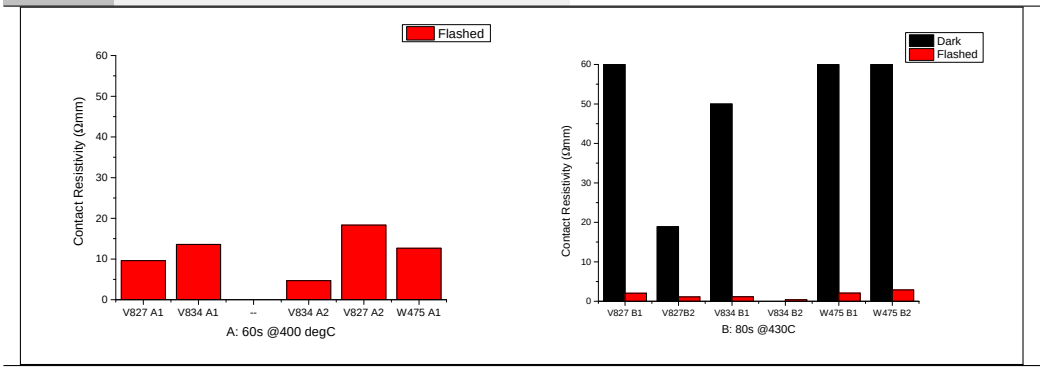

The devices of batch α were TLM devices, fabricated with a primary aim to determine the success of a recipe, (labelled as "B") in comparison with adjustments (labelled as "A") due to using a different annealer and wafers. These devices followed characterisation of the Assessment chips at RHUL as well as macroscopically gated devices (with one large gate over the mesa), to cross-calibrate between RHUL and the Cavendish Laboratory in the first instance, while also determining the ability of the new V-wafers to be gated, as they had not been used before. Following the success of cross-calibration and gateability, these series of test devices were made to determine the optimal annealing conditions for low resistance.

Devices of annealing condition B (430°C, 80 s anneal) performed consis-

tently well in the dark and light, while devices of type A (400°C, 60 s anneal) were highly resistive in the dark and light. For these reasons devices of type A of batch α were considered underannealed. Under an optical microscope they showed a uniform appearance as expected for an underalloyed contact, as described in the previous chapter. These devices established:

1. Equivalence between V and W wafers (grown in different chambers). The depth of 2DEG and carrier density are equivalent, but wafers V827 and V834 had not been used for this type of work before.

2. Out of two annealing conditions; 400°C, 60 s and 430°C, 80 s Rapid Thermal Anneal of contacting material of the same eutectic composition, 430°C for 80 s produced the highest yield and more reproducible low resistance devices, while 400°C for 60 s produced highly resistive devices ($> 1\text{M}\Omega$) without flashing the sample, making a TLM fit inaccurate in the "dark".

3. Agreement with the TLM model's average resistance per square of 2DEG and of that obtained for the wafer from transport measurements at 1.2 K in the Cavendish assessment laboratory. This is indicative of the high homogeneity of the V-wafers and the samples fabricated from them.

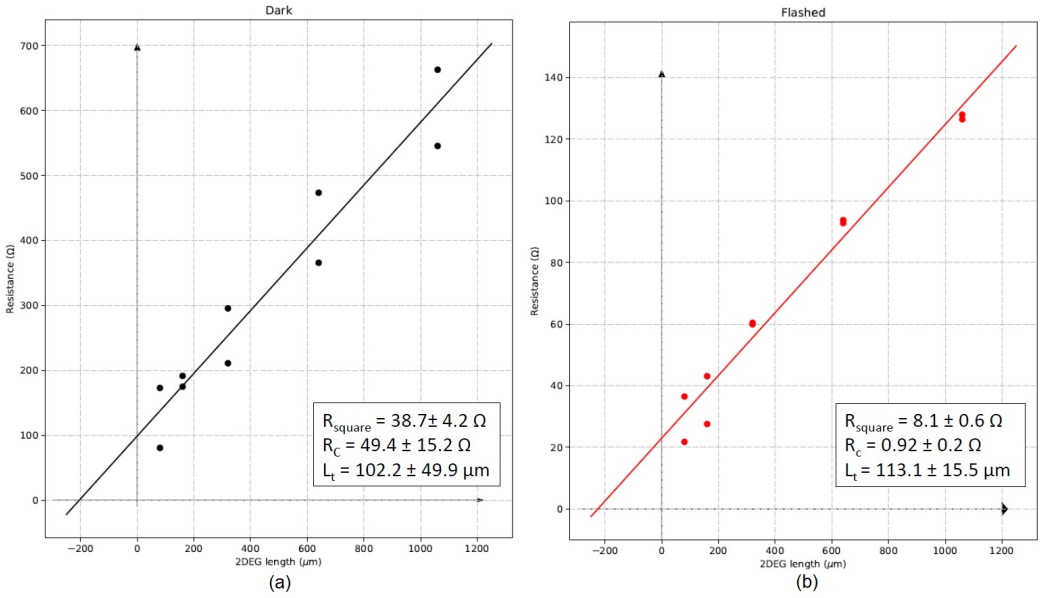

Figure 4.8: (a) Dark and (b) flashed (illuminated sample) data from Transmission-Line Measurements on V834 TLM α B2 annealed at 430°C, 80 s. Two-terminal resistance of sets of adjacent on-mesa contacts of increasing distance are plotted. This sample had 2 bars of identical contact distances and they are both included in these plots, for the same distance, one bar is more resistive than the other, this demonstrates slight variation of the wafer, clearly illuminating improves homogeneity over contacts of the same bar, as well as those of different bars.

4.2 TLM Measurements on New Test Devices

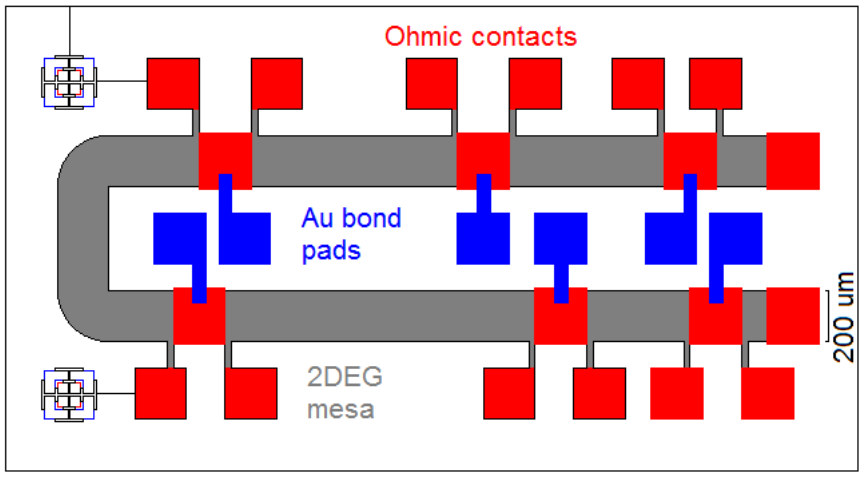

Figure 4.9: The NTLM mask for test devices. The ohmic contacts (red) are all kept as 200 μm $\times$ 200 μm squares on a mesa (black) of 200 μm width. On-mesa contacts allow for standard Transmission Line Measurements, while the extra voltage probes near the on-mesa contacts allow measuring the contacts without measuring the 2DEG contribution, as well as the 2DEG alone, in order to accurately determine the individual resistance contributions. Optional gold layer (blue) to bond onto the on-mesa contact also included.

Due to the inability of the TLM model to characterise and separate the contributions of resistance due to averaging instead of direct measurement, a new mask was designed, the New-TLM mask (NTLM). The addition of voltage probes on either side of an on-mesa ohmic contact enables probing the sample's resistance independently and accurately. Figure 4.9 shows a schematic of the NTLM mask designed to probe the resistance of the 2DEG and the contacts independently.

The contacts were chosen to be of a size 200 μm $\times$ 200 μm on a mesa of 200 μm width to establish scaling of contact resistance between the TLMs and also have similar contacts to the noise thermometer ohmic contact of our 4 mm $\times$ 4 mm devices intended for ultra-low temperature transport measurements. To characterise this type of device, a series of standard electrical measurements are employed, through a series of combination of 4-terminal measurements in order to test the quality of sample. The direct 4-terminal measurement of resistance parameters provides more accuracy than solving

simultaneous equations of combinations of TLM (2-terminal) measurements. The contact resistance and sheet resistance of the two-dimensional electron gas can be determined separately and reproducibility and homogeneity under fabrication can be demonstrated.

By directly measuring different resistances R_{2DEG}, $R_C + R_{2DEG}$ and R_C to the left and right of an on-mesa contact, the contributions can be separated. This is a more reliable test and it is a better method for determining if a sample has low enough contact resistance and total sample resistance, without variations along the sample, to be considered for low-temperature cooling in a dilution refrigerator.

Batch β included the newly designed NTLM and standard TLM devices, to show equivalence between the two test structures. Condition 'B' from batch α was kept the same, condition 'A' changed to a lower temperature anneal, for longer time. Condition 'B' again resulted in a better yield. A typical TLM plot for a NTLM device annealed at the optimal annealing condition ('B') is shown in Figure 4.10.

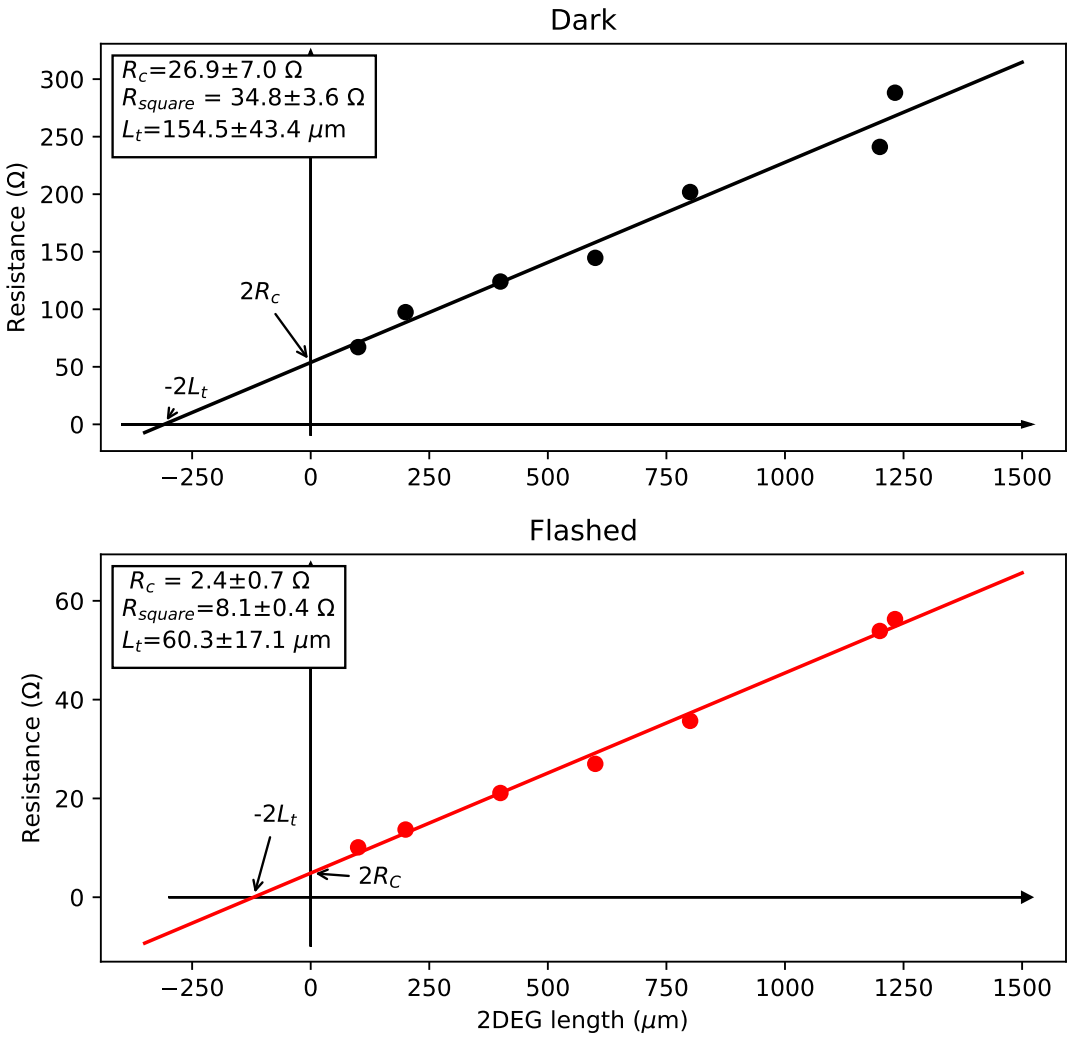

Figure 4.10: Transmission Line Measurement on NTLM type device, batch β. Characterisation at 4.2 K of sample V834 B3, later cooled on the ND3 cryostat for an end-resistance measurement. For samples fabricated under the same conditions, resistance scales from TLM (80 μm) to NTLM (200 μm) contacts.

While samples from the lower temperature anneal ('A') show large resistances and variations, samples annealed at 430°C for 80 s produce consistent low contact resistance of the order 1 Ωmm. The new condition of 120 s at 370°C also showed results suggesting underalloying attributed to the lower temperature both in electrical measurements and by appearance under optical microscope.

Table 4.3 shows TLM results for the two types of devices of different scales of contacts, those of the 80 μm TLM Hall bars and the 200 μm NTLM horseshoe. A quick TLM measurement, easily determines optimal annealing condition for the devices. In this batch of samples, the annealing condition of 430°C for 80 s was kept while the first condition at a lower temperature was altered to 370°C for a longer period of 120 s. The result did not change, 430°C for 80 s remained the optimal condition, matching previous results. Note that the axis for the "A" condition is cropped at 50 Ωmm, corresponding to an average contact resistance of 250 Ω, in order for the illuminated data to still be visible on this scale, with many contact resistances averaging to well above 10 kΩ. Devices fabricated under an anneal of 430°C for 80 s (condition 'B') achieved a low contact resistance of less than 1 Ωmm after illumination. It is also worth mentioning that dark data for the devices annealed using condition 'B' also worked in the dark, with favourably low contact resistance of around 30 Ω, comparable to the resistance of the unilluminated 2DEG. The value of 1 Ωmm matches (if not surpasses) the lowest contact resistance values reported in the literature. The samples batch β were made with the same eutectic composition of 139(AuGe)/35(Ni)/175(Au) layers.

Table 4.3: TLM data from resistor test devices of batch β characterised at 4.2K dipping station. The NTLM devices have a mesa of width 200 μm, larger in dimension than the standard 80 μm TLM bar and allow for direct resistance measurements of the sample. TLM measurement on both types of devices shows scaling with geometry, expressed in r_c (Ωmm). AuGe/Ni/Au composition of 139/35/175. This batch of samples did not have a Ni wetting layer.

Sample	Dark				Illuminated			
β	$R_\square(\Omega/\square)$	R_c (Ω)	r_c (Ωmm)	L_t (μm)	$R_\square(\Omega/\square)$	R_c (Ω)	r_c (Ωmm)	L_t (μm)
A: 120s @ 370C								
V827 NTLM A-1	1185.0	34093.0	6818.6	11508.2	14.2	64.0	12.8	1805.5
V827 NTLM A-2	22.3	88.3	17.7	1584.7	20.2	32.9	6.6	651.5
V827 NTLM A-3	429.9	2995.9	599.2	2787.8	7.1	33.8	6.8	1891.9
V827 TLM A	687.0	28905.0	2312.4	6731.9	33.3	89.3	7.1	429.6
V834 NTLM A-1	15.6	250.8	50.2	6413.8	8.8	5.9	1.2	265.9
V834 NTLM A-2	16.8	310.2	62.0	7389.4	10.3	6.9	1.4	269.5
V834 NTLM A-3	44.5	70.5	14.1	634.0	10.5	3.1	0.6	116.4
V834 TLM A	16522.0	7888.1	631.1	76.4	11.8	44.8	3.6	605.0
B: 80s @ 430C								
V827 NTLM B-1	52.4	18.7	3.7	142.8	11.1	1.9	0.4	68.9
V827 NTLM B-2	55.8	25.6	5.1	183.6	12.0	3.1	0.6	104.0
V827 NTLM B-3	52.9	22.6	4.5	170.5	12.2	1.7	0.3	56.1
V827 TLM B	56.7	179.6	14.4	506.6	12.4	19.7	1.6	254.6
V834 NTLM B-1	33.7	36.9	7.4	438.8	10.6	3.6	0.6	134.8
V834 NTLM B-2	33.1	33.4	6.7	403.9	9.6	3.7	0.7	154.9
V834 NTLM B-3	34.8	26.8	5.4	308.0	8.1	2.3	0.5	115.6
V834 TLM B	36.2	55.7	4.5	122.6	8.1	11.0	0.9	108.4

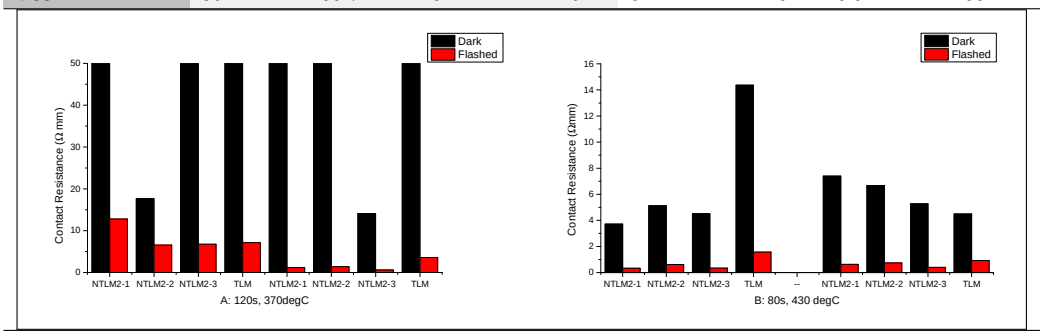

The subsequent batch, on wafers V827 and V834, γ, included 4×4 samples annealed at the optimal temperature and anneal time as well as samples fabricated from edge pieces of the V834 wafer annealed at longer temperatures. TLM data for this batch is presented in Table 4.4. The edge pieces did not have a great yield, with significant variations in resistance per square resulting in unreliable TLM results on possibly damaged parts of wafer.

Table 4.4: TLM averages for batch γ. The purpose of this batch was to determine consistency of scaling of resistances to different geometries TLM and NTLM. Ungated 4×4 devices were also produced at the same time as the TLM and NTLM devices with a 430°C 80 second anneal- these were later cooled on dilution cryostats. The samples made in the 430°C, 140 s condition were from edge pieces of the V834 wafer.

	Dark				Illuminated			
Sample	**$R_\square$ ($\Omega/\square$)**	**R_C (Ω)**	**r_C (Ωmm)**	**L_t (μm)**	**$R_\square$ ($\Omega/\square$)**	**R_C (Ω)**	**r_C (Ωmm)**	**L_t (μm)**
430°C, 80 s								
V827 NTLM 1	53.8	42.2	8.4	156.8	11.4	3.8	0.8	66.7
V827 NTLM 2		246.3	29.6		6.4	12.8	2.6	400.3
V827 TLM 1	145.8	785.3	62.8	430.8	15.7	51.4	4.1	261.3
V834 NTLM 1	34.8	44.4	8.9	255.4	9.1	6.8	1.4	148.9
V834 NTLM 2	49.0	102.2	20.4	416.6	10.7	7.9	1.6	147.4
V834 TLM 1	285.9	914.1	73.1	255.8	9.7	39.0	3.1	323.2
430°C, 140 s								
V834 NTLM A	53.8	42.2	8.4	156.8	13.4	3.8	0.8	56.9
V834 NTLM B	42.0	23.3	4.7	110.8	6.6	11.5	2.3	348.5
V834 NTLM C	136.1	421.2	84.2	619.0	29.7	73.7	14.7	495.9
V834 NTLM D	255.3	1556.1	311.2	1219.3	14.7	22.2	4.4	301.9
V834 TLM A	27.8	190.3	15.2	547.0	12.3	27.8	2.2	180.5

The main purpose of this batch was to establish a baseline for the contact resistance scaling from TLM to NTLM and 4mm type samples. The annealing condition 430°C for 80 s showed once again reliably low contact resistance. TLM and NTLM samples annealed for longer, 140 s, were also produced as an additional check but these performed poorly due to fabrication using only edge pieces of the wafer. The fixed annealing condition, 430°C for 80 s resulted in low-resistance contacts on all three sample types. Characterisation of 4×4 samples is presented in part 4.5. This was a necessary step to establish baselines before using up much more wafer to produce gated 4 mm samples.

4.2.1 Direct Measurement of Contact Resistance

As we saw before, contact resistance is the sum of all resistances resulting from contacting the heterostructure with an alloy. Since contacts are used to measure our samples and our cooling is done through leads below 1K, where the phonons are effectively frozen out, the driving focus has been to minimise this contact resistance for ultra-low temperature work.

Figure 4.11 depicts the contact model that inspired the design of this mask, with the resistance contributions separated to two components; one of

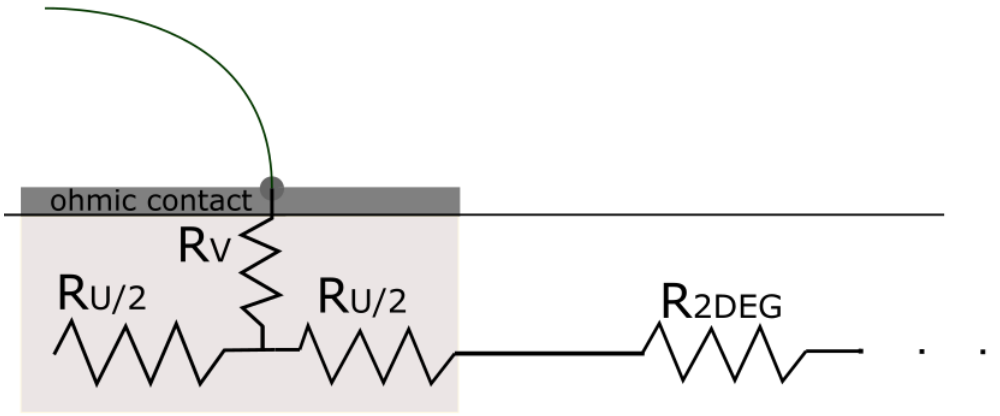

Figure 4.11: Resistor network model of a contact, the contact resistance can be split into contributions from the alloy, the vertical resistance, R_V, and that of the "damaged 2DEG" under under the contact, R_U.

the alloy in the vertical direction, R_V, and that of the area of semiconductor underneath R_U. The important distinction in this model is that the resistance under the contact is not implied to be the same as that of the 2DEG.

The contact resistance, R_C, on an NTLM structure can be directly measured by putting current and a voltage probe on an on-mesa contact and placing the other voltage probe on the voltage probe ohmic, with the current ground further down the path. This is sometimes referred to as a 3-terminal measurement as the current and voltage probes are shorted onto the main contact by a T-piece (or Y-bond).

A significant difference in the work in this study has been the addition of a Y-bond onto the contacts, as depicted in the SEM image in Figure 4.4, which allows for the measurement of the resistance of the contact more accurately, without any resistance in series other than the necessary and negligible (< 3 mΩ) resistance of the bond-wires. This allows us to measure the contact with a 4-Terminal measurement. Typical contact resistance values of samples in this work are 3 Ω (flashed), 10 Ω (dark) for 200×200 contacts, matching the best values achieved in literature of 1 Ωmm.

4.2.2 End-Resistance Measurement

The end-resistance measurement was first proposed by Reeves and Harrison [112]. The resistance measured by this measurement is denoted as R_V and it

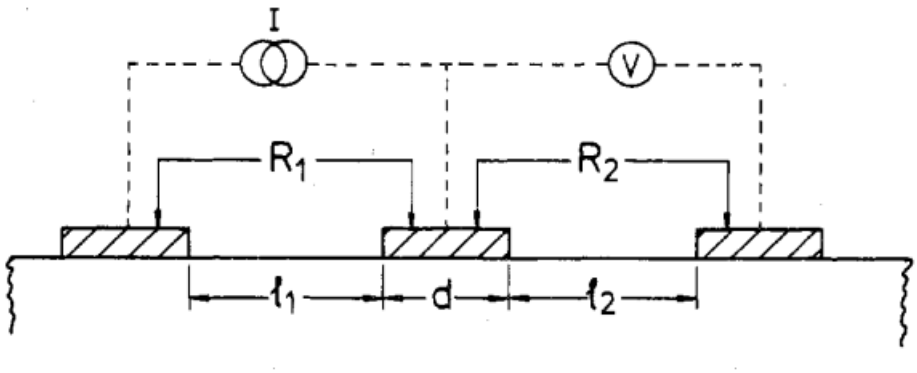

Figure 4.12: Measurement setup for obtaining total resistance and contact end-resistance of a sample. From the work of Reeves and Harrison [112].

is made by sinking the current on a main contact and measuring the voltage dropped from that contact to another contact further down the bar that is un-biased. This measurement can be made simultaneously with the typical contact resistance measurement, as in Figure 4.12. The measured voltage is the potential dropped due to the alloy/2DEG interface alone and is typically less than 50 mΩ, dark or illuminated, at 4.2 K.

The end-resistance of an ohmic contact can be measured directly, as in Figure 4.12. Once the value of the two resistances R_C and R_V is known, the transfer length can be calculated using [36, 112]:

$$L_t = \frac{d}{arccosh(\frac{R_C}{R_V})} \tag{4.5}$$

This is then the length current travels under the contact, and therefore the resistance under the contact can be calculated by scaling the contact resistance by the width of the contact, w, and dividing by the transfer length, L_t, as:

$$R_{SK} = \frac{wR_C}{L_t} \tag{4.6}$$

For our 200 μm $\times$ 200 μm contacts on the NTLM devices, $w = d = 200$ μm.

R_V Measurement Protocol

- Sample must be Y-bonded on the drain contact. Y-bonds can help also check integrity of bonds at room temperature, this a useful check

before dipping the sample.

- Dip to 4.2K and allow some time for the dewar/probe/sample to thermalise (5 mins) before ungrounding - even resistor samples can spike in resistance and take time to settle. It is very important to keep a contact grounded at all times, especially before putting a current in the device to avoid electrostatic discharge to the sample.

- Conduct standard series of TLM measurements and 4-terminal measurements of 2DEG to verify sample is homogeneous and confirm resistance values vs assessment or previous dips.

- Contact resistance measurements to the left and right of every possible on-mesa contact (not possible for source/drain contacts, so this measurement can only happen on NTLM/TLM devices).

- At 4.2 K, on the dipping station setup an increase of the input current is often needed, due to the small magnitude of R_V, to overcome background noise fluctuations (minimum 100 kΩ resistor). If heating the sample is a concern, a high input impedance pre-amplifier is preferable to eliminate some of the noise and improve measurement accuracy, the EG&G preamp that is powered at the back of the DSP 7265 LIAs is ideal for this without adding too many components to the circuit. Alternatively, the SRS LIA and SRS resistance bridge are more accurate and can easily measure this resistance with minimal current in the sample.

4.2.3 Measurements On NTLM Mask Samples

In order to distinguish between variations due to resistance of 2DEG and the contact resistance of a sample, one needs to be able to independently probe the 2DEG with a voltage measurement, without an ohmic contact annealed directly on it. Figure 4.9 shows a CAD drawing of such a device (NTLM).

A device size with mesa width 200 μm was chosen so that it is similar to those used for the 4mm samples, designed with a geometry ideal for ultra-low-temperature measurements. The addition of voltage-probe contacts around the main contact allow a series of combinations of electrical measurements

to be employed to separate resistance contributions, indicating sample homogeneity, wafer quality, yield from fabrication and reproducibility of the ohmic contacts.

TLM measurements at 4.2 K for devices produced in the second batch of samples (β) showed scaling of contact resistance with respect to the width of the contact, with identical annealing conditions showing a resistance remaining approximately the same when scaled as $R_C \times w$ and quoted in Ωmm (the TLM results were shown in Table 4.3).

Table 4.5: Averages of direct resistance measurements on NTLM devices of batch β.

Sample	**Dark**					**Flashed**				
	Rv (Ω)	Ru (Ω)	Rc (Ω)	$R_\square$ (Ω/□)	L_t (μm)	Rv (Ω)	Ru (Ω)	Rc (Ω)	$R_\square$ (Ω/□)	L_t (μm)
370 C, 120 s										
V827 NTLM2 A-1	25949.9	73604.4	98507.8	10172.5	99.5	34.3	184.7	161.5	23.7	89.6
V827 NTLM2 A-2	337.5	561.8	2477.0	52.1	74.6	79.7	180.3	66.4	51.3	
V827 NTLM2 A-3	68.2	236.1	1096.7	236.1	57.6	0.8	54.0	28.6	54.0	47.4
V834 NTLM2 A-1	1.2	284.1	397.0	111.2	30.6	0.7	11.4	6.5	16.0	67.7
V834 NTLM2 A-2	202.7	759.4	299.1	210.1	212.7	117.5	30.7	69.9	25.1	
V834 NTLM2 A-3	332.5	128.3	316.1	33.7		21.4	53.8	14.7	25.1	
430 C, 80 s										
V827 NTLM2 B-1	0.9	178.0	25.8	43.5	49.7	0.9	7.8	4.7	10.3	87.0
V827 NTLM2 B-2	1.1	43.4	29.2	51.9	49.8	0.9	9.5	5.5	10.6	81.5
V827 NTLM2 B-3	1.3	58.9	23.0	58.9	56.1	1.1	7.7	5.0	12.7	92.5
V834 NTLM2 B-1	2.1	59.0	31.2	59.0	59.2	2.1	10.7	7.8	8.2	102.0
V834 NTLM2 B-2	1.0	184.4	51.8	86.1	42.9	1.2	10.7	6.8	22.5	82.5
V834 NTLM2 B-3	1.6	53.4	28.1	28.0	55.9	1.0	7.7	4.8	7.3	88.2

The result of the averages of direct electrical measurements on NTLM devices on samples of batch β are shown in Table 4.5. R_U is the resistance as measured from the voltage dropped across a contact. R_C is given as the average from the top of a contact to the left/right voltage probe, without including the 2DEG contribution. $R_\square$ is the resistance per square of 2DEG, measured by a direct 4-terminal measurement and scaled according to the width/length ratio of the sample. L_t is the transfer length, as obtained from eq 4.5. R_V is the end-resistance, including wire series resistance at this stage. As clearly seen from this table the measurement is completely masked by the resistance of the approximately 1 Ω leads. The main conclusions were:

1. Contact resistance scales with the width of the contact/semiconductor interface, according to the TLM model.

2. Annealing condition 430°C , 80 s showed a high yield and reproducible results, while 370°C for 120 s annealing showed slightly higher resis-

tance, especially in the dark and a transfer length corresponding often a length larger than the contacts, due to large possible variations in the slope.

3. NTLM measurements showed agreement with the TLM average.

4. The value of 1 Ω for end-resistance is the noise floor when measuring such a device without Y-bonds.

5. A relationship of $R_U = 2R_C$ can be inferred in the most homogeneous samples in the light, this is characteristic of a contact that is long compared to the transfer length (more detail on this on section 4.3).

4.3 Current Crowding and Transfer Length

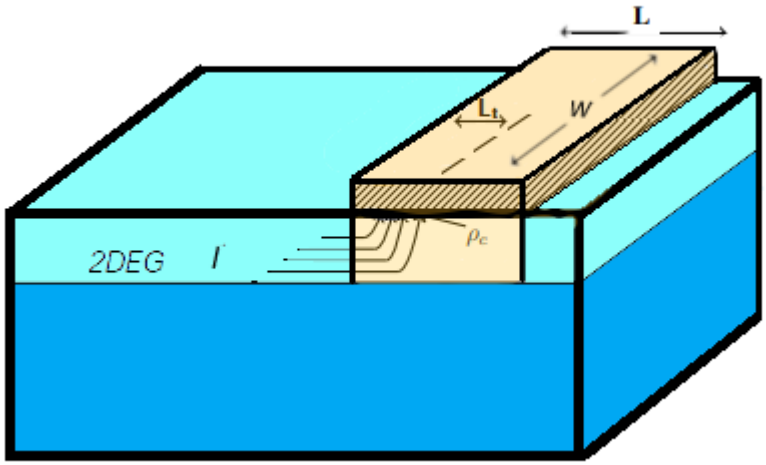

Figure 4.13: Schematic of current crowding occurring under an ohmic contact to a 2DEG. The transfer length L_t defines the length current flows under the contact.

The improvement of contact resistance by illumination resembles that of the 2DEG. This property detaches a component from properties of the alloy of the contact, and therefore this can be perceived as an area of "damaged", to various degrees, 2DEG. This was the "resistance under the contact", R_U in

the resistor network model depicted in Figure 4.11. Less degradation of the substrate was thought to result in a resistance identical to the resistance of the 2DEG per square and that this could be achieved with clean processing and correct amount of doping.

Measurements on NTLM samples (and on NTLM-Hall devices, Appendix C) showed that what was previously thought to be a resistance of the 2DEG is actually the resistance of the contact measured as a whole, a relationship of $R_U = 2R_C$ can be inferred for homogeneous contacts by the measurement of the voltage dropped across the contact being the sum of the contact resistance as measured to the left and right of an on-mesa contact. This is explained by the alloy shorting the 2DEG path and the contact being long ($L \gg L_t$) compared to the transfer length, such that current does not flow past the middle of the 200 μm $\times$ 200 μm contact. Figure 4.14 depicts the ratio of the R_U measurement and twice the average contact resistance for all the contacts of each sample fabricated from batches β and γ by a 430°C for 80 s anneal. The relationship $R_U = 2R_C$ holds for samples experiencing PPC, in the illuminated condition and masked by inhomogeneity in other cases, however it is seen to hold even for bad contacts.

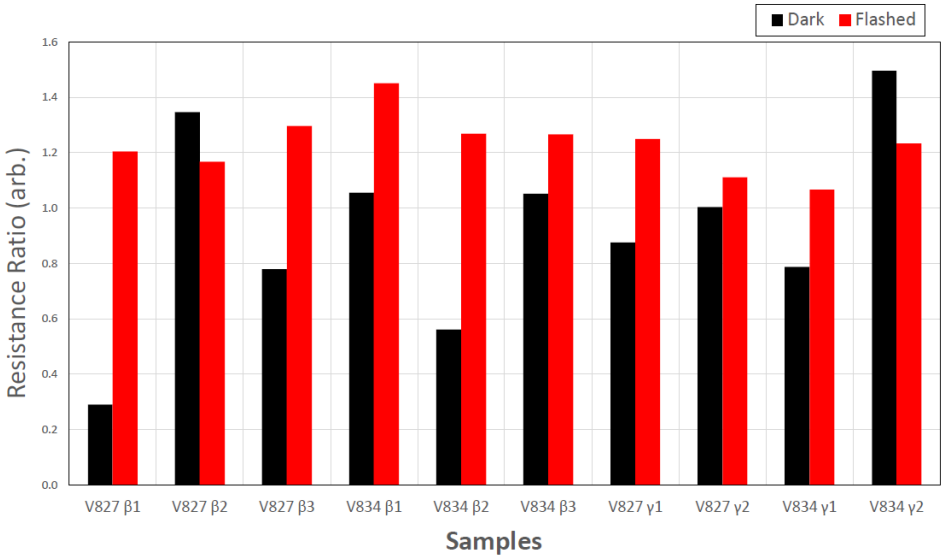

Figure 4.14: The bar chart shows the ratio of the "resistance under the contact" and twice the contact resistance for NTLM samples of batch β and γ annealed at 430°C for 80 s averaged for all on-mesa contacts of each sample.

Characterisation of NTLM samples on the two wafers in batches β and γ initially determined consistently low vertical resistance on the contacts of 1 Ω. The measurement was refined with the addition of Y-bonds and the end-resistances of all samples were subsequently remeasured, producing the results summarised in Table 4.6. As touched on previously, the end-resistance is much less than 1 Ω, the measurement was completely masked by the resistance of the probe copper wires, which also change from room temperature to 4.2 K ($\sim 3\ \Omega \rightarrow \sim 1\ \Omega$).

Table 4.6 shows illuminated data for NTLM devices that have subsequently been remeasured with Y-bonds, due to the accurate measurement of R_v, a more accurate measurement of the transfer length is also obtained. With knowledge that R_U is simply a measurement of the resistance across a contact, amounting to the sum of its contact resistance to the left and right, equation 4.6 was used to determine the resistance under the contact from the transfer length relationship of equation 4.5. The resistance per square, $R_\square$ is also shown where possible to illustrate that the resistance under the contact is more resistive than the resistance of the unalloyed 2DEG, as expected from the process of annealing.

Table 4.6: Illuminated data of contact resistance parameters of samples bonded with Y-bonds on NTLM devices. The Transfer Length, L_t is calculated from eq.(4.5). And the resistance under the contact, R_{SK}, is determined by eq.(4.6), from the ratio of contact resistance to the transfer length, scaled by the contact width, w. For these samples $w = 200\ \mu m$. A Y-bonded sample is the only setup that allows an accurate measurement of end resistance and by extension L_t and R_{SK}.

Sample	$R_\square$ ($\Omega/\square$)	R_C (Ω)	R_V(mΩ)	L_t (μm)	R_{SK} (Ω)
V827 βA1		155.2	56	23 ± 4	1337 ± 231
V827 βA2	9.8	30.2	35	27 ± 7	225 ± 60
V827 βA3		46.3	36	26 ± 5	3363 ± 75
V834 βA1	8.7	7.9	29	32 ± 10	50 ± 17
V834 βA2		10.7	31	31 ± 10	70 ± 24
V827 βB1	8.1	5.7	46	36 ± 18	32 ± 17
V827 βB2		10.1	46	33 ± 17	61 ± 32
V827 γB1	7.9	9.5	18	29 ± 5	67 ± 13
V834 γB1		5.8	42	35 ± 16	33 ± 16
V834 γA1		16.2	27	28 ± 7	115 ± 29
NTLM3 ϵ1	7.4	3.5	34	38 ± 13	19 ± 9
NTLM3 ϵ2	7.5	3.3	13	32 ± 5	21 ± 7
NTLM3 ϵ3	7.1	2.8	45	41 ± 18	14 ± 8

The vertical resistance, R_V, did not change by illumination, while the contact resistance improved significantly, as in the previous averages. The main difference in these measurements is the accurate measurement of the end-resistance, allowing for accurate determination of the transfer length and from it an indication of the resistance of the region under the contact, within reasonable error. The determined R_{SK} shows evidence of flashing under the contacts, as expected from the drop in contact resistance. In this model where contact resistance is very low, but the vertical resistance is of the order of mΩ, current crowds at the edge of the contact, preferring the path of least resistance in the vertical direction.

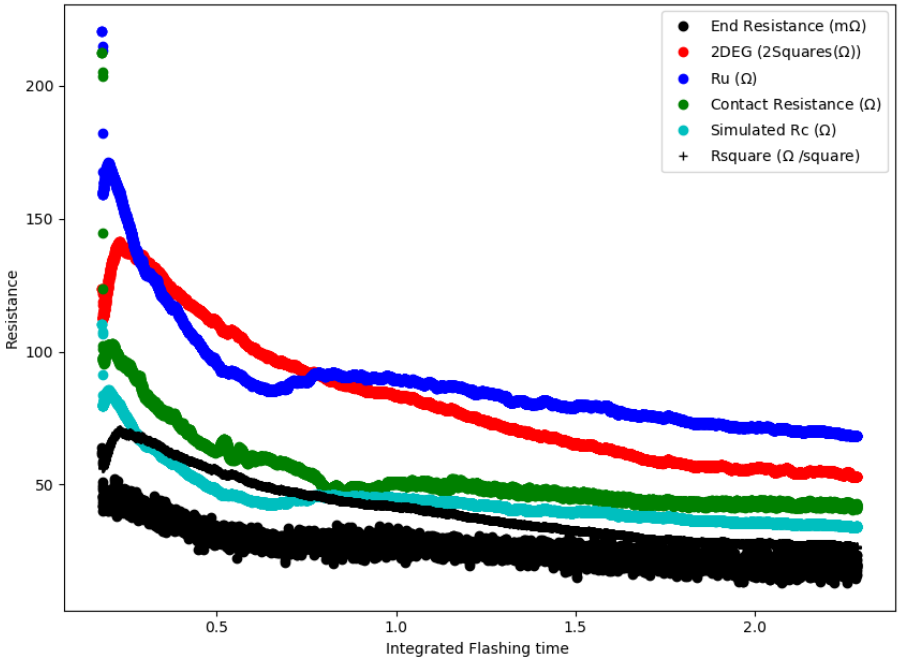

Figure 4.15: Simultaneous measurement of contact resistance parameters under illumination. Pulses are programmed using a DAC as a trigger for a TTL switch of an Agilent 2605 waveform generator to provide an accurate wave - peak of 250μs to illuminate with a red LED. The resistances R_C, R_U and $R_\square$ are measured using a 7265 DSP LIA, while the end-resistance R_V by an SRS analog LIA, using a Y-bond. Sample was allowed to equilibriate for 2 minutes after each pulse. Measurement taken at an input current of 1 μA as defined by a 1 MΩ resistor.

Figure 4.15 shows the contact resistance parameters monitored after being illuminated by a series of 250 μs pulses. It is evident that the end-resistance is not significantly changed, while that of the resistance as measured across the contact, previously called R_U is essentially twice the contact resistance, with the same characteristic trace under illumination.

Experimentally, the transfer length is shown to follow $L_t = \frac{d}{\text{arccosh}(R_C/R_V)}$ (from [115] and [112]), with our lowest resistance samples showing transfer lengths of less than half the width of the contact. This makes sense considering the $R_U = 2R_C$ relationship determined by the NTLM measurement. The contact therefore shorts the 2DEG and when measuring the voltage dropped across a contact the interfacial resistance to the 2DEG is measured in both directions of the current path, as well as the minimal resistance of the alloy (of order 300 mΩ).

The transfer length thus depends on only one variable for a given (fixed) contact dimension, the ratio in the argument of the $\text{arccosh}^{-1}(x)$ in equation 4.5, R_C/R_V. The curves of figure 4.16 illustrate the variation of transfer length due to varying these two elements of contact resistance, keeping the other fixed at their typical experimentally measured values ($R_c \sim 3\ \Omega$, $R_V \sim 30\ \text{m}\Omega$). The curves intersect at the resistance value of 0.3 Ω, which is the sheet resistance of such a contact as measured by a direct 4-terminal measurement with bond-wires on every corner of the square contact $R_{\square}^{TOP} \sim 300\ m\Omega$.

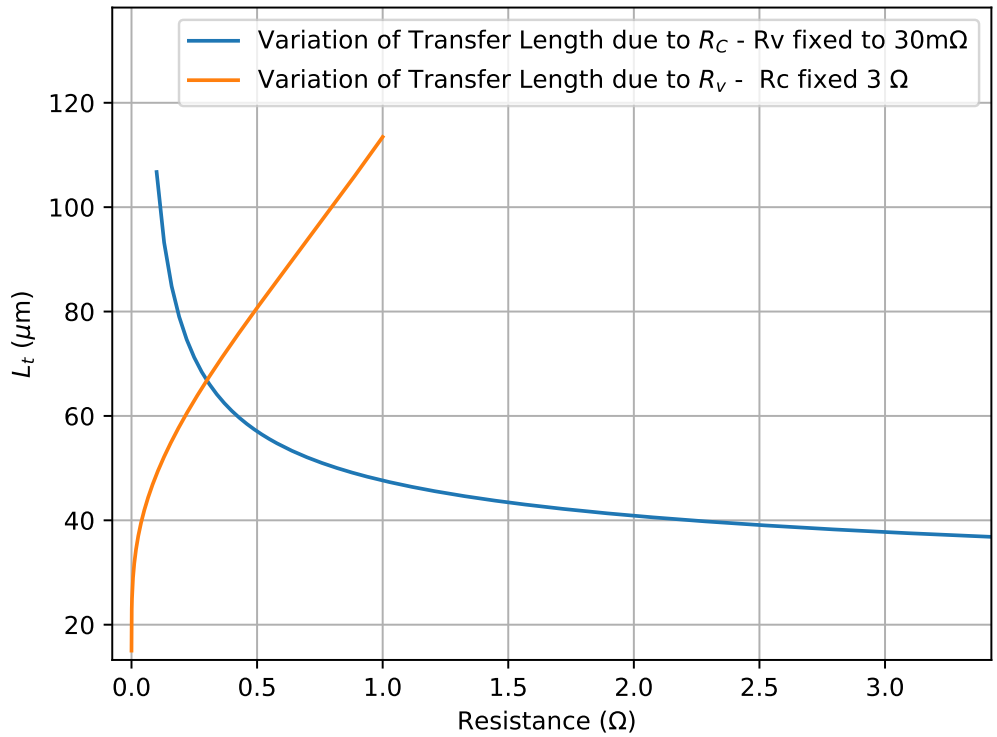

Figure 4.16: Transfer Length due to variation of contact resistance parameters. Orange curve shows variation of transfer length due to $R_V \in (10^{-5}, 1]$, keeping R_C fixed at 3 Ω. Blue curve shows variation of transfer length keeping R_V fixed at 30 mΩ and $R_C \in [0.1, 4]$. It is readily seen that variation due to R_C does not significantly contribute to the resulting transfer length for realistic values. At a value of 0.3 Ω (the sheet resistance of the contact along the top) the lines intersect. A vanishing R_V produces a lower of roughly 20 μm for a 200 μm width contact.

For a 200 × 200 contact, the variation due to R_C plateaus completely to around 17 μm, while for low-resistance contacts, the most drastic variation even for an almost vanishing value, gives approximately 15 μm. For our low-resistance contacts, transfer length is in the range of 40-60 μm depending on the R_C/R_V ratio ($\sim$ 100 in our case). This model is asymptotic to $\sim$17 μm even for extremely high contact resistance and a fixed low vertical resistance, limiting perhaps the smallest possible ohmic contact operating size.

A limiting factor for a contact to operate as intended is the transfer length and that the contact needs to be significantly larger. This limit is most likely the reason why the 5 μm crenellations of the 4 mm × 4 mm samples did not significantly reduce contact resistance further.

The current crowding phenomenon suggests that the resistance of the contact should scale with the perimeter as defined by the effective resistance measured multiplied by the transfer length, such that the resistance R_{SK}, that of the damaged 2DEG, is the total semiconductor-metal interfacial resistance and that measured by electrical characterisation is the effective contact resistance of the least resistance path.

AuGeNi Sheet Resistance

To measure the sheet resistance of the contact, at the top, samples were bonded in different patterns. Four bonds on each corner of the square contact make it easy to measure with a 4-terminal measurement. Additional bonds (up to 9) have also been placed on 200 μm × 200 μm contacts to check continuity and symmetry of the alloy at the top. A square 200 μm × 200 μm contact has a resistance of 300 mΩ at 4.2 K, on V-wafers.

Furthermore, the end-resistance (R_V) measurement is the resistance of the alloy in the vertical direction. On a multi-bonded sample, with a contact bonded with 9 additional bonds on the top, a series of R_V measurements was thought to possibly give a different value; however, it remained unclear whether small variations were due to bond integrity, damage from multiple bonds on the sample or a change in current path; the contact is continuous and therefore shorting at the top electrically, such that this measurement could not determine a significant difference. In chapter 5, a sample bonded in such a way was subsequently cooled on the ND4 dry fridge to characterise the temperature dependence of the contact's sheet resistance in a magnetic

field, showing conclusively continuity of the alloy at the top and a clean superconducting transition (section 5.3).

4.4 Strategy to reduce R_C for Low Temperatures

The motivation for the optimisation of ohmic contacts has been to minimise resistance such that a device can achieve being cooled to ultra-low temperatures. The wafers that are chosen have a typical 2DEG that is 90 nm deep and of high mobility. The resistance of the 2DEG scales with device size so that a device that is designed with a geometry that is wider than it is long is going to be less resistive, just like any other conductor. In this way, the 2DEG resistance is controllable. In order for this scaling to be achieved in a 4 mm device, the importance of a homogeneous 2DEG was stressed and achieved on V-wafers.

With the 2DEG contribution accounted for, the main factor limiting the ultimate base temperature was the contact resistance, R_C. For optimal thermalisation, ease of measurement and insignificant Joule heating, the contact resistance should be ohmic and of the order of 1 Ω, such that achieving a recipe of resistivity of 1 Ωmm, such us ours, and scaling it over an area of about 4 mm makes this readily achievable. As phonon coupling becomes increasingly insignificant below 1 K, our cooling is done mostly through leads for ULT; this is also the reason why the source and drain contacts on the 4×4 devices are so big and span the sides of the sample. To measure the 2DEG resistance and ensure that the sample is homogeneous and to allow the option to conduct magnetoresistance measurements on the sample without the contact resistance in series, two on-mesa voltage-probe contacts are added. The cooling power of these is insignificant in comparison to the source-drain contacts, as shown in the current-balancing checks of section 4.5. We measure the electron temperature by a noise thermometer coupled to a 200 μm $\times$ 200 μm contact, labeled NT and placed solely on the opposite side of the voltage contacts on the midpoint of the device. This is so that thermalisation of the sample is modelled as in the Thermal Model (section 1.3), as that of a simple resistor.

Conclusions on Contact Resistance

1. From previous work on W-wafers, bonding directly on the contact was thought to increase contact resistance by $\sim$3 Ω. There is evidence of increased plasticity of the substrate when gold is applied [116]. This however is difficult to determine when there are cooldown variations and overall sample inhomogeneity and poor yield which was likely more significant factors affecting reproducibility. Subsequent tests on V-wafers showed no evidence of this, even with 9 bonds placed on an on-mesa contact.

2. Y-bonds should be used and can be either on the contact itself or shorted to the LCC or immersion cell silver-sintered bond pads for accurate measurement. For ultra-low temperature measurements, the immersion cell silver-sintered pads are gold plated, which is why a distinct layer of gold is also needed on the contact. This should be evaporated or deposited by e-beam to ensure it is a distinct gold layer.

3. The sheet resistance of the surface of a (AuGeNiAu) contact is of order 300 m$\Omega/\square$ at 4.2 K for V-wafers fabricated with a 430°C 80 s anneal, as measured by a 4-terminal measurement with Y-bonds on the corners of 200 μm $\times$ 200 μm contact. This is reproducible on 200$\times$200 contacts and samples of other dimensions showed the same when scaled for a per square value. This is therefore the resistance of the alloy at the top.

4. End-resistance is the vertical resistance of the alloy to the semiconductor and is of order 30 mΩ. Surface profilometer measurements have determined the contact material to be $\sim$375 nm, therefore with scaling, roughly the same resistance per square as a 4-terminal measurement on the top of the alloy.

5. No evidence that Ni wetting makes a difference. Ni(Ge) grains redistribute to the heterostructure surface, regardless of initial wetting layer or not, as discussed in chapter 3. The total amount of nickel to gold ratio is important, in accordance with the literature review of section 3.2.1. Electrical resistance measurements resulted in identical contact resistivity.

6. Layered (V-wafers) and 'slug' eutectic (W476) ohmic contacts can both achieve low contact resistance, with similar processing conditions. Both types of ohmic contact are equivalent - having taken similar precautions in the processing and using a dedicated evaporator to avoid contamination, low contact resistance can be achieved.

7. Our ideal annealing condition is 430°C for an 80 s Rapid Thermal Anneal, producing a reliable low contact resistance of 1 Ωmm.

8. In practice, crenellations of 5 μm were added to the contacts of samples intended for low-temperature measurements. When annealed with a photolithographic mask (of accuracy around ± 2 μm), end up with an actual width of 7 μm. Due to the fact that transfer length is shown to be asymptotic around 20 μm and larger than 5 μm, these do not make a significant improvement and are not considered when scaling contact resistance.

9. The contacts are found to be long compared to the transfer length, such that the total resistance can be split into the sum of the effective contact resistances as defined by the transfer length and shorted by the negligible resistance of the alloy at the top.

10. The sheet resistance of the W476 4×4 B ohmic contact was measured using the same technique, giving a value of $\sim$3 Ω, which is significantly higher than the sheet resistance measured for V-wafers. This is likely attributed to the difference in fabrication and the eutectic used ("slug" type). It is worth mentioning that devices of these type had historically more bonding issues, with material coming off during bonding.

4.5 4×4 Samples

We cool our sample from the leads. In order to study a 2DEG to as low a temperature as possible, the effective resistances of the circuit needs to be minimised, to improve thermal conductivity and reduce Joule heating. The 4×4 samples are designed to minimise contact and 2DEG resistance. By design, the 2DEG is wider than it is long, approximately half a square, to further allow for easier thermalisation. The sample has two large contacts,

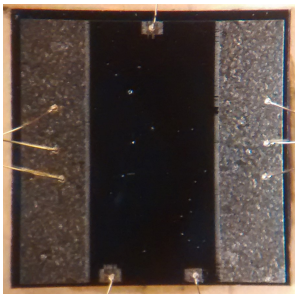

(a) W476 4 ×4 sample cooled to 1 mK

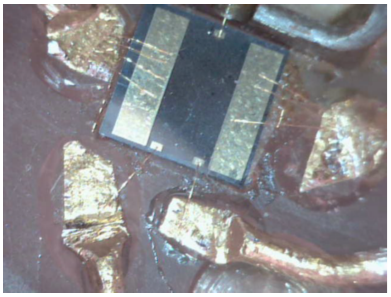

(b) Sample bonded to gold-plated silver-sinter pads of ND3 immersion cell.

Figure 4.17: The W476 4 mm × 4 mm sample inside the ND3 cryostat's ^{3}He immersion cell. The ohmic contacts are bonded onto gold-plated silver-sintered wires for thermalisation with 20 μm gold bondwire. The large contacts are bonded with an array of 3 bonds, while the NT ohmic is bonded with a bond shorting to an Au pad on the Noise Thermometer. Cooling is done through leads, while a dedicated wire serves as a thermal ground to cool the lattice efficiently and is where the sample is mounted onto.

for use as source and drain in measurements, spanning the width of the 4 mm sample. Two voltage probes on one side allow 4-terminal measurement of the 2DEG and a sole contact is used to measure thermalisation in the mid-line of the sample, by coupling to a noise thermometer via a bond-wire, depicted in Figure 4.17 (b). The device shown in Figure 4.17 was the original W476 device that reached the boundary of the μK regime. The new devices from batch γ and gated devices from batch δ resulted in a significantly lower 2DEG and ohmic contact resistance than the original sample.

Another version of 4 mm samples exist (gated) from batch δ, depicted on the RHS of Figure 4.18, where the noise thermometer is coupled capacitively through two large gold pads. The gates on these devices were designed with the same electron beam lithography pattern as that of our Hall bars. Ultimately, the gating of such devices proved successful, more detail in characterisation of gates for these devices is shown in Appendix A.

Table 4.7 presents resistance measurements on 4 mm × 4 mm samples and the determination of the resistance of the contacts and resistance per square of the 2DEG from these measurements by considering the sample dimensions.

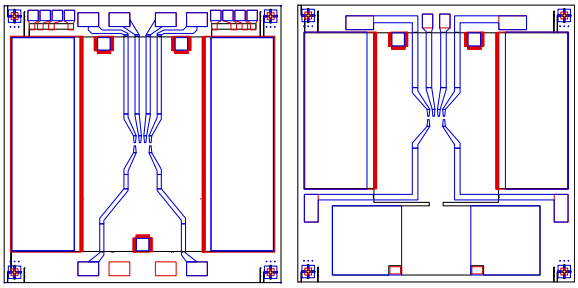

(a) Gated 4 × 4 devices

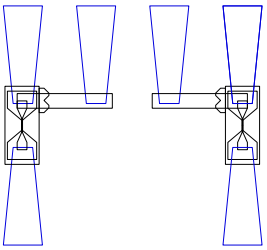

(b) Electron Beam Lithography for QPCs

Figure 4.18: New 4mm devices, working mesa size/ohmic slightly smaller, to accommodate off-mesa contacts for bonding gates. The e-beam pattern is also standardised, so that the effective area of the QPC is the same. The two samples are as similar as possible, the main difference being the two large capacitive contacts instead of a simple 200 μm × 200 μm ohmic such as the original 4 × 4 sample.

Current Balancing and Symmetry Checks

Since the sample has mirror-symmetry by design, thermalisation to the middle of the sample can be simulated by adjusting current flow from all contacts to an equipotential as measured to the NT contact. At equipotential, the effective resistance to the NT ohmic is simply $R_{NT:IV} = \frac{V}{\sum I}$.

Balancing current flow to the NT contact then determines the current path used for thermalisation and simulates the contacts under thermal equilibrium with the bath when cooling through leads; this needs to be known as, ultimately, the electron temperature is measured by a noise thermometer coupled to the isolated NT contact. To achieve this, a synchronised stack of four 7265 DSP LIAs were used, all having the same phase within 0.5° and same amplitude within 1%.

Through this method, it is determined that cooling is dominated by the

Table 4.7: Measurements on 4mm × 4mm samples on wafers V827 and V834. In grey, measurements of unilluminated samples and in light blue illuminated measurements. The link to determining the resistance of the contacts as well as the resistance per square of the 2DEG are given by the geometry factors, obtained by the width to length ratio of the device. These samples were fabricated in batch γ.

Sample	2T I+I- (Ω)	2T V+V- (Ω)	4T (Ω)	I^+I^- geometry	V^+V^- geometry	Rc I+I- (Ω)	R_C V+V-(Ω)	$R_\square$ (Ω/□)
	54273.0	57.6	8.3			27130.0	24.7	23.0
V827 4x4 A	23.5	14.6	3.2	1.571	2.768	9.2	5.7	8.9
	28.4	45.4	14.8			2.6	15.3	41.0
V827 4x4 B	7.8	12.1	2.7	1.571	2.768	1.8	4.7	7.5
	21.5	39.9	10.9			2.2	14.5	30.1
V834 4x4 A	7.2	9.8	2.8	1.571	2.768	1.4	3.5	7.8
	18.8	35.6	14.0			1.6	10.8	38.6
V834 4x4 B	5.7	8.6	2.5	1.571	2.768	0.9	3.0	7.0

large ohmic contacts and an indication of the homogeneity of the 2DEG can be inferred. Details on this measurement can be found in Appendix D.

4.6 Summary

This chapter described device characterisation at 4.2 K, which determined the optimal annealing conditions for low-resistance contacts on previously unprocessed wafers.

An overview of the TLM method and its use to characterise the performance and homogeneity of a device efficiently was provided and the limitations of the model were highlighted. The results of this method on batches with different annealing conditions were discussed. The TLM results were compared to direct resistance measurements made possible by a modified testing device (NTLM), which allowed measurements on the 2DEG and the contact separately. Equivalence is shown between the two types of devices through the TLM model and, by extension, a scaling of contact resistance is seen. With this new type of test device, it was determined that the on-mesa ohmic contacts short the 2DEG on both sides, while the resistance under the contact is damaged by the process of annealing a contact, and an estimate for this resistance is given. The resistance per square of the 2DEG is readily measured to be as quoted from the Assessment laboratory, something that was previously an inhibiting factor for low-temperature transport measurements with previous wafers.

The end-resistance is measured precisely and accurately and is the alloy resistance in the vertical direction, scaling inversely with contact size. Accurate measurement of this resistance allows for a correct determination of the transfer length and the resistance of the 2DEG under the contact.

The optimal annealing condition was determined to be 430°C for an 80 s anneal, with reproducibly low contact resistance throughout fabrication batches and different device types. Using these conditions, 4×4 devices were fabricated specifically for low-temperature measurements and the method of characterisation of devices of this type was outlined.

The gating of V-wafers was also tested, producing low-resistance samples without significant reduction in mobility, no leakage current in a 0.1 fA background and compatible with ultra-low-temperature measurements.

In the following chapter, we will see that ohmic contacts from these devices, as well as past devices with AuGeNi contacts, superconduct below 1 K.

Chapter 5

Low Electron Temperatures and Ohmic Superconductivity

Following the optimisation of contact resistance and important advances in our understanding of the contacting mechanism of the ohmic contact to the 2DEG, 4 mm devices were cooled to low-temperature and measured accurately with Y-bonds. A superconducting transition was observed. Subsequent investigations showed this transition to be a property of the alloy, as suggested by the end-resistance measurement, which also shows a characteristic superconducting transition under 1 K. Here, data of accurate measurement of the resistance of samples at low temperatures are presented and, in combination with the contact structure study, it is determined that this observed superconducting transition occurs due to the existence of the Au+Ga compounds in the contact.

5.1 Measurement Techniques

In early 2016, a simple 4 mm × 4 mm gateless GaAs/AlGaAs 2DEG sample fabricated on wafer W476 was cooled in the ^{3}He immersion cell on the ND3 copper nuclear demagnatisation cryostat. The goal was to achieve submilliKelvin electron temperature on a standard 2DEG. At low temperatures, phonon freezing decouples the conducting electrons from the lattice, making cooling via this mode increasingly difficult [15, 18] and the primary mode of cooling is through the conducting electrons and therefore the contacts of

the sample. Electrical leads to the sample are thermalised via sintered-silver heat exchangers in a ^{3}He bath thermally anchored to the nuclear stage, the coldest point of the demagnetisation fridge.

In order to infer electron temperature a gold wire connects an isolated contact in the midpoint of the 4 × 4 sample to a current-sensing noise thermometer (CSNT) attached to the 2DEG via a dedicated ohmic contact (called NT) and read out by a DC Superconducting QUantum Interference Device (SQUID). The immersion cell setup was first designed on ND3, shown in the schematic of Figure 5.1, and subsequently on the Kelvinox. For a thermometer to be in thermal equilibrium with the sample, the coupling to the sample must be better than that to the environment. This condition was thought to be satisfied below 5 mK: being thermally coupled to the bath via Wiedemann-Franz law - cooling through leads, while to the bath through Kapitza resistance (acoustic/phonon coupling). The heat leak to the thermometer must also be small enough to avoid inducing overheating. The heat leak to the thermometer is addressed through the requirement for the sample to have low enough heat leak to achieve sufficient cooling, such that if a sample is of low enough resistance, its ohmic contacts will always thermalise preferably to the 2DEG "heat bath".

With the heat leak $\dot{Q}_e$ being of the order 3 fW on the ND3 cryostat and bath temperature of the nuclear stage (200 μK), a 2DEG of resistance of order 5 Ω should thermalise to the temperature of the nuclear stage, following Wiedemann-Franz law, to approximately 0.1 mK. However, the lowest electron temperature measured of 1.0 ± 0.1 mK, by a current sensing noise thermometer coupled to the NT contact of the 4×4 sample, did not fit the theoretical prediction of the thermal model, requiring the Lorentz number to be scaled by a factor of 0.1 to compensate.

Following the extensive ohmic study described in the previous chapters, this Wiedemann-Franz law violation was attributed to a superconducting transition in the contact, noting a jump in resistance of the order of 1 Ω, corresponding to what was thought to be the value of end-resistance - the resistance of the alloy at the time, and also from a literature review of the possible compounds in the ohmic and overlooked evidence of gold gallium alloy superconductivity [117]. This motivated a series of measurements of 4×4 devices on the Kelvinox cryostat, with an aim to measure this super-

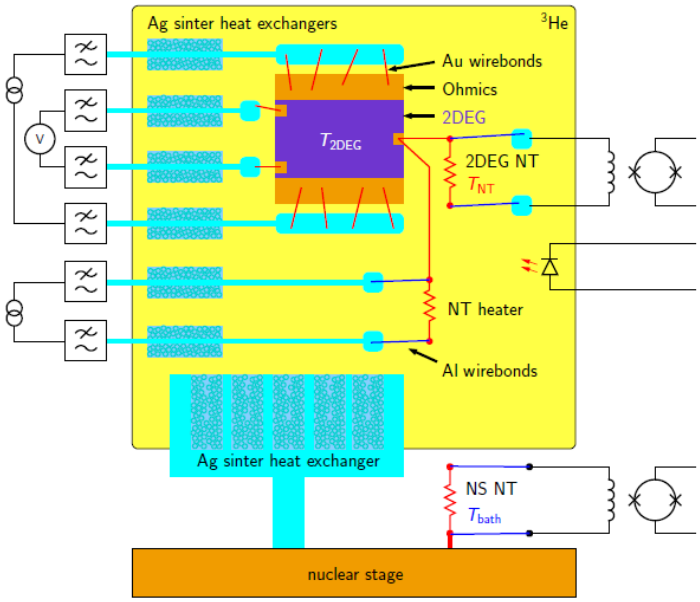

Figure 5.1: Experimental setup of ND3. A two dimensional electron gas sample, 4mm × 4mm in size with large ohmic contacts in thermal contact to large silver sintered pads, in a 1266 stycast cell filled with ^3He thermally bridged to the nuclear stage. A noise thermometer equipped with a heater is attached to the 2DEG via an ohmic contact to measure temperature accurately. Au wire-bonds are shown in red, while blue depict Al wire-bonds which are placed as a thermal break.

conductivity and break it using magnetic field.

Table 5.1 summarises measurements taken on 2DEG samples on fridges at RHUL. The W476 4×4 B sample was cooled on the ND3 immersion cell a multitude of times (2016-2019), showing a reproducible jump in the total resistance of the sample. The V834 4×4 A sample was cooled on the ND3 mixing chamber and showed a sharper transition in the same temperature range. The V827 NTLM sample showed a vanishing end-resistance, with the transition starting in the same temperature range as the jump of the two 4×4 samples. Samples fabricated in the same conditions on wafers W476 and V834 as those cooled on ND3 were measured in field on the Kelvinox to determine the critical field of the superconducting transition. Finally, the sheet resistance of an ohmic contact of the W476 4×4 B sample, was measured on the ND4 dry fridge in a magnetic field.

Table 5.1: Summary of samples cooled to low-temperature.

Samples on Fridges	Cryostat	Measured
W476 4×4 B	ND3 Immersion Cell	Temperature dependence, cooled to ULT (multiple times 2016-2019)
V827 4×4 B	ND3 Mixing Chamber	Temperature dependence
V834 NTLM B3	ND3 Mixing Chamber	Temperature dependence of end resistance
W476 4×4 D	Kelvinox	Two Kelvinox Runs in perpendicular B field
V834 4×4 B	Kelvinox	Two Kelvinox Runs in parallel B field
W476 4×4 B	ND4	Sheet resistance of ohmic contact in field

5.2 Ohmic Contact Superconductivity

5.2.1 The Coolest 2DEG & ND3 Immersion Cell

A 4 mm × 4 mm sample of wafer W476 was cooled on the immersion cell of the nuclear demagnatisation cryostat (ND3) to ultra-low-temperature, to measure a low electron temperature. At fridge base temperature and for an illuminated sample, the SQUID read out an electron temperature of 1.0 ± 0.1 mK, the coldest 2DEG reported.

It evident that the sample did not cool as efficiently as expected, with the discrepancy of a factor 10 initially attributed to a Wiedemann-Franz law violation in the 2DEG, an unusual phenomenon which is sometimes also seen in silver and superconductors [32]. The resistance jump is of the order of 1 Ω and it is depicted in the temperature dependence of Figure 5.2. The resistance plotted is offset by the initial resistance value before the"jump" occurs to clearly show the magnitude of the jump for this transition, note that the jump is identical whether the sample is in the "dark" or "flashed" state, experiencing the effects of persistent photoconductance.

The resistance jump is masked in a typical measurement in various ways: firstly, Y-bonds are needed to eliminate the otherwise large series resistance of the fridge wires, which obscure this ∼1 Ω resistance jump. Furthermore, the total resistance of the sample would typically also hide this small jump as a source-drain measurement such as this includes the resistance of the two contacts and the 2DEG in-between them, for a Hall bar type sample of around a kΩ this would also make this observation impossible to notice. It is only through the process of minimising the resistance of all components of the sample and with the addition of Y-bonds that this detail could be observed.

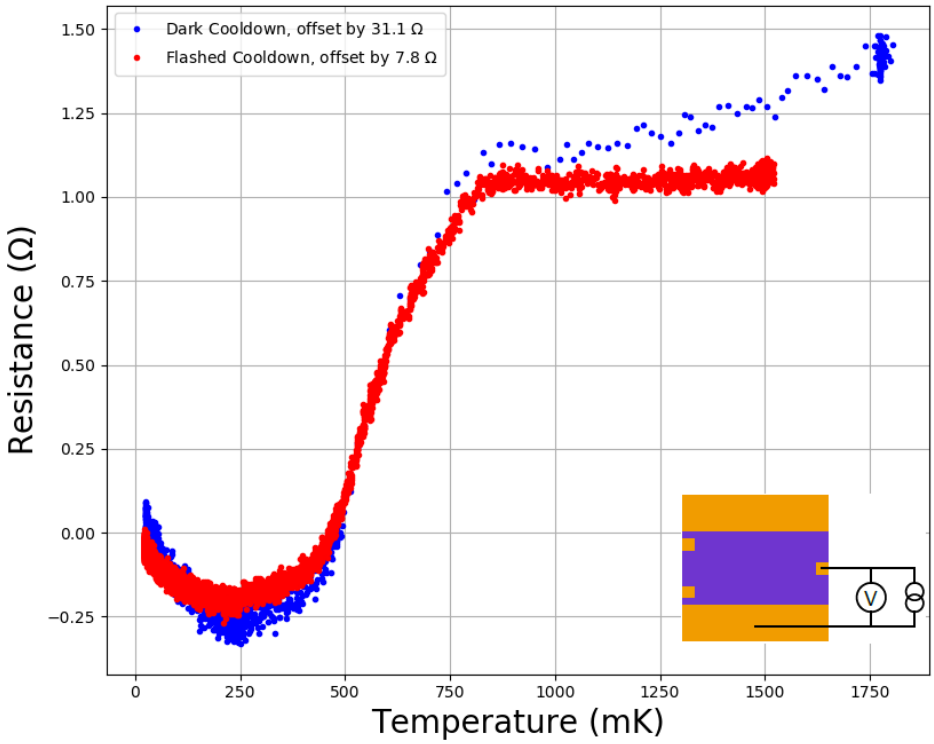

Figure 5.2: W476 4×4 temperature dependence, cooled on ND3 immersion cell to ULT, measured as in insert. Data is offset for clarity by the above-transition resistance value. Sharp drop in resistance seen in both cases, with a transition starting around 0.75 K and ending at 0.5 K. The magnitude of the jump remains unchanged from illumination. Below 0.1 K, there is a resistance increase consistent with a Kondo effect, the 2DEG resistance is unvaried in the cooldown. This effect is only visible when the contacts are included in the measurement.

The sample on the immersion cell was bonded using the Y-bond technique in order to allow measurement of the gold bondwire while also providing some redundancy in measurement should a bond fail during cooldown. The Y-bond technique allows for a direct 4-terminal measurement of the sample, with only the negligible resistance of the bondwires in series (2.2×10^{-8} Ωm). An accurate measurement of the temperature dependence shows the transition in the total sample resistance below 0.8 K.

In the temperature dependence trace of Figure 5.2 the total resistance plotted includes the resistance of both source and drain ohmic contacts and the 2DEG. Due to limited number of lines available (8) on the ND3 cryostat, the 2DEG was not separately measured in these temperature dependence

Table 5.2: Electrical resistances measured in the W476 4×4 sample. 2DEG resistance measured by a 4-terminal measurement using the voltage probe ohmics over an area corresponding to 0.3 $R_{\square}$.

W476 4×4	Dark (Ω), at 4 mK	Illuminated (Ω), at 2 mK
R_{2DEG}	9.75 ± 0.04	1.86 ± 0.04
$R^{I^+ \leftrightarrow I^-}$	16.76 ± 0.04	4.41 ± 0.04
$R^{NT \leftrightarrow I^-}$	31.37 ± 0.04	7.73 ± 0.08
$R^{NT \leftrightarrow I^+}$	30.30 ± 0.05	7.65 ± 0.07

traces, but provides a small series resistance at just 0.3 squares. Both dark and illuminated data are shown in Figure 5.2.

Figure 5.3 depicts the temperature dependence of the resistance of a large contact (I^-) to the noise thermometer (NT) to which the thermometer is coupled in comparison with the resistance per square of the 2DEG ($R_{\square}$), for the dark and illuminated sample. The resistance of the 2DEG remains unchanged after the transition is seen - there is no positive slope with lowered temperature in contrast to the measurement with the resistance of the contacts in series.

Table 5.2 presents resistance measurements of the sample taken in the dark and illuminated states of the W476 sample at milliKelvin temperatures. The 2DEG resistance is measured using the voltage probe contacts over an area corresponding to 0.3 $R_{\square}$. Measurements are also given for the $I^+ \leftrightarrow I^-$ resistance of the sample, which includes a 2DEG contribution as well as the two large contacts in series and that of combinations of large ohmic contact to NT-contact resistance. The later two are important as this electrical measurement links directly to the thermal resistance, as the temperature is measured from a Noise Thermometer coupled to the 200×200 NT ohmic contact.

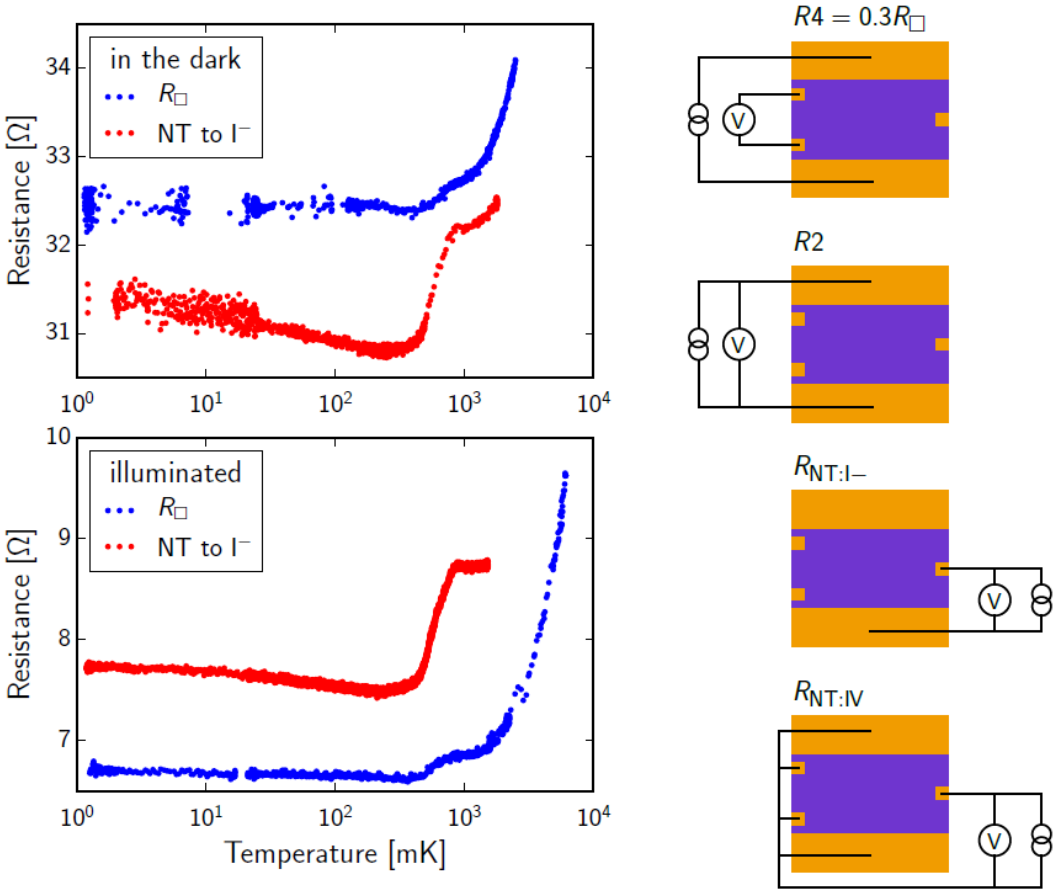

Figure 5.3: Temperature dependence of the resistance per square of the 2DEG, $R_\square$, and 2-Terminal resistance R^{NT} to I^-, including contributions of resistances of the ohmic contacts and the 2DEG in between. The right-hand panel demonstrates the measurement schemes available on such a device. Data from work presented in [26].

This result was surprising and in contrast to direct measurements of thermal conductivity of 2DEGs in the past which have shown agreement with Wiedemann-Franz law [33, 34]. Following a literature review, it was noticed that alloys of gold with gallium superconduct [117], something previously missed from the semiconductor literature. To investigate this further, two 4×4 samples were cooled in magnetic field described further in section 5.2.2.

Samples on ND3 Mixing Chamber

Following the systematic study of optimisation of contact resistance, described in chapter 4, and using the optimal recipe, a 4×4 sample of the wafer V827 was also characterised with Y-bonds at low temperatures, mounted on the mixing chamber of the ND3 cryostat (by wiring a PLLC sample holder), to determine its temperature dependence. Thermalisation for this experiment is not particularly difficult as the temperatures needed to reach to see this transition are the warmest edge of a dilution fridge's spectrum. The PLCC mount provides sufficient thermal contact and easy sample mounting/unmounting and proved to be especially useful when investigating temperatures that are not at the ultra-low limit and improving the turnaround time for experiments. The Mixing Chamber sample mount also has a calibrated red LED for illumination.

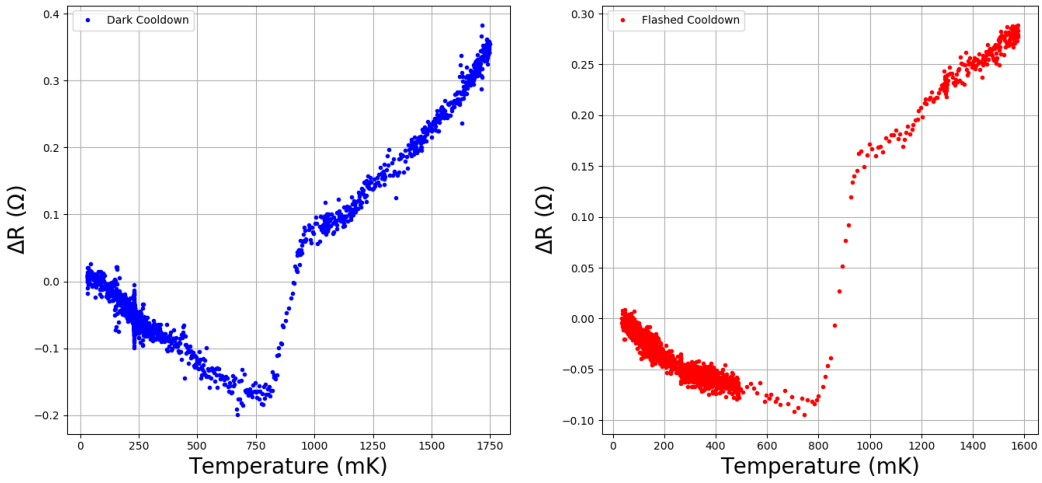

(a) (b)

Figure 5.4: V827 4×4 B2 from batch γ temperature dependence on ND3 Mixing Chamber. The differential resistance data is that of the resistance of a large ohmic contact, to the noise thermometer contact and is offset to depict the magnitude of the resistance jump clearer. (a) Dark cooldown offset by 33 Ω, the resistance value above T_C. (b) Data after illuminating with a red LED to saturation, the trace is offset by 6.1 Ω.

Figure 5.4 shows the temperature dependence of the sample in dark (a) and illuminated (b) conditions. The transition for this sample is still at

the same temperature, but is characteristically sharper, suggesting a cleaner superconducting transition.

It should be further noted that below 1 K the 2DEG mobility does not vary significantly, such that the jump in resistance is not attributed to the 2DEG, but the contacts. The difference between the positive linear (V827) and the non-linear (W476) temperature dependence past transition is characteristic of a Kondo effect in the alloy, which is mostly gold, as the temperature dependence relates to the amount of impurities [118, 119].

To decouple from the 2DEG contribution to the total resistance, an NTLM device of wafer V834 was cooled on the ND3 mixing chamber, bonded using gold Y-bonds such that an accurate end-resistance measurement can be made. Through characterisation at 4.2 K it was suspected that this would be the resistance of the alloy contribution to the contact resistance.

Due to reported effect of Ni wetting improving morphology of surface roughness, a sample without a wetting layer of nickel was chosen, but with otherwise identical consistency, this was a sample fabricated in batch β. The temperature dependence of the vertical resistance, R_V was first measured at low temperature on a V834 NTLM sample mounted on the Mixing Chamber of the ND3 cryostat, with no field, using the PLCC mount on the Mixing Chamber and showed a clear superconducting transition (this is shown in Figure 5.5). The resistance value is invariant to illumination, suggesting the end-resistance measurement is a measurement of the contact alone. This was also checked over a series of measurements at 4.2 K including simultaneous measurement of contact resistance and 2DEG properties under μs pulses of red light, as discussed in chapter 4.

In Figure 5.5, the end-resistance of the contact is 26 mΩ above T_C = 0.85 K and the superconducting transition is much sharper, occurring up to 0.65 K. The temperatures depicted in Figure 5.5 are those read out by a SQUID, thermally coupled to the sample on the Mixing Chamber.

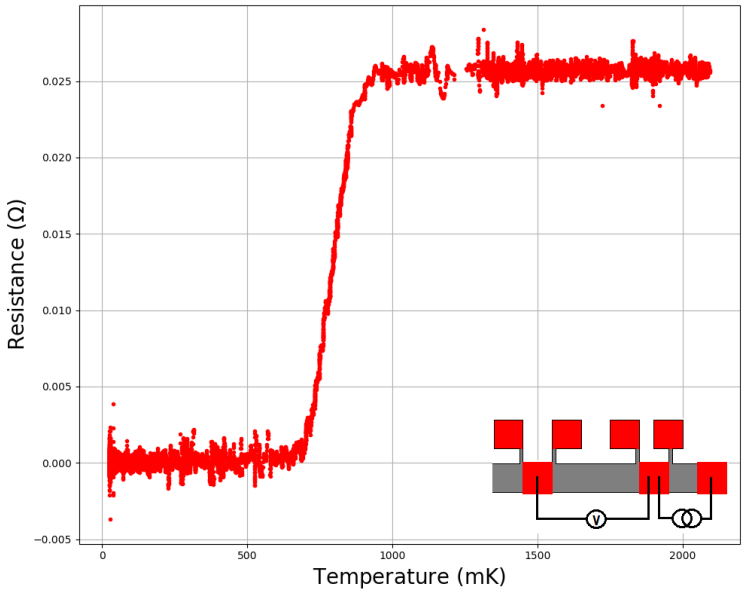

Figure 5.5: Temperature dependence of end-resistance of sample V834 NTLM B 3 cooled on the Mixing Chamber of the ND3 cryostat. This is a measurement of the alloy contribution to contact resistance. The temperature characteristics show a clear superconducting transition under 800 mK.

The result of Figure 5.5 is significant since it shows unambiguously that the superconducting transition occurs in the alloy, as well as that there is a superconducting path available from the top of the contact to the 2DEG. Looking at the morphology of the contacts, described in chapter 3, this highly suggests that the superconductor is that of a gold-based gallium alloy.

5.2.2 Kelvinox Cooldown : Temperature Dependence in Magnetic Field

From the observation of the resistance jump in Figure 5.3, the thermalisation experiment suggesting a violation of Wiedemann-Franz law and investigation of the literature suggesting gold-gallium superconducts, samples were cooled on the Kelvinox, using the 16 T magnet to see the effect of a magnetic field on these samples and find the critical field of the superconducting transition below 1 K. The expected result for a superconductor in a magnetic field is to increase the resistance of the superconductor, making it normal, such that the resistance jump of order 1 Ω is no longer seen.

Methodology for measurements in magnetic field

Two samples of the 4×4 type, one of the wafer W476 from the same batch as the original cooled to ultra-low temperature, annealed in the same conditions and in the same batch and a V834 sample with the optimised annealing conditions and of the same batch as the V827 cooled on the ND3 mixing chamber were cooled on the Kelvinox dilution refrigerator, in a magnetic field.

There is a 16 T magnet on the Kelvinox. Such a large field is achieved by a large number of superconducting coils that need careful calibration to ensure the zero-offset and low-field characteristics do not drift, especially when looking for effects in small magnetic fields and thermally cycling the magnet.

For this experiment, Hall sensors were mounted on the fridge; on the mixing chamber, to check whether the Noise Thermometer of the Kelvinox is indeed in the field-cancelled region, and also a sensor was mounted near each sample in the adapter to make sure that the field within the magnet bore's radius does not vary.

A 2DEG is usually placed in a perpendicular magnetic field for transport measurements, inducing further confinement due to the Lorentz force; the well known Quantum Hall and Shubnikov-de Haas effects are realised in the transverse and longitudinal resistance of a sample, respectively.

The primary aim of measuring these 4×4 devices was to determine the conditions of superconductivity breaking in the contact resistance to samples

identical to the one on the ND3 immersion cell cooled to ULT. The 2DEG resistance being in series needs to be investigated as well, as contributions of the longitudinal magnetoresistance can disguise the measurement. To achieve a comparative trace between different fields, data was offset to the zero-field value and a decrease in the jump is seen as the sample is cooled down with increasing field. At the point Shubnikov-de Haas oscillations begin, it is difficult to extract what contribution is from the 2DEG and what from the contacts and therefore no higher field data than that of the onset of the oscillations is presented.

For measurements in a perfectly parallel field ($\theta = 0$), there should be no Hall coefficient, unless the sample is slightly misaligned, with a factor $\sin(\theta)$ arising in magnetoresistance [120, 121]. The expectation of a thin superconduccting film in parallel field is that the field required to break this superconductivity is higher, due to the smaller area available for the creation of vortices [122].

Low-current (up to 1A) sweeps of the magnet were taken using a K2400 SMU and a Yokogawa 7561 DC current source. Larger field sweeps were taken using the National Instruments magnet power supply (which is able to drive the full 16 T field).

A large effect on the resistance of the 2DEG is seen, even at very low fields. This effect is the longitudinal magnetoresistance as observed in the Shubnikov-de Haas effect and is temperature dependent, with the onset of the oscillations beginning at lower fields at colder temperatures.

For this reason, the total resistance of the sample at a magnetic field increases. For the purposes of presenting the results and noticing the subtle transition, the sweeps presented in Figure 5.6 have the resistances offset to the zero-field resistance value.

Similarly, for the V834 4×4 sample in parallel magnetic field, the field required to make the superconductor normal is larger (about a factor of 4), Figure 5.10. The traces show a large linear dependence, due to a slight misalignment to field (of about 3°), which adds a Hall slope to the magnetoresistance trace of the parallel field sample. The sweeps of Figure 5.10 are offset to the zero field total resistance value also.

This observed dependence on orientation (perpendicular vs parallel magnetic field) is consistent with what is expected from a thin-film superconduc-

tor such as an electrical contact. Superconductivity breaking relates to the amount of created vortices of the electron pairs and in the parallel direction of a thin-film there is less total flux and area for the vortices to develop, such that a larger field is required to break the superconductivity mechanism of Cooper pairs [122].

V834 shows a singular and much sharper transition than W476. This can probably be attributed to cleaner fabrication conditions, producing a cleaner or "better" superconductor. The variation in the positive slope at lower temperatures past transition, is also consistent with the Kondo effect in gold, with varying degrees of impurities [118, 119, 123].

W476 perpendicular field

Figure 5.6 shows the effect of a perpendicular field on the cooling of the W476 sample. V834 transition shows a single transition, as expected from a 'clean' superconductor, while that of W476 shows two jumps, consistent with a type II superconductor composed of mixed states. This difference is most likely attributed to differences in the fabrication processes of these two samples rather than significant difference between the wafers or materials used. The W476 sample was fabricated using a eutectic slug in a common evaporator, while the V834 uses the layered technique in a dedicated evaporator, avoiding cross-contamination with other devices and materials.

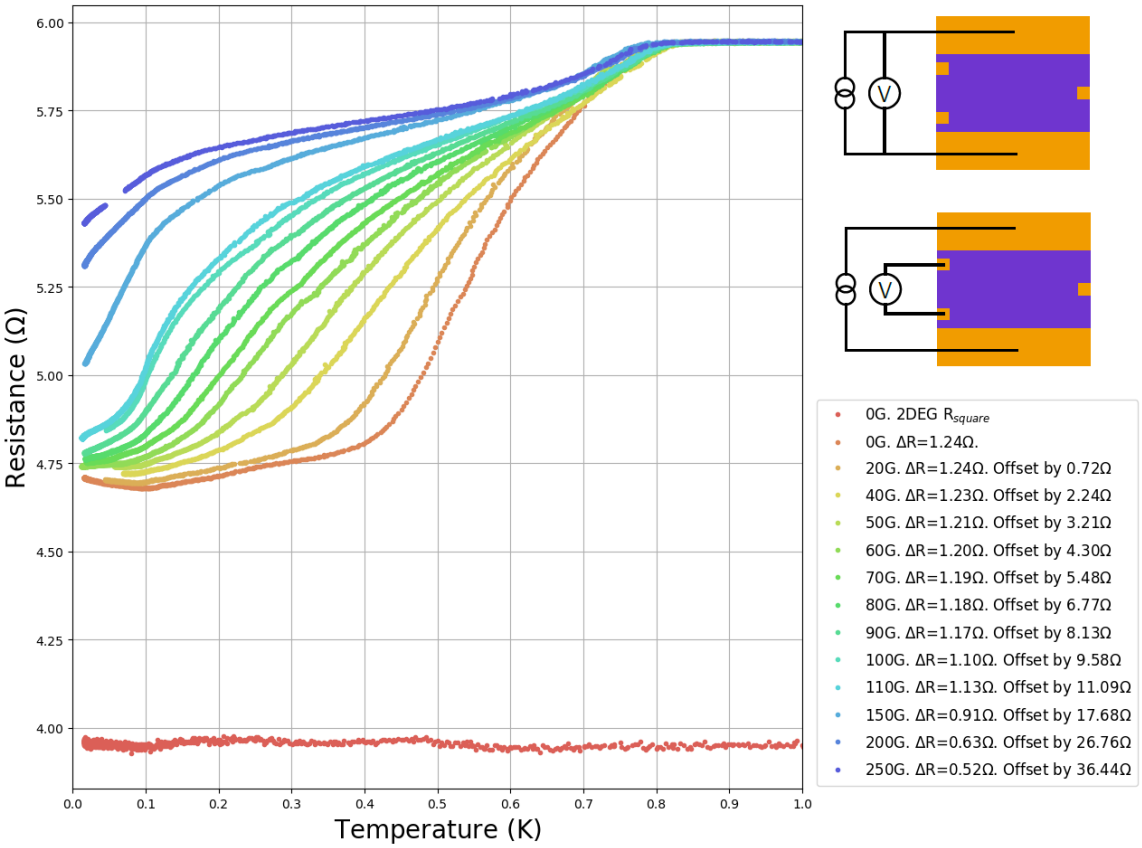

Figure 5.6: Temperature dependence of illuminated 4×4 W476 B sample cooled on the Kelvinox in a perpendicular magnetic field. The two dimensional electron gas resistance alone is plotted for comparison. Data is offset to the zero field value of the resistance, to remove contribution of the 2DEG magnetoresistance in the perpendicular field. The resistance per square of the 2DEG is plotted at zero-field; note the lack of jumps in this temperature dependence.

A complication arises from measuring the sum of contact resistance and the 2DEG contribution in a magnetic field. At low temperatures Shubnikov-de Haas oscillations begin early for a high mobility sample such as ours (order 3×10^{11} cm^{-2}) thereby contributing to the 2DEG magnetoresistance such that the traces of Figure 5.6 had the zero-field contributions of 2DEG and the contact resistance of the source-drain subtracted. The same broad transition is seen at around 0.8 K to 0.4 K in the zero-field case and when field was increased to approximately 400 Gauss R(T) became approximately linear.

At higher temperatures, the maxima and minima of the Shubnikov-de Haas measurements as well as potential drift of the magnetic field complicate the measurement, such that each trace requires a calibration of the magnetic field dependence before it is measured. Sweeps were taken at base (before warming) and 1 K temperatures before each cooling curve measurement.

Similarly to the source-drain data of Figure 5.6, temperature dependence of the voltage probe contacts is shown in Figure 5.7.

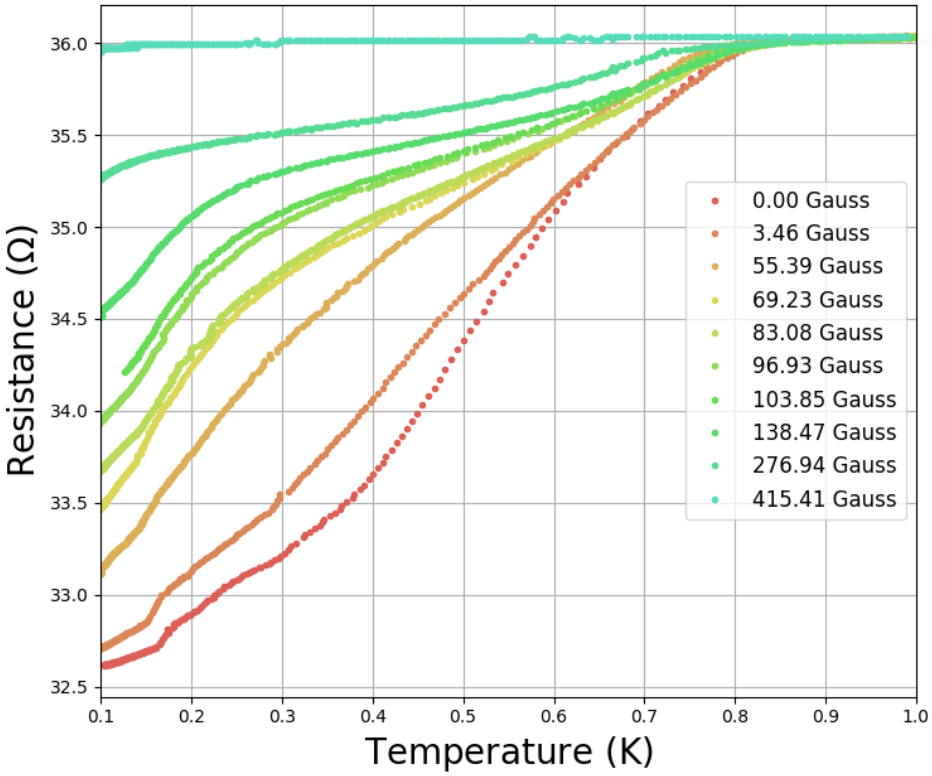

Figure 5.7: Temperature dependence of the voltage probe (200μm $\times$ 200 μm) contacts in applied perpendicular fields for the W476 4×4 B sample, in the dark. Curves offset to the zero-field value for clarity.

Figure 5.8 shows the temperature dependence of the 200×200 contacts of the W476 sample in constant perpendicular magnetic field after illuminating the sample to saturation. Note that the superconducting jump in this case is of the order of 3 Ω as estimated by the characterisation of the test devices for this recipe for contacts of the same size. The magnitude of the jump is the same in both cases dark and flashed.

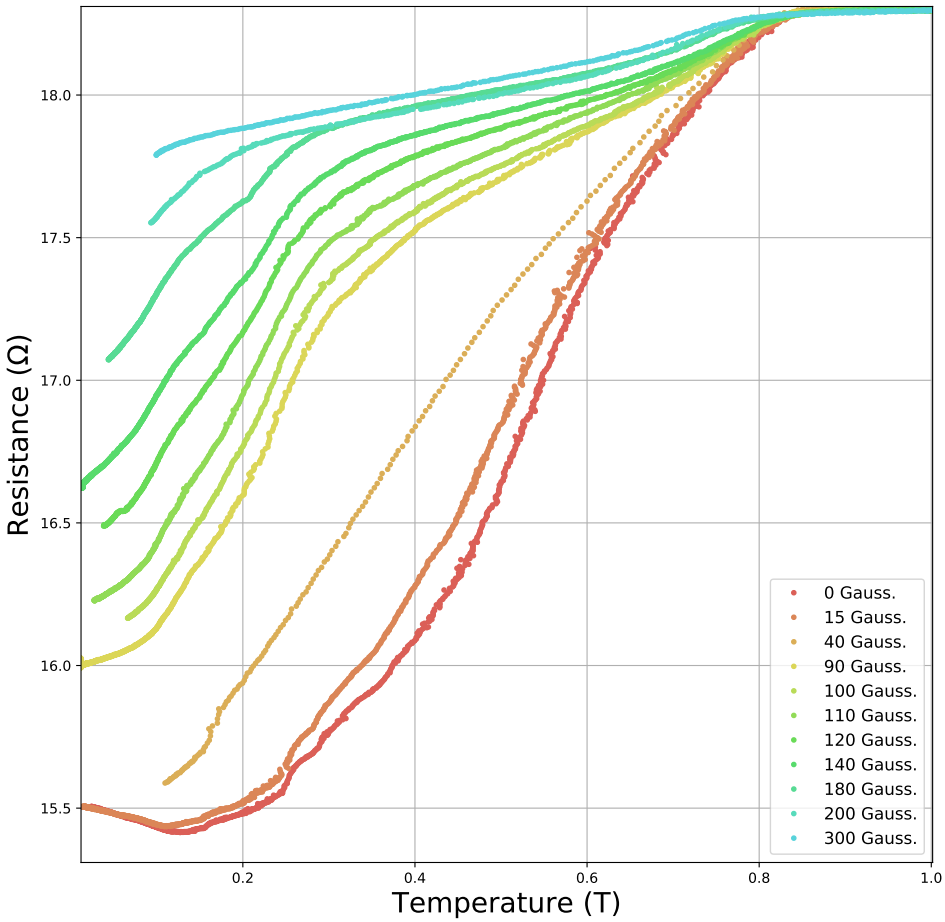

Figure 5.8: Temperature dependence of 200×200 contacts of illuminated W476 sample, in constant perpendicular magnetic field. The transition is still at the same temperature.

Figure 5.9 shows the temperature dependence of the 2DEG at constant low perpendicular magnetic field. The 2DEG is temperature-independent below 1 K, but strongly dependent on field due to the well-known Shubnikov-de Haas effect. At low temperatures, the oscillations onset earlier, due to less damping from electron-phonon scattering.

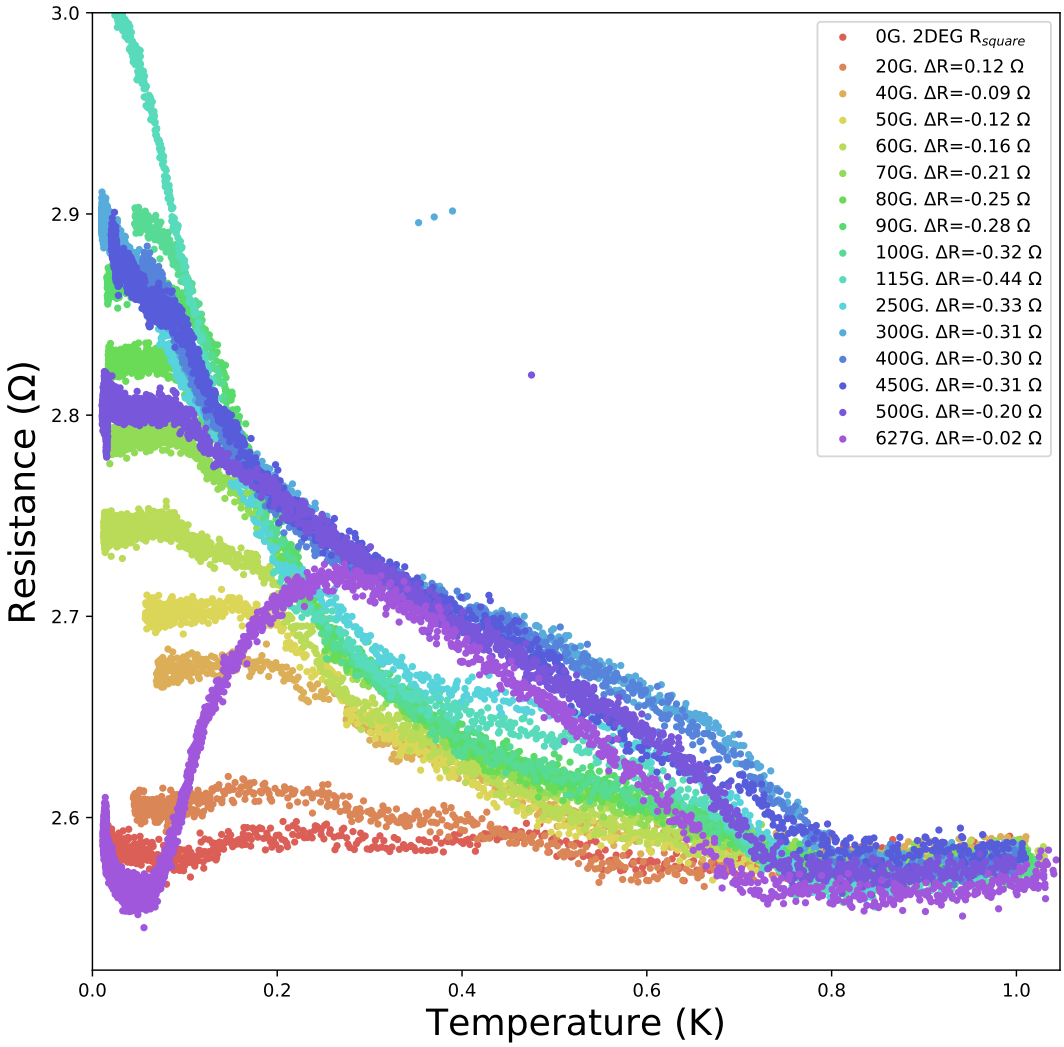

Figure 5.9: W476 4×4 temperature dependence of the 2DEG measured 4-terminally at low fields. Sweeps are aligned at the zero-field value, although as seen by the offset ΔR, this change is minute. The oscillatory behaviour is due to the temperature dependent onset of the SdH oscillations.

V834 parallel field

The V834 4×4 sample was cooled at the same time as the W476 4×4 in parallel magnetic field. There was a complication with drain contact (I^-) in this run (large contact), such that temperature measurements using it were not optimal. Traces taken on the V834 sample where of the two 200 μm × 200 μm contacts normally used to probe the 2DEG. These on-mesa contacts otherwise resemble the NTLM device's contacts so the expectation is their flashed resistance to also be of the same order, $3 - 5\ \Omega$.

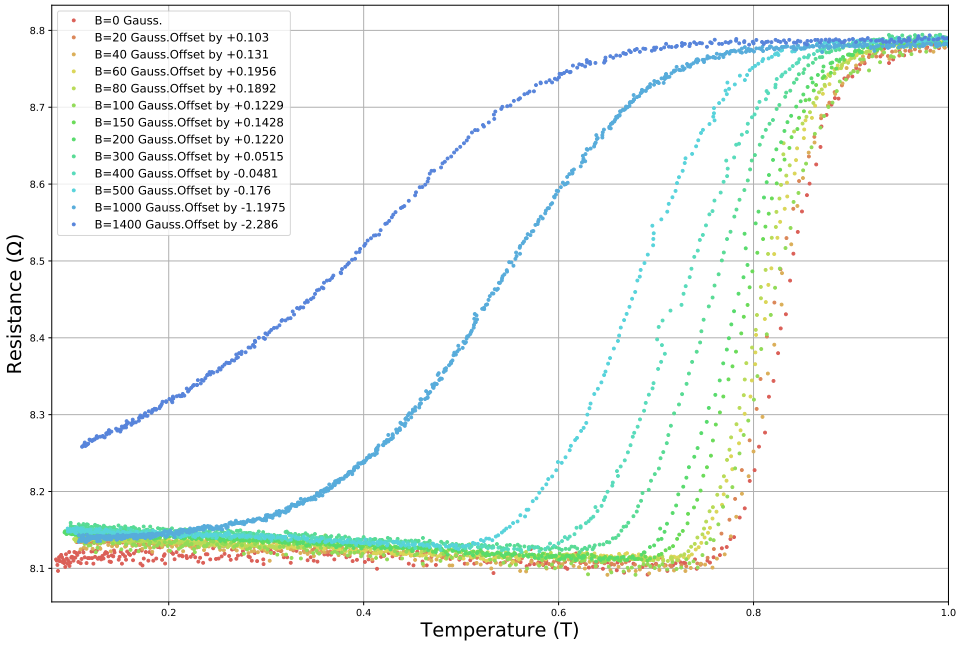

Figure 5.10: Temperature dependence at fixed parallel $\overrightarrow{B}$ field, of the current I^+ to V^- voltage contacts of the illuminated V834 4×4 sample. At sufficient field, R(T) becomes approximately linear.

The magnetic field required to break the superconductivity, Figure 5.11, in parallel magnetic field is larger, this is an asymmetry consistent with what is expected from superconductivity, the ohmic contacts resemble a thin-film.

Plotting the mid-points of these transitions against the applied field, gives a superconducting critical field of 0.2 T for 0.3 K (past T_C), as in Figure 5.11.

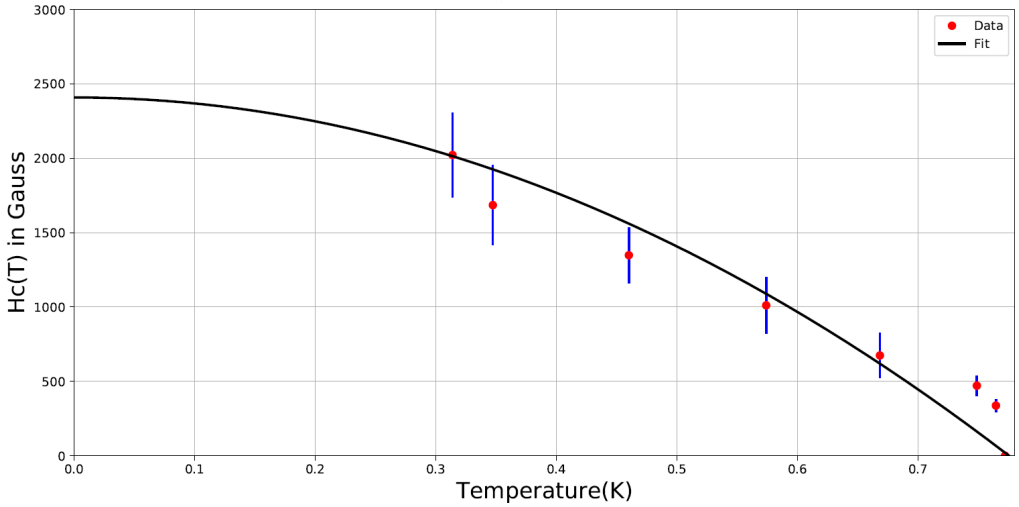

Figure 5.11: Field dependence of the midpoint of the superconducting transition of V834 4×4, in parallel field.

Critical Current Measurements

Another way to break superconductivity is introducing a large-enough current through the sample such that superconductivity is not possible in this system due to the formation of vortices. Once a current of enough magnitude - the critical current, I_C - is reached, the superconductor becomes normal.

A measurement of critical current was attempted for both samples on the Kelvinox, to compare the findings to the critical field. This measurement does not depend on orientation with respect to magnetic field and therefore is a desirable measurement to demonstrate equivalence between the two superconducting samples. However, critical-current measurements in this system are ambiguous, as the 2DEG is known to be sensitive to AC heating currents and in series with the ohmic contacts in the measurement. Therefore the magnitude of this current in the sample can heat the 2DEG first, obscuring a direct measurement of critical current.

A current of 500 μA was enough to flatten the cooling trace in both samples in the range 1 K to 0.1 K. At such a high current however, this is more likely due to heating the device.

5.2.3 Superconducting properties

The critical temperatures for the superconducting transition and critical fields were measured using the 4-terminal technique, with T_C estimated as the midpoint of the transition of the curve.

There is clear dependence on orientation with respect to field, comparing the critical fields obtained for the two very similar wafers W476 (Figure 5.6, perpendicular field) and V834 (Figure 5.2.2, parallel field) in two different orientations in field, an asymmetry often seen in superconductors.

Careful measurement of the 2DEG needs to be done first, from Shubnikov-de Haas traces, since there are low-field effects in the resistance of the sample before the onset of the oscillations. The resistance measured in this case from the 4×4 sample includes contribution of the longitudinal resistance of the two dimensional electron gas and the contact resistance of the source-drain (to first order these can be assumed the same, from symmetry checks it can be determined that they are very similar, for a homogeneous 2DEG).

An applied perpendicular magnetic field, saturates the sample faster, however, there are complications in the measurement, in that the 2DEG resistance is also contained in the measurement (due to the device's geometry), such that this effect needs to be accounted for in the field chosen to take a temperature dependence trace, as that contribution would appear when cooling below 1 K at earlier fields. Furthermore, for the parallel direction of field a small misalignment can cause a large linear magnetoresistance to appear which is due to the Hall effect from the not perfectly aligned sample. The value of saturation, H_C in perpendicular field is around 300 Gauss, while critical field is 2400 Gauss in the parallel direction, past T_C.

The temperature dependence of the vertical resistance, R_V was first measured on the ND3 cryostat on an NTLM sample, with no field, showing a clear superconducting transition. This resistance is the resistance of the alloy contribution to the contact resistance. Measured carefully and over long timescales for accuracy, the resistance value does not change upon illumination. This was also checked over a series of measurements at 4.2 K.

In Figure 5.5, the end-resistance of the contact is 26 mΩ above $T_C = 0.85$ K, the superconducting transition is relatively broad and occurs up to 0.65 K. The temperatures depicted in Figure 5.5 are those read out by a SQUID, thermally coupled to the sample on the mixing chamber. It is

also worth noting that, contrary to the total sample resistance, this alloy resistance measured by the end-resistance measurement is constant above 1 K. Thermalisation for this experiment is not particularly difficult as the temperatures needed to reach to see this transition are the warmest edge of a dilution fridge's working temperature range, the results can be replicated by using Y-bonds and dedicating 4 fridge lines to an ohmic contact.

5.3 Alloy Resistance at Low-Temperature

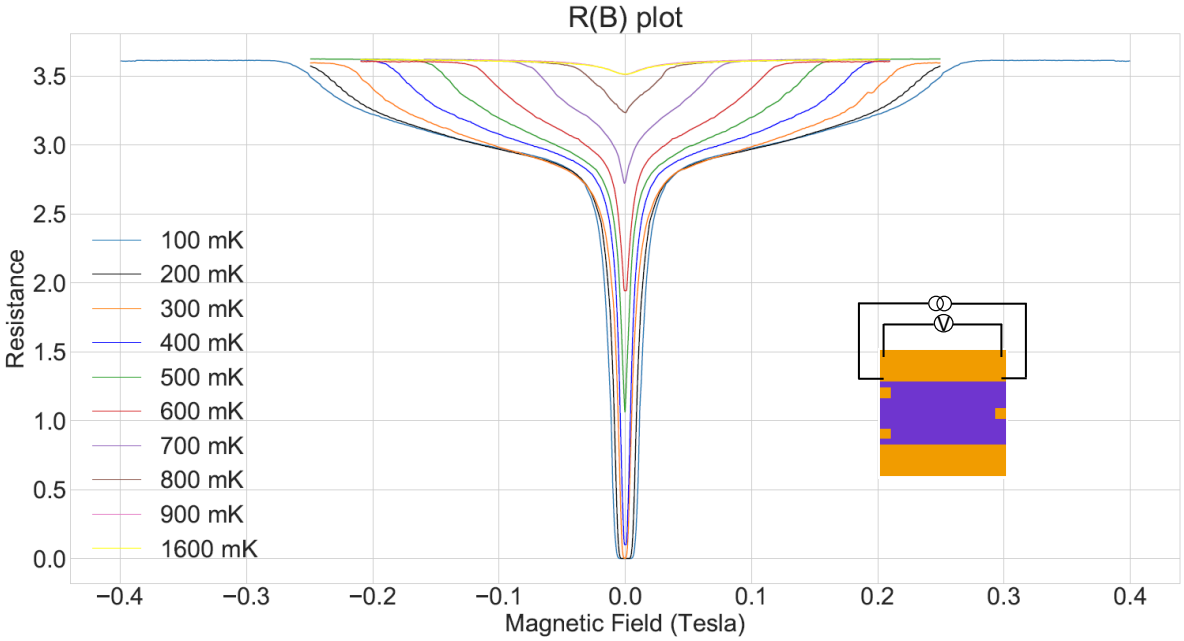

Figure 5.12: Magnetoresistance of the 4T resistance of the top of the ohmic contact at fixed temperatures. Data from the original W476 4×4 sample cooled on the ND4 cryostat in perpendicular field.

Extra bonds were placed on the large contacts of the W476 4×4 sample as depicted on the insert of Figure 5.12, in order to measure the temperature dependence of the resistance of the top of the contact. A PCB adapter was designed in order to connect Y-bonds to the sample which remained in the immersion cell lid, so that no extra bonding to the sample was required,

therefore minimising potential damage from handling and remounting to the dry fridge, ND4.

The expectations from the end-resistance measurement results highly suggested that the measurement is the vertical resistance of the alloy to the semiconductor and since it is superconducting, a measurement of the resistance along the top was expected to show the same superconducting behaviour if the contact at the top is continuous.

The traces of Figure 5.12 show magnetic field data taken at set temperatures, showing that the field required to break the superconductivity is 30 mT, as was the same from the previous measurement on the Kelvinox of the W476 device from the same batch. An additional inflection point is seen, in these sweeps, with a critical field of over 0.15 T. This measurement further verified that the top of the contact is indeed continuous, with the superconducting compound being the gold-rich alloy at the top region of the contact, which extends throughout the contact to the 2DEG.

The resistance of the alloy in the normal condition is 3.5 Ω, the effect of field is dependent on temperature, with the field required to break superconductivity being 30 mT, the two inflection points suggest two phases of superconductors as was determined by the 'bumpy' temperature dependence of the source-drain measurement of the W476 4×4 sample cooled on the Kelvinox.

Figure 5.13 shows the temperature dependence at set perpendicular magnetic fields of the sheet resistance of the ohmic contact. The critical magnetic field is about 30 mT (300 G) as was determined by the source-drain measurement for a perpendicular sample. The importance of this measurement is in showing the superconducting transition to be located at the contact, without the magnetoresistance of the 2DEG in series, complicating the measurement. It shows the contact is also electrically continuous at the top and, combined with the end-resistance data it conclusively shows this common alloy to superconduct with the superconducting path extending from the top to the 2DEG. This result is consistent with the morphological studies of the samples described in chapter 3 and what is expected from a gold-based superconductor. The resistance of the ohmic contact remained unchanged by illumination.

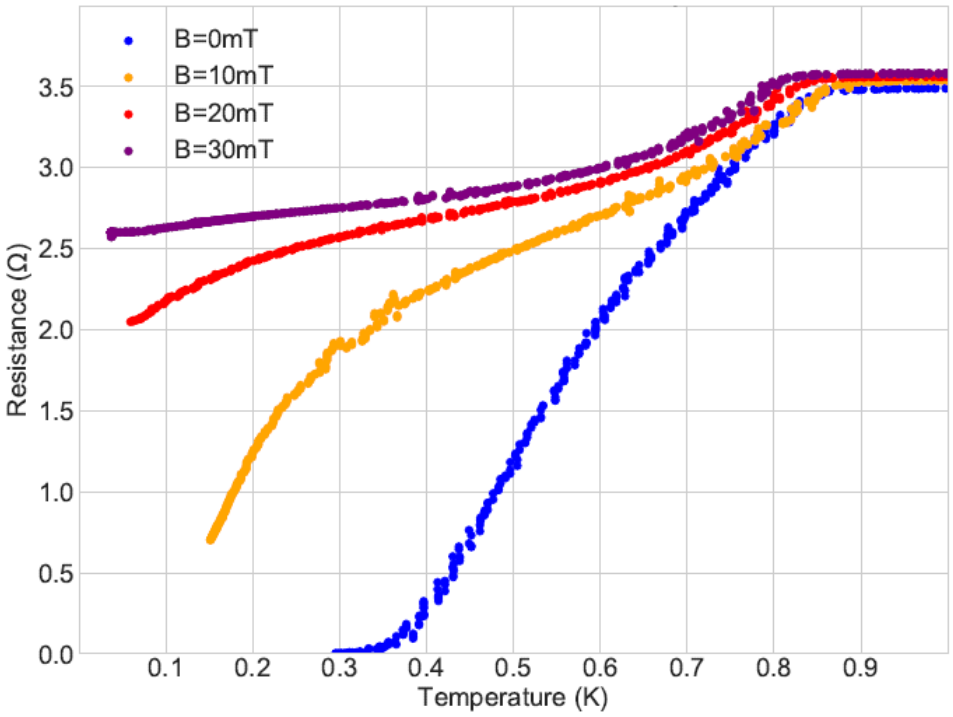

Figure 5.13: Temperature dependence of resistance of ohmic contact of W476 4×4 sample measured 4-terminally along the top, on ND4, in applied constant perpendicular magnetic field. The traces are identical to those of the 4×4 measurements on the other fridges described previously, without the resistance of the 2DEG in series. The contact is shown to superconduct. Further measurements have shown the curve to flatten, even at the top inflection point at over 150 mT.

Superconductivity in W476 samples

The W476 4×4 B sample was cooled on the ND3 immersion cell, achieving the lowest reported electron temperature of a 2DEG so far, by a current sensing noise thermometer coupled to a contact of the device. A reproducible resistance jump was seen in all ND3 runs from 2016-2019, which was attributed to a superconducting transition in the resistance of the contact. Measuring the sheet resistance of the ohmic contact at the top in a perpendicular magnetic field, a superconducting transition was observed with multiple inflection points, due to the ohmic contacts becoming superconducting, with a critical field of 0.03 T at 0.1 K.

A direct measurement of ohmic contact sheet resistance at the top showed this superconductivity to be a property of the contact conclusively, as in the

plot of Figure 5.13. Comparing this temperature dependence of the ohmic contact sheet resistance with that of traces taken on the Kelvinox at zero-field, of a device from the same batch, as in Figure 5.6 and that of ND3, Figure 5.3, the same transition is seen over the exact same temperature range of 0.8 → 0.4 K. The comparison is shown in Figure 5.14.

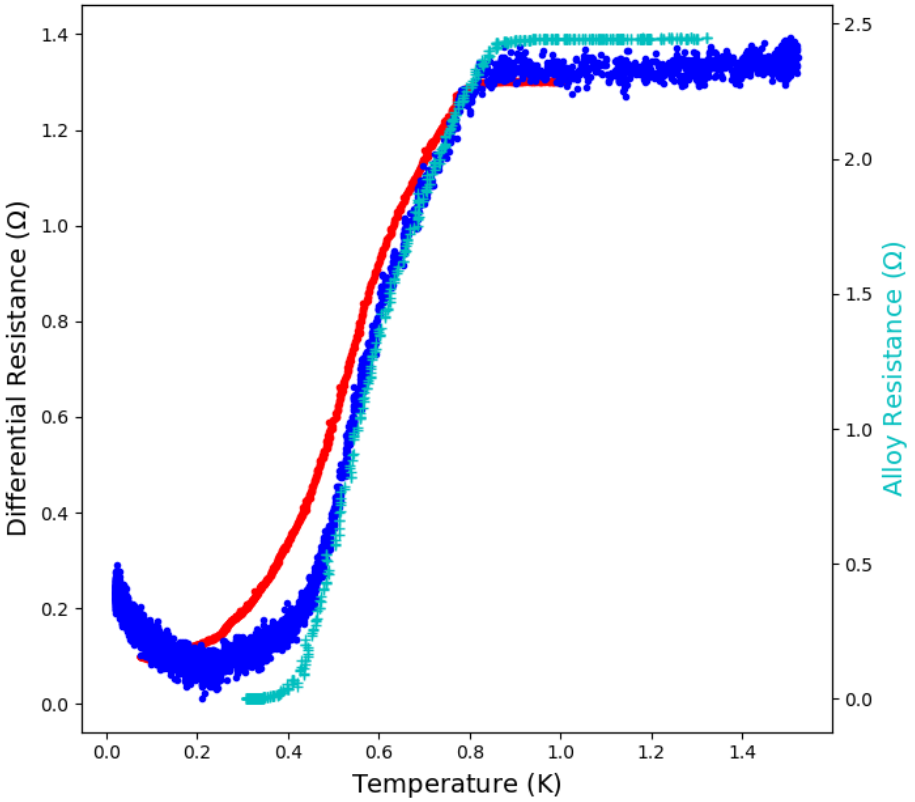

Figure 5.14: Comparison of W476 4×4 samples on ND3 (in blue, offset by 7.5 Ω) and Kelvinox (in red, offset by 8.0 Ω) cryostats and the resistance of the ohmic contact (cyan) measured along the top on the ND4 cryostat. The transitions are identically broad, with the 4-terminal measurement of the alloy resistance along the top conclusively showing the contact to be continuous along the top and superconducting. A Kondo effect is seen at low temperatures when measuring the total resistance of the samples with the 2DEG in series (I^-:NT), as expected from gold containing impurities.

Magnetic field sweeps show the inflection point at higher temperature (0.8 K) to completely flatten at a field above ∼0.15 T (Figure 5.12), suggesting multiple phases of superconductor in the alloy. Breaking of this second

inflection point was obscured by the onset of oscillations in the initial measurement of the total resistance of the sample in perpendicular field.

Superconductivity in V834/V827 samples

Samples fabricated in wafers V834 and V827 showed a much sharper transition, as on Figure 5.5 and Figure 5.10. This is attributed to cleaner processing, using a dedicated evaporator and different fabrication technique, a layered annealing of the alloy instead of using a standard eutectic 'slug' (pellet) as in the case of W476 samples.

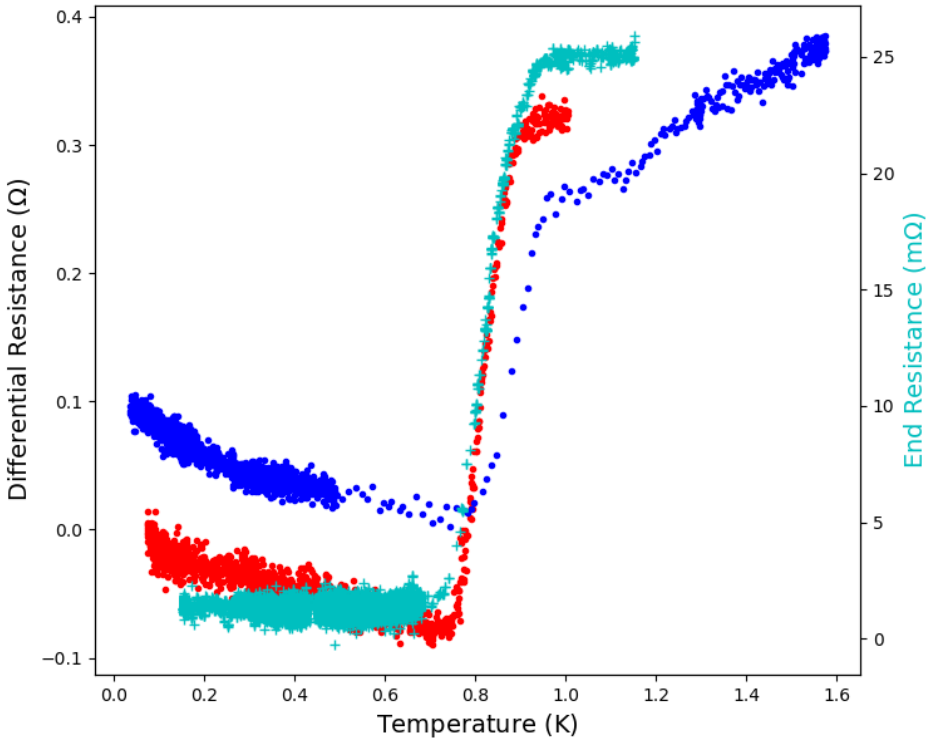

Figure 5.15: Comparison of transition in V-wafers. Differential resistance of two 4×4 samples: in red, V834 with a jump of $\Delta R = 0.32\ \Omega$ (13 Ω subtracted) and, in blue, V827 ΔR=0.24 Ω (6 Ω subtracted). Both 4×4 samples are from batch γ, fabricated under the same conditions, using the same recipe. The end-resistance of V834 NTLM β sample is shown in cyan. The resistance jump in all cases is sharper than that of W476 devices indicating a cleaner superconducting transition, while the linear Kondo effect when measuring with the 2DEG in series is also indicative of a smaller amount of impurities in the superconducting alloy.

The sharper resistance jump in the range of ∼1→ 0.8 K, Figure 5.4 indicated that this effect is not dependent on the wafer used, at least for the very similar standard 2DEG depth (90 nm) wafers used in this work. Figure 5.15 compares the transition seen on the V827 (ND3) and V834 (Kelvinox) 4×4 samples and the end-resistance of a V834 NTLM sample showing a superconducting transition in the same temperature range.

The resistance jump occurring at the same temperature range shows that it is indeed a property of the alloy, while the end-resistance is the resistance of the thin alloy that is the ohmic contact in the vertical direction. The end-resistance measurement further indicates that there exists a continuous superconducting path from the top of the contact to the 2DEG-contact interface, such that this resistance is seen to vanish past transition.

The positive slope past transition at low temperatures seen in both W476 and V-devices suggests a Kondo effect, which has been previously measured in gold [124] and well-known to occur with impurities (mostly iron in the literature) and can have a varying temperature dependence, dependent on the level of impurity [123]. This effect is not measured in the end-resistance because in that measurement the path of least resistance of current flow towards the contact is only measured, so that it will always be zero past transition in a continuous superconducting alloy.

Since the transition is much sharper than the W476 samples, it would be interesting to measure the resistance of the top of this alloy in perpendicular magnetic field to determine a more accurate critical field and estimate the asymmetry of the superconductor in field, to compare with findings from the W476 samples.

Candidate superconductors

There is substantial evidence for various gold-gallium compounds forming in the contact, some of which are known to superconduct and others which have not been investigated as extensively. Ni does not superconduct and is magnetic until annealed over 100°C [92]. When annealed with eutectic AuGe, nickel forms compounds with Ge and is essential for sufficient doping and low contact resistance, as described in chapter 3.

While the reported formation of AuGa/$Au_{1-x}Ga_x$ compounds is highlighted in the literature, it is overlooked that this alloy is superconducting and

therefore ultimately incompatible for low-temperature measurements without magnetic field, without corrections.

Throughout the literature, as described in chapter 3, it is unclear which gold-gallium phase might be responsible for the superconducting transition, β-AuGa is the only phase that has not been reported to superconduct, while α-AuGa [125], AuGa (T_C = 1.24 K) [126] and $AuGa_2$ (T_C = 0.34 K [117] or T_C = 1.21 K [127], depending on pressure; ambient vs over 5 bar, respectively) are known to superconduct.

The literature widely reports the existence of β-AuGa in the contactas necessary for low-resistance [79, 93], however, β-AuGa is unstable above 400°C [93] and there is no mention of other Au+Ga compounds, which in other studies are observed.

There is evidence all these phases exist in a typical AuGeNi contact to GaAs after annealing [61, 77, 79], such that there is a mixture of such Au+Ga phases throughout the ohmic contact, making it difficult to conclude what the most likely candidate is for the observed transition, with the temperature dependence of W476 samples indicating multiple superconducting compounds. It is important to highlight that the conditions under which a contact forms under Rapid Thermal Annealing are chaotic, with little control over processing, in order to fabricate an engineered phase. Considering dilution of Ga into the annealed Au, the percentage of gallium becoming soluble in gold will vary throughout the contact alloy, making it much more likely for the contact to be composed of a multitude of phases, rather than a distinct ordered phase. Upon consideration of the Au+Ga binary system and the wide array of phases available for this temperature range and the rapid thermal anneal by which the contact is formed, it leaves the conclusion that the formation of a single phase is highly unlikely.

Hamilton *et al.* [126] first reported superconductivity in the gold-gallium system. The most detailed analysis of the gold-galium system and their critical temperature is from Hein *et al.* [128], stating that transition widths indicate whether a compound is single phase or not, T_C as well as $\left(\frac{dH_C}{dT}\right)_{T_C}$ increases with gallium concentration in $Au_{1-x}Ga_x$ compounds. The relatively broad transition width on our ohmic contacts compared to a clean step-wise transition as expected from an ideal superconductor, suggests this is a multiple phase superconductor of type II, as is most common for superconducting

alloys [129]. Furthermore, the two different transition widths in the W476 samples and the V-samples suggest a difference in the cleanliness of the superconductor, with the much broader W476 being a more-impure alloy. This is in accordance with the general sample quality and fabrication procedures resulting in a cleaner superconductor in the case of the contacts annealed on V-wafers.

Ohmic Contact Model Including Superconductor

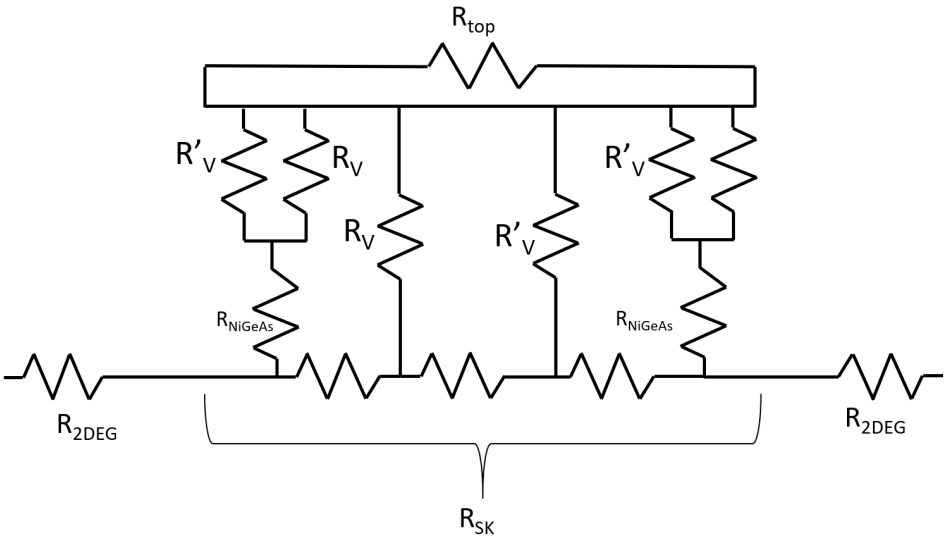

Figure 5.16: Resistor model for contact resistance: superconducting component of the vertical (end) resistance, R_V, in parallel with a possible normal component, R'_V, in series with the (negligible) resistance of the Ni-rich region, R_{NiGeAs} - shorted by a superconducting alloy of 0.3 Ω sheet resistance at the top. For $R_V \to 0$ very little of the resistance under the contact, R_{SK}, is likely to be seen past transition.

Empirically, superconductors above critical temperature typically have high resistance, therefore it is possible that the resistor network switches past T_C conducting favourably through the superconductor and through the normal nickel-rich region before critical temperature is reached. The resistance of the contact at the top is very small and, as determined by the microstructure studies conducted at the Cavendish Laboratory (section 3.3.3), it might be that the contact is a type of superconductor not adhering to the convention

of high-resistance above critical temperature. Gold is a great conductor, therefore, a superconducting alloy of mostly gold would also be of very low resistance. The resistance at the top is of the order of 1 Ω, measured as low as 300 mΩ.

Figure 5.16 depicts a contact model, containing a normal and a superconducting component to contact resistance. R_{SK} is the resistance of the damaged 2DEG under the contact, which in the case of our contacts is the interfacial contact resistance in the alloy-semiconductor interface.

As measured at low temperatures, the end-resistance of the contact vanishes past 0.6 K (Figure 5.15). There exists a continuous path of least resistance from the top of the contacting alloy to the semiconductor interface and superconducts. The end-resistance value above critical temperature is around 30 mΩ. Intuitively, the end-resistance measurement is the voltage dropped due to the alloy alone, such that this resistance is the vertical resistance of the alloy and is small due to the dimensionality of the contact. The NiGe(As) inclusions are considered to not contribute to contact resistance as they are stoichiometric and responsible for doping the substrate (as in the proposed tunneling mechanism in Braslau's work [63]); therefore, it is most likely that the end-resistance, which is measured to vanish, is simply the resistance of the gold alloy with the nickel-rich inclusions in series being of negligible resistance.

Both the vertical and sheet resistance at the top of an ohmic contact superconduct, so the model past transition is one of an impure superconductor, with "normal" inclusions. A future measurement of a device of the NTLM or NTLM-Hall type in magnetic field would give further insight to the contacting mechanism, specifically determining L_t and R_{SK} past transition, with a simultaneous measurement of the contact resistance parameters, R_V, R_C, R_{2DEG} and looking at the magnetoresistance dependence. This is the setup depicted in schematic of Figure 5.17: The I^+I^- resistance is measured on contacts 1 to 2 or 3 to 2, the end and contact resistance are measured on contact 2. The minimum number of bonds is ideally 8. Instead of a Y-bond on contacts 1 or 3, a bond on a voltage probe can also give the resistance per square of 2DEG, without losing any accuracy, since one of the on-mesa contacts (1 or 3) will only be used to inject current.

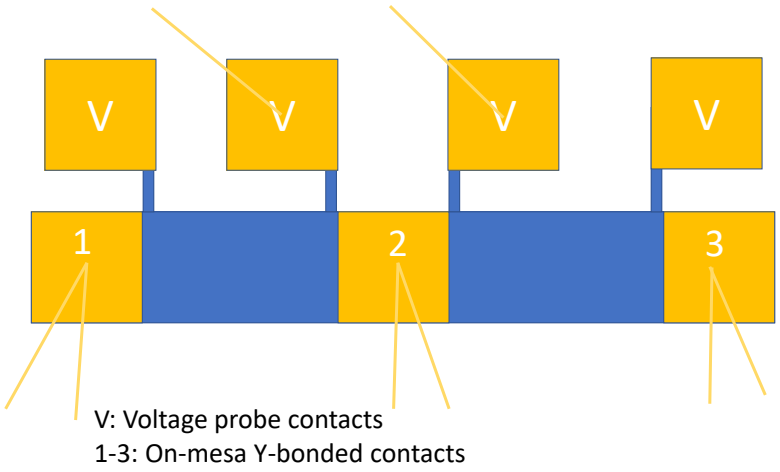

Figure 5.17: Schematic depicting the minimum number of bonds required for a direct measurement of contact resistance parameters at low-temperature, using a device of the NTLM type. The end-resistance can then be measured at contact 2, at the same time the contact resistance is measured. An additional bond on a voltage contact would give the resistance per square of 2DEG, which is desirable.

Solution to superconducting problem

Research has been done with on-chip demagnetisation by the Lancaster group [30], using a magnetic field to achieve nuclear demagnetisation on the electrical contacts to the sample. This has been achieved with a quantum dot device to 10 mK. Since thermalisation is done through leads also in this case, the superconductivity of the contacts in these devices needs to also be considered.

Since the superconductivity arises from gold alloys in the contact, using contacts without gold and ideally using contacts of compounds which are known *not to superconduct* might be useful to explore. There is not extensive research in this field (ohmic superconductivity is an oxymoron), so that a more practical approach would be to cool the sample in a field such that the contacts are not superconducting, which would allow the sample to thermalise and a low electron temperature to be achieved. The perpendicular critical field is low enough that it can be reached with a homewound magnet. Since a noise thermometer will not work in a field, the electron temperature would need to be determined ideally from the amplitude of the longitudinal

magnetoresistance.

Cooling at high fields, even with a purely superconducting ohmic contact, can also make it possible to cool the 2DEG and subsequently isolate the system. The advantage of AuGeNi ohmic contacts to other superconducting contacts would be that they can achieve low resistance in their normal state. This is something that should be looked into in future work, especially since it does not require large modifications to well-established procedure, other than a constant magnetic field to cool the sample. Fractional Quantum Hall studies, or even lower field magnetoresistance studies are well above the critical field of the contact as determined through this work, such that this does not directly inhibit such attempts for low electron temperatures, once low field series resistance past T_C is accounted for. Ohmic contact superconductivity needs to be considered in low field studies studies in GaAs/AlGaAs annealed with gold-based contacts.

From work achieved and described in this study there exist samples with very low contact resistance (< 1 Ωmm) capable of achieving low electron temperatures (in field) which have already been characterised at 4.2 K. This includes gated Hall bars and 4×4 devices which would be good candidates for further attempts at low electron temperatures and show promise for interesting high-field effects. With knowledge of the superconducting transition and optimised contact resistance, cooling in a field will still yield a low electron temperature.

Due to the wide availability of GaAs wafer and gold for evaporation and general fabrication techniques, as well as the relative ease of fabricating such a superconductor (annealing vs more complicated processes such as sputtering) this knowledge could have applications to the fabrication of cheap superconducting components for low-temperature applications.

5.4 Summary

Experiments on contact resistance at low temperatures are presented in this chapter. The initial experiment in the ND3 immersion cell of the W476 4×4 2DEG sample that achieved the lowest recorded electron temperature of a 2DEG device of 1 mK is presented and a jump in the resistance of the sample was observed. A device of similar geometry, using the optimal fabrication

recipe as determined from chapter 4, was cooled on the ND3 mixing chamber and showed a similar jump in resistance. Two devices of identical make to these two devices were cooled on the Kelvinox cryostat to measure the effect of field on the resistance jump.

A measurement of the end-resistance of a test device, showed an unambiguous superconducting transition, therefore the transition can be attributed to the contacting alloy, which is continuous from the top of the contact.

Furthermore, the resistance of the contacting alloy of the original device was measured in magnetic field, conclusively showing this superconductivity to be a property of the contact alone and that it is electrically continuous at the top.

Comparing these findings with the study on contacting mechanism of chapter 3 and the methods of characterisation of chapter 4, it is evident that this must be the Au+Ga alloy and a property fundamental to gold-based contacts on GaAs. Future experiments below 1 K using gold-based contacts on GaAs or GaAs/AlGaAs devices should consider these new findings.

Chapter 6

Quantum Lifetime and 1D Devices: Motivations for Future Work at Low-Temperature

This chapter presents further work at low-temperature, including analysis of the magnetoresistance sweeps at constant temperature for the W476 sample, taken in sequence with the characterisation of the superconductivity in the ohmic contacts on the Kelvinox cryostat, as described in the previous chapter. The quantum lifetime of this device is determined and a relationship of quantum lifetime against temperature is found.

Low-temperature measurements of a gated 4×4 device in the Kelvinox immersion cell are presented and motivations for cooling similar devices in an immersion cell are discussed.

6.1 Quantum Lifetime

Though mobility is an intrinsic characteristic of a device and a good indicator of sample quality, other factors can influence the overall sample quality. One such factor is scattering and through fractional quantum Hall effect studies, which depend strongly on a sample quality and a dissipation-free environment, the quantum scattering time/quantum lifetime τ_q has been proposed as a more appropriate indicator of sample quality.

Mobility can be defined in terms of a transport lifetime, that depends on

the effective electron mass and electronic charge, τ_t [130]:

$$\tau_t = m^* \mu / e \tag{6.1}$$

This lifetime is particularly sensitive to large-angle scattering. The quantum lifetime is another measure of 2DEG quality that is often used in conjunction with mobility measurements to determine dominant scattering mechanisms [131]. Quantum lifetime is different from transport lifetime in that it weights all scattering events equally, while transport lifetime is sensitive only to large angle scattering events [130]:

$$\frac{1}{\tau_q} = \frac{m^*}{\pi \hbar^3} \int_0^\pi |V_q|^2 d\theta. \tag{6.2}$$

The quantum lifetime τ_q is a quantitative way to describe the mean time that a carrier in a conductor remains in a particular momentum eigenstate, before scattering into a different state and losing the initial information completely. Such quantum lifetimes can be extracted from magnetotransport measurements, by Shubnikov de Haas oscillation analysis from a fit to the magnetotransport data and determination of the thermal damping factor. At low fields, the density of states of a 2DEG becomes oscillatory. Isihara and Smrcka [132] derived a functional, phenomenological form for the density of states from which Qian *et al.* [10] determined a phenomenological function for the Shubnikov de Haas oscillations:

$$\Delta R_{xx} = 4R_0 \exp\left(\frac{-\pi}{\omega_c \tau_q}\right) \cos\left(\frac{2\hbar\pi^2 n}{m^* \omega_c} - \pi\right) \chi(T) \tag{6.3}$$

with R_0 being the zero field resistance, $\chi(T)$ the thermal damping factor given by $\chi(T) = (2\pi^2 k_B T/\hbar\omega_c)/\sinh(2\pi^2 k_B T/\hbar\omega_c)$ and $\omega_c = eB/m$.

According to the treatment by Coleridge *et al.* [133, 134] and Qian *et al.* [10] the quantum lifetime can be found by a Dingle plot of the damping factor plotted versus 1/B. Data from the W476 4×4 sample cooled in perpendicular field (section 5.2.2) was analysed according to this formalism.

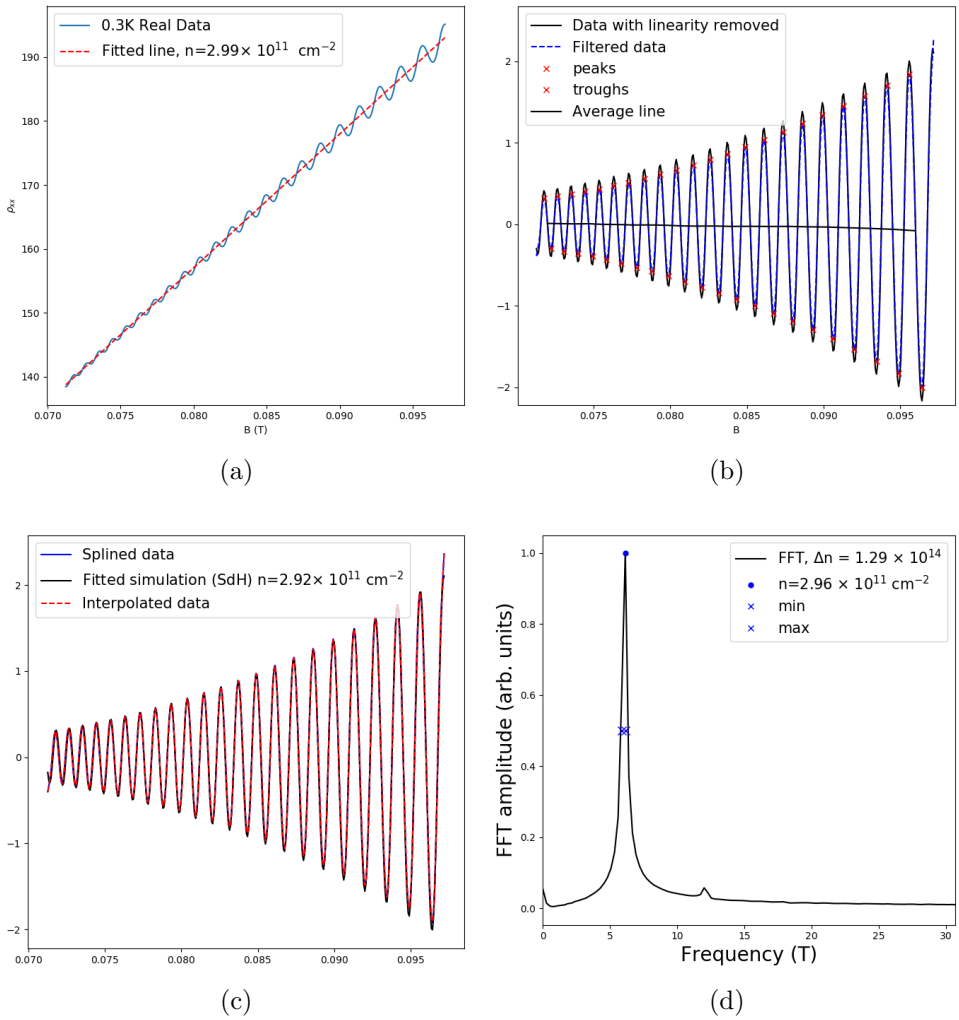

Figure 6.1: Analysis of W476 4×4 B magnetoresistance at 0.3 K: (a) Linear fit to low-field data, carrier density determined from the linear Hall effect. (b) Identifying crests and troughs with linear background removed. (c) Interpolated oscillations from the data and simulated oscillation. (d) Fourier transform of the oscillations to determine the carrier density of the sample.

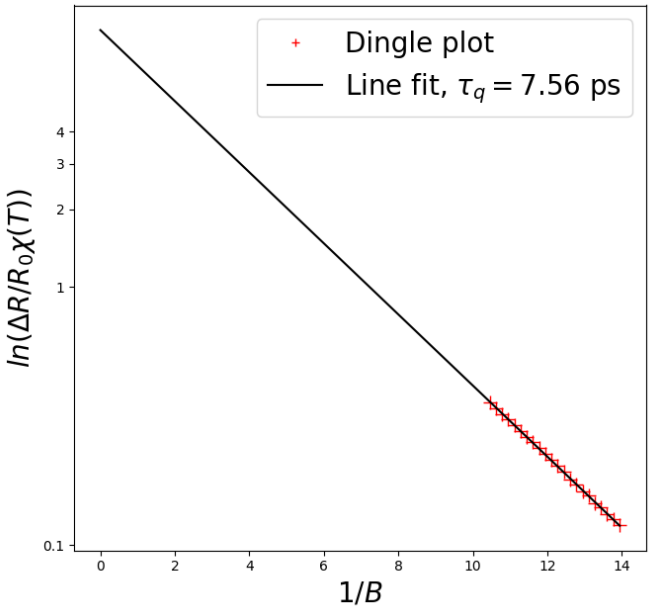

Figure 6.2: Dingle plot from data at 0.3 K as determined from the fit of Figure 6.1 to the Shubnikov de Haas oscillations with linear background removed. Quantum lifetime is calculated from the slope of the linear fit of the normalised amplitude over the thermal damping factor ($\Delta R/R_0\chi(T)$) vs 1/B.

Figure 6.1 shows the magnetic field dependence of the longitudinal magnetoresistance of the W476 sample and analysis done to determine the quantum lifetime of the electrons in the device. The I^+I^- resistance shows oscillations at high enough field, which is the Shubnikov-de Haas effect with the contacts in series. The linear background, arising from the Hall effect due to the contacts spanning the width of the sample, is subtracted and the oscillations become apparent. In order to remove the contribution of the resistance change of the superconducting ohmic contacts, the fit is in a range above the critical field value ($B^{\text{initial}} \sim 0.06$ T). Additionally, a condition for this treatment to hold is before spin-splitting occurs, so the range is kept to low fields and typically just below 0.1 T. Magnetic field sweeps at set temperatures for an ohmic contact of a sample fabricated under identical conditions show an additional inflection point in the superconducting resistance jump with a critical field above 0.15 T (Figure 5.12), this field is higher than the range these sweeps were taken.

The linear fit of the normalised amplitude over the thermal damping

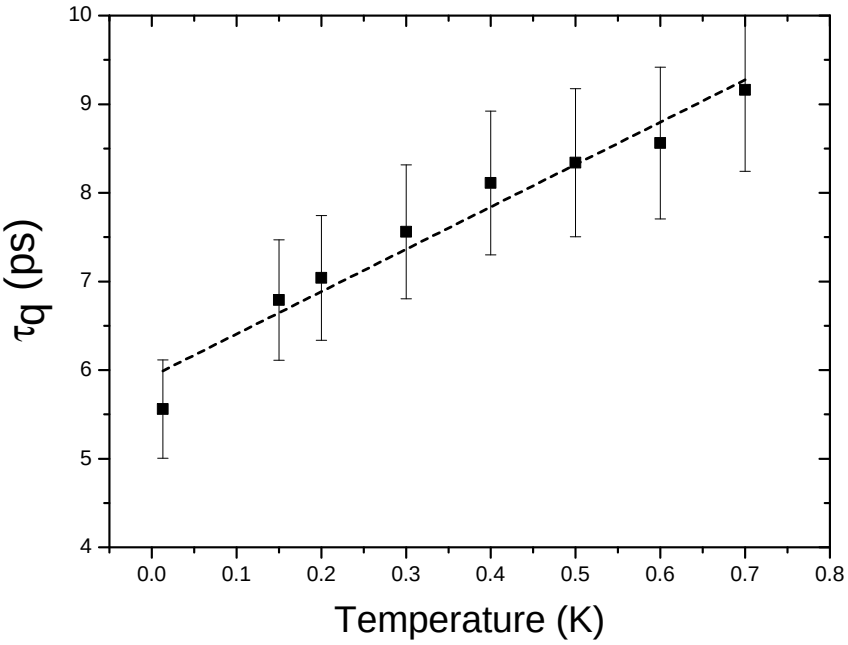

Figure 6.3: Quantum lifetime against temperature as determined from the longitudinal magnetoresistance traces of W476 4×4 B taken at set temperatures. The lifetime is found to decrease linearly with temperature.

factor ($\Delta R/R_0\chi(T)$) against inverse magnetic field, Figure 6.2, is called a Dingle plot, and is a plot used to determine the quantum lifetime. The quantum lifetime is obtained from the slope of the fit. For a homogeneous 2DEG, the y-intercept should be 4 – this is not the case for this sample. Possible explanations might be the geometry of the sample, the difference in measurement technique (with ohmic contacts in series to the measurement) or, more likely, interaction effects which might not be accounted for in the model used for this analysis. If higher field data was taken for these traces, a better understanding and estimate of the carrier density inhomogeneity of the sample would be realised.

Figure 6.3 shows quantum lifetime as determined from different field sweeps at set temperature. The trend is linear, with lifetime decreasing as temperature lowers. For this experiment, samples were mounted using an adapter to the immersion cell, such that they remained in (non-magnetic)

LCCs and therefore the immersion cell was not used to it's full cooling potential. Cooling a V-wafer device, which shows high homogeneity and low-resistance, in the immersion cell and perpendicular field would provide valuable information in interpreting this result.

6.2 1D 4×4 Device at Low-Temperature

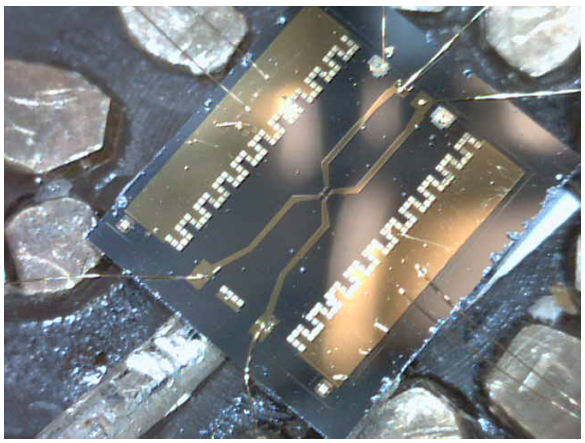

Figure 6.4: Gated 4×4 device, W475 SG1, mounted on the Kelvinox immersion cell lid. The contacts have large crenellations which are made up of smaller contacts, shorted together by subsequent annealing and an extra Au layer deposited by EBL when gates are fabricated. Imaged at RHUL.

Plateaus in conductance become more defined at low-temperature. At a field at which there is filling of Landau levels, the plateaus in quantisation become even more pronounced. The most successful attempt at cooling a 1D device in the immersion cell was an experiment on a 4×4 gated device, W475 SG1, depicted in Figure 6.4.

Figure 6.5 shows Split-Gate sweeps, with the Top-Gate varying the carrier density through the 1D channel in zero-field and a constant 3 T perpendicular field, for the flashed sample in the cell, after filling with ^{3}He. The effect of the persisting magnetic field on the conductance plateaus is readily observed. Figure 6.6 shows the derivative of the conductance traces of Figure 6.5, called the transconductance. Transconductance plots clearly show the filling factor, the number of electron states available in the system ($\nu = 4$ in Figure 6.6).

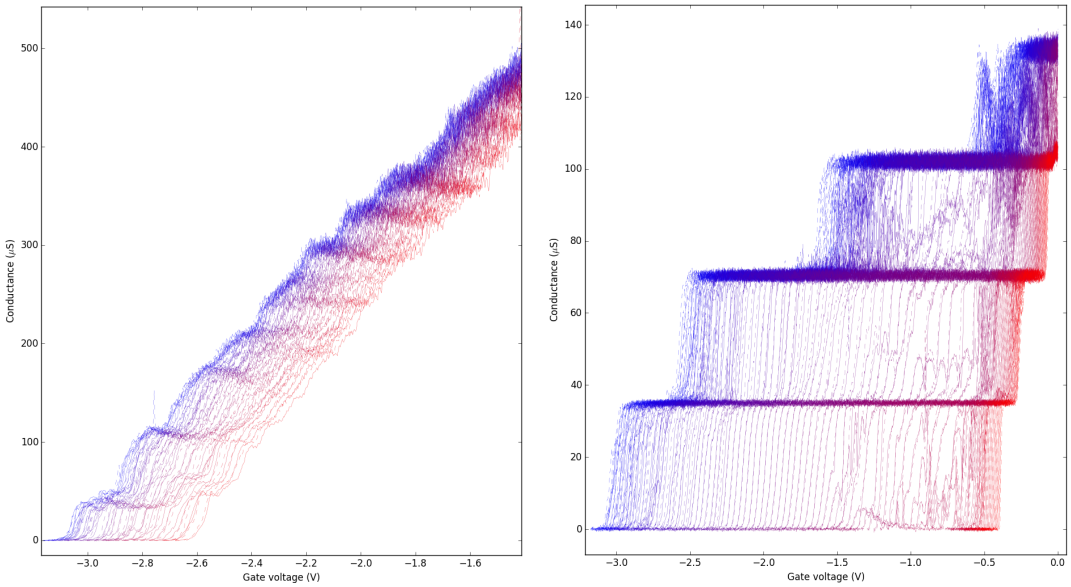

(a) (b)

Figure 6.5: Conductance traces of Split-Gate swept while Top-Gate is stepped by -0.05 V between each successive sweep, starting from 0 V. Clear effect of magnetic field on plateaus (a) zero-field, (b) B ∼3 T (at plateau corresponding to filling factor of $\nu = 4$). The sample is flashed to saturation and the ^{3}He cell full at base temperature. The series resistance (8 kΩ) of the wires and an AIVON low-pass filter is subtracted from this measurement.

The motivation for this experiment was an "anticrossing" seen in transconductance by a past collaborator on a quantum point contact (similarly gated Hall bar) [135]. This effect would be realised as a jump in conductance plateaus and an almost-crossing of the available states in transconductance, an effect not seen in our sample.

Complications on this run arose due to the ^{3}He fill-line to the cell not being fully isolated and in contact with the screened-room, which has it's own dedicated earth (i.e. creating an earth-loop) and ultimately resulting in the early termination of this experiment. After the low-temperature experiment, this sample was unmounted from the immersion cell and re-mounted onto an LCC to recharacterise at 4.2 K. The sample was damaged in the process (e.g. the I^- contact measured infinite resistance to any other contact) after unmounting from the cell-lid and remounting onto an LCC. This was due to mounting with GE varnish directly to the cell, which made the sample

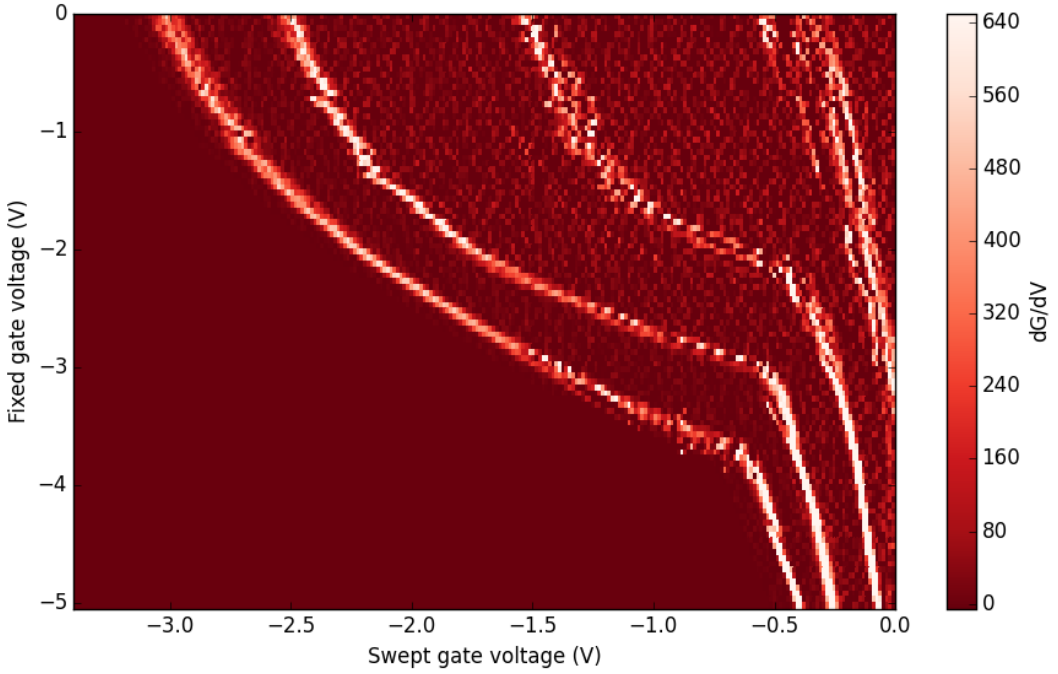

Figure 6.6: Split-Gate swept while Top-Gate is stepped by voltage of 0.05V. Data for this plot is obtained from the derivative of the traces shown in 6.5 (b). The filling factor is clearly shown in transconductance.

difficult to remove and likely contaminated in the process. A subsequent modification to the immersion cell mounting procedure (see also Appendix B) has been the addition of a Cu mounting plate, that allows the sample to be mounted onto the plate and subsequently to the immersion cell lid using a PEEK screw to prevent this in the future.

Previous characterisation of the Split-Gate/Top-Gate of this sample at 4.2 K is shown in Figure 6.7. The contact resistance of each large contact of this sample was estimated at ∼41 Ω in the dark and ∼20 Ω flashed.

Gated devices produced following the characterisation of chapter 4 show promise for similar measurements at low-temperature. Gate-traces at 4 K of the new devices (see Appendix A, A.2) show cleaner characteristics, while the typical I^+I^- resistance of the samples is ∼10 times lower, with sub-Ω contact resistance per large ohmic. Cooling these devices in field and making use of the immersion cell cooling technique would therefore prove fruitful in future experiments.

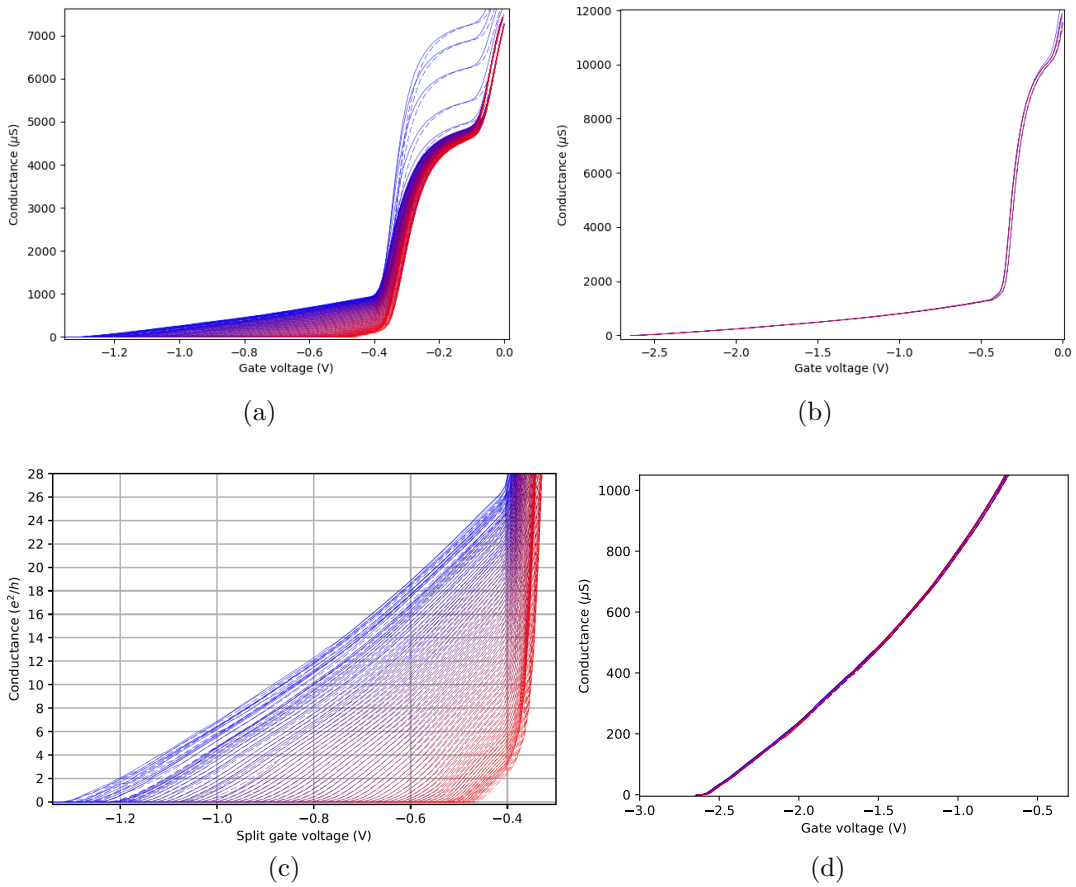

Figure 6.7: Characterisation of gated W475 4×4 device at 4.2 K. (a) Dark and (b) flashed gate-traces. Sweep order is blue → red, dashes are up-sweeps and the Top-Gate is stepped negatively by 25 mV starting from 0 V. The double definition (-0.06 and -0.4 V) is indicative of parallel conduction in the sample. The effect in the dark close to definition (-0.4 V) is typical of a device that has some impurities or charge trapped under the gates and eventually improves, without drift. (c) Zoomed-in dark sweep, plotted in units of $\frac{e^2}{h}$. (d) Flashed gate-trace, zoomed-in to the 1D channel.

6.3 Summary

This chapter provided further analysis on low-temperature measurements of a 2DEG, investigating the quantum lifetime as determined from longitudinal magnetoresistance traces in perpendicular field. The quantum lifetime is determined to range from ∼5 to 9 ps and an approximately linear relationship

with temperature is extrapolated. Results from an experiment on a gated 4×4 device are presented to motivate future work at low-temperature using already existing samples designed and characterised in this work.

Chapter 7

Conclusions

The aim of low electron temperatures led to the observation of an unusual phenomenon, manifest through a resistance jump in temperature dependence. In this study, it was determined that this was due to a superconducting transition in the AuGeNi ohmic contacts of our devices.

The importance of looking at every component of an experiment cannot be overstated. With accurate measurement using Y-bonds, the resistance jump in the 1 K$\rightarrow$ 0.5 K temperature range is readily observed. With knowledge of the magnetic field dependence as well as drawing from the literature and the power of hindsight, following the extensive study of the contacting mechanism and device characterisation, it is concluded that although annealing temperature and composition of the contacting material are significant to achieving low resistance the main contacting mechanism is fundamentally the same and occurs at the microstructure of the sample.

Through a series of experiments, samples from three different wafers, different annealing methods (eutectic and layered) and of various geometries have been observed to superconduct. It is further predicted that similar contacts on GaAs/AlGaAs using annealed gold will superconduct due to the creation of Au+Ga compounds. The sharpness of the resultant superconducting transition will reflect the cleanliness of the superconductor in the width of the transition.

Finally, this superconducting transition in the ohmic contacts is what impeded cooling to the μK regime. It is unlikely that contact resistance can improve to significantly lower value than 1 Ωmm, with contacts of the 4 mm samples being in the order of 0.3-0.6 Ω. However, the infrastructure

is there within the RHUL low-temperature group to provide an ultra-low-temperature platform with the sub-mK regime readily available and capable of measuring an accurate low electron temperature. The critical field of the superconductor is small in the perpendicular direction and can be surpassed using a homemade magnet coil, also allowing for transport measurements on the device. There is merit to investigating the gated devices fabricated using low contact resistance recipe at ultra-low-temperature, as they are capable of reaching the μK boundary and show promising characteristics which will produce interesting results even at low-temperatures, in perpendicular field.

Valuable information for the contacting mechanism would be gained by cooling an NTLM device using Y-bonds in a field, at low-temperature. Specifically this would provide information relating to the contact model past transition, simultaneously measuring contact resistance parameters. The transfer length past transition would be accurately determined and current crowding in the vanishing end-resistance limit could be understood.

Future work should include attempting to find a recipe of ohmic contacts that do not superconduct, avoiding the use of annealed gold onto the GaAs cap of the heterostructure. There are also applications of this discovery which could be used to make SNS junctions, SQUIDs, or indeed other superconducting components for low-temperature work in a relatively easy way.

Bibliography

[1] Z.-M. Wang, L.-A. Wu, C. A. Bishop, Y.-J. Gu, and M. S. Byrd, Physical Review A **88** (2013) 10.1103/physreva.88.032303.

[2] L. W. Smith, W. K. Hew, K. J. Thomas, M. Pepper, I. Farrer, D. Anderson, G. A. C. Jones, and D. A. Ritchie, Phys. Rev. B **80**, 041306 (2009).

[3] W. K. Hew, K. J. Thomas, M. Pepper, I. Farrer, D. Anderson, G. A. C. Jones, and D. A. Ritchie, Phys. Rev. Lett. **102**, 056804 (2009).

[4] B. Antonio, A. Bayat, S. Kumar, M. Pepper, and S. Bose, Physical Review Letters **115** (2015) 10.1103/PhysRevLett.115.216804.

[5] D. M. Basko, I. L. Aleiner, and B. L. Altshuler, Phys. Rev. B **76**, 052203 (2007).

[6] Y. Jompol, C. J. B. Ford, J. P. Griffiths, I. Farrer, G. A. C. Jones, D. Anderson, D. A. Ritchie, T. W. Silk, and A. J. Schofield, Science **325**, 597 (2009).

[7] D. C. Tsui, H. L. Stormer, and A. C. Gossard, Phys. Rev. Lett. **48**, 1559 (1982).

[8] M. Kataoka, C. Ford, G. Faini, D. Mailly, M. Simmons, D. Mace, C.-T. Liang, and D. Ritchie, Physica E: Low-dimensional Systems and Nanostructures **6**, 495 (2000).

[9] B. K. Ridley, Reports on Progress in Physics **54**, 169 (1991).

[10] Q. Qian, J. Nakamura, S. Fallahi, G. C. Gardner, J. D. Watson, S. Lüscher, J. A. Folk, G. A. Csáthy, and M. J. Manfra, Phys. Rev. B **96**, 035309 (2017).

[11] M. J. Manfra, Annual Review of Condensed Matter Physics **5**, 347 (2014).

[12] K. v. Klitzing, G. Dorda, and M. Pepper, Phys. Rev. Lett. **45**, 494 (1980).

[13] J. A. Simmons, H. P. Wei, L. W. Engel, D. C. Tsui, and M. Shayegan, Phys. Rev. Lett. **63**, 1731 (1989).

[14] C. Beenakker and H. van Houten, in *Semiconductor Heterostructures and Nanostructures*, Vol. 44, edited by H. Ehrenreich and D. Turnbull, Solid State Physics (Academic Press, 1991), pp. 1–228.

[15] F. Pobell, *Matter and methods at low temperatures* (Springer, 2007).

[16] F. Bloch, Zeitschrift für Physik **59**, 208 (1930).

[17] E. Grüneisen, Annalen der Physik **408**, 530 (1933).

[18] N. J. Appleyard, J. T. Nicholls, M. Pepper, W. R. Tribe, M. Y. Simmons, and D. A. Ritchie, Phys. Rev. B **62**, R16275 (2000).

[19] N. Balkan, H. Çelik, A. J. Vickers, and M. Cankurtaran, Phys. Rev. B **52**, 17210 (1995).

[20] S. J. Manion, M. Artaki, M. A. Emanuel, J. J. Coleman, and K. Hess, Phys. Rev. B **35**, 9203 (1987).

[21] N. Samkharadze, A. Kumar, and G. A. Csáthy, Journal of Low Temperature Physics **160**, 246 (2010).

[22] Z. Iftikhar, A. Anthore, S. Jezouin, F. D. Parmentier, Y. Jin, A. Cavanna, A. Ouerghi, U. Gennser, and F. Pierre, Nature Communications **7** (2016) 10.1038/ncomms12908.

[23] L. Casparis, M. Meschke, D. Maradan, A. C. Clark, C. P. Scheller, K. K. Schwarzwälder, J. P. Pekola, and D. M. Zumbühl, Review of Scientific Instruments **83**, 083903 (2012).

[24] L. Spietz, R. J. Schoelkopf, and P. Pari, Applied Physics Letters **89**, 183123 (2006).

[25] J. Xia, E. Adams, V. Shvarts, W. Pan, H. Stormer, and D. Tsui, Physica B: Condensed Matter **280**, 491 (2000).

[26] H. van der Vliet, "Platforms for new quantum technologies - addressing the challenges in cooling and exploring the properties of strongly correlated electron systems", English, PhD thesis (Royal Holloway, University of London, 2018).

[27] R. Willett, J. P. Eisenstein, H. L. Störmer, D. C. Tsui, A. C. Gossard, and J. H. English, Phys. Rev. Lett. **59**, 1776 (1987).

[28] D. Bradley, R. George, D. Gunnarsson, R. Haley, H. Heikkinen, Y. A. Pashkin, J. Penttilä, J. Prance, M. Prunnila, L. Roschier, and M. Sarsby, Nature communications **7**, 10455 (2016).

[29] G. Nicolí, P. Märki, B. A. Bräm, M. P. Röösli, S. Hennel, A. Hofmann, C. Reichl, W. Wegscheider, T. Ihn, and K. Ensslin, Review of Scientific Instruments **90**, 113901 (2019).

[30] D. I. Bradley, A. M. Guénault, D. Gunnarsson, R. P. Haley, S. Holt, A. T. Jones, Y. A. Pashkin, J. Penttilä, J. R. Prance, M. Prunnila, and L. Roschier, Scientific Reports **7**, 45566 (2017).

[31] A. T. Jones, C. P. Scheller, J. R. Prance, Y. B. Kalyoncu, D. M. Zumbühl, and R. P. Haley, *Progress in cooling nanoelectronic devices to ultra-low temperatures*, 2020.

[32] K. Gloos, C. Mitschka, F. Pobell, and P. Smeibidl, Cryogenics **30**, 14 (1990).

[33] R. T. Syme, M. J. Kelly, and M. Pepper, Journal of Physics: Condensed Matter **1**, 3375 (1989).

[34] S. Jezouin, F. D. Parmentier, A. Anthore, U. Gennser, A. Cavanna, Y. Jin, and F. Pierre, Science **342**, 601 (2013).

[35] B. Baudouy, CERN Proceedings of the CAS-CERN Accelerator School (2015).

[36] R. E. Williams, *Modern GaAs Techniques, The Science of Microfabrication* (Artech House, 1990).

[37] L. Pfeiffer and K. West, Physica E: Low-dimensional Systems and Nanostructures **20**, 57 (2003).

[38] A. Anselm and R. S. Bank, *What is MBE?*, May 2012.

[39] E. F. Schubert, *Doping in III-V Semiconductors*, Cambridge Studies in Semiconductor Physics and Microelectronic Engineering (Cambridge University Press, 1993).

[40] L. N. Pfeiffer, K. W. West, R. L. Willett, H. Akiyama, and L. P. Rokhinson, Bell Labs Technical Journal **10**, 151 (2005).

[41] K. Berggren and M. Pepper, Philosophical transactions. Series A, Mathematical, physical, and engineering sciences **368**, 1141 (2010).

[42] R. Dingle, W. Wiegmann, and C. H. Henry, Phys. Rev. Lett. **33**, 827 (1974).

[43] L. Chang and L. Esaki, in *Molecular Beam Epitaxy*, edited by B. R. Pamplin (Pergamon, 1980), pp. 3–14.

[44] R. Tsu and J. C. Lofgren, Journal of Crystal Growth **227-228**, Proceeding of the Eleventh International Conference on Molecular Beam Epitaxy, 21 (2001).

[45] *The Nobel Prize in Physics 1998*, en-US.

[46] R. Dingle, A. C. Gossard, and W. Wiegmann, Phys. Rev. Lett. **34**, 1327 (1975).

[47] A. Cho and J. Arthur, Progress in Solid State Chemistry **10**, 157 (1975).

[48] G.-C. Wang and T.-M. Lu, RHEED Transmission Mode and Pole Figures, 73 (2013).

[49] T. Ihn, *Semiconductor Nanostructures Quantum States and Electronic Transport* (Oxford University Press, Jan. 2010).

[50] P. Y. Yu and M. Cardona, *Fundamentals of semiconductors. physics and materials properties* (Springer, 2005).

[51] L. Vegard, Zeitschrift für Physik **5**, 17 (1921).

[52] S. V. Gaponenko and H. V. Demir, "Quantum confinement effects in semiconductors", in *Applied Nanophotonics* (Cambridge University Press, 2018), pp. 52–91.

[53] W. Walukiewicz, H. E. Ruda, J. Lagowski, and H. C. Gatos, Phys. Rev. B **30**, 4571 (1984).

[54] T. J. Thornton, M. Pepper, H. Ahmed, D. Andrews, and G. J. Davies, Phys. Rev. Lett. **56**, 1198 (1986).

[55] J. Gallop, Philosophical Transactions: Mathematical, Physical and Engineering Sciences **363**, 2221 (2005).

[56] C. Rössler, T. Feil, P. Mensch, T. Ihn, K. Ensslin, D. Schuh, and W. Wegscheider, New Journal of Physics **12**, 043007 (2010).

[57] M. Hayne, A. Usher, J. J. Harris, V. V. Moshchalkov, and C. T. Foxon, Phys. Rev. B **57**, 14813 (1998).

[58] S. Prasad, Journal of Applied Physics **89**, 4907 (2001).

[59] N. Samkharadze, A. Kumar, M. J. Manfra, L. N. Pfeiffer, K. W. West, and G. A. Csáthy, Review of Scientific Instruments **82**, 053902 (2011).

[60] N. Braslau, Thin Solid Films **104**, 391 (1983).

[61] A. Callegari, E. Pan, and M. Murakami, Applied Physics Letters **46**, 1141 (1985).

[62] A. M. Cowley and S. M. Sze, Journal of Applied Physics **36**, 3212 (1965).

[63] N. Braslau, Journal of Vacuum Science and Technology **19**, 803 (1981).

[64] J. Crofton, P. A. Barnes, and M. J. Bozack, American Journal of Physics **60**, 499 (1992).

[65] J. B. Gunn, IBM Journal of Research and Development **8**, 141 (1964).

[66] K. Heime, U. König, E. Kohn, and A. Wortmann, Solid-State Electronics **17**, 835 (1974).

[67] G. Robinson, Solid-State Electronics **18**, 331 (1975).

[68] J. B. Gunn, IEEE Transactions on Electron Devices **23**, 705 (1976).

[69] N. Braslau, J. Gunn, and J. Staples, Solid-State Electronics **10**, 381 (1967).

[70] M. Otsubo, H. Kumabe, and H. Miki, Solid-State Electronics **20**, 617 (1977).

[71] W. H. Anderson, A. Christou, and J. E. Davey, 1977 International Electron Devices Meeting, 192 (1977).

[72] P. O'Connor, A. Dori, M. Feuer, and R. Vounckx, IEEE Transactions on Electron Devices **34**, 765 (1987).

[73] W. Patrick, W. S. Mackie, S. P. Beaumont, and C. D. W. Wilkinson, Applied Physics Letters **48**, 986 (1986).

[74] T. S. Kuan, P. E. Batson, T. N. Jackson, H. Rupprecht, and E. L. Wilkie, Journal of Applied Physics **54**, 6952 (1983).

[75] T. C. Shen, G. B. Gao, and H. Morkoç, Journal of Vacuum Science & Technology B: Microelectronics and Nanometer Structures Processing, Measurement, and Phenomena **10**, 2113 (1992).

[76] E. J. Koop, M. J. Iqbal, F. Limbach, M. Boute, B. J. van Wees, D. Reuter, A. D. Wieck, B. J. Kooi, and C. H. van der Wal, Semiconductor Science and Technology **28**, 025006 (2013).

[77] A. Baranska, A. Szerling, P. Karbownik, K. Hejduk, M. Bugajski, A. Laszcz, K. Gołaszewska-Malec, and W. Filipowski, Optica Applicata **43**, 5 (2013).

[78] M. Yoder, Solid-State Electronics **23**, 117 (1980).

[79] N. E. Lumpkin, G. R. Lumpkin, and M. G. Blackford, Journal of Materials Research **14**, 1261 (1999).

[80] E. Kinsbron, P. Gallagher, and A. English, Solid-State Electronics **22**, 517 (1979).

[81] M. Murakami, Materials Science Reports **5**, 273 (1990).

[82] A. Baca, F. Ren, J. Zolper, R. Briggs, and S. Pearton, Thin Solid Films **308-309**, 599 (1997).

[83] T. S. Abhilash, C. R. Kumar, B. Sreedhar, and G. Rajaram, Semiconductor Science and Technology **25**, 035002 (2010).

[84] R. P. Taylor, P. T. Coleridge, M. Davies, Y. Feng, J. P. McCaffrey, and P. A. Marshall, Journal of Applied Physics **76**, 7966 (1994).

[85] H. Goronkin, S. Tehrani, T. Remmel, P. L. Fejes, and K. J. Johnston, IEEE Transactions on Electron Devices **36**, 281 (1989).

[86] A. Valeille, K. Muraki, and Y. Hirayama, Applied Physics Letters - APPL PHYS LETT **92** (2008) 10.1063/1.2912034.

[87] D. Taneja, F. Sfigakis, A. F. Croxall, K. D. Gupta, V. Narayan, J. Waldie, I. Farrer, and D. A. Ritchie, Semiconductor Science and Technology **31**, 065013 (2016).

[88] J. Gyulai, J. W. Mayer, V. Rodriguez, A. Y. C. Yu, and H. J. Gopen, Journal of Applied Physics **42**, 3578 (1971).

[89] M. Ogawa, Journal of Applied Physics **51**, 406 (1980).

[90] A. Piotrowska, A. Guivarc'h, and G. Pelous, Solid-State Electronics **26**, 179 (1983).

[91] R. Bruce and G. Piercy, Solid-state Electronics - SOLID STATE ELECTRON **30**, 729 (1987).

[92] A. Thanniyil Sebastian, R. K. Ch, and G. Rajaram, Journal of Physics D: Applied Physics **42**, 125104 (2009).

[93] M. Murakami, K. D. Childs, J. M. Baker, and A. Callegari, Journal of Vacuum Science Technology B: Microelectronics and Nanometer Structures **4**, 903 (1986).

[94] H. Okamoto, Journal of Phase Equilibria and Diffusion **34**, 174 (2013).

[95] D. Jendrzejczyk-Handzlik, Journal of Phase Equilibria and Diffusion **38**, 305 (2017).

[96] J. Liu, C. Guo, C. Li, and Z. Du, Journal of Alloys and Compounds **508**, 62 (2010).

[97] J. Wang, Y. Liu, L. Liu, H. Zhou, and Z. Jin, Calphad **35**, 242 (2011).

[98] R. P. Elliott and F. A. Shunk, Bulletin of Alloy Phase Diagrams **2**, 356 (1981).

[99] T. Yoshiie, C. Bauer, and A. Milnes, Thin Solid Films **111**, 149 (1984).

[100] T. J. Magee and J. Peng, physica status solidi (a) **32**, 695 (1975).

[101] X.-F. Zeng and D. Chung, Thin Solid Films **93**, 207 (1982).

[102] D. Chung and E. Beam, Thin Solid Films **128**, 299 (1985).

[103] Y. Shih, E. L. Wilkie, and M. Murakami, Journal of Vacuum Science & Technology A **5**, 1485 (1987).

[104] F. Vidimari, Electronics Letters **15**, 674 (1979).

[105] D. K. Schroder, *Semiconductor Material and Device Characterization* (Wiley-Interscience, USA, 2006).

[106] D. P. Kennedy and P. C. Murley, IBM Journal of Research and Development **12**, 242 (1968).

[107] H. Murrmann and D. Widmann, IEEE Transactions on Electron Devices **16**, 1022 (1969).

[108] H. Berger, in 1969 IEEE International Solid-State Circuits Conference. Digest of Technical Papers, Vol. XII (Feb. 1969), pp. 160–161.

[109] H. Berger, Solid-State Electronics **15**, 145 (1972).

[110] A. e. Goetzberger, A. Goetzberger, R. M. Scarlett, and S. D. Clevite Corporation, *Research and Investigation of Inverse Epitaxial UHF Power Transistors : Technical Documentary Report*, English (NTIS Distributor, Palo Alto, CA, 1964).

[111] W. Shockley, Bell System Technical Journal **28**, 435 (1949).

[112] G. K. Reeves and H. B. Harrison, IEEE Electron Device Letters **3**, 111 (1982).

[113] L. Gutai, IEEE Transactions on Electron Devices **37**, 2350 (1990).

[114] L. Gutai, IEEE Transactions on Electron Devices **37**, 2361 (1990).

[115] M. J. Iqbal, Electronic Proceedings in Theoretical Computer Science (2012).

[116] G. Patriarche, E. [Bourhis], D. Faurie, and P. Renault, Thin Solid Films **460**, 150 (2004).

[117] H. R. Khan, Gold Bulletin **17**, 94 (1984).

[118] W. Star, Physica **58**, 623 (1972).

[119] J. Kopp, Journal of Physics F: Metal Physics **5**, 1211 (2001).

[120] R. Dingle, H. Störmer, A. Gossard, and W. Wiegmann, Surface Science **98**, 90 (1980).

[121] A. T. Hatke, M. A. Zudov, L. N. Pfeiffer, and K. W. West, Phys. Rev. B **85**, 241305 (2012).

[122] G. D. Cody and R. E. Miller, Phys. Rev. Lett. **16**, 697 (1966).

[123] M. A. Blachly and N. Giordano, Phys. Rev. B **46**, 2951 (1992).

[124] W. [Haas] and G. [D. Berg], Physica **3**, 440 (1936).

[125] R. F. Hoyt, A. C. Mota, and C. A. Luengo, Phys. Rev. B **14**, 441 (1976).

[126] D. Hamilton, C. Raub, B. Matthias, E. Corenzwit, and G. Hull, Journal of Physics and Chemistry of Solids **26**, 665 (1965).

[127] J. Wernick, A. Menth, T. Geballe, G. Hull, and J. Maita, Journal of Physics and Chemistry of Solids **30**, 1949 (1969).

[128] R. Hein, J. Cox, J. Willis, H. Khan, and C. Raub, Journal of the Less Common Metals **62**, 197 (1978).

[129] A. Abrikosov, Reviews of Modern Physics - REV MOD PHYS **76**, 975 (2004).

[130] S. Das Sarma and F. Stern, Phys. Rev. B **32**, 8442 (1985).

[131] M. J. Manfra, S. H. Simon, K. W. Baldwin, A. M. Sergent, K. W. West, R. J. Molnar, and J. Caissie, Applied Physics Letters **85**, 5278 (2004).

[132] A. Isihara and L. Smrcka, Journal of Physics C: Solid State Physics **19**, 6777 (1986).

[133] P. T. Coleridge, Phys. Rev. B **44**, 3793 (1991).

[134] P. T. Coleridge, R. Stoner, and R. Fletcher, Phys. Rev. B **39**, 1120 (1989).

[135] A. Bayat, S. Kumar, M. Pepper, and S. Bose, Phys. Rev. B **96**, 041116 (2017).

Appendices

A Characterisation of gated devices

Here are shown results of some of the new types of gated devices. Devices presented here are some that are yet to be characterised at low-temperature, but are promising for such measurements on a fridge.

Apart from standard gate-traces, the gated device leakage current must also be characterised, to determine compatibility with ultra-low-temperature. A test done on Split-Gate devices showed that most do not leak to a sufficient scale, with the ones observed to leak having obvious traces that are not desirable - with poor definition, irreproducibility and often do not pinch-off. Leakage current results on Split-Gate devices obtained by taking DC I-V traces are presented in Table A.1.

Table A.1: Gated Hall bar characterisation at 4.2K

Sample	Best Gate	Comments	Summary
V827A	B1D1	Sample re-cleaved due to mesa/gate short	4/6 devices do not leak
V827 B	L1F2. B2D2	More resistive than A	Some gates double definiton after flashing later demonstrated to leak
V827 C	F1L2	Less resistive than B	B1D1 leaking (drift in n), D2B2 leaking
V834 A	L2F1, H1K2	More resistive than V827	L1F2, D2B2 are leaking at 1nA background
V834 B	All	Less resistive sample	2 gates (B1D1,H1K2) leak at fA resolution.

It is noticed that if a gate is fabricated correctly and the yield is good, devices do not leak (at a 0.1 fA background) and the resistance from the top of a gate to an ohmic contact is over hundreds of MΩ, meaning that the gate is reasonably isolated. For lower and measurable resistances, current from applied voltage to the gates is certain to leak to the 2DEG.

Following the success of this test, Split-Gate/Top-Gate devices were fabricated which show great characteristics at 4.2 K.

A.1 Gated Hall device

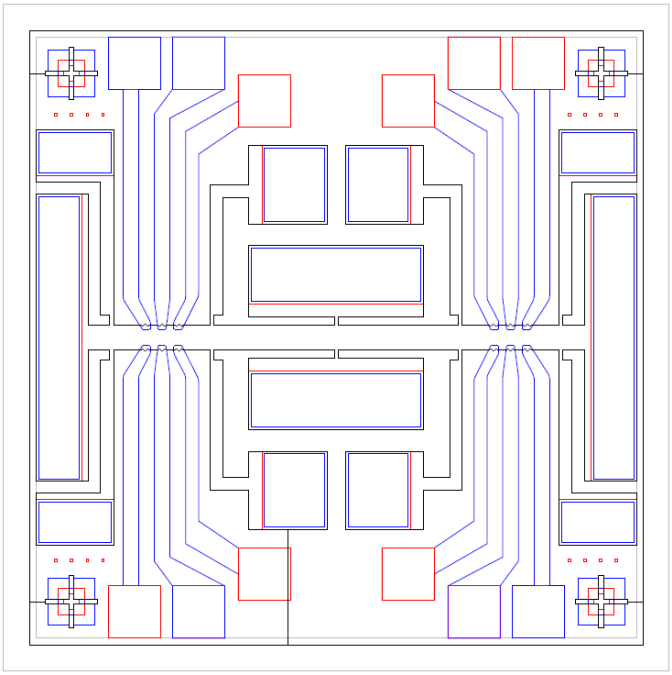

Figure A.1: CAD design of new Hall bar devices intended for ultra-low-temperature work. The mesa/contact overlap is maximised to lower contact resistance, 4 Split-Gate/Top-Gate pairs can be placed on the device. An additional layer of Au is deposited on the contacts by e-beam along with the gates.

After the optimisation of contact resistance and sample quality, the gating of devices without a drop in mobility was possible on V-wafers. Split-Gate/Top-Gate devices were fabricated on wafer V834, intended for ultra-low-temperature, using the optimised recipe (see Chapter 4) and a new mask, shown in Figure A.1, to minimise contact resistance by maximising the I^+I^- contact/mesa overlap. Characterisation at 4.2 K, shown in Figure A.2, showed promising results for low-temperature work and a significant improvement from past gated devices.

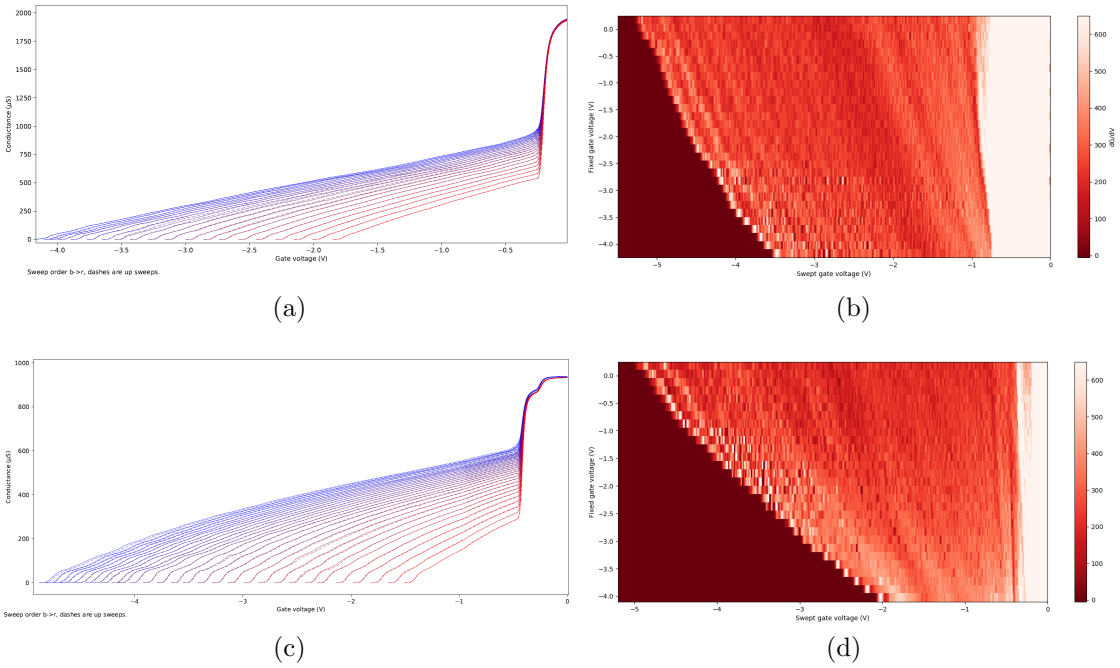

Figure A.2: Split-Gate/Top-Gate sweeps of two QPCs on a gated Hall bar, designed with ohmic geometry for ULT measurements.(a) Trace of device 1, the conductance of this channel is extremely large due to the low-resistance contacts, 1D channel is defined at around 1kΩ. (b) Transconductance of device 1, (c) Trace of device 2 with an added resistance of 1kΩ in the measurement circuit so the definition of the plateaus is shown clearer.

A.2 Characterisation of Gated 4×4 device

The gated 4×4 devices fabricated on V-wafers have low contact resistance and a low resistance per square, making them ideal for future measurements at low-temperatures. The trace of Figure A.3 shows gate-sweeps taken of a flashed device, with an added series resistance of 1 kΩ in order to be able to measure the unusually high conductance of this geometry.

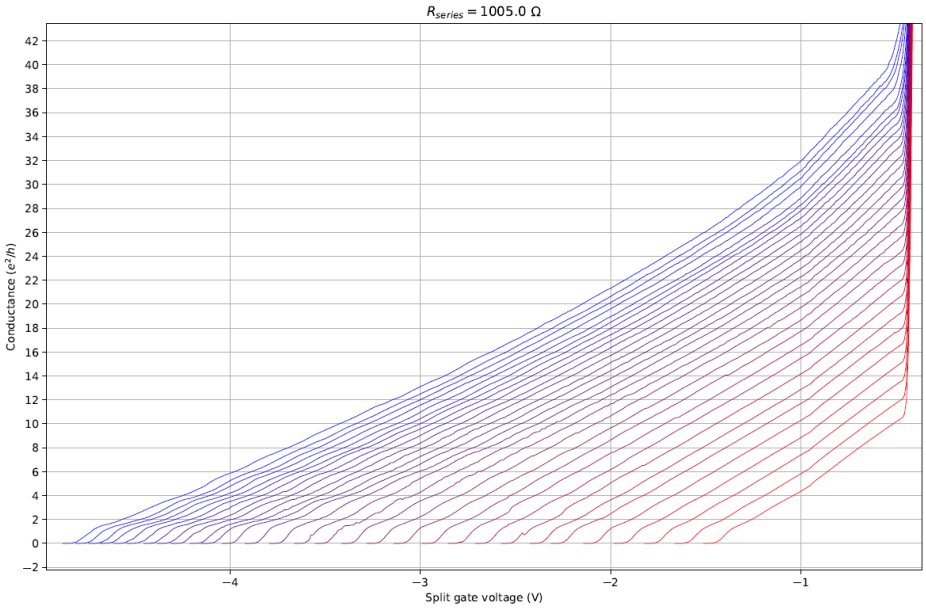

Figure A.3: Split-Gate traces of a gated 4×4 device, with the Top-Gate at a set voltage, traces blue → red in steps of -0.25mV. In units of $\frac{e^2}{h}$. The sample resistance and added 1 kΩ resistor in series with the measurement is subtracted.

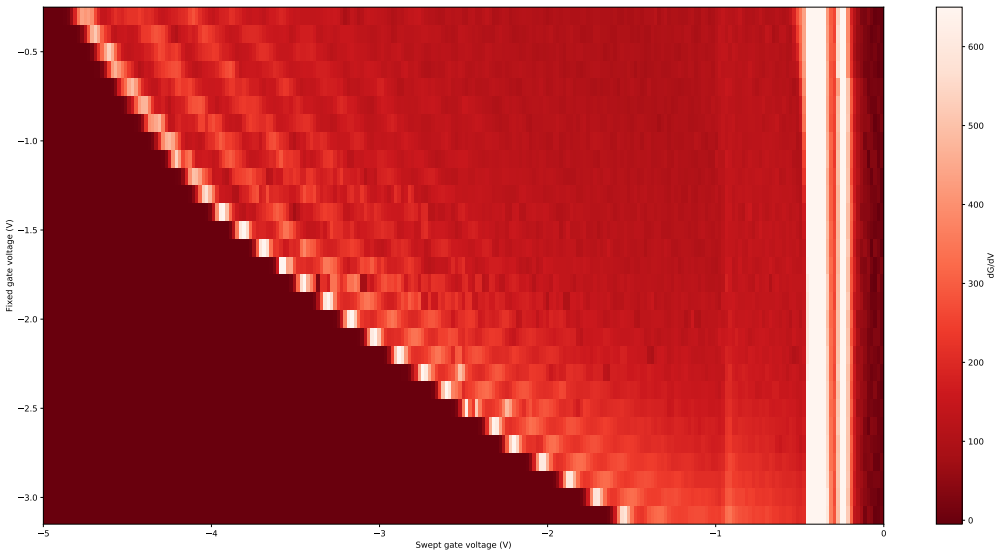

Figure A.4: Transconductance of gated 4×4 device of Figure A.3.

B Methodology for mounting samples to immersion cell

Clean sample thoroughly.

1. Ensure working area is safe from electrostatic discharge (ESD): grounding mat, grounding bracelet and ESD safe tweezers to reduce chance of electrostatic discharge (especially for samples that are gated).

2. Clean/scratch silver pads on immersion cell lid to aid bonding - ensure the CINCH end is grounded with the copper braided connector.

3. Mount sample with epoxy (Ag paint or GE varnish) on Cu plate.

4. Assemble sample and mount onto the cell lid with PEEK screw.

5. Screw the cell-lid onto immersion cell and leak check the cell.

With sample secured with PEEK screw on the immersion cell lid, take cell lid with top hat cover and move to bonder. Ground ESD bracelet to the grounding mat available, especially is the sample is gated :

1. Check bonder parameters are optimal (height, power, number of bonds required can all influence the integrity of bonds).

2. Turn de-ioniser on, directed towards the general bonding area (avoid having it too close to the bonder as it can move the bondwire, making bonding more difficult).

3. Use Au wire only, ideally using a dedicated bonding tip.

4. Bond first to the largest contacts, this is the least resistive path to ground.

5. Subsequently bond to the contact pads of gate arms, allowing for 30s rest in between each bond to eliminate mechanical errors as well as build up of charge.

6. Check integrity of bonds under microscope and by applying a burst of N gas onto the sample after bonding.

The immersion cell for perpendicular field has 11 silver sintered pads to bond to, the 12th line is a dedicated thermal ground to make sure the lattice cools as well. A copper plate sits on the thermal ground and the sample is mounted with Ag paint or GE varnish.

C NTLM-Hall devices

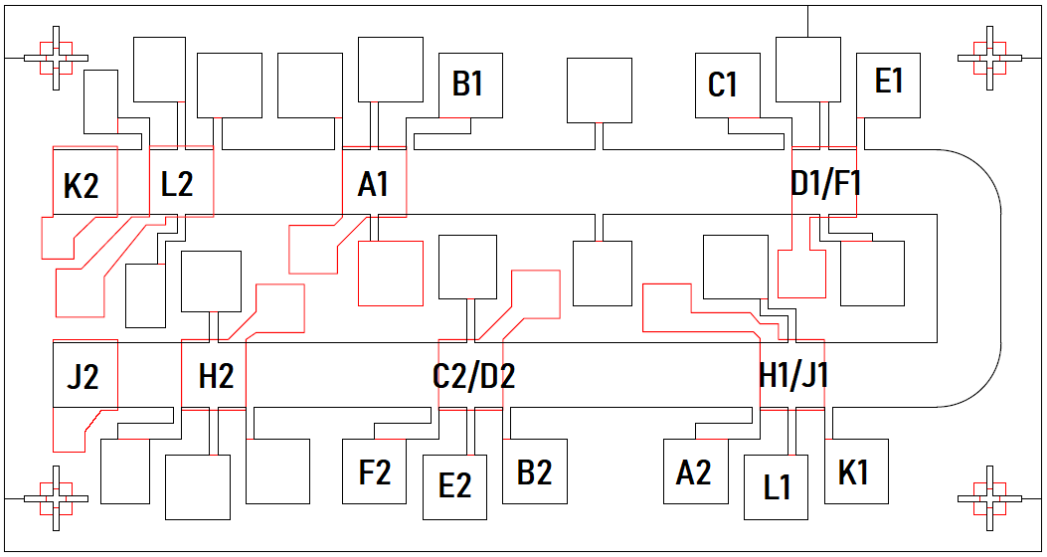

Figure C.5: New NTLM design allows for bonding off-mesa to reduce likelihood of damage to the contacting area, while also having voltage probes to enable measuring the Hall effect to characterise the 2DEG carrier density and additional contacts across each on-mesa contact in order to conduct the same measurement across a contact. Annotated as per bonding of sample V834 NTLM3 ϵ-2, characterisation of which is presented in Table C.2

.

The NTLM-Hall mask, depicted in Figure C.5, was initially designed with the idea to measure the magnetoresistance "under" the contact. Instead, these devices conclusively showed that the voltage measurement across the contact is actually a measurement of the total contact resistance of the contact, so that they serve as additional voltage probes to the middle of the on-mesa ohmic contact. Through electrical characterisation at 4.2 K, it was determined that the extra voltage contacts probe the main contact alone, giving a relationship of $R_{\text{“}under\text{”}} = 2R_C + R_v$, with small contribution from

Table C.2: Summary of electrical measurements on sample V834 NTLM3 ϵ 2, at 4.2K, demonstrating the characterisation of individual resistances of 2DEG and constituents of contact resistance.

Source-Drain	**Dark (Ω)**	**Flashed (Ω)**	**4T**	**Dark (Ω/□)**	**Flashed (Ω/□)**	**4T**	**Dark (Ω)**	**Flashed (Ω)**
K2/L2	45.7	12.4	**Squares**	**2DEG/ □**		**Voltage Across Ohmic**		
L2/B1	277.1	70.7	**4**	36.2	7.1	F2B2	26.9	6.4
A1/D1F1	374.6	106.6	**6.125**	31.4	8.0	F2E2	11.3	2.9
D1F1/H1J1	201.7	55.9	**6**	30.4	7.3	E2B2	14.6	3.5
J1H1/C2D2	150.9	34.9				A2K1	24.2	6.3
C2D2/H2	116.2	28.8				A2L1	11.4	2.8
H2/J2	59.2	16.3				L1K1	12.8	3.5
						C1E1	21.8	6.1

I+V+	**V-**	**Contact Resistance (Ω)**		**End Resistance (mΩ)**		**Transfer Length (μm)**	
		Dark	Flashed	Dark	Flashed	Dark	Flashed
D1F1	**C1**	12.51	2.98	17.5	32.0	27.5	38.3
	E1	10.08	3.02	29.6	5.7	30.7	28.7
	K1	12.55	3.61	19.3	5.1	27.9	27.6
H1J1	**A2**	11.35	2.94	17.5	8.2	27.9	30.4
	B2	14.04	3.67	18.4	23.6	27.3	34.8
C2D2	**F2**	11.29	3.69	18.5	5.0	28.1	27.4

R_v and more accurately, noting that resistance to the left and right of a contact may vary: $R_{\text{“}under\text{”}} = R_C^L + R_C^R$. As discussed before, this is the case when the contact is long compared to the transfer length. These devices were further used as a way to probe the end-resistance of on-mesa contacts using the extra voltage contacts, similar to the cross-bridge Kelvin method [1] with results being independent of the voltage probe chosen.

Table C.2 shows the combination of measurements done on such a device. Note that the sum of the contact resistances directly measured equals the 4-terminal measurement of the “voltage across the ohmic contact”. Samples of this type were also bonded with a multitude of wires to check continuity of the contacts’ surface at 4.2 K and variations in end-resistance with respect to bond placement, as well as to measure the sheet resistance of the ohmic contact alloy at the top. Bonding was selective due to the limited number of LCC pads (20) of the LCC the sample is mounted onto, so samples were redipped and rebonded numerous times.

The results were identical whether bonding off-mesa on a bondpad shorting to an on-mesa contact, on the on-mesa contact or placing multiple bonds on it. Samples of this type were fabricated at a 430°C for 80 s RTA and the resistance of the top layer of on-mesa 200 μm × 200 μm contacts was 300 mΩ/□.

D Current Balancing on a 4 × 4 device

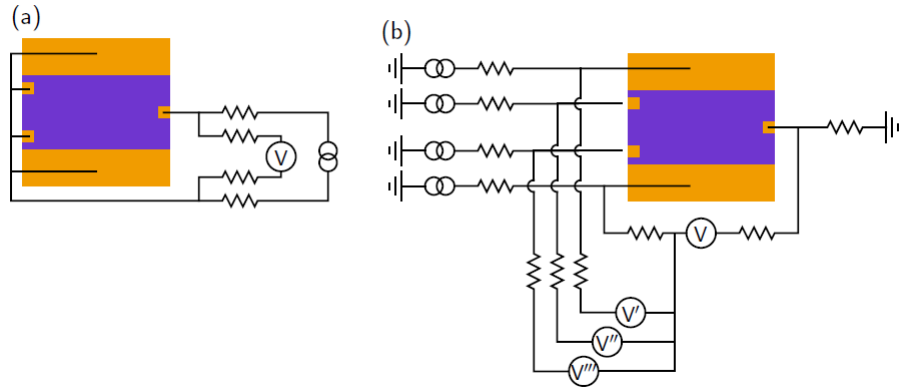

Figure D.6: Measurement setups for measuring electrical resistance to Noise Thermometer contact. (a) Asymmetrically measuring current fron NT to the larger contacts, (b) simultaneously driving current through all the contacts, with the NT contact earthed.

The 2DEG resistance per square is measured by a standard 4-terminal measurement to be 30.1 $\Omega/\square$ in the dark. Driving all individual contacts I^+, I^-, V^+, V^- with independent currents and NT contact earthed until the potentials measured are equal, as a test of the symmetry of current flow in 4×4 samples and the effective resistance for thermalisation to the NT contact. AC signal is adjusted until all LIAs read the same value, $52.89 \pm 0.02\mu V$, using MΩ resistors to define the current. All current flows to the Noise Thermometer contact, and therefore we can compute:

$$R_{IV:NT} = \frac{52.89\mu V}{\frac{1.000V}{0.9947M\Omega} + \frac{1.027V}{0.9947M\Omega} + 2 \times \frac{0.015V}{1M\Omega}} = = 25.57 \pm 0.01\Omega \qquad \text{(D.1)}$$

This is the effective thermal resistance to the NT contact in the dark.

Subsequently, removing the drive from V^+V^-, current is only applied from the large 4 mm ohmic contacts to the NT. Then the two voltages to the NT contact are balanced:

$V_{I^+:NT} = V_{I^-:NT} = 52.05 \pm 0.02\mu V$,

$$R_{I^\pm:NT} = \frac{52.05\mu V}{\frac{2.027V}{0.9947M\Omega}} = 25.54 \pm 0.01\Omega, \tag{D.2}$$

so that the resistance experienced by current flowing the NT contact remains largely the same as measured by both methods in equations (D.1, D.2) due to the sample symmetry and the much smaller resistance of the large contacts. With $V_{V^+:NT} = 51.72\mu V = V_{V^-:NT}$, so that current is symmetric left and right of the NT contact by design and due to the homogeneity of the 2DEG. Furthermore, this shows the large contacts dominate thermal transport as it is the most efficient path of current flow. As a further test, current was driven through the main contacts individually to check for symmetry. These are summarised in Table D.3.

The sample was illuminated with red LED using a K2400 SMU at 10 mA for 3 minutes. The resistance per square of 2DEG was remeasured to be 7.7 $\Omega/\square$ after illumination.

Table D.3: Symmetry checks on 4mm sample. All voltages measured to the NT ohmic, to determine the effective resistance by current flowing to it. Dark measurements in white background, light blue background measurements after illumination. Sample illuminated with red LED using a SMU current at 10 mA for 3 minutes.

Current source	I^+:NT (μV)	I^-:NT (μV)	V^+:NT (μV)	V^-:NT (μV)	R: NT (Ω)
I^+	32.4	20.1	29.9	22.1	31.4
	7.02	4.50	6.48	4.94	6.80
I^-	19.5	31.78	19.5	29.5	31.6
	6.87	6.87	4.84	6.34	6.83
I^+ & I^-	52.05	52.05	51.72	51.72	25.54
	11.30	11.38	11.38	11.31	5.593
$I^+I^-V^+V^-$	52.89	52.89	52.89	52.89	25.57
	11.57	11.57	11.57	11.57	5.603

Repeating current balancing, drive current through all contacts, to determine effective thermal resistance to NT contact under equipotential in the illuminated condition:

$V_{I^+:NT} = V_{I^-:NT} = V_{V^+:NT} = V_{V^-:NT} = 11.57 \pm 0.01\mu V$

$$R_{IV:NT} = 5.603 \pm 0.005\Omega \tag{D.3}$$

And driving current from both large contacts to the N.T. :
I^+ 1.024 V via 0.9947 MΩ.
I^- 1.000 V via 0.9947 MΩ.

$$\begin{aligned} V_{I^+:NT} &= V_{I^-:NT} = 11.38 \pm 0.01\mu V \\ V_{V^+:NT} &= 11.30 \pm 0.01\mu V \\ V_{V^-:NT} &= 11.31 \pm 0.01\mu V \end{aligned} \tag{D.4}$$

Thus the illuminated resistance under equipotential to the N.T. contact is $R_{I^\pm:NT} = 5.593 \pm 0.005\Omega$.

Concluding Remarks on Symmetry Checks

This series of electrical measurements indicates the resistance experienced by current flowing to the NT contact under equipotential conditions, which is equivalent to the current path for thermalisation to the Noise Thermometer such that the effective resistance to the NT contact is $R_{NT:IV} = \frac{V}{\sum I}$, with all contacts being at an equipotential. The symmetric design of the 4×4 is key to being able to determine this accurately.

Thermalisation happens mainly through the large ohmic contacts. There is no large variation in contact resistance of the ohmic contacts and the two dimensional electron gas is homogeneous w.r.t. L.H.S and R.H.S. of the NT contact, making the current thermal model sufficient to describe this system.

This sample was cooled to low temperatures (see chapter 5), measuring the temperature dependence of the I^+I^- source drain resistance to show a superconducting jump below 1 K.

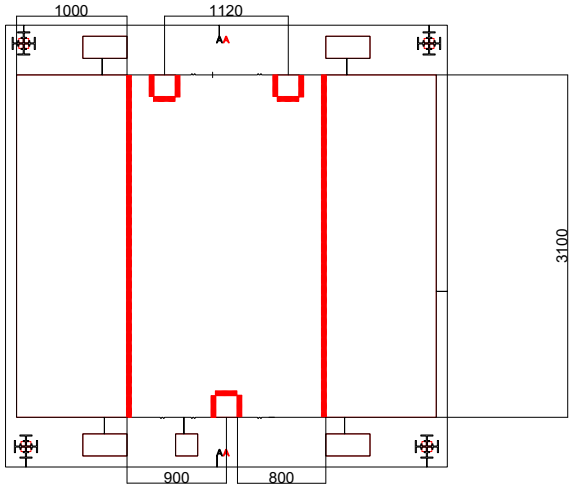

Figure D.7: Dimensions of the 4 mm sample. The voltage probes exist for checking 2DEG resistance, while the isolated contact is to be coupled to a Noise Thermometer, to determine thermalisation in the middle of the sample. The sample is symmetric by design, current balancing tests therefore show thermalisation is analogous to a bar with two fixed temperatures at each end, with equilibrium being reached in the middle of the bar, therefore giving an upper bound on electron temperature in the sample, as discussed in the introduction (section 1.3).

E Thermometry

There are two types of thermometers; primary and secondary. Primary thermometers depend on a physical effect and are universal, secondary thermometers are calibrated against such a primary thermometer to indicate temperature. On the Kelvinox we have both types. Secondary thermometers are used for their small size and ease of use, their primary function is to monitor the temperature of different fridge stages. A current sensing noise thermometer (primary thermometer) was installed on the mixing chamber, in the same specifications as the publication of Royal Holloway's low temperature group [2], for accurate determination of temperatures achieved by the dilution process. A ^{3}He viscometer, tuning fork thermometer, is used in the immersion cell to determine the temperature of the bath and the silver sintered heat exchangers of the leads to the sample.

Resistive Thermometry

Resistive thermometers are the cheapest and most common secondary thermometers. By secondary, it is meant that they are not based on a reproducible physical phenomenon, but rather they are well calibrated over a temperature range. This is the obvious downside of secondary thermometers, they often need recalibration against a primary thermometer to make sure that the temperature dependence has not changed. The advantages of secondary thermometers are:

1. Ease of measurement; they do not need a lot or specific equipment to measure.
2. Short time constants for an accurate resistance measurement.
3. Stability and reproducibility; well calibrated over a certain temperature range.
4. Small size, so that they do not take up significant space in the fridge.
5. Insensitive to environmental changes such as applied magnetic fields.
6. Good and well calibrated temperature response over a certain range.
7. Low-cost and easy to make.

The Kelvinox setup uses carbon resistors (Allen-Bradley type) as well as Ruthenium Oxide resistors (RuO_2) which are more accurate in the same temperature range and calibrated for slightly lower temperatures (down to 0.05K). Due to the effect of field on these resistors, they are mounted past the field cancelled region, and therefore introduce a further error to measuring the sample temperature, since there is some difference in thermalisation.

Our most accurate secondary thermometer is a ruthenium oxide (RX-202A) from Lakeshore Cryogenics mounted on the mixing chamber.

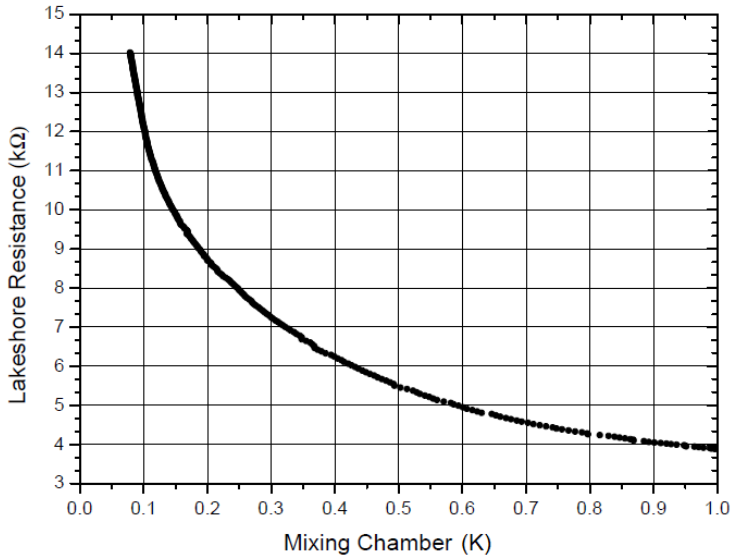

Figure E.8: Lakeshore Ruthenium Oxide (type RX-202A) Thermometer on Mixing Chamber cross-calibrated with the Kelvinox's mixing chamber temperature as read from the Oxford Instruments IGH software.

Tuning Fork

The immersion cell is equipped with a tuning fork thermometer. The tuning fork sits inside the immersion cell, which is filled with ^{3}He, and measures the change in the frequency response of the tuning fork due to the known temperature dependence of the viscosity of ^{3}He. ^{3}He does not become a superfluid in regular dilution temperatures and also has a viscosity dependence that is well characterised with temperature, so that determining this viscosity can be used as a thermometer with ease, especially if cross-calibrated with other thermometers.

The optimal working range of temperature ofa ^{3}He viscometry thermometer is 5-100 mK [3] , which is ideal since ruthenium-oxide resistors are unreliable below 100 mK. The viscosity of ^{3}He is related to temperature through Stokes' hydrodynamic model:

$$\eta T^2 = const. \tag{E.5}$$

The quality factor (Q-factor) of the oscillation is inversely proportional to the dampening mechanism, the viscosity of the liquid, then, after additionally

applying an empirical correction term for low temperatures, a relation can be made to be used for viscometry [3, 4]:

$$Q \propto T\sqrt{1 - 2.92T} \tag{E.6}$$

with the constant of proportionality of equation E.6 to be determined by calibration from another thermometer, in our case this was done by recalibrating against the existing RuO_2 thermometer of the mixing chamber, itself calibrated against the mixing chamber current sensing noise thermometer.

The in-phase resonant current is measured using a frequency sweep. The shape of the curve is that of a Lorentzian. The resonant current is a linear function of the quality factor and therefore:

$$I \propto Q \propto T\sqrt{1 - 2.92T} \tag{E.7}$$

Figure E.9 shows a frequency scan of the resonant current before and after filling the ^{3}He immersion cell on the Kelvinox cryostat.

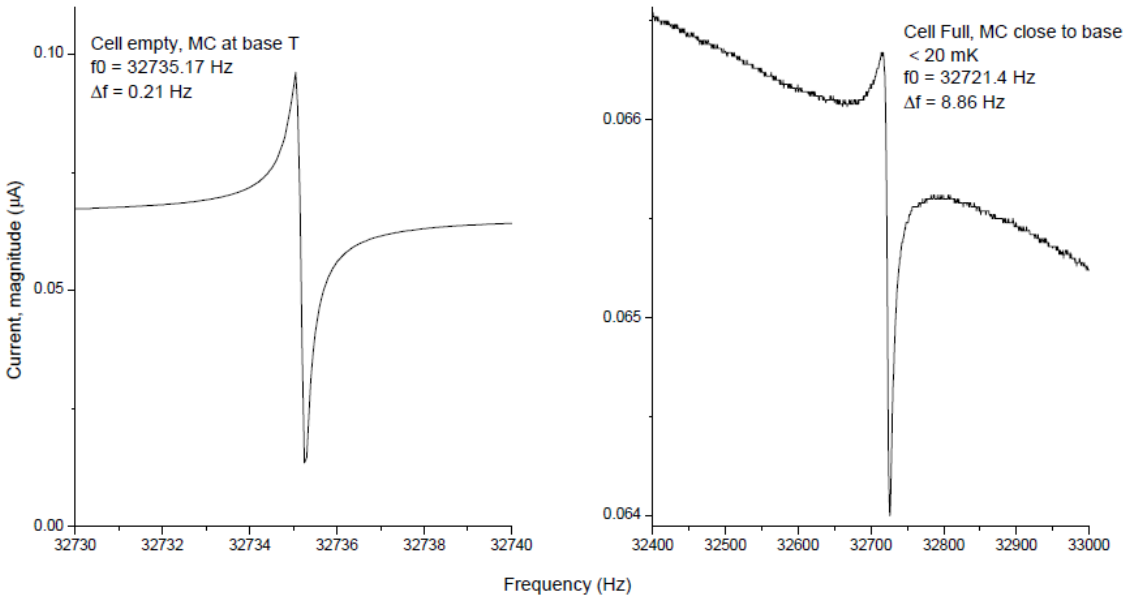

Figure E.9: Tuning fork peaks before and after ^{3}He cell fill. Data taken at 6 mK.

The tuning fork thermometer is most accurate in the low mK range, where resistive thermometers are unreliable. Furthermore, it has been shown that

even when empty, there is no effect of applied magnetic field to the oscillation, therefore it is also ideal for in-field measurements. Most importantly, this method provides the possibility of measuring the temperature constantly, especially if the range of the frequency scan is optimised.

By taking a series of traces such as Figure E.9, the relationship between the resonance linewidth, the difference between the 3 dB frequencies (Δf) and temperature can be mapped as shown in Figure E.10. Each trace is fitted to a Lorentzian to accurately determine the resonance frequency, as shown in Figure E.11. The resonance linewidth of the tuning fork has been calibrated at various set temperatures of the Kelvinox fridge, by warming the mixing chamber of the fridge to a stable temperature, cross calibrated with the noise thermometer and secondary resistive thermometers.

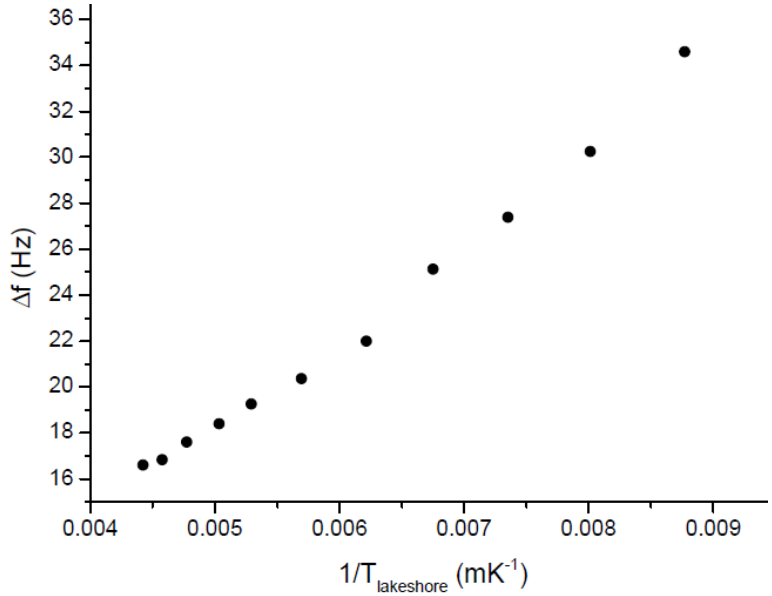

Figure E.10: Tuning fork resonance linewidth calibration. All data here is with ^{3}He cell full.

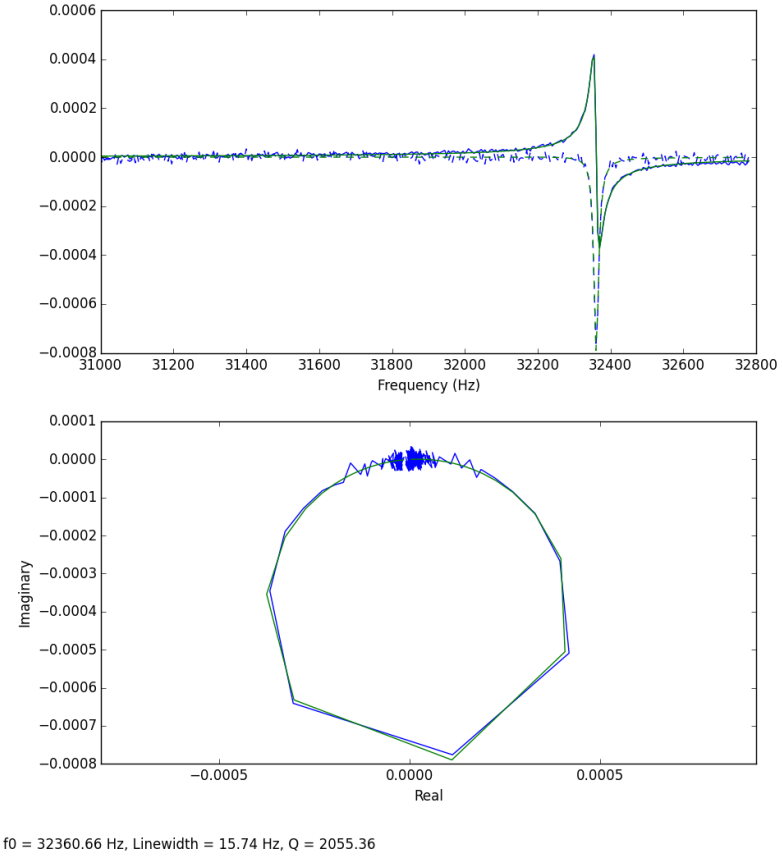

Figure E.11: Lorentzian fit to tuning fork spectrum. This plot is used to determine resonant frequency (f_0), linewidth (Δf), quality factor (Q) and goodness of fit.

Calibration against Mixing Chamber RuO_2 Resistor

Using a resistor coupled to the mixing chamber through a PID loop, the Kelvinox's mixing chamber was warmed at various temperature stages, in order to calibrate the temperature achieved by each heating current. This is because at another stage the same was done to heat the fridge and take magnetoresistance measurements at these different ranges. The tuning fork works in field, but the resistive thermometers are unreliable both in field and close to base temperature, therefore this calibration was needed prior to embarking on more interesting experiments. Figure E.12 shows the calibration of temperature vs power applied to the mixing chamber.

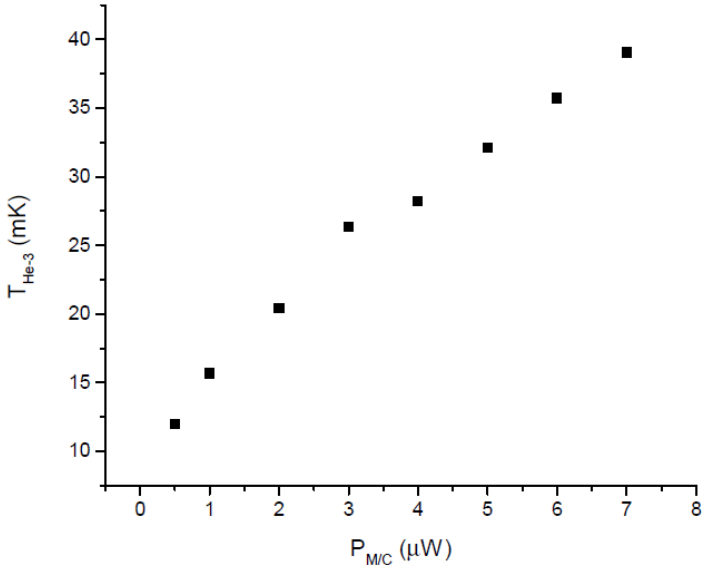

Figure E.12: Calibration of Mixing Chamber heater power of the Kelvinox against ^3He immersion cell temperature as measured with a Tuning Fork located inside the filled immersion cell.

Electron Thermometry-SdH Oscillations T_e vs T_{fridge}

The amplitude of longitudinal magnetoresistance oscillations is strongly temperature dependent. Such effects are those oscillations of the Aharonov-Bohm [5, 6] and Shubnikov de Haas effects [7, 8]. As such, in a well calibrated setup, these oscillations would give exact electron temperature and apart from interesting electron-electron effects that might arise in the low temperature regime, this type of thermometry was also a driving factor in many experiments on the Kelvinox cryostat. The temperature dependence of the Aharonov-Bohm effect is shown in Figure E.13 and unsuccessful attempts at Shubnikov-de Haas thermometry at Appendix E.

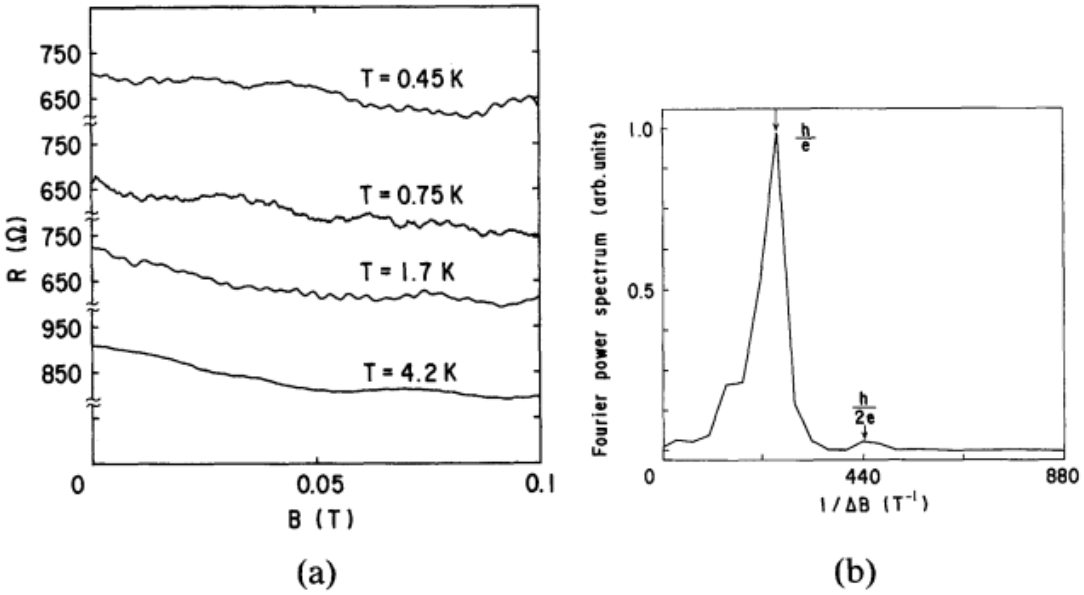

Figure E.13: Image taken from [9]. Temperature dependence of Aharonov-Bohm effect on GaAs/AlGaAs. (a) Longitudinal magnetoresistance at different temperatures, (b) Fourier peaks at 0.75 K corresponding to h/e and h/2e oscillations. The amplitude of the peaks can be used for primary thermometry and accurate electron temperature.

Two Aharonov-Bohm devices were characterised (Figure E.14) at 4.2 K for the possibility of such a measurement, designed by Prof Chris Ford.

Anti-dot characterisation 4.2K

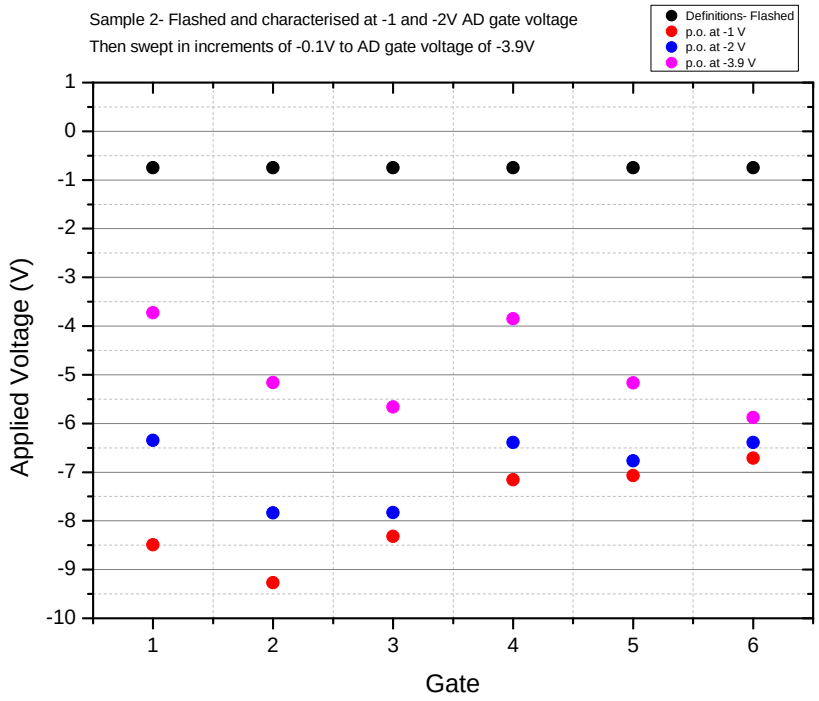

Figure E.14: Pinch-off Voltages of AB device 2's Split Gates, for different antidot Gate voltages, at 4.2K. Definition is shown in black points, pinch-off at -1 V on the antidot gate is shown in red, blue at -2 V and pink at -3.9 V, in zero-field.

Shubnikov-de-Haas Thermometry Attempts

A first attempt to correlate magnetoresistance with thermometry was not successful - the sample depicted in Figure E.15 started drifting upwards in resistance in the middle of the fridge run, becoming extremely resistive. Data of Figure E.15 shows the effect of flashing to the low-field Shubnikov de Haas effect: longitudinal resistance drops, inhomogeneities are reduced, the traces become non-hysteretic and there are more oscillations onsetting earlier, consistent with the sample having more carriers.

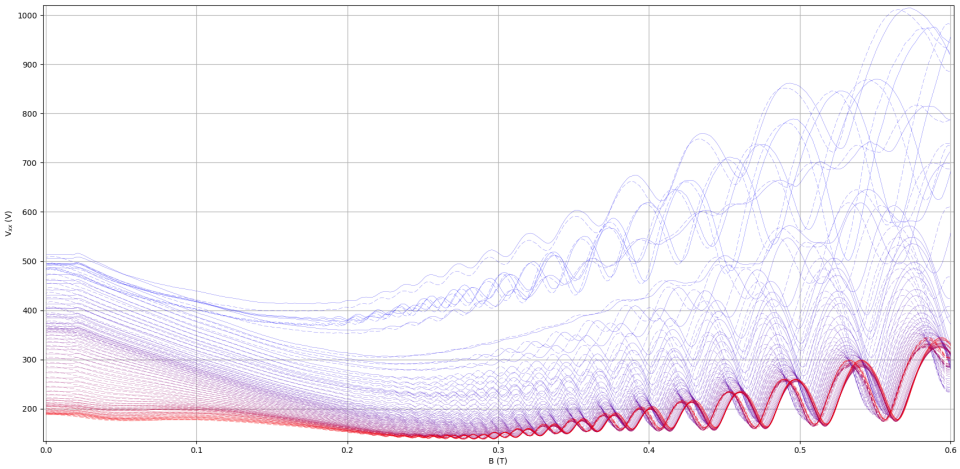

Figure E.15: W475 4×4 gated sample cooled on the Kelvinox. Sample was flashed incrementally with longitudinal magnetoresistance to measure the Shubnikov de Haas effect and the effect of flashing. Blue → red shows the effect of flashing, dashed traces are traces are ramping down in field. The traces become reproducible when the sample is illuminated to saturation.

Figure E.16 shows such magnetoresistance traces, taken at base temperature of a W475 gated Hall bar and after heating the mixing chamber. The inhomogeneity ("ringing") arising at base temperature made this impossible to calibrate. This effect was attributed to improper isolation of the screened room introducing noise and masking the measurement. In subsequent runs these issues were addressed.

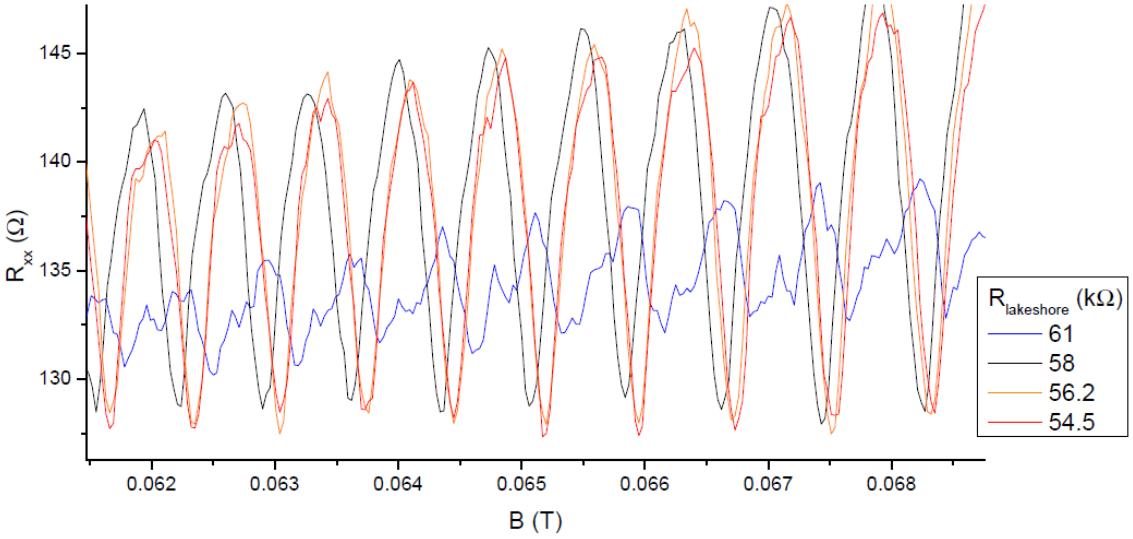

Figure E.16: Zoomed-in Shubnikov de Haas traces, on a gated Hall bar on wafer W475, with the immersion cell filled with pure ^{3}He. Base temperature trace is shown in blue, subsequent heating traces show the large inhomogeneity disappearing, however there was no direct correlation that could be drawn from these traces sufficient for thermometry.

Bibliography

[1] G. Reeves, A. Holland, B. Harrison, and P. Leech, in (Oct. 1997), pp. 492–495.

[2] A. Casey, F. Arnold, L. V. Levitin, C. P. Lusher, J. Nyéki, J. Saunders, A. Shibahara, H. van der Vliet, B. Yager, D. Drung, and et al., Journal of Low Temperature Physics (2014) 10.1007/s10909-014-1147-z.

[3] N. Samkharadze, A. Kumar, M. J. Manfra, L. N. Pfeiffer, K. W. West, and G. A. Csáthy, Review of Scientific Instruments **82**, 053902 (2011).

[4] M. P. Bertinat, D. S. Betts, D. F. Brewer, and G. J. Butterworth, Journal of Low Temperature Physics **16**, 479 (1974).

[5] M. Kataoka, C. J. B. Ford, G. Faini, D. Mailly, M. Y. Simmons, D. R. Mace, C.-T. Liang, and D. A. Ritchie, Phys. Rev. Lett. **83**, 160 (1999).

[6] M. Kataoka, C. J. B. Ford, G. Faini, D. Mailly, M. Y. Simmons, and D. A. Ritchie, Phys. Rev. B **62**, R4817 (2000).

[7] Q. Qian, J. Nakamura, S. Fallahi, G. C. Gardner, J. D. Watson, S. Lüscher, J. A. Folk, G. A. Csáthy, and M. J. Manfra, Phys. Rev. B **96**, 035309 (2017).

[8] P. T. Coleridge, Phys. Rev. B **44**, 3793 (1991).

[9] K. Aihara, M. Yamamoto, K. Iwadate, and T. Mizutani, Japanese Journal of Applied Physics **30**, L1627 (1991).